Polyelectrolyte nanocapsules as modern drug delivery system for lipophilic drug candidates

D i s s e r t a t i o n

zur Erlangung des akademischen Grades

doctor rerum naturalium (Dr. rer. nat.)

vorgelegt der

Naturwissenschaftlichen Fakultät I

Biowissenschaften

der Martin-Luther-Universität Halle-Wittenberg

von

Frau Apothekerin Claudia Nyakas

geb. Preetz, am 08.01.1982 in Stendal

Gutachter:

1. Prof. Dr. Karsten Mäder

2. Prof. Dr. Reinhard Neubert

3. Prof. Dr. Wolfgang J. Parak

Halle (Saale), 16.07.2012

„Was wir Ergebnisse nennen, ist nur der Anfang.“

(Ralph Waldo Emerson)

TABLE OF CONTENTS

LIST OF ABBREVIATIONS

AF4	asymmetrical flow field-flow fractionation
AFM	atomic force microscopy
AGP	arabinogalactan protein
BCS	biopharmaceutical classification system
CARR	λ-carrageenan (in tables)
CDC	colloidal drug carriers
CHI	chitosan (in tables)
CLSM	confocal laser-scanning microscopy
CMC	critical micelle formation concentration
DDS	drug delivery system
DiI	1,1'-dioctadecyl-3,3,3',3'-tetramethylindocarbocyanine perchlorate
DiR	1,1'-dioctadecyl-3,3,3',3'-tetramethylindotricarbocyanine iodide
DLS	dynamic light scattering (=PCS)
DZP	diazepam
E-No.	e. g. E 1450 – identification number for food additives
EPR	electron paramagnetic resonance spectroscopy (synonym: ESR electron spin resonance)
FFF	field-flow fractionation
GA	gum arabic
GEL	gelatin type A
^{1}H NMR	proton nuclear magnetic resonance
HD-PMI	2-heptadecyl-2,3,4,5,5-pentamethylimidazolidine-1-oxyl
HAc	acetic acid
HPH	high-pressure homogenisation
i.v.	intravenous route of application
LBL	layer-by-layer technique
LCT	long-chain triglycerides
LD	laser diffraction
log$P$	octanol-water partition coefficient
MALS(D)	multi-angle light scattering (detector)
MCT	medium-chain triglycerides
M_r	relative molecular weight
M_w	weight average molar mass (in AF4)
MWCO	molecular weight cut off
NaPP	tetrasodium pyrophosphate
NC	nanocapsules (in general)
NC3 / NC5	NC-OSA-CHI-CARR-2.5% / NC-OSA-CHI-CARR-CHI-CARR-1.11%
n. d.	not determined
NDDS	nanoscaled drug delivery system
NIBS	non-invasive back scattering
NLC	nanostructured lipid carriers
NR	nile red (5H-Benzo(α)phenoxazin-5-one, 9-(diethylamino)-)
OSA starch	octenyl succinic anhydride-modified starch
PCL-b-PEO	polycaprolactone-block-poly(ethylene oxide)
PCS	photon correlation spectroscopy
PDI	polydispersity index
PE	primary emulsion template E-OSA5-5%
PEG	polyethylene glycol
PES	polyether sulphone
Ph. Eur.	European Pharmacopoeia
pI	isoelectric point
pK_a	negative logarithm to the base 10 of the acid dissociation constant K_a
PLA	poly(lactic) acid
p.o.	peroral route of application
PSD	position sensitive photo detector

pTHPP	5,10,15,20-tetrakis-(4-hydroxyphenyl)-21H,23H-porphine
PVDF	polyvinylidene fluoride
RI	refractive index
RID	refractive index detector
RSV	resveratrol
s. d.	standard deviation
SAL	salicylic acid
SBP	sugar beet pectin
SDS	sodium dodecyl sulphate
SLN	solid lipid nanoparticles
SLS	static light scattering (=LD)
SNOM	scanning near-field optical microscopy
SPM	scanning probe microscopy
STM	scanning tunneling microscopy
TB	tempol benzoate (4-Hydroxy-2,6,6,6-tetramethylpiperidine-1-oxyl)
TEM	transmission electron microscopy
TG	thermogravimetry
UF	ultrafiltration
UHV	ultra-high vacuum
URT	ultrasonic resonator technology
% (v/v)	volume percentage
% (w/w)	weight percentage

SAMPLE DESCRIPTION CODES

E-OSA5-<u>5%</u>	emulsion obtained from a 5 % OSA solution, containing <u>5 % MCT</u> (for preparation in detail see Table 2)
NC-OSA-GEL-GA-3%	nanocapsules obtained from an OSA emulsion, a gelatin type A (GEL) solution, and a gum arabic (GA) solution, containing 3 % MCT (for preparation in detail see Table 4)

1 INTRODUCTION

1.1 The need of nanocapsules

Richard P. Feynman became the father of nanotechnology as he first dealt with atomic matter in a lecture titled 'There's Plenty of Room at the Bottom' in 1959 [1]. However, only in 1974 the term 'nanotechnology' was firstly mentioned by Norio Taniguchi [2]. Although this has now been plenty of years ago, it is still considered a modern field of physical fundamental research, allowing the manipulation of matter in the atomic scale [3]. In the broadest sense, today nanotechnology includes all areas dealing with nanostructures. The prefix 'nano' (n) has its origin in the Greek language and means 'dwarf'. In science and technology 'nano' stands for the order of magnitude 10^{-9} and thus describes very small dimension units between 'micro' (μ, 10^{-6}) and 'pico' (p, 10^{-12}). Hence, 1 nm is equal to 10^{-9} m.

During the past decades, research on nanostructures and their practical applications attracted an increased attention which also reached the sectors of medicine, food technology, and articles of daily use. In the sector of medicine, the trend led to the establishment of the term 'nanomedicine', defined in 1999 as the medical application of nanotechnology by Robert A. Freitas Jr. [4], who described it as 'the comprehensive monitoring, control, construction, repair, defense, and improvement of all human biological systems, working from the molecular level, using engineered nanodevices and nanostructures'. Shortly after the creation of this word, a rising number of scientific publications using this term was observed, followed by the release of the journals 'Nanomedicine: Nanotechnology, Biology and Medicine' (2005) and the 'International Journal of Nanomedicine' (2006). In the meanwhile they were accompanied by 'The Open Nanomedicine Journal' (2008), 'Nanomedicine and Nanobiotechnology' (2009), the 'Journal of Nanomedicine and Nanotechnology' (2010), and the 'Journal of Nanomedicine and Biotherapeutic Discovery' (2011). One focus of nanomedical research is the use of nanotechnology in the administration of medicines. In pharmaceutical research the development of modern colloidal drug carriers (CDC) is currently one of the main topics. They show great promise for overcoming the common problems of poorly water-soluble drugs and drug candidates, especially for those of the classes II (high permeability) and IV (low permeability) of the biopharmaceutical classification system (BCS) [5-7]. Due to their poor bioavailability those drugs have to be administered in large dose rates which result in a higher risk and more frequent occurrence of side effects. There is a need for nano-sized carriers due to the fact that often the therapeutic goal cannot be achieved with micron-sized or even larger drug delivery systems (DDS). Regarding intravenous application, poor water solubility of injection candidates and drug targeting are some of the tasks which have been solved by nanoscaled dosage forms. Especially for the parenteral way of application, dosage forms in the nanoscale are preferable because they can be administered without any risk of embolia due to a size considerably smaller than one micrometer. Furthermore, high food dependence or insufficient bioavailability of drugs after peroral application can be circumvented by carriers in the nanoscale. They stand out due to the facility of transport through biological barriers [8].

In the group of CDC, approaches have led to nanostructured lipid carriers (NLC), cubosomes, solid lipid nanoparticles (SLN), nanodispersions, nanocapsules, nanospheres, nanoemulsions, nanotubes, and microemulsions. CDC with an aqueous core instead of oil are liposomes and polymersomes (polymer-based vesicles) [9,10]. The term 'nanoparticle' is frequently used only for nanospheres due to their solid state, sometimes including nanocapsules [11,12]. Nanospheres are polymeric particles with a completely solid character which the drug is dispersed in throughout the particle. Nanoemulsions are usually distinguished from nanoparticles because of the liquid state. In nanoemulsions and nanocapsules the drug is located in the oily core which is in case of nanocapsules surrounded by a solid polymeric shell [13]. Hence nanocapsules are CDC which can morphologically be ranged between nanoemulsions and nanospheres [14] (Figure 1).
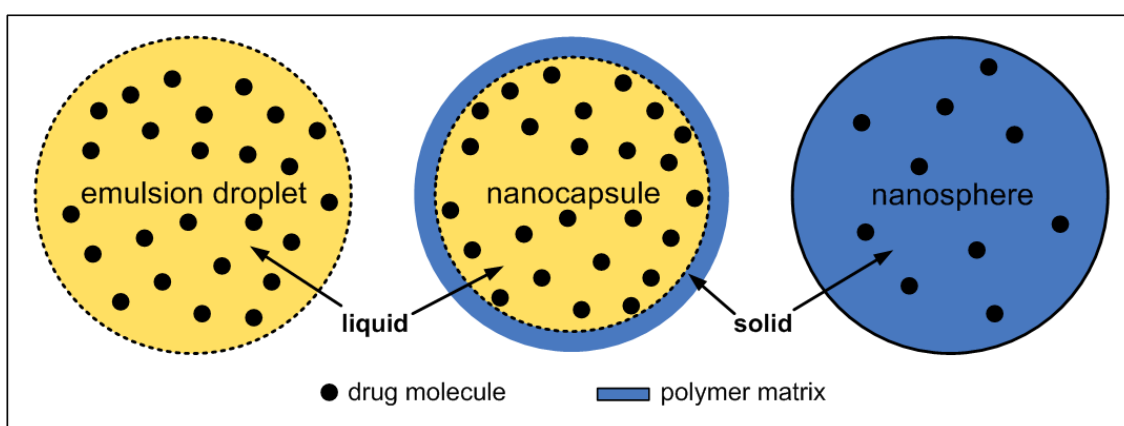
Figure 1 Schematic design of an emulsion droplet, a nanocapsule, and a nanosphere

In theory, nanocapsules are superior to nanoemulsions because the shell prevents direct contact of the encapsulated drug with the environment. Therefore, interactions between drug and physiological contents should be minimized. Degradation of entrapped drug molecules and irritation at the site of administration might be reduced. Furthermore, the polymeric shell is responsible for the long-term stability of the particles (i.e. enables storage). Since they are expected to exhibit increased stability and reduced permeability through the shell, nanocapsules might allow controlling the release rate in contrast to emulsions by manipulating the characteristics of the polymer envelope. The advantage of nanocapsules over nanospheres is chiefly a much higher degree of drug load [14]. In physically loaded nanocapsules, the drug to polymer ratio can be as high as 5:1, when the core consists of pure drug, while this ratio is usually around 1:10 for nanospheres [15]. Another advantage is the low polymer content compared to nanospheres. However, nanosuspensions display a considerable alternative to emulsions or capsules due to an equivalent or even higher drug load capacity. This can be explained by the fact that liquids are capable of uptaking higher amounts of drug than solids. But nanosuspensions need to solve the task to stabilise the dispersed drug in the dispersant. Among nanoemulsions and nanodispersions, nanocapsules compete with lipid-based nanocarriers like SLN and NLC (oil-loaded SLN). Though for both systems nearly 100 % incorporation rate, controlled release and protection from the outer environment have been claimed [16-20], former [21-23] and newer studies [24] showed fundamental problems within these formulations. For both systems, missing protection from the outer environment and low incorporation capacities as well as poor long-term stability (gelation, particle growth) were found. These findings are not surprising considering that crystalline solid lipids do not tend to incorporate

large amounts of foreign molecules. With respect to peroral application, the low incorporation rates are unfavourable, whereas particle growth and platelet shape are a risk for the intravenous route. Hence, nanocapsules are preferred over SLN and NLC.

Several nanosized DDS have reached the commercial market in the past, including mixed micelles (Konakiom MM™, 2000), microemulsions (Sandimmun Optoral™, 1994, Neoral™, 1995) nanosuspensions (Rapamune™, 2001; Megace ES™, 2005; Abraxane™, 2005), nanoemulsions (Intralipid™, 1962; Diazepam Lipuro™, 2006) and liposomes (AmBisome™, 1993, i. v. administration; DaunoXome™). However, nanocapsules are still in the research state although the term 'nanocapsule' has been named in a pharmaceutical context even in 1973 by Birrenbach [25]. Due to the advantages of this dosage form, such as high drug load, protection capacity against external influences, long-term stability, improved bioavailability for water-insoluble drugs and suitability for intravenous application, further research on nanocapsules is essential.

1.2 Research objectives

The aim of the present thesis was to contribute to the development of core-shell structured nanocapsules and thereby to improve the administration and bioavailability of lipophilic drugs by a dosage form for intravenous application. Thus, the desired nanocapsules were required to be produced by a non-intricate preparation process, resulting in a size in the submicron range with a narrow size distribution, in good long-term dispersion stability, as well as a drug load capacity (i.e. oil content) as high as possible, allowing for a high incorporation rate for lipophilic substances. After development, the nanocapsules had to be well characterised physico-chemically in order to identify whether the desired properties had been achieved. As it is a requirement for drugs in general, a focus of this work was to prepare physiologically tolerable formulations only. A further aim was to improve the capsule shell properties in terms of thickness, rigidity, and stiffness. The purpose was to achieve a better mechanical stability against external load such as during storage and injection into blood vessels compared to emulsions. Moreover, a solid capsule shell was expected to have a beneficial impact on the light protection capability for incorporated light-sensitive drugs. Additionally, a thicker and mechanically more resistant shell might be capable of prolonging the release of encapsulated drugs. Hence, nanocapsules with a varying shell composition were intended to be developed and investigated *in vitro* regarding their mechanical and release properties. Finally, selected nanocapsules were aimed to be characterised *in vivo* and *ex vivo* in order to study their *in vivo* release behaviour and physiological fate.

2 THEORETICAL BACKGROUND AND METHODICAL APPROACH

2.1 Development and preparation of polyelectrolyte nanocapsules

The aimed nanocapsules were supposed to be a physiologically tolerable drug delivery system in terms of pH value, as well as by use of only biocompatible, non-toxic components. In the past, polyelectrolytes both had proved to be appropriate for the preparation of nanocapsules and are commonly accepted substances since many of them are authorized as food additives (E number) due to good tolerability for the human body. A significant step for the preparation of nanocapsules composed of polyelectrolytes was done by Sukhorukov et al in 1998 [26]. Hollow capsules were fabricated by layer-by-layer (LBL) assembly of polyelectrolyte film-coated colloidal particles and subsequent removal of the colloidal core. In this technique the most extensively used polymer pair for multilayer films consisted of the synthetic polyelectrolytes poly(styrenesulfonate) and poly(allylamine hydrochloride) [27-29]. Other synthetic polyelectrolytes were used as well [30-32]. Only a few groups are working on nature-based polyelectrolytes [33-35]. Low cost and non-toxic (or even biodegradable) raw materials were preferred in this work for the development of core-shell-structured nanocapsules. Hence, the following substances were intended to be investigated with respect to forming a solid polymer shell:

(i)   modified starch (E 1450), gathered from waxy maize
(ii)   pectin (E 440), extracted from sugar beet pulp
(iii)   carrageenan (E 407), isolated from red seaweed
(iv)   gum arabic (E 414), extracted from *Acacia Senegal* species
(v)   chitosan, obtained from the shell of coldwater shrimps or prawns
(vi)   cationic gelatin (type A), produced from collagen isolated from pig skin

The oily core of the nanocapsules contained medium-chain triglycerides (MCT). It is listed in the *European Pharmacopoeia* (*Ph. Eur.*) and thus regulated regarding quality and purity for pharmaceutical use. This liquid component was aimed to represent the solvent for potentially encapsulated drug molecules because it is known to be faster biodegradable than lipids with longer fatty acid chains. Moreover, it has a long shelf-life, good physiological tolerance and dissolving power for lipophilic substances. Due to missing toxicity on skin and mucous membrane, MCT found use in dermal products as permeation enhancer, in peroral products as lubricant and drug solvent, and in parenteral formulations as solution enhancer [36].

2.1.1 Complex coacervation

Another character of polyelectrolytes, supporting the decision for their use in this work, is that they carry numerous functional groups and thus possess a charged polymer surface in dependence on the acidic or basic environment. The electrostatic interaction of polyelectrolytes with opposite surface charges allows for their complexation and hence for the creation of a polymer-rich phase, resulting in the solidification of the dissolved polymers. This reaction between vicinal charged polyelectrolytes is called complex coacervation [37-39] and has been applied for the formation of core-shell structured nanocapsules with three polyelectrolyte shell layers by Rübe [14]. The principle of polyelectrolyte deposition on dispersed oily nanodroplet templates for following nanocapsule formation was intended to be optimised with respect to a small particle size, narrow size

distribution, high drug load capacity, and improved physico-chemical properties such as dispersion stability. For this purpose, the polyelectrolytes (i) to (vi) listed above were investigated in this study with the aim of forming the polymeric shell of stable nanocapsules.

The term of complex coacervation was introduced in 1949 [37], and is also called polyelectrolyte complexation [38] or phase separation. The principle was originally studied by Tiebackx in 1911 and H. G. Bungenberg de Jong in 1929 with mixtures of gelatin and gum arabic [39,40]. Coacervation means the transformation of dissolved polymer molecules into a polymer-rich separated phase by means of desolvation [12,41]. Thereby a solid coacervate is formed which is a concentrated phase of one or more polymers. The second phase contains mainly the solvent [42]. This technique serves for the encapsulation of liquids, solids and dispersions thereof, depending on the procedure of coacervation. Phase separation can be induced by different triggers. In case of simple coacervation, these can be the addition of salts or ethanol as well as a change in temperature or pH value. In case of complex coacervation, the deposition of polymeric wall material of the particles is reached by electrostatic attraction of topologically separated segments of oppositely charged polymers [13,43], followed by charge equalisation. The attraction of polyanions and polycations yields a dispersion of solid particles composed of the polymers as a result of desolvation [44]. Beside gelatin type A with gum arabic, typical polymer pairs are gelatin type A with gelatin type B, gelatin type A with heparin, and chitosan with insulin [12,41,45].

2.1.2 High-pressure homogenisation

The most commonly used preparation methods of nanocapsules in the past were the interfacial polymer deposition method introduced in 1998 by Fessi et al [46] and the mentioned LBL technique applied by Möhwald and co-workers, and others [27,33,47-49]. However, they include disadvantages such as to require the use of organic solvents, to be tedious and time consuming with respect to the removal of excess (not adsorbed) polyions by washing steps, or to allow for filling of the hollow capsule core with substances only belated after removing the preformed template of melamine formaldehyde or poly(styrenesulfonate) using their acidic solubility. These aspects have led to the aim of avoiding these established methods in this study, but to pursue the idea of Rübe [14] for the development of polyelectrolyte nanocapsules. Thus, high-pressure homogenisation (HPH, Figure 2) was aimed to be applied as this process is capable of achieving a nanoscaled and homogeneous particle size.
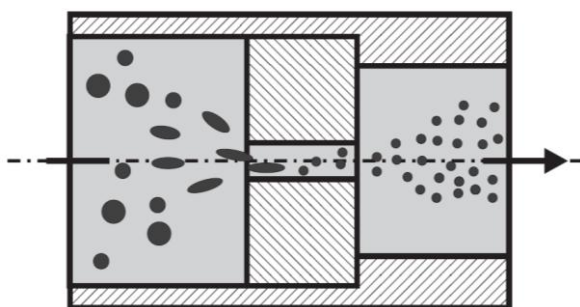

Figure 2 Principle of high-pressure homogenisation, from [50]. The sample passes a small gap under high pressure. Thereby, particles are disrupted down to a homogeneous nanoscaled size.

HPH is the most significant procedure to produce parenteral fat emulsions or suspensions with dispersed liquids or solids in the nanoscale, since smallest droplet diameters are obtained by this method [51]. The process starts with pre-dispersing the oil phase in a surfactant solution by a high-sheer mixer. The oil droplets, thereby being delivered in the microsized range [52], can afterwards be reduced down to a diameter of ≈100 nm by applying HPH. During this process, the dispersion passes a small homogenisation gap (valve) under high pressure up to 2000 bar and high streaming rates, and is accelerated. Due to high energy transfer (shear, impact and cavitation forces) into the product [53], a reduced and uniform particle size in the nanoscale is gained, especially by multiple cycling HPH [51]. More detailed information is available from [11,51]. A nanoscaled and homogenous particle size was aimed in this work due to improved stability, reduction of coalescence of the oil phase, and the feasibility of nanocapsules for intravenous injection [54,55]. Hence, HPH seemed to be an adequate preparation method. Furthermore, it allows for reducing the particle size by increasing the homogenising pressure, or by operating with heat since the viscosity of the dispersed phase (low viscous oils such as MCT) and thus the diameter of the oil droplets is decreasing with increasing temperature [56,57].

2.1.3 Critical micelle formation concentration

The technique of polyelectrolyte deposition on dispersed (emulsified) oil droplets for subsequent nanocapsule formation is based on emulsion templates. For the preparation of an emulsion, the emulsifying power of the used surfactant is an important characteristic. Surfactants are compounds that possess hydrophilic as well as hydrophobic constituents in their molecular structure. Thus, the surface-active molecules accumulate at the interface of water/air. With growing concentration, the degree of coverage of this boundary layer increases, until saturation with surfactant molecules is reached. A further increase of the surfactant concentration leads to an increased formation of aggregated structures of surfactant molecules within the water. These structures, so-called micelles, generally have a spherical or rod shape [58-60]. The formation of micelles occurs spontaneously and is mainly driven by the hydrophobic effect and an increase of entropy [61,62]. The minimum concentration at which the formation of micelles from surfactant monomeres starts is called 'critical micelle formation concentration' (CMC). A continued increase of the surfactant concentration beyond the CMC generally does not result in a further significant reduction of the static surface tension of the solution. Therefore the CMC and the associated surface tension are important parameters of a surfactant, the knowledge of which is crucial for the efficient use of surfactants for emulsion preparation.

Thus, determination of the CMC of the used emulsifying polyelectrolytes was meaningful for the subsequent nanocapsule development. In this work, the Wilhelmy plate method based on force measurement was applied [12]. The principle is to measure the static interfacial or surface tension σ as a function of the surfactant concentration c to determine the CMC. In analogy to the Lecomte du Noüy ring method, initially the liquid level is increased until contact with the plate is registered. The sample is then lowered again until a liquid film beneath the plate is produced. As the film is stretched, a maximum force emerges which is recorded in the measurement by a torsion balance. The force is calculated by the following equation [63]:

$$\sigma = \frac{F}{L} cos\theta \qquad \text{eq. (1)}$$

with σ (mN/m) = surface tension, F (mN) = force acting on the balance, L (m) = 2*l = wetted length of the plate, and θ = contact angle. At the maximum the force vector is exactly parallel to the direction of motion. Thus, at this moment the contact angle θ is 0°. This means that the term cos θ has a value of approximately 1, so that only the measured force and the wetted length of the plate need to be taken into consideration. It follows:

$$\sigma = \frac{F}{2*l} \qquad \text{eq. (2)}$$

where l is the plate length (wetted on both sides). F is measured by the torsion balance.

In practical terms, the CMC is often determined from plots of the surface tension as a function of the logarithm of the concentration. The CMC is then defined as the concentration at which the surface tension stops decreasing and reaches a plateau value [64].

2.2 Physico-chemical characterisation of the prepared nanocapsules

To follow the properties of the prepared emulsions and nanocapsules, an extensive physico-chemical characterisation was necessary afterwards. One main focus was to investigate whether the aimed nanoscaled capsule size had been achieved. However, particle size determination on nanoscale is not trivial: Objects smaller than approximately 0.5 µm are observable but not measurable with optical devices such as light microscopy since they appear larger than they really are [13]. Moreover, sedimentation or sieve analysis is not applicable since the Brownian motion outweighs possible sedimentation. Thus, the application of methods which make nanostructures 'visible' was required in this work. Additionally, non-invasive investigation techniques without the need of sample manipulation were preferred whenever possible. Besides, the use of a broad variety of techniques based on different measurement principles is demanded to minimise artefacts. Size characterisation methods fulfilling these demands on nanoscale are light scattering techniques such as photon correlation spectroscopy (PCS) and laser diffraction (LD), advanced microscopic techniques such as transmission electron microscopy (TEM) and atomic force microscopy (AFM), and field-flow fractionation (FFF). Hence, these advanced methods were applied for the size determination of the nanocapsules in this study.

2.2.1 Photon correlation spectroscopy

Photon correlation spectroscopy (PCS) is based on the scattering of laser light by colloidally dispersed particles. Temporal fluctuations of the light intensity, induced by light-scattering particles diffusing through the dispersion, are enregistered by detectors. The smaller the particles are, the faster is their rate of diffusion and the higher are the frequencies of the fluctuations of the scattered light. This is based on the Stokes-Einstein equation:

$$D = \frac{k_B \text{T}}{6\pi\eta r} \qquad \text{eq. (3)}$$

which reflects that the radius r is indirectly proportional to the diffusion coefficient D while the parameters k_B (Boltzmann constant), T (temperature), and η (viscosity of the dispersant) are constant. From the Einstein-Smoluchowski-relation (Brownian motion):

$$D = \mu k_B \mathrm{T}$$

<div align="right">eq. (4)</div>

it is apparent that a large value for D results in a higher mechanical mobility μ of the particles.

PCS can be applied for particle sizes especially smaller than 1 µm since they show strong Brownian motion which outweighs possible sedimentation. It yields volume or intensity weighted particle size distribution curves. The fundamental criteria to judge the quality of dispersions, the hydrodynamic diameter (z-average) and the polydispersity index (PDI), are provided by PCS. The determination of the PDI is based on cumulant analysis. The PDI appears as a mathematical definition, accounting for the relative error between curve fit and experimental values [55,65]. It is a measure for the dispersity quality of colloidal dispersions and discloses good quality (monodispersity) at values near 0.1 or smaller and poor quality (polydispersity) for values between 0.5 and 1. In general, products with a PDI as small as possible are desirable; values between 0.1 and 0.15 are commonly reachable for emulsions. Values from 0.15 to 0.2 are still acceptable, whereas a PDI larger than 0.3 reflects a broad or inhomogeneous size distribution. A PDI value larger than 0.5 indicates a polymodal distribution which is undesired in dispersions due to the risk of particle growth by time (Ostwald ripening).

2.2.2 Laser diffraction

During laser diffraction (LD), a helium-neon-laser is irradiated onto the sample dispersion. The laser beam is diffracted in a certain angle depending on the size of the dispersed particles. Smaller particles show a stronger diffraction angle than larger ones, but lower intensities. The instrument measures the angle of diffracted laser light as a result of the impact on spherical particles and interference of light waves in the shadow of the particles. Several detectors in different positions detect the diffraction spectrum and the intensity of light. Following the Mie theory, a volume-weighted size distribution is calculated in dependence on the enregistered intensity and position of the detectors. Therefore, optical material properties (refractive index, absorption) are necessary [13,66]. For monomodal particles, the d(0.5) value, which is the cumulative frequency of 50 % of the size distribution curve, is the major relevant result parameter of this method. The d(0.9) value is representative for a whole sample since only 10 % of the particles are larger than this value. The method can detect particles with a size from 0.1 to 2000 µm. It was mainly utilised in order to identify potential micron-sized nanocapsules in the sample dispersions not fulfilling the size requirements.

2.2.3 Transmission electron microscopy

Among these light scattering techniques, transmission electron microscopy (TEM) is one of the microscopy methods frequently used for the size determination of particles in the nanometer scale [8]. It was applied with the aim to confirm the previous size measurements results. Besides, TEM allows for the investigation of the shape, morphology and surface structure of the polyelectrolyte nanocapsules and can serve for the estimation of the shell thickness.

2.2.4 Atomic force microscopy - topographic analysis

The atomic force microscopy (AFM) belongs to a series of scanning probe microscopes (SPM) invented in the 1980s. This series started with the scanning tunneling microscope (STM) presented by Binnig, Rohrer, and Gerber in 1982 [67], which allowed the imaging of surfaces of conducting and semiconducting materials. It became possible to image single atoms on flat surfaces. In parallel, the scanning near-field optical microscope (SNOM) was invented which allowed for light microscopy below the optical resolution limit. The last and presently most important one of the SPM family is the AFM, invented by Binnig et al. in 1986 [68]. It enables imaging of the topography of conducting and insulating surfaces, even with atomic resolution [69]. Major applications are medical diagnostics, imaging the human epidermis, DNA, proteins, viruses, or liquid crystals [70-76]. Measurement is possible in different media such as ultra-high vacuum, air, protective gas, water, and other fluids.

2.2.4.1 Principle of AFM and modes of operation

Comparable to the needle of a record player, in AFM a line-by-line scanning of the surface in x- and y-direction is carried out with a very fine tip mounted to a cantilever (Figure 3).
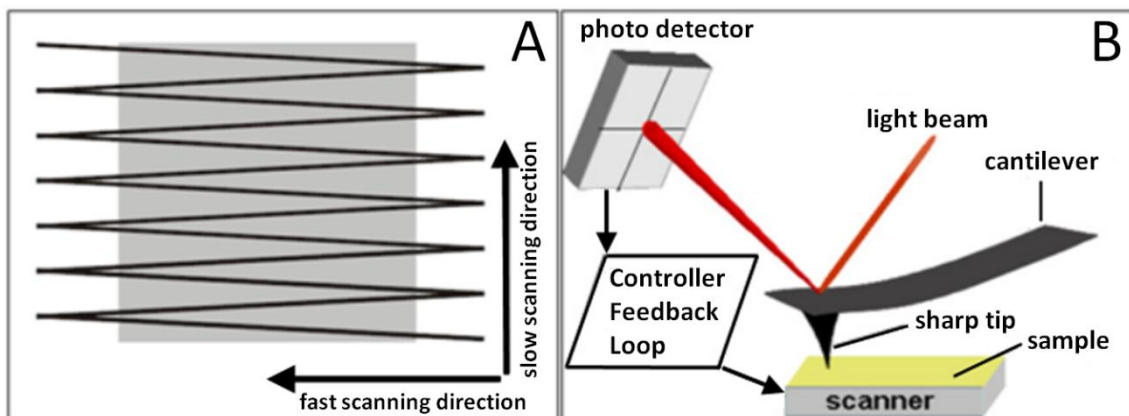
Figure 3 Principle of AFM. A: Line-by-line scanning in x,y-position. B: Principle components of an AFM. When the tip hits an object of the sample, the cantilever deflects and the feedback loop adjusts the corresponding z-direction (tip-sample-distance, height) to the setpoint. The image is generated by plotting the cantilever deflection (z-adjustment) versus its x,y-position on the sample.

The cantilever is linked with a piezoelectric tube scanner which accurately controls the movement along the sample [77]. Depending on the surface structure of the sample, the cantilever deflection is changing. Deflections of the cantilever are monitored by a simple optical device in which a laser light beam is reflected from the back of a cantilever on to a highly sensitive four-quadrant photodiode (position sensitive photo detector, PSD) [78]. The signal of the photodiode can be used to control the movement of the piezoelectric translation stage via a feedback mechanism between the photodiode and the scanner [79]. Thus, the height position of the cantilever is controlled by the feedback loop which maintains a constant force between tip and sample. The height and the cantilever deflection are saved as image file information. A topographic image of the sample is obtained by plotting the cantilever deflection versus its position on the sample [69]. An image contrast arises because the force between the tip and sample is a function of both tip–sample separation and the material properties of tip and sample. To date, in most applications image contrast is obtained from the

very short range repulsion, which occurs when the electron orbitals of tip and sample overlap (Born repulsion). Thereby topographic images are obtained. However, further interactions between tip and sample can be used to investigate properties of the sample, the tip, or the medium in between. These studies are usually known as force measurements. For topographic analysis and force analysis two different modes of operation have to be applied. Hence, the AFM capabilities include measuring topography, surface energy, and elasticity of samples at the nanometer, even molecular scale [69].

All SPM techniques are based on measurements of the interactions between the sample and the tip separated by a small distance. Interactions between the atoms of the tip and those of the sample vary according to Hooke's law [80]:

$$F_z = k_c\,Y_z$$

<div align="right">eq. (5)</div>

where F_z is the force, k_c the cantilever spring constant and Y_z the deflection of the extremity of the cantilever. Their spring constants vary according to their shape, size and composition, typically ranging from 0.01 Nm^{-1} to 100 Nm^{-1}. Due to the fabrication process, the exact value of the spring constant varies from one probe to another and therefore must be determined for each AFM tip, a process that is crucial for quantitative force measurements, but not for imaging.

Several interaction forces between the tip and the sample cause a deflection of the AFM cantilever. The most commonly measured forces in AFM are well described by the Lennard-Jones potential *U(r)* [79]:

$$U(r) = \frac{\alpha}{r^{12}} - \frac{\beta}{r^6}$$

<div align="right">eq. (6)</div>

where *r* is the distance between the atoms, and α and β are constants. At small distances ($U(r) \approx 1/r^{12}$), the potential is positive and corresponds mainly to repulsive forces, i.e. due to the exclusion of the electronic clouds surrounding the atoms as they start to overlap (Pauli principle). At larger distances ($U(r) \approx -1/r^6$) an attractive potential appears due primarily to van der Waals dispersion forces.

AFM modes and appearing repulsive and attractive forces in dependence on the Lennard-Jones potential are shown in Figure 4.
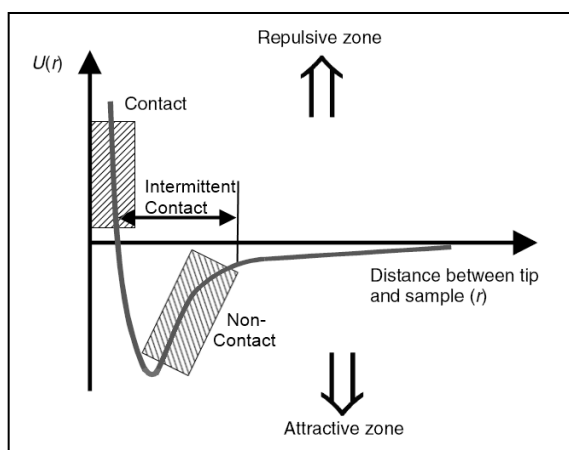
Figure 4 Lennard-Jones potential *U* in dependence on the distance *r* between tip and sample. Attractive and repulsive zones are used in AFM modes: contact mode, intermittent contact ('tapping') mode, non-contact mode.

Both the attractive and repulsive regions of the force–distance curves can be used to produce topographic images of sample surfaces. The most conventional imaging mode in AFM is *contact mode*, in which the tip is in close contact with the surface in the repulsive force regime. By the first direct contact (approach) between tip and sample the atoms of the cantilever tip are affected by a repulsive force which is induced by overlapping of their electron orbitals with those of the atoms of the sample. In this mode, forces are typically in the range of 10^{-7} to 10^{-9} N when the AFM is operated in air and as small as 10^{-12} N in liquids. The lower forces can be probed under liquid conditions due to the elimination of the strong capillary forces that are present between the AFM probe and the surface when the imaging is performed in air [79]. The main limitation of the contact mode imaging arises from the significant lateral forces, created by the dragging motion of the tip across the sample, which can damage poorly attached objects [81]. In AFM applications to soft materials, such as polymers and biological samples, it was found that high tip-to-sample forces in the contact mode and especially the presence of lateral forces often led to mechanical deformation of the surface [82]. The need to avoid surface damage was one of major motivations for the development of other modulation modes: the intermittent mode (syn. tapping mode) [83] and non-contact mode [84].

In the *tapping mode*, the tip is oscillating at the resonance frequency of the cantilever ω_0, which is typically 150-400 kHz, with a given free amplitude A_0, that is typically in the range of 10–100 nm. The oscillation is excited by means of the piezoelectric scanner and can be amplitude-modulated [85] or frequency-modulated [86]. As the probe is brought almost into contact with the surface (few femtometers), i.e. in the repulsive regime of the force curve, the tip–sample interaction will alter the tip oscillation. By maintaining the oscillation at constant amplitude via a feedback signal based on the tip to sample distance, it is possible to generate a topographical image of the surface from the required movements of the piezoelectric scanner [79]. In tapping mode, the *intermittent contact* between tip and surface minimizes the inelastic deformation of the sample. Since the tip only briefly interacts with the surface, this imaging mode reduces shear forces that are applied to the sample and consequently can be used to study weakly immobilised molecules. Numerous examples confirmed that the effective forces experienced by the sample in the tapping mode are smaller than in the contact mode [82]. Differences between tapping and contact mode are given in Figure 5 and in Table 1.
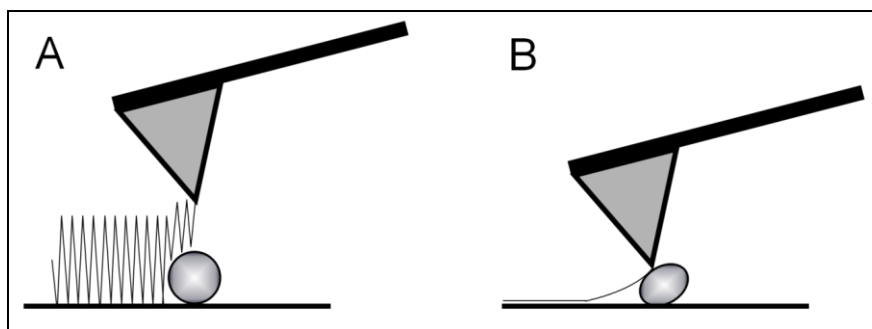
Figure 5 AFM modes (modified from [87]), <u>A:</u> tapping mode (for topographic images), <u>B:</u> contact mode (for force measurements)

Table 1 Comparison of contact mode and tapping mode; UHV: ultra-high vacuum

parameter	contact mode		tapping mode
height (z)	a) z = const.	b) z = measured	$z = z_o + z \sin(w_o t)$
force (F)	F= measured	F = const.	F = f (v. d. Waals)
spring constant	0.005...0.5 N/m (softer)		0.2...50 N/m (harder)
advantage	water film resistant		reduced sample destruction
tip-sample distance	< 1 nm		1...20 nm
resolution in z direction	1 Å (no atomic resolution)		0.1 Å (genuine atomic resolution)
lateral resolution	0.1 nm (in UHV)		1 nm (depends on tip radius)

The *non-contact mode* (not shown) relies on a similar principle to the tapping mode except that the cantilever is oscillated above the surface at distances at which the tip is in the attractive regime of the intermolecular force curve. In this case, the tip to sample distance and the oscillation amplitude are of the order of 1 nm and 10 nm, respectively. Due to the relatively large tip to sample distances and the correspondingly small forces that are exerted on the sample, this mode is non-invasive, making it ideal for imaging soft and fragile samples. On the other hand, due to the relatively large separation of the tip and the sample, the resolution of the non-contact mode is necessarily lower than that obtained in the contact or tapping mode. Furthermore, the non-contact mode is more difficult to operate than the tapping mode due to the instability of the attractive signal with respect to jumps on the surface, especially when the AFM is operated under ambient conditions [79].

2.2.5 Field-flow fractionation

Field-flow fractionation (FFF) is a flow-based particle separation technology possessing characteristics both of chromatography and of electric field-based separation methods like electrophoresis [88]. As the Brownian motion contributes to the separation principle, FFF also features analogies to PCS and is especially suitable for the separation of very small particles. The origins go back to the 1960´s when Giddings described FFF [89]. In the past ten years, FFF has developed from a matter of research to an extensively used method utilised e. g. for characterisation of liposomes [90]. In FFF, fractionation is performed in a channel through which a liquid is pumped giving a laminar flow. By applying an external field which is a force effecting perpendicularly to the channel flow, a parabolic velocity profile is induced in the laminar flow channel [91,92]. The diffusion of the

analytes competes against these external field-induced forces. As small and large particles differ in their diffusion coefficient and thus in the extent of the exposure to the external field, FFF can be utilised for the separation of different sized particles in the channel. Since FFF is based on interactions between the laminar flow and Brownian motion, flow FFF is currently applicable for particles in the range from 0.001-50 µm [91]. Owing to the possibility to be combined with multi-angle light scattering (MALS) detectors [93], which are comparable to the LD measuring principle, the technique has gained in importance for the particle size determination as well as of the molar mass of dissolved molecules [93-97]. For these reasons, the samples were decided to be investigated by FFF-MALS as an additional method contributing to a comprehensive idea of the nanocapsule size.

The particle separation in FFF is based on a laminar liquid flow in a channel, combined with an external field effecting perpendicularly to the channel flow and thus inducing a parabolic velocity profile in the channel. The most commonly used external fields in FFF are (i) sedimentation field (using gravitational or centrifugal forces), (ii) thermal field (using diffusion based on a thermal gradient in the channel), and (iii) flow field (using a perpendicular cross-flow) [91]. While sedimentation and thermal FFF require high operative efforts and costs, the cross-flow FFF possesses a rather simple assembly (cf. Figure 6).

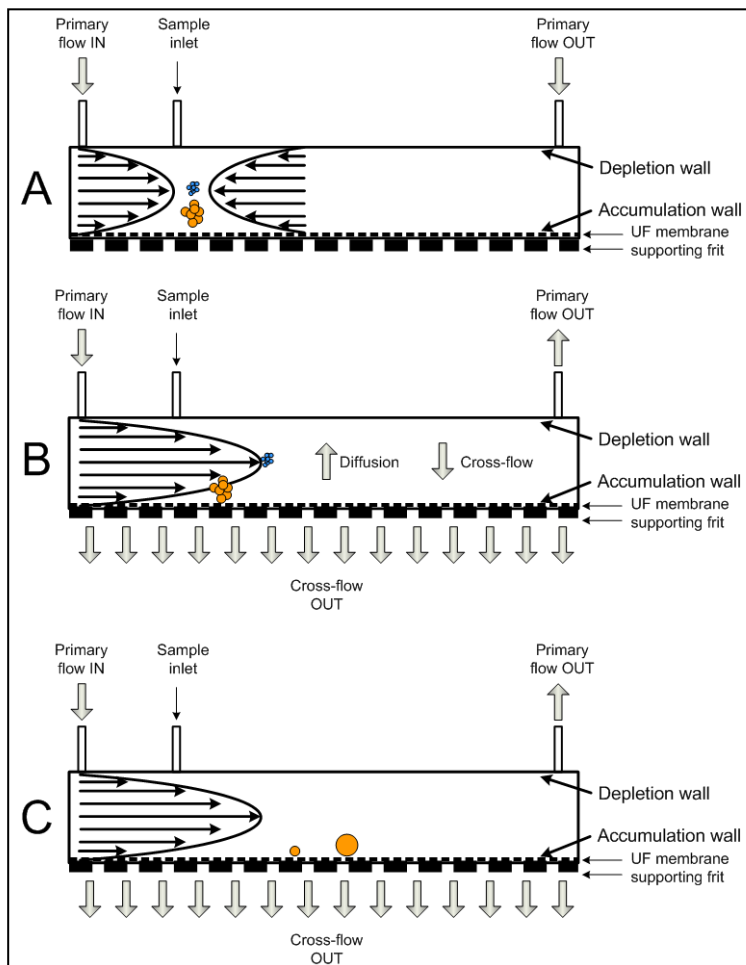**Figure 6 Localisation of differently sized particles in the AF4 channel during:**
A: focusing, B: normal separation, and C: steric elution

(UF = ultrafiltration)

The cross-flow is a second independent hydraulic flow of liquid carrier applied perpendicularly to the primary laminar flow [94] from the porous upper wall (depletion wall) to the lower frit covered by an ultrafiltration (UF)

membrane (accumulation wall). These semi-permeable walls ensure that the solvent can pass through, but the sample (macromolecules and particulate systems) is retained in the channel. Thereby, the lower analytical limit of resolvable molecular weights is set by the nominal cut-off limit of the UF membrane (5,000-10,000 Daltons), in aqueous systems mostly consisting of polysulfone or cellulose [94]. The upper size limit is practically defined by the diameter of the smallest capillary used. Aqueous or organic solvents can serve as carrier systems. In this work, the asymmetrical flow field-flow fractionation (AF4), an advancement of the flow FFF, was applied. In the AF4, there is no second independent flow, and the depletion wall is a non-porous transparent glass or plastic plate. Accordingly, the cross-flow originates from within the channel itself, where the cross-flow rate corresponds to the loss of axial flow that occurs as the carrier fluid moves down through the membrane and the frit [98].

During addition of the sample, AF4 allows for sample focusing in the channel which increases the separation efficiency [99]. When the channel is operated in the focusing mode (cf. Figure 6A), solvent is pumped into the channel from two directions: from the solvent flow inlet and from the primary flow outlet. Both flows are adjusted to equilibrium, resulting in a channel flow velocity of 0 mL/min in the region of sample inlet where thus the sample analytes are concentrated. As a consequence, the solvent leaves the channel by the lower accumulation wall (cross-flow). The analytes keep in the sample inlet region of the channel and localise at a certain distance from the UF membrane according to their size.

Figure 6B shows a schematic representation of the flow channel and separation principle which is started after focusing. The external cross-flow forces the different sized particles against the UF membrane. Diffusion based on Brownian motion of the analytes competes against these field-induced forces, pushing them towards the upper depletion wall. At equilibrium of these two forces, the analytes occupy localized regions of the parabolic flow profile based on their diffusion coefficients D. Having higher diffusion coefficients, the smaller particles/molecules move towards the channel centre, while larger particles/molecules are pushed towards the accumulation wall due to smaller diffusion coefficients. Since the drift velocity varies at different points of the parabolic flow profile, particles with a smaller hydrodynamic diameter move faster than larger particles located near the UF membrane. Thus, the sample is separated by size. The formed fractions elute at different points of time, with the smaller particles normally eluting first.

This normal elution behaviour can be observed up to the 'transition point', a particle size of approximately 500 nm which is dependent on the separation conditions, especially the field strength [94]. However, flow FFF offers a size range for separation of up to a few micrometers. Particles larger than approximately 500 nm are separated by a principle different than normal which is called 'steric elution' [91]. These particles are too large; they practically do not diffuse into the centre of the channel and they are maximum pushed towards the UF membrane by the cross flow (Figure 6C). They virtually lie on the membrane. Since they have a relatively large diameter, however, the particles extend into the interior of the channel and receive a higher acceleration due to the faster central fluid flow. Thus in steric elution larger particles elute first; the order of separation is inverse compared to normal elution.

In case of the normal elution order, there is a strong relationship between the analytes´ size, the diffusion coefficient and the retention time. Knowing the retention time t_r, the analyte´s diffusion coefficient D can be determined by the following equation [92]:

$$D = \frac{t^0 F_c w^2}{6V^0 t_r}$$

<div align="right">eq. (7)</div>

where t^0 is the void time, F_c is the cross flow rate, w is the channel thickness, and V^0 is the void volume of the channel [92]. Finally, the particle size can be related to the retention time as follows using the Stokes-Einstein equation:

$$d_H = \frac{2kTV^0 t_r}{\pi \eta t^0 F_c w^2}$$

<div align="right">eq. (8)</div>

where d_H is the hydrodynamic diameter, k is the Boltzmann constant, T is the temperature, and η is the viscosity of the liquid [92]. It is thus evident that FFF enables fractionation as well as size determination. However, the determination of the particle size and the molar mass of the analytes by solely FFF is not usually the case, since the retention time may be affected by the interaction between the analytes and the UF membrane [88] possibly resulting in artefacts. For these purposes, it is more reliable to couple the FFF with further methods such as multi-angle light scattering (MALS). The theory behind MALS is based on the fact that the intensity of the scattered light depends on many factors, including the concentration, the scattering angle θ, and the weight average molar mass (M_w) as follows [92,100]:

$$R_\theta = K M_W c P(\theta)[1 - 2A_2 M_W P(\theta)c].$$

<div align="right">eq. (9)</div>

Equation (8) is equal to the 'Zimm equation' [95] and can be rephrased to:

$$\frac{Kc}{R_\theta} = \frac{1}{M_W P_\theta} + 2A_2 c$$

<div align="right">eq. (10)</div>

where R_θ is the Rayleigh ratio (which is a quantity used to characterise the scattered intensity as a function of the scattering angle θ), M_w is the weight average molar mass, c is the concentration, K is a constant, $P(\theta)$ is the particle scattering function, and A_2 the second virial coefficient. K and $P(\theta)$ are given by the equations [92]:

$$K = \frac{2\pi^2 n_0^2}{\lambda^4 N} \left(\frac{dn}{dc}\right)^2 \qquad \text{and}$$

<div align="right">eq. (11)</div>

$$P^{-1}(\theta) = 1 + \frac{16\pi^2}{3\lambda^2} \langle r_g^2 \rangle \sin^2\left(\frac{\theta}{2}\right)$$

<div align="right">eq. (12)</div>

where λ is the wavelength of light in vacuum, n_0 is the refractive index of the solvent, N is the Avogadro's number, dn/dc is the refractive index increment of the scattering species in the solvent, and r_g the root mean square (RMS) radius. In very dilute solutions (usually in FFF) the term $2A_2c$ in Eq. 10 can be neglected. When θ is equal to zero, $P(\theta)$ is equal to unity, thus:

$$\frac{Kc}{R_\theta} = \frac{1}{M_W} .$$

eq. (13)

Accordingly, measurements are carried out at different angles and concentrations. Plotting Kc/R$_\theta$ versus the angle θ, a graph is obtained which is usually known as 'Zimm plot'. The intercept of this plot, gained from extrapolation of the curve to zero angle ($\theta = 0$), is equal to 1/M_w, and the slope is equal to [92]:

$$\frac{\partial(Kc/R_\theta)}{\partial \sin^2(\theta/2)} = \frac{16\pi^2}{3M_W\lambda^2} \langle r_g^2 \rangle .$$

eq. (14)

Thus the intercept delivers the molecular weight, and the slope can be used to determine the size of the molecules or particles. It depends on M_w and r_g. The RMS radius (r_g) depends on the internal mass distribution of the particle/molecule and is independent of the shape. For compact spheres the geometric radius can be calculated according to Eq. 15 [101]:

$$r_{geom} = \sqrt{\frac{5}{3}} \cdot RMS$$

eq. (15)

For a more detailed insight on FFF, many reviews are available [100,102,103].

2.2.6 ζ-potential

Among the size smaller than one micrometer and an isotonic state, potential use of the nanocapsules as a drug carrier for intravenous administration demands for further properties. One is the long-term stability of the aqueous suspension at physiological conditions in the body, stability over sterilisation, and over high temperature as it may occur during transport. Alternatively a stable size after lyophilisation is desired.

A measure for the stability of dispersions is the ζ-potential. The ζ-potential is the Volta-potential of charged particles in the shear plane during migration [13]. It is the only electric potential of charged particles which is experimentally accessible. That is why it gained in importance for particle characterisation. It is commonly accepted that a ζ-potential greater than |±30| mV is a strong hint for a stable dispersion because the dispersed particles are prevented from aggregation or coalescence due to electrostatic repulsion. The experimental determination of the ζ-potential is based on the electrophoretic migration in an applied electric field. Particles will migrate with a velocity proportional to the ζ-potential. The frequency or phase shift of an incident laser beam caused by the moving particles is measured as electrophoretic particle mobility u, from which the ζ-potential is calculated by consideration of the Smoluchowski or Huckel theories [104] and the Helmholtz-Smoluchowsky-equation [66]:

$$u = \frac{\varepsilon * \zeta}{\eta}$$

eq. (16)

where η is the dispersant viscosity, and ε is the dielectric constant.

In conclusion, the higher the ζ-potential of a dispersion is, the better its theoretical long-term stability is. Thus, a high final ζ-potential (preferably > |±30| mV) was aimed for the developed polyelectrolyte nanocapsules. Moreover, they were intended to possess a final negative surface as this is better accepted by the organism than positively charged particles. Among the evaluation of the capsules´ dispersion stability, the ζ-potential could serve for studying the subsequent deposition of polyelectrolyte layers around the emulsion droplet template by the determination of the final surface charge of the particles.

2.2.7 Isostatic high pressure

High-pressure processing has potential for food preservation purposes because it can inactivate microorganisms and enzymes [105] by bursting. It has a promising future due to some advantages such as the inactivation not only of vegetative microorganism cells but also of their resistant dormant bodies (spores). Vegetative cells, including yeasts and moulds, are rather pressure sensitive; i.e. they can be inactivated by pressures of 300-600 MPa. Bacterial spores, on the other hand, are highly pressure resistant, since pressures exceeding 1200 MPa may be needed for their inactivation [105]. Besides, the antimicrobial effect is relatively independent of the temperature. That means that temperature-stable as well as labile microorganisms are eliminated. The main advantages of this technology include instant distribution of the active principle (pressure) throughout the samples and consequent independence of size and geometry. This poses a significant advantage over conventional thermal processes where the dependence on size and geometry for mass and heat transfer are critical process variables and limitations [106].

It has been suggested that the efficiency of high-pressure (microbial) enzyme inactivation is improved by applying pressure cycles. Successive applications of high pressure resulted in higher inactivation of many enzymes (trypsin; chymotrypsin; *Bacillus subtilis*-amylase), i.e. the activity after a multi-cycle process was lower than that of a single-cycle process with the same total duration [105].

2.3 Mechanical properties of the nanocapsule shell

After the development and characterisation of different nanocapsule formulations it was aimed to choose one successful nanocapsule sample for further investigation of the capsule shell assembly and advancement of the capsule shell. So far little is known about the mechanical properties of the shell of nanocapsules. However, the mechanical properties of the shell under external load as a measure for the deformation behaviour of the drug carrier are important for dosage forms being intended for injection into blood vessels [107]. Thus, the aim was to develop a thicker and more rigid capsule shell, resulting in better mechanical stability. In theory, the capsule shell might gain in thickness, rigidity, and mechanical resistance if the shell consisted of as many shell layers as possible being formed by complex coacervation. Thus, the development of nanocapsules with an increased number of shell layers was intended by maximum polyelectrolyte layering on a nanoemulsion. In order to follow the changes in their mechanical properties after each preparation step, the 'consecutively prepared samples' (emulsion template and nanocapsules with an increasing number of shell layers based on the emulsion) had to be investigated and compared by adequate and independent techniques. However, the characterisation of nanoscaled dosage forms is a great challenge because it is not known whether invasive

techniques have any impact on the samples, such as formation of artefacts. The use of direct and non-invasive techniques helps to avoid misleading results. Moreover, taking advantage of a broad variety of techniques helps to provide a better understanding of the nanocapsule wall assembly. Hence, information about the required parameters was expected to be gained from transmission electron microscopy (TEM), nuclear magnetic resonance spectroscopy (NMR), atomic force microscopy (AFM), and ultrasonic resonator technology (URT), with NMR and URT including two non-invasive methods.

2.3.1 ^{1}H nuclear magnetic resonance spectroscopy

While the thickness of a capsule shell can be estimated relatively easy from freeze-fractured nanocapsules as delivered by TEM, information about mechanical properties cannot be gained. However, the extent of immobilisation of MCT in the capsule core as well as of the polyelectrolytes in the capsule shell can be investigated from NMR spectra as a measure for the rigidity. Comparing the chemical shift and shape of the NMR signals of MCT in the emulsion and nanocapsules with those of pure MCT allows for conclusions about the MCT state in the capsule core. MCT protons can further be identified because those located near or at the glycerol part of the lipid have higher ppm values [24]. In contrast to relatively mobile 'fluid' polyelectrolytes in aqueous solution, in nanocapsules the polyions are drawn towards the relatively immobile MCT droplet with its oppositely charged surface by Coulombic forces. In consequence, in comparison to the dissolved molecules, the polyelectrolytes are bound to the surface and thus immobilised. Consequently, the polyelectrolyte adopts a rigid conformation. In NMR spectra, immobile bound polymers experience spectral broadening; thereby their nuclear resonance becomes unobservable [108]. Solid ingredients are not detected under the experimental conditions due to immobilisation and very short relaxation times [24]. Thus, the NMR signal shape of polyelectrolytes may point out whether the polyelectrolyte wall features fluid or solid characteristics.

2.3.2 Atomic force microscopy - force-curve analysis

Beside the investigation of the shape and morphology, a further considerable application of AFM established in the past is the procedure and force-curve analysis in order to understand mechanical and physical properties especially of soft samples [69,109-111]. Different kinds of forces can be detected: friction forces, magnetic forces, electrostatic forces, binding forces, elastic and plastic deformation, capillary forces. Mechanical properties can be mapped by measuring the local stiffness of the sample [112]. Despite the significance of AFM force-curve analysis for obtaining information about mechanical properties, the deformation behaviour of microcapsules or nanocapsules as drug delivery systems under external load, which is accessible by AFM, has been investigated only by few groups [107,113]. Hence, until now, knowledge about shell properties of nanocapsules is rather limited. The mechanical properties at different stages of the nanocapsule preparation process (from nanoemulsion to multi-layered capsules) were aimed to be investigated by AFM. Analysis of the shell stiffness does not only have the potential to contribute to an improved comprehension of the nanocapsule formation, but also to follow the transition of emulsions into capsules. Hence, AFM stiffness analysis was intended to be applied on these samples in this work.

2.3.2.1 Theory of force-curve analysis

Force-volume analysis is a mode of operation of AFM which is feasible to characterise different samples in terms of their stiffness and thereby to report about their rigidity. During AFM force-curve (syn. force-volume) analysis the tip attached to the cantilever is moved downwards to the sample (approach) in perpendicular direction, followed by an upward movement of the tip (retract). Vertical position (height z) of the tip and corresponding deflection of the cantilever are recorded and converted to force-versus-distance curves, briefly called 'force-curves'. Due to varying mechanical properties, in each point of the scanned region the force-curve profile might be different. The progress of the force-curve is generally predicted by repulsive and attractive forces between tip and sample, depending on the distance r (also called z as the third dimension of the tip movement; height of the tip). For this reason, a force-curve is quite similar to the Lennard-Jones potential $U(r)$ curve. The profile of a schematic force-curve is shown in Figure 7 (modified after Takano *et al.* [78]).
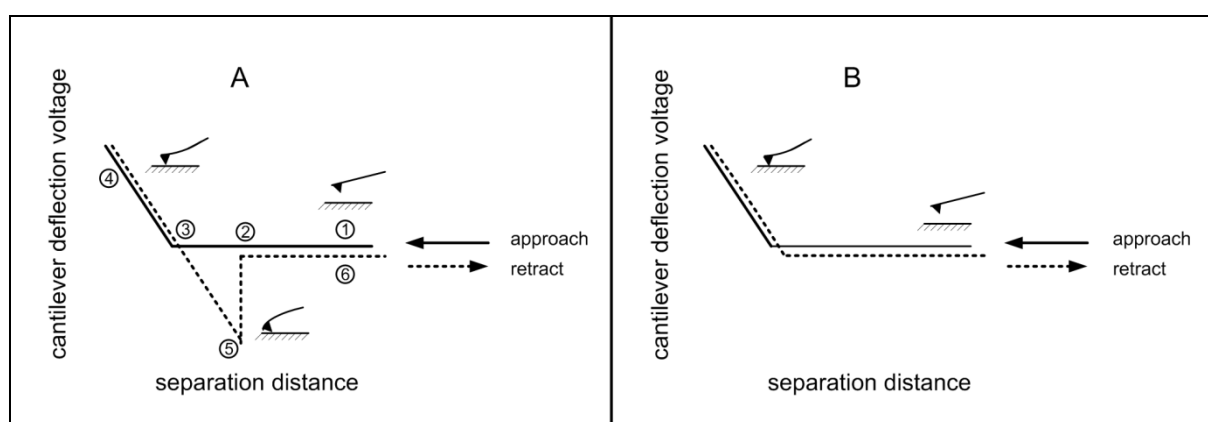
Figure 7 <u>A</u>: Idealised force-distance curve for an adhesive contact (capillary forces) when operated in air. <u>B</u>: Idealised force-distance curve obtained in liquids (absence of tip-sample interactions such as adhesion).

(1) The tip and sample are sufficiently separated such that there is no detectable interaction force. At these distances, the cantilever is in its non-interacting equilibrium position.

(2) As the separation distance decreases, various long- and short-range forces can induce a deflection of the cantilever. The long-range forces include attractive/repulsive electrostatic interactions, which are the result of the electrical double layer formed in aqueous electrolyte, and van der Waals interactions. At very small separations in liquid media, surface-induced solvent ordering and hydrogen-bonded force may be detected (short range) [114].

(3) As the separation distance decreases further to a certain value, the gradient of interaction force exceeds the force constant of the cantilever and the tip jumps into contact with the surface.

(4) As the tip moves further towards the sample, a positive linear cantilever deflection is observed as the tip and sample move together. The tip and surface are in contact inducing a positive deflection of the cantilever. It is in this region that elastic properties of the sample can be measured. As the tip removes from the sample (retract, i.e. increasing the distance z), a similar cantilever deflection line is traced as the tip and sample remain in contact due to attraction forces.

(5) Because of the adhesion between the tip and sample, a negative deflection of the cantilever is detected until the adhesive force of the tip-sample micro-contact is overcome by the restoring force exerted by the bending of the cantilever and the contact ruptures. The magnitude of this negative deflection is related to the adhesion force of the micro-contact which is also referred to rupture force or pull-off force. The tip breaks away from the sample.

(6) The cantilever has returned to its non-interacting equilibrium position. The tip and sample are sufficiently separated.

The raw data for force detection is the cantilever deflection voltage (V) (y-axis in Figure 7). By means of the deflection sensitivity (V/nm) of the cantilever (experimentally determined on hard surface: mica) and the spring constant (nN/nm) of the cantilever (known from producer) the corresponding force can be calculated. The force F is plotted versus the distance z.

2.3.3 Ultrasonic resonator technology

Since stiffness analysis on nanoscaled drug carriers is still a new field, it is necessary to support AFM and NMR results by further techniques in order to avoid artefacts. URT seemed to be feasible for this purpose as the parameters obtained from URT, ultrasound propagation (velocity) and absorption (attenuation), give information about the state of aggregation of the sample. For liquid dispersions, a velocity of around 1500 m/s can be expected which is a typical value for aqueous fluids [115]. Materials of solid state feature a faster ultrasound propagation (>5000 m/s) than those of liquid state [116]. Hence, the investigation of the velocity might contribute to find out whether complex coacervation of the polyelectrolytes forming the nanocapsule shell led to a solidification of the capsule wall. According to Wood [117], apart from the mass the stiffness of the material, through which the sound passes, is the crucial factor determining sound velocity. Thus, detecting the possible effect of an increasing number of nanocapsule shell layers on the shell stiffness (solidity) was the intention of URT investigations.

2.4 *In vitro* release behaviour of polyelectrolyte nanocapsules

The physical properties of the polymeric membrane are also critical parameters for the protection and release of encapsulated drugs. Besides, they affect the rate of polymer degradation [118]. Hence, mechanical characterisation of the nanocapsule shell was also of high interest for the drug release. Since a solid wall might have the potential of a diffusion barrier, nanocapsules with several shell layers might be advantageous drug delivery systems with respect to prolonged release in contrast to nanoemulsions. Thus, one further section of this thesis deals with the release behaviour of the polyelectrolyte nanocapsules. The focus was to investigate whether the release profile of incorporated drugs can be influenced by the number of polyelectrolyte layers surrounding the oily capsule core, possibly with the capability of achieving a controlled drug release. Another aspect is the potential correlation between the release rate and the stiffness or the rigidity of the shell with an increasing shell thickness (number of layers). Hence, the impact of the shell modification on the release behaviour of lipophilic model drugs was intended to be investigated by comparison of an emulsion and multi-layered emulsion-based nanocapsules.

Different strategies of 'controlling' the drug release include locally controlled, pH-, enzyme-, peristaltic pressure-, and time-controlled release systems [119,120]. The advantage of time-controlled (sustained) drug liberation is to overcome the need for frequent dosing of medicines and thus to maintain plasma drug levels within the therapeutic concentration range for hours. Cancer pain treated with opioids [121,122] or benzodiazepines [123], and hypertension [124] are some of the main applications of sustaining the drug release. At present microsphere formulations are state of the art technology for the slow release of drugs such as azithromycin and oxycodon, administered in oral, buccal, nasal, ocular, rectal, and vaginal routes [125]; they can be tailored for desired release profiles and for organ-targeted release [126]. Earlier, tablets had been successfully developed as oral controlled release dosage forms [121,127-131], allowing zero order release kinetics (e. g. osmotic pumps) [132-135]. In the recent past, hormones or opioids containing [122] transdermal therapeutic systems (TTS), adhesive tapes with matrix or membrane technology, entered the market of constant drug uptake over several weeks. A further strategy is drug delivery by *in situ* forming implants [136,137]. The task of time-controlled (sustained) drug release from nanoscaled drug delivery systems (NDDS), however, is still a challenge. While liposomes have provided the potential for controlled release of intravenously injected hydrophilic drugs [138], to the current knowledge there is still no submicron delivery system that meets this need for lipophilic drugs. The great advantage of NDDS is the small particle diameter, allowing themselves to be administered parenterally or intravenously without any risk of embolisation.

Although the diffusion pathways through NDDS amounts to only very short distances, sustained release from these carriers over several hours or longer have been claimed by other groups [139-146]. However, diffusion coefficients between 10^{-6} and 10^{-13} cm^2/s, frequently observed for different drugs passing through commonly used polymers [139,141,142,147-151], theoretically allow a diffusion time of only few seconds to minutes to pass distances of 10 nm, calculated according to the Einstein-Smoluchowski-diffusion-equation [152-154]:

$$x^2 = 2Dt \hspace{6cm} \text{eq. (17)}$$

where x is the average distance of a particle/molecule from its origin position, which increases proportionally by the square root of the diffusion time t, and strongly depends on the diffusion coefficient D. The discrepancy between theoretical assumptions and published data on the release behaviour of NDDS reflects the lack of knowledge and requirements of further investigations in this field. Thus, liberation experiments were conducted in this study in order to provide information on the question whether the prepared nanocapsules offer the possibility of sustained release in comparison to a nanoemulsion. Independent sophisticated techniques using different lipophilic model drugs were necessary as the paddle or basket apparatus and flow-cell, which are common for disintegrating tablets [155], cannot be applied for NDDS.

The *in vitro* liberation techniques, enabling the study of nanostructures and thus being utilised in the release study, are (i) the dialysis bag method, (ii) modified release into supernatant lipid phase, (iii) ultrafiltration (UF) at low pressure in a stirring cell, and (iv) electron paramagnetic resonance (EPR) spectroscopy.

2.4.1 Dialysis bag, modified release, and ultrafiltration at low pressure

During (i) the dialysis bag experiments, the release of incorporated nile red[1] (NR) and the lipophilic carbo-cyanine DiI[2] from the emulsion droplets or capsule core into a dialysis tube filled with MCT was observed. Both drugs are fluorescence dyes and were determined quantitatively by fluorescence imaging of the dialysis bag. In case of (ii) the modified release performed in a rotation apparatus, the sample was covered with MCT. Migration of NR and the fluorescent temoporfin derivative pTHPP[3] out of the capsule core into MCT was investigated. The quantification and plot of the release profile was based on fluorescence spectroscopy of the oily phase. A further suitable method for determination of the liberation kinetics of colloidal carriers is (iii) ultrafiltration at low pressure [156-158]. By dilution of the dispersion with release medium, the liberation of incorporated salicylic acid is triggered. The dispersant is filtered through a fine membrane by application of low pressure. Its concentration detected in dependence on time yielded the release profile. Finally, (iv) electron paramagnetic resonance (EPR) spectroscopy was applied to complement the nanocapsule release behaviour study. The release results obtained from the presented four methods were collected to achieve an extensive characterisation image of the liberation profile of the prepared polyelectrolyte nanocapsules.

2.4.2 Electron paramagnetic resonance

The electron paramagnetic resonance (EPR, syn. electron spin resonance (ESR)) spectroscopy offers the unique opportunity to perform non-invasive studies in non-transparent samples both *in vitro* and *in vivo*. Information on non-transparent samples or submicron particles, which are otherwise difficult to access, can be provided [159]. The technique has entered the field of pharmacy [160-166] to determine the micro-viscosity and micro-polarity [167], to monitor the microacidity in biodegradable polymers [168,169], and to follow drug delivery processes [170,171] or release mechanisms [172]. EPR is based on the interaction of electron spins with an applied magnetic field [173]. It requires materials with unpaired electrons. These natively paramagnetic molecules can be found as free radicals or metal ions. If the matter of interest does not fulfill this property itself, which is mostly the case in pharmaceutics, spin probes are used as labelling agent. Stable nitroxide radicals are the most frequently used spin probes in aqueous systems.

Analogue to the NMR principle for protons, the parallel or antiparallel alignment of unpaired electrons in an applied magnetic field during EPR measurements follows the Zeeman splitting. The transition of electron spins from the ground level (electron spin quantum number m_s = -½) to the excited level (m_s = +½) is induced by discrete levels of energy of electromagnetic radiation satisfiing the resonance condition [173,174]. In nitroxide radicals (isotope ^{14}N, natural abundance 99.64 %), electrons are often located in the vicinity of nitrogen. The nuclear spin is quantised, too, resulting in the spin quantum numbers m_I = -1, 0, and +1. The local magnetic field for unpaired electrons of both orientations (m_s = +½ and -½) will be increased, when the nucleus spin (+1) is in the direction of the external magnetic field and vice versa (-1). It is left unchanged (0), when no coupling occurs. As a consequence, microwave energy is absorbed at three levels, leading to a triplet of lines (Figure 8).

---

[1] nile red = 9-(diethylamino)-5*H*-Benzo(α)phenoxazin-5-one; log*P* 3.8
[2] DiI = 1,1'-dioctadecyl-3,3,3',3'-tetramethylindocarbocyanine perchlorate
[3] pTHPP = (5,10,15,20-tetrakis-(4-hydroxyphenyl)-21*H*,23*H*-porphine

These lines have well defined superhyperfine splittings, line distances, and narrow spin packet linewidths. Because of the line simplicity and reproducibility, spectral changes can be used to report characteristics of the fluids in which they are dissolved [175]. The shape of an EPR signal is related to the microenvironment (solvent type) and thus the mobility of the spin probe as follows [159,173,176]:

(i)   high micropolarity (e. g. water) → large hyperfine splitting constant a_N
(ii)   high microviscosity (e. g. oils) → large line width.
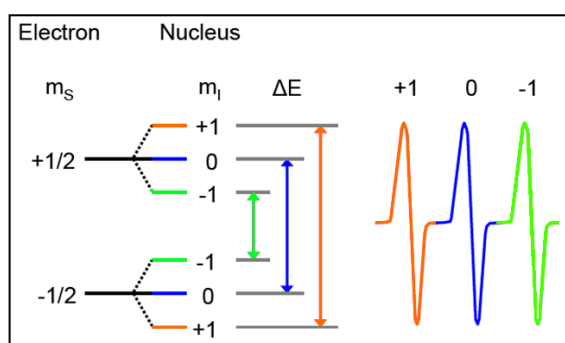
Figure 8 Theoretical background behind an EPR signal of a nitroxide radical (s=½, I=1), modified after Bolton/Wertz [173]. The energy levels and transitions are displayed in the left part. In the right part, the resulting hyperfine structure of the EPR signal (triplet) is shown.

The EPR active spin probe used during release experiments in this study is the lipophilic stable nitroxide radical tempol benzoate[4] (TB, Aldrich Chemical Co., USA, Figure 9B left).
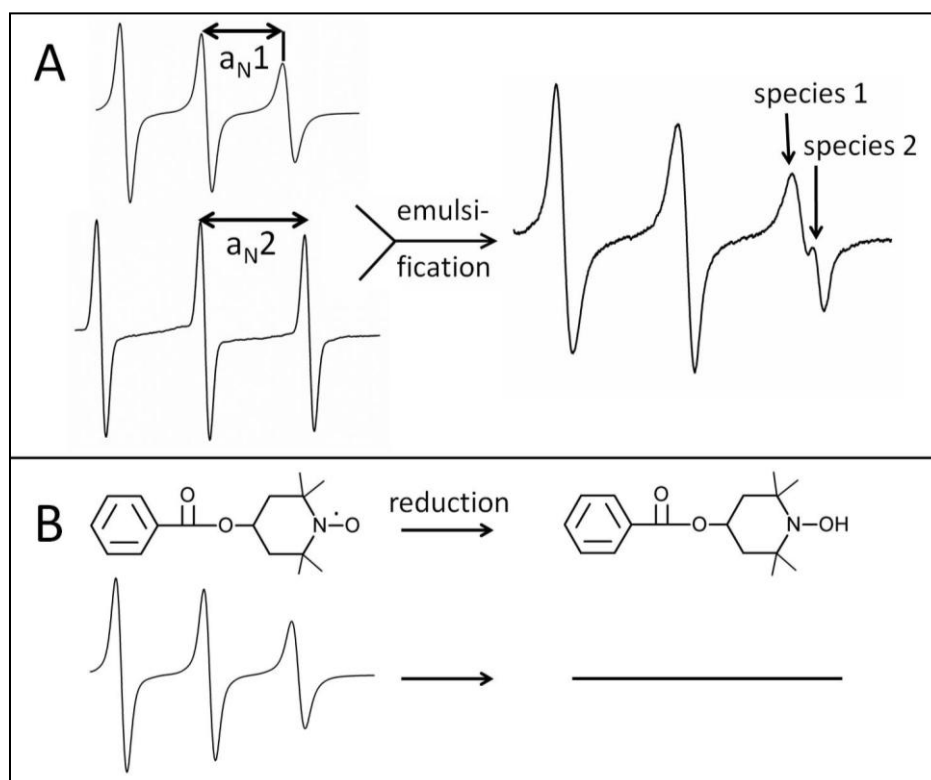
Figure 9 A: EPR signals of two tempol benzoate (TB) species in pure solvents (a_N1: in MCT, a_N2: in water) with different a_N-values (left). Their superimposed signal in an emulsion shows both species (right). B: Loss of EPR signal of TB radical during reduction with ascorbic acid to the EPR silent hydroxylamine.

During potential release of TB from the oily nanocapsule core into the aqueous release medium, induced by dilution of the sample dispersion, the environment of TB would change if TB molecules diffused through the capsule shell. Due to the partition of the spin probe between the capsule core and the water phase according to its log*P* value, two environmental TB species emerge, giving different EPR spectra. Species I of TB has a

---

[4] Tempol benzoate (TB) = 4-Hydroxy-2,6,6,6-tetramethylpiperidine-1-oxyl; log*P* 2.46

lipophilic viscous environment (oily capsule core), indicated by a small a_N value and a broader line width. Species II of TB has a larger a_N value and small line width; hence those signal is generated by a hydrophilic low-viscous medium (aqueous dispersant phase). The signals of these species overlap in case that both of them exist parallel (two-phase system), such as in an emulsion or nanocapsule (Figure 9A).

Release of TB was induced by dilution of the dispersion with water (dilution assay), giving information about the distribution of the spin probe species by the molecular environment and about the release kinetics. However, in this study, EPR served not only for the investigation of release kinetics, as it had been used for by other scientists before [170,172,177-181], but also of the protection capacity of the polyelectrolyte capsule shell against environmental influences, depending on the number of shell layers. This was done using the reduction assay (Figure 9B). The reduction of the paramagnetic nitroxyl radical TB by ascorbic acid as reducing agent leads to a loss of the signal intensity (amplitude) since a non-paramagnetic (EPR silent) hydroxylamine emerges and hence quenches the EPR signal [182]. The signal shape varying with time can be evaluated after exposure to ascorbic acid. By simulation of the spectra, the both species can be identified and quantitatively evaluated by fitting the 3rd peak of the signal.

2.5 *In vivo* and *ex vivo* animal study of nanocapsule formulations

The last section of this thesis deals with the investigation of the *in vivo* fate of selected polyelectrolyte nanocapsules on nude mice. After labelling with fluorescence dyes, *in vivo* and *ex vivo* fluorescence imaging was performed to study the *in vivo* distribution of the drug carrier in the body after peroral application (gavage), the fluorescence intensity changes by time, and the potential accumulation in special tissues or organs. The aim of these experiments was also to investigate the *in vivo* release behaviour of molecules from the nanocapsules after peroral administration, potentially with the option of correlation with the *in vitro* studies.

Two fluorescence dyes, the near infrared carbocyanine DiR[5] and the short-wave (green light) absorbing dye nile red (NR), were used in this study as model drugs for incorporation into the oily nanocapsule core. They differed in lipophilicity. Due to better water solubility, NR was expected to be released from the oily core faster than DiR. Since NR does show only marginal fluorescence in water, the diffusion-controlled release from the oily capsule core into the surrounding water phase was expected to be accompanied with a decrease in fluorescence intensity. Moreover, NR shows solvatochromism. Hence, the fluorescence emission wavelength depends on the polarity of the solvent. This is based on differences in dipole moment between the ground and excited states of the chromophore. This hypsochromic spectral shift (blue shift) in polar environments of NR theoretically offers the possibility of non-invasive investigations of the polarity of the environment of NR. In contrast, DiR has a long-wave excitation fluorescence maximum in the near infrared region. This high wavelength is very important to avoid autofluorescence and allows many tissues to be optically transparent. Another advantage of red light is the greater penetration of the sample and decreased scattering owing to the wavelength dependence of Mie scattering ($1/\lambda^3$). By replacing green (NR: emission 580 nm) with far red light

---

[5] DiR = 1,1´-dioctadecyl-3,3,3´,3´-tetramethylindotricarbocyanine iodide

(DiR: 750 nm), the scattering was expected to be diminished by a factor of 3, and thus a higher image quality would be obtained from deeper in the animal [183]. The resulting advantages of DiR for fluorescence imaging are reduced tissue and coat fluorescence of the mice and thus stronger signals from the samples out of the animal body than for short-wave absorbing dyes like NR. Hence, a lot of information can be gathered without the necessity of sacrificing the experimental animals.

2.5.1 Confocal laser-scanning microscopy

In contrast to conventional light microscopy, in confocal microscopy not the whole sample but only a small region of interest (most frequently just a light spot restricted by optical diffraction) is focussed at each moment. By means of that small excitation light spot, the sample is scanned point by point. The particularity is a pinhole in the optical path of the detected light which can withhold light from above or below the focal plane. Thus, the depth of sharpness is reduced remarkably which in turn increases the resolution along the optical axis (z-direction). Emission light of the excitation focus passes the same lens again and is separated by the pinhole. Thus, excitation and detection focus lie confocal, i.e. super-imposed. Hence, optical information from outside the focal plane is double-eliminated [184,185]. The emitted light intensities are detected by a photomultiplier. Due to their high axial resolution, confocal microscopes enable the collection and combination of many images in different focal planes and thus the non-invasive reconstruction of a sharp three-dimensional image [185,186].

The confocal microscopes used nowadays are most frequently operated with laser light (confocal laser-scanning microscope, CLSM). As fluorescence dyes are excited, they are a matter of fluorescence microscopes. The described technique facilitates the *in vitro* and *in vivo* visualisation of highly contrasted images of histochemically stained subcellular organelles, morphological details of tissues, the observation of tumor angiogenesis, and examination and control of the microstructure of complex foods [184,187-189]. In order to study biological samples such as to examine receptor-ligand interactions, material properties, and cell behaviour, fluorescence imaging in combination with optical methods such as CLSM are used [190].

Due to the qualification for imaging of biological samples, CLSM was applied with the aim to investigate the *in vivo* absorption of fluorescence dyes, and of the nanocapsules respectively, into intestine membranes. After *in vivo* administration of the dye DiR-labelled nanocapsules to mice, the aim was to find out whether the polyelectrolyte nanocapsules present a suitable carrier to release the model drug DiR into intestine membranes. DiR was selected as it is practically not soluble and not fluorescent in water, but highly fluorescent and quite photostable when incorporated into membranes. Thus, it is especially appropriate for membrane staining. It has an extremely high extinction coefficient and short excited-state lifetimes (≈1 nanosecond) in lipid environments [191]. Focus of e*x vivo* fluorescence CLSM was to study the accumulation of the dye in intestine membranes or even certain organs as well as possible systemic absorption of the dye and/or the nanocapsules during the passage of the small intestine. Hence, CLSM was performed as the final method in this animal study.

3 MATERIALS

3.1 Polyelectrolytes

Polyelectrolytes are polymers composed of partly charged monomers induced by dissociation of numerous functional groups. The monomers of natural polyelectrolytes can be amino acids or sugar molecules, thus the polyelectrolytes usually represent proteins or carbohydrates. Due to their charged character, polyelectrolytes feature polarity and good water-solubility. Depending on the pK_a value of the relevant functional groups, some of the substances possess an electric charge only in specific pH ranges. In such a case, they are called weak electrolytes, for example those with amino or carboxyl groups. In contrast, electrolytes with sulphate groups belong to the group of strong electrolytes which carry a negative charge independent of the pH value. For this work, it is rather important to classify the applied polyelectrolytes into positively and negatively charged molecules. Octenyl succinic anhydride-modified (OSA) starch (E 1450), pectin (E 440), gum arabic (E 414), and carrageenan (E 407) are the negatively charged, gelatin type A and chitosan are the positively charged polymers used for the assembly of the nanocapsule wall. Their structures and charged characters are given in Figure 10 (gelatin not shown).
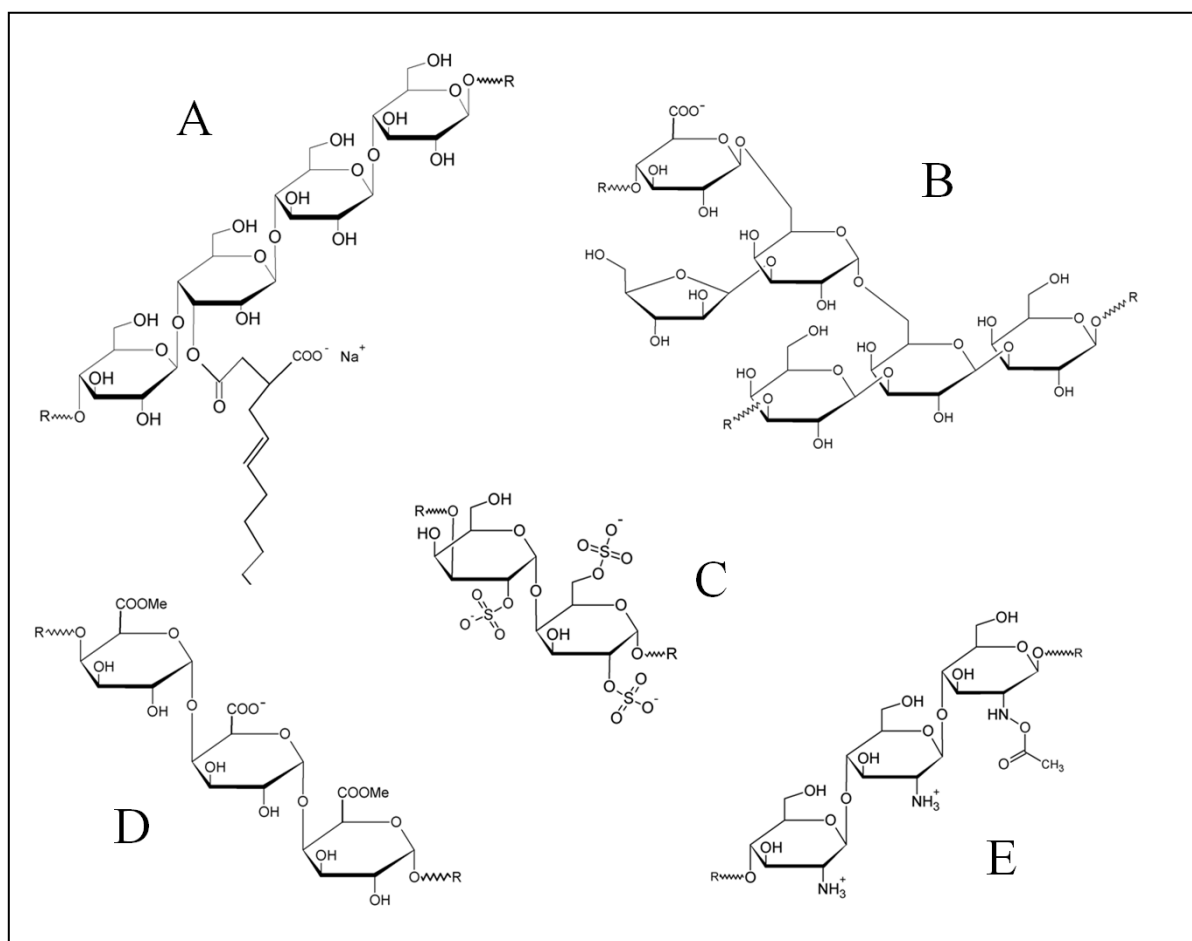

Figure 10 Structure of A: OSA starch, B: gum arabic, C: λ-carrageenan, D: sugar beet pectin, E: chitosan

Interestingly, all of these substances belong to the category of hydrocolloids [192-195]. For this reason, they are widely used in food industry as thickening or gelling agents, texturisers, stabilisers and emulsifiers. High viscosity is induced by increasing the effective volume of polymer molecules due to repulsion of equal charges in the chains. The polyelectrolytes furthermore stand out owing to their biocompatibility and extremely low toxicity, which are required for polymers in life sciences [196]. In addition, chitosan [197,198], OSA starch [199,200], gelatin [201,202], and pectin [203] are biodegradable. Gum arabic is not biodegradable due to ß-linkage of the monomers of the main chain which is not enzymatically accessible. λ-Carrageenan is hardly biodegradable, too. The sole known and reported depolymerising enzyme (hydrolysis of β-(1→4) linkage) is λ-carrageenase having been isolated from *Pseudoalteromonas carrageenovora* [204].

The charge density of the used polyelectrolytes is defined either by their degree of esterification (OSA starch, sugar beet pectin), degree of deacetylation (chitosan), degree of sulfate esters (carrageenan), content of glucuronic acid (gum arabic), or the amount of free amino groups (gelatin), respectively. Except chitosan, all other polyelectrolytes were dissolved in distilled water.

Several hydrocolloids could have been used for the preparation of emulsions due to their emulsifying capability. An emulsifying potential is known for pectin [205], gum arabic, modified starch, gelatin, carrageenan, alginates, xanthan and locust bean gum [192]. However, focus of this work was not to develop emulsions but nanocapsules. Hence, only substances with good emulsifying capability were selected. Modified starch, sugar beet pectin and gum arabic were investigated in view of their capability of forming emulsion templates for the development of nanocapsules.

3.1.1 Octenyl succinic anhydride-modified starch

The modified starch used in this study (Purity Gum 2000 E 1450; National Starch, Hamburg, Germany) is an octenyl succinic anhydride-modified (OSA) starch and derived from waxy maize. The α-(1→4)-glycosidically linked glucose molecules are esterified with succinate in position 3, which carries an octenyl moiety. It features good water solubility, a degree of esterification of 0.2 %, and a molecular weight of about 4×10^5 g/mol with a broad distribution [206]. Due to its amphiphilic structure, the OSA molecule can place very well in the interface between hydrophilic and lipophilic phases like in emulsions. Thereby it can be assumed that the octenyl chain will be incorporated in the inner oily phase due to its lipophilic character, while the glucose molecules themselves will tend to locate in the outer water phase. OSA starch is an emulsifier well known from food industry since it yields emulsions with good tolerability for the human body without toxic effects. In this work a second property of OSA starch is utilised: the anionic polyelectrolyte character due to free carboxylic groups.

3.1.2 Sugar beet pectin

The anionic polysaccharide sugar beet pectin (SBP; GENU® pectin type β, CP Kelco, Lille Skensved, Denmark) is mainly composed of α-(1→4)-glycosidically linked methoxylated galacturonic acid (degree of esterification typically 55 %). It is extracted from sugar beet pulp residues of *Beta vulgaris* [207]. The poly-galacturonic acid chain molecule is negatively charged at neutral pH (pK_a value approx. 3.5, [208]) and may contain (1→2)-glycosidically linked rhamnose. In general, pectin is swellable and at pH 3 it acts as a gelling agent (thermically

reversible gels) in the presence of calcium ions. Sugar beet pectin itself, however, has poor gelation properties, which are mainly attributed to a higher proportion of branched regions, the presence of the acetyl ester groups and the reduced size of its molecules [205,209,210]. Besides, sugar beet pectin has a potential as a food emulsifier [211,212], which can be explained by the content of ≈2 % protein [210,213], probably represented by arabinogalactan protein (AGP) [214]. Moreover, it is preferable over citrus peel or apple pomace pectin since it contains ≈1 % of the known antioxidant phenol ester ferulic acid (*trans*-4-hydroxy-3-methoxycinnamic acid) [207,210]. The pectin used in this study apparently displayed a good nutrient medium for germs. Weakly microbial contaminated pectin in high concentrated (5 %) aqueous solutions was vulnerable for growth of colony forming units (cfu) after few days. However preservation was not conducted in order to minimise a potential impact of the preservative on the emulsion and nanocapsule stability. Thus the use of low pectin content (max. 2.5 %) and only short storage intervals of the solutions at 2-8 °C were preferred. These actions proved to be effective with respect to microbiological contamination.

3.1.3 Gum arabic

Gum arabic (GA; Eficacia XE, Colloides Naturels International (cni) GmbH, Frankfurt, Germany) is a complex mixture of polysaccharides and glycoproteins and is primarily used in the food industry as a stabiliser. It is extracted from *Acacia senegal* species, purified and spray dried. It mainly consists of arabinic acid, which is a branched heteropolysaccharide of arabino-galactan-type, composed of a main chain of *ß*-(1→3)-linked D-galactose units and branched chains (in position 6 of galactose) with L-arabinose, D-galactose, L-rhamnose, glucuronic acid and 4-*O*-methyl-D-glucuronic acid [215,216]. Since 30 to 45 % of gum arabic are covered by each galactose and arabinose [216], and the ratio of arabinose:galactose: rhamnose:glucuronic acid in arabinic acid is 3:3:1:1 [217], the portion of glucuronic acid can be calculated to be 10 to 15 % of the gum arabic, which is responsible for the negative charge. It is a weak polyelectrolyte that carries carboxyl groups. 'Instant gum' which is chemically similar to the used 'Eficacia' showed a negative charged above pH 2.2 during microelectro-phoretic measurements [42]. The emulsifying character of gum arabic arises mainly from the presence of an AGP fraction in the product like in sugar beet pectin.

3.1.4 *λ*-Carrageenan

The large family of carrageenans (CARR) is represented by water-soluble sulfated polysaccharides from red seaweed which are well-known for their gelling properties. They are built up of linear chains of galactose with alternating *α*-(1→3) and *ß*-(1→4) linkages. In these galactans the *ß*-linked galactose units as well as the *α*-linked galactose units are in the D-configuration. *κ*- and *ι*-carrageenans form thermoreversible gels in aqueous solutions, their rigidity decreasing strongly with the degree of sulfation [204]. With three sulfate groups per carrabiose unit (repeating dimer), *λ*-carrageenan is the most negatively charged galactan from red algae. Since *λ*-carrageenans do not feature (3→6)-anhydride-bridges, they are more hydrophilic than *κ*- and *ι*-carrageenans and do not make physical gels but highly viscous solutions. Hence, *λ*-carrageenan is a non-gelling hydrocolloid.

The used *λ*-carrageenan (Viscarin GP 109 NFS A001; FMC, Rockland, Maine) is mainly composed of galactose sulfate esters (esterification degree around 35%). Due to the low pK_a value of -3 of the free sulfate groups, carrageenan represents a strong (poly-)electrolyte carrying an anionic charge independent of the pH value.

3.1.5 Gelatin type A

Gelatin type A (GEL; Gelita, Eberbach, Germany) is the product of acidic hydrolysis of collagen from pig skin and hence contains a protein based structure. The main amino acids are glycine (21 %), proline (14 %), hydroxyproline (12 %), alanine (9 %), arginine (8 %), glutamic acid (7 %), and aspartic acid (4 %) [192]. Arising from its amino acid content, gelatin is remarkably rich in free amino ($-NH_2$) and carboxyl ($-COOH$) groups [202]. In this work a gelatin with a low Bloom value of 180 g and a high isoelectric point (pI) between 8.9 and 9.2 was used. The gelatin had pharmaceutical quality (*Ph. Eur.*) and a grinding size of 0.8 mm.

3.1.6 Chitosan

Chitosan (CHI; Chito Clear FG 95 batch TM1369; Primex, Siglufjordhur, Iceland) is a chitin-derived, acetylated polysaccharide (*ß*-(1→4)-glycosidically linked *N*-acetyl-glucosamine and glucosamine monomers) with a degree of deacetylation of 95 % and a pK_a value between 6.3 and 7 [218] leading to a positive charge of the molecule upon exposure to acidic media. In contrast to chitin, chitosan is water-soluble (at low pH) due to protonated amino groups [198]. The results of field-flow fractionation measurements by Augsten and Mäder show a molecular weight of 1.4×10^6 g/mol with a high variability between different batches [219]. It was dissolved in 0.1 M acetate buffer pH 4.5 (concentration 0.2 %) or pH 4.0 (concentration 2 %).

3.2 Further materials

Medium-chain triglycerides (MCT, see Figure 11) (Miglyol® 812 Ph.Eur. 5.0; Caelo, Hilden, Germany; synonym: DAC: oleum neutrale) is a synonym for liquid triglyceride mixtures composed of the following fatty acids: caproic acid ($C_{6:0}$) max. 2 %, caprylic acid ($C_{8:0}$) 50 % to 65 %, capric acid ($C_{10:0}$) 30 % to 45 %, lauric acid ($C_{12:0}$) max. 2 % [36]. It is produced semi-synthetically e. g. from palm oil. Free fatty acids are obtained by acidic hydrolysis or basic saponification of natural fat. Afterwards, acids of the desired chain length ($C_{8:0}$ to $C_{10:0}$) are separated by fractionated distillation. After hydration of potential double bonds the free fatty acids are esterified with glycerol to gain the saturated triglycerides. MCT has a melting point of less than 0° C and is a lipid (oil) of low viscosity. MCT displayed the oily core component of the primary emulsions and the polyelectrolyte nanocapsules.
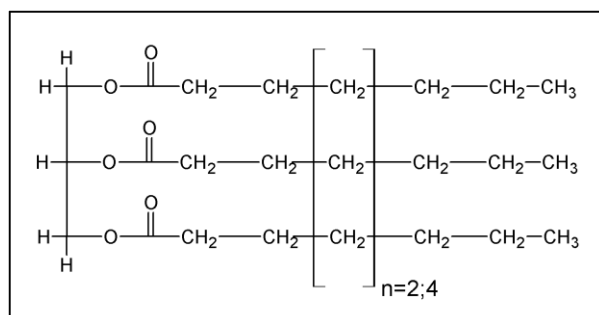

Figure 11 Structure of MCT

Poly(ethylene glycol)-poly(D,L-lactide) (MePEG2kDaPLA20-kDa), a PLA polymer (Figure 12 left) containing 10 % poly(ethylene glycol) (PEG-PLA-10%), was kindly provided by Prof. A. Göpferich, University of Regensburg, Germany. It was used for preparation of PEG-PLA-nanocapsules (NC) for AFM studies. Its structure is given in Figure 12 (right).
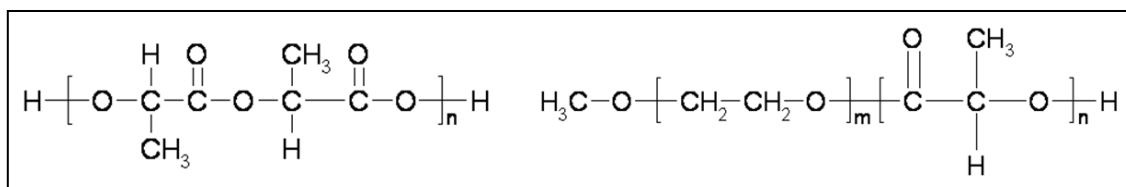
Figure 12 Structure of PLA (left) and PEG-PLA-10% (right)

Poloxamers are block copolymers consisting of blocks of polyoxypropylene (POP) and polyoxyethylene (POE). POP und POE form the hydrophobic and hydrophilic component of such block polymers, frequently in normal three-block type: HO-(POE)$_x$-(POP)$_y$-(POE)$_z$-H [12]. They possess emulsifying properties and are widely used as detergent substances. Poloxamer 188 (Lutrol® F 68, syn. Pluronic F68) was purchased from BASF AG, Germany. It is composed of POE and POP with x, z = 75, and y = 30. It has the function of a non-ionic tenside and stabiliser and was used for preparation of the PEG-PLA-10%-nanocapsules (for AFM). Poloxamer 124 *Ph. Eur. 6.0* (x, z = 10 to 15; y = 18 to 23) is a liquid that contains 44.8 to 48.6 % POE and has a mean molecular weight of 2,090 to 2,360 Da. Poloxamer 124 (Synperonic® PE/L 44) was obtained from Croda GmbH, Nettetal, Germany, Lot. No. 2704HD0702. It served as control sample during the animal studies.

The hydroxylated stilbene *trans*-resveratrol (*trans*-3,4′,5-trihydroxystilbene [220], RSV, M$_r$ 228.24 g/mol) was purchased from Sigma Aldrich, Steinheim, Germany. The substance is poorly water soluble and has a log*P* of 3.08 [257]. A temoporfin-analogue porphyrin (5,10,15,20-tetrakis-(4-hydroxyphenyl)-21*H*,23*H*-porphine, pTHPP, log*P* 7.6 [257], M$_r$ 678.73 g/mol) as well as salicylic acid (pK$_a$ 2.98, log*P* 2.26, M$_r$ 138.12 g/mol [257]) were obtained from Sigma-Aldrich, Schnelldorf, Germany, too. Diazepam (DZP, pK$_a$ 3.4, M$_r$ 284.74 g/mol, log*P* 2.9 [257]) was supplied by Fagron GmbH, Barsbüttel, Germany. Their structures are shown in Figure 13.

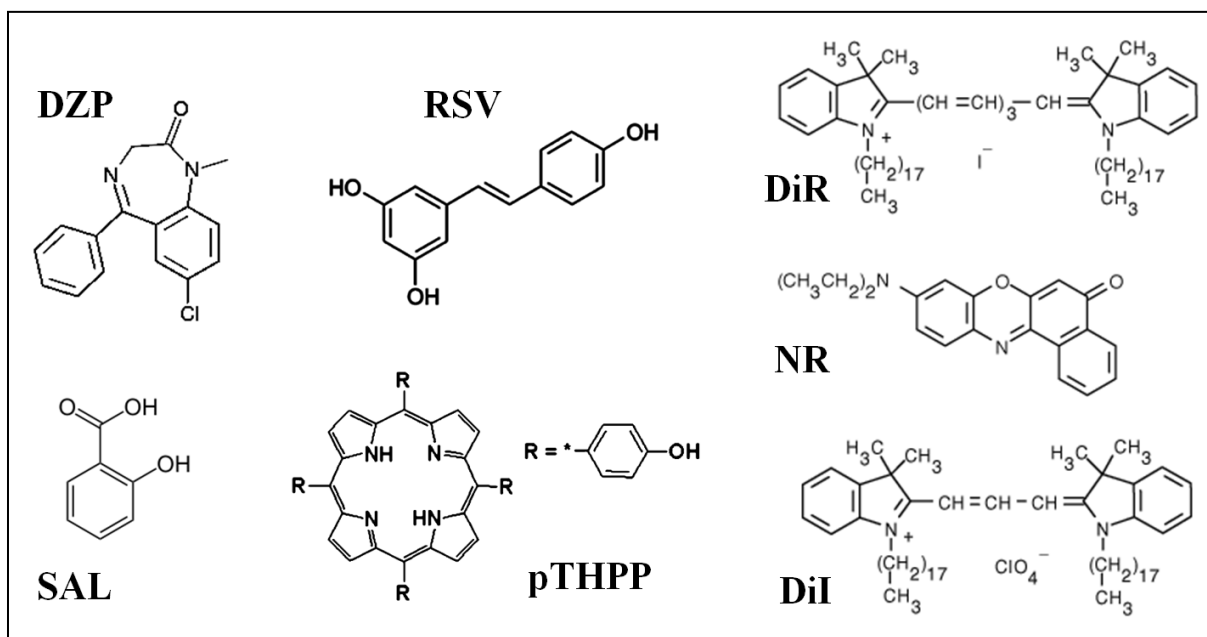**Figure 13 Chemical structures of DZP (diazepam), RSV (resveratrol), SAL (salicylic acid), pTHPP (5,10,15,20-tetrakis-(4-hydroxyphenyl)-21*H*,23*H*-porphine), DiI (1,1′-dioctadecyl-3,3,3′,3′-tetramethylindo-carbocyanine perchlorate), DiR (1,1′-dioctadecyl-3,3,3′,3′-tetramethylindotri-carbocyanine iodide), and NR (9-(diethyl-amino)-5*H*-Benzo(α)phenoxazin-5-one; nile red). The substances were used as model drugs.**

Nile red (NR; 9-(diethylamino)-5*H*-Benzo(α)phenoxazin-5-one; log*P* 3.8; M_r 318.37 g/mol [257]) was obtained from Sigma, Steinheim, Germany. The very lipophilic dialkylindocarbocyanines DiI (1,1´-dioctadecyl-3,3,3´,3´-tetramethylindocarbocyanine perchlorate, M_r 933.88 g/mol, log*P* 3.76 [254]) and DiR (1,1´-dioctadecyl-3,3,3´,3´-tetra-methylindotricarbocyanine iodide, M_r 1013.41 g/mol) were purchased from Sigma-Aldrich BioChemika, Schnelldorf, Germany (structures see Figure 13). The fluorescence dyes were used for further characterisation of the nanocapsules. Samples were labelled with DiI during investigation of their light protection capability. Release profiles were obtained using DiI, DiR, and NR. For the determination of the *in vivo* behaviour of the nanoscaled samples, DiR and NR were incorporated into the core.

For size determination during AF4, the tenside FL 70 (Lux clean®, Exaclean GmbH, Duisburg, Germany) was added to the mobile phase. It represents an alkali-containing fat dissolving concentrate (pH 13.5) consisting of water soluble solvents, anionic tensides, and auxiliary substances. Its function was to prevent particles from adhering to the membrane.

The parenteral fat emulsion (Lipovenös® MCT 10 %, parentFE) used for AFM investigations contained 10 % (w/v) oil as inner phase, composed of each 5 % medium-chain triglycerides (MCT) and long-chain triglycerides (LCT, from soy bean oil). It was purchased from Fresenius Kabi GmbH, Bad Homburg, Germany. Further components were glycerol (2.5 %, w/w), phospholipids from eggs (0.6 %, w/w; about 80 % thereof were phosphatidylcholine), sodium oleate, sodium hydroxide, and water for injection purposes. Poly-L/D-lysine hydrobromide was supplied by Sigma, Steinheim, Germany.

L(+)-ascorbic acid sodium salt was utilised as reducing agent and was obtained from Fluka BioChemika, Buchs, Switzerland.

The dialysis membrane (Spectra/Por® molecularporous membrane tube, Spectrum Lab. Inc., Rancho Dominguez, CA, USA) with 20.4 mm in diameter (volume 3.3 mL/cm) was composed of cellulose acetate with a molecular weight cut off (MWCO) of 6-8 kDa.

3.3 Experimental animals

Male, nude mice of the stock SKH1-Hr were purchased from Charles River Laboratories GmbH (Germany). All animal experiments followed the protocol approved by Animal Ethics Committee of the State Saxony-Anhalt and the commissary of animal protection from Martin-Luther-University Halle. Animal housing, feeding and treatment was performed according to the international standards and according to the European Community guidelines. Mice were hairless (albino-background coat), immunocompetent, at the age of 10 months and had a weight of 33 g to 43 g. They were housed under controlled conditions (12 h light/dark schedule, 24 °C) and received mice chow and tap water *ad libitum*.

4 EXPERIMENTAL

4.1 Preparation methods

4.1.1 High-pressure homogenisation

High-pressure homogenisation (HPH) was carried out in two steps (two-stage high-pressure valve homogeniser nG7400.270P, Stansted Fluid Power Ltd., Stansted, United Kingdom). For the emulsions, the first step consisted of five continuous cycles at 1000 ± 100 bar combined with 100 bar back pressure at the second homogenising valve, followed by the second step of one cycle at 400 bar. In case of the nanocapsules, the pre-dispersed samples were treated with four cycles at 800 bar combined with 100 bar back pressure, followed by one cycle at 400 bar. Some samples, especially those containing gelatin, required heating during preparation to prevent gelation. The minimum sample volume was 40 mL due to death volume of the tube system. For all systems the flow rate of the liquid samples through the high-pressure homogeniser was determined using a pump rhythm of two hits per second. A flow speed of 20 mL per minute was found, i.e. the homogenisation time per cycle accounts to 2 minutes for a volume of 40 mL (one cycle) and accordingly 10 minutes for five homogenisation cycles (emulsions). Since during downtime of the high-pressure homogeniser its tubes contain water (hydraulic operation), the sample gets partly diluted when it is pumped through the instrument. Therefore, before and after homogenisation, each 5 mL of the possibly diluted sample were discarded in order to keep the oil content constant.

4.1.2 Preparation of nanoemulsion templates

In a first step, an emulsion template containing the oil (medium chain triglycerides, MCT) and an aqueous solution of the negatively charged emulsifier (OSA starch, gum arabic or sugar beet pectin) was prepared. The emulsifier fulfilled two functions: it was used both as stabiliser for the oily phase and as the first negatively charged polyelectrolyte layer of the shell. In detail, the emulsion was induced by injecting different percentages (v/v) of MCT into an aqueous solution of the emulsifier (21-G needle, inner diameter 0.8 mm, length 4 cm; Braun, Melsungen, Germany). The bulk oil was dispersed in the aqueous phase under stirring at 18,000 rpm for 3 minutes with a rotor-stator high-sheer mixer (Ultra Turrax, IKA T18 basic; IKA-works, Taquedo, Brasil) and reduced to micron-sized droplets. Subsequently, HPH (at ambient temperature) was applied to obtain nanoscaled MCT droplets as a template for the nanocapsules. In order to maximise the oil content of the emulsion and thereby the loading capacity for lipophilic drug candidates, the MCT ratio in the primary emulsion was varied from 5 % up to 25 % (v/v), depending on the emulsifier. Emulsions of the following compositions were prepared (Table 2):

Table 2 Overview of the preparation of different primary nanoemulsions (E = emulsion; MCT = medium-chain triglycerides, OSA = OSA starch, CHI = chitosan, GA = gum arabic, SBP = sugar beet pectin)

No.	sample	% (v/v) MCT	MCT (mL)	Emulsifier used	Volume (mL) and concentration (% w/w) of emulsifier
1	E-OSA5	5 %	2.5 mL	OSA starch	47.5 mL of 5 % OSA solution
2		10 %	5 mL	OSA starch	45 mL of 5 % OSA solution
3		12.5 %	6.25 mL	OSA starch	43.75 mL of 5 % OSA solution
4		15 %	7.5 mL	OSA starch	42.5 mL of 5 % OSA solution
5	E-OSA7.5	10 %	5 mL	OSA starch	45 mL of 7.5 % OSA solution
6	E-OSA11.25	15 %	7.5 mL	OSA starch	42.5 mL of 11.25 % OSA solution
7	E-OSA15	20 %	10 mL	OSA starch	40 mL of 15 % OSA solution
8	E-OSA18.75	25 %	12.25 mL	OSA starch	37.75 mL of 18.75 % OSA solution
9	E-GA5	5 %	2.5 mL	gum arabic	47.5 mL of 5 % GA solution
10	E-GA7	5 %	2.5 mL	gum arabic	47.5 mL of 7 % GA solution
11	E-GA10	5 %	2.5 mL	gum arabic	47.5 mL of 10 % GA solution
12	E-SBP1	5 %	2.5 mL	sugar beet pectin	47.5 mL of 1 % pectin solution
13	E-SBP2	5 %	2.5 mL	sugar beet pectin	47.5 mL of 2 % pectin solution
14	E-SBP2.5	5 %	2.5 mL	sugar beet pectin	47.5 mL of 2.5 % pectin solution
15	E-SBP5	5 %	2.5 mL	sugar beet pectin	47.5 mL of 5 % pectin solution
16	E-OSA4.5 /SBP0.5	5 %	2.5 mL	OSA/ SBP-mix	47.5 mL solution with 4.5 % OSA and 0.5 % pectin
17		10 %	5 mL	OSA/ SBP-mix	45 mL solution with 4.5 % OSA and 0.5 % pectin

4.1.3 Preparation of polyelectrolyte nanocapsules

The process has been schematically described in references [221,222] and is given in Figure 14 for three-layered nanocapsules composed of OSA starch, chitosan and λ-carrageenan. The formation of the capsule wall composed of three or five layers by complex coacervation is illustrated in Figure 15.
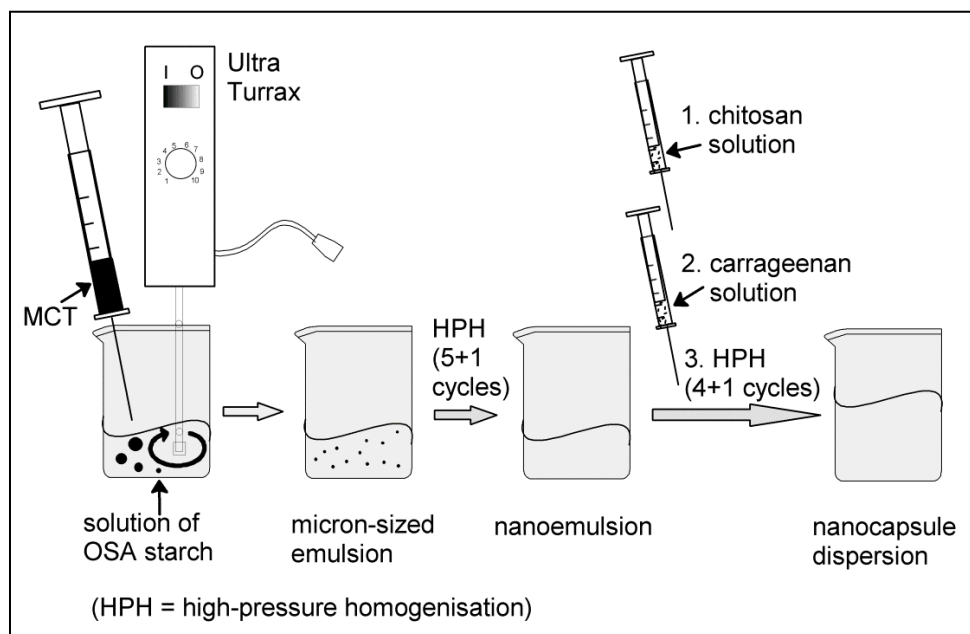
Figure 14 Schematic illustration of the nanocapsule preparation (example NC-OSA-CHI-CARR-2.5%)

Capsules were obtained by slow, consecutive injection of cationic and anionic polyelectrolyte solutions into the high-pressure homogenised primary emulsion. Cationic polyelectrolytes (chitosan or gelatin type A) formed the positively charged second layer (→ interstage), while the anionic polyelectrolytes λ-carrageenan, sugar beet pectin or gum arabic formed the third capsule shell layer. Based on three-layered nanocapsules (NC3), five-layered nanocapsules (NC5) were developed by addition each of one more layer of the second and third layer.
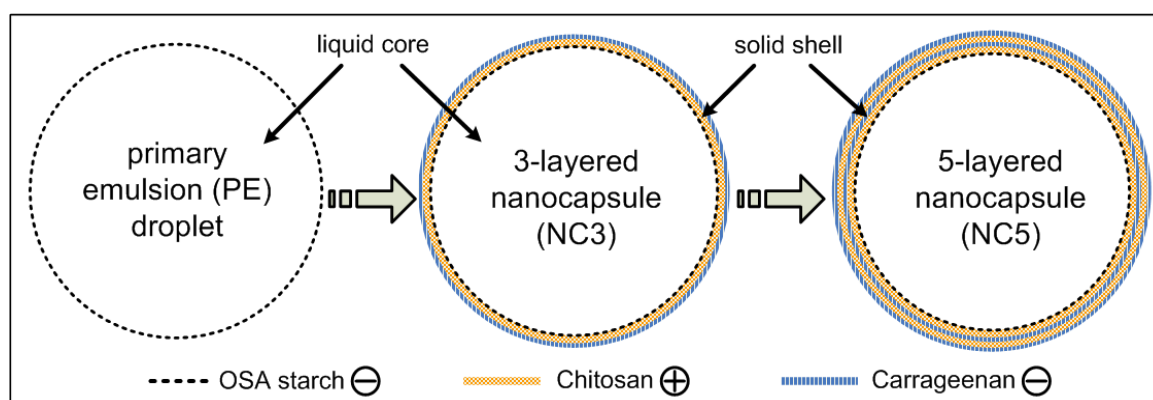
Figure 15 Schematic assembly of nanocapsules with three- and five-layered shells (NC3 = NC-OSA-CHI-CARR-2.5% and NC5 = NC-OSA-CHI-CARR-CHI-CARR-1.11%) from an emulsion (PE = E-OSA5-5%). The formation of a solid capsule wall is driven by electrostatic attraction of oppositely charged polyelectrolytes.

The produced nanocapsule dispersion was finally high-pressure homogenised and centrifuged for 15 minutes at 4000 rpm to separate the nanocapsules from polyelectrolyte aggregates, which were not encapsulated. The successive addition of oppositely charged polyelectrolytes to the nanoemulsion led to polyelectrolyte

nanocapsules with an oily core and a solid wall of three or five layers. The development of the quantity (concentration, volume) of the polyelectrolytes that were necessary in each shell layer to completely cover the oil droplets (investigated by conversion of the ζ-potential) was the focus of the preparation section.

4.1.3.1 Screening of different polyelectrolytes regarding their complex formation properties

One necessary requirement for the conversion of emulsions into nanocapsules is the formation of polyelectrolyte complexes in terms of complex coacervation between the oppositely charged hydrocolloids forming a solid capsule shell. That is why preliminary investigations on that behaviour between anionic and cationic polyelectrolytes had to be carried out. Since the complex coacervation between OSA starch and chitosan, and between chitosan and carrageenan, respectively, had already been proven [52], only the remaining combinations needed to be studied (see Table 3).

Table 3 Investigated polyelectrolyte pairs regarding complex formation behaviour (n.d. = not determined)

	Chitosan (+)	Gelatin A (+)
OSA starch (-)	n. d.	x
λ-carrageenan (-)	n. d.	x
Sugar beet pectin (-)	x	x
Gum arabic (-)	x	x

The test was performed by adding a solution of one of the cationic substances to one of the anionic polyelectrolyte solution, or vice versa. Potential complex reactions occurring in terms of precipitation were observed and documented by taking photographs.

4.1.3.2 Overview of the prepared nanocapsule samples

Based on the emulsifying power of the individual polyelectrolytes studied, and the results of complex formation capability between oppositely charged polyelectrolytes, nanocapsules of the different compositions as given in Table 4 were prepared:

Table 4 Overview of the prepared nanocapsule formulations (NC = nanocapsules with 3 or 5 shell layers; E = emulsion;, OSA = OSA starch, CHI = chitosan, CARR = λ-carrageenan, GA = gum arabic, GEL = gelatin, SBP = sugar beet pectin); (#) preparation at 50 °C required due to high viscosity, gelation or aggregation

No.	sample	% (v/v) MCT	Template (= shell layer 1)	Shell layer 2	Shell layer 3
1	NC-OSA-CHI-CARR (NC3)	2.5%	E-OSA5-5%, 20 mL	0.2 % CHI solution, 10mL	0.45 % CARR solution, 10 mL
2		4.35%	E-OSA5-5%, 40 mL	2 % CHI solution, 2 mL	2.25 % CARR solution, 4 mL
3		8.6% (#)	E-OSA5-10%, 40 mL	2 % CHI solution, 2.2 mL	2 % CARR solution, 4.5 mL
4	NC5-OSA-CHI-CARR-CHI-CARR (NC5)	1.11%	NC-OSA-CHI-CARR-2.5% (NC3), 20 mL	layer 4: 0.2 % CHI solution, 10 mL	layer 5: 0.45 % CARR solution, 15 mL
5	NC-OSA-CHI-GA	2%	E-OSA5-5%, 20 mL	0.2 % CHI solution, 10mL	4 % GA solution, 20 mL
6		3.7%	E-OSA5-5%, 30 mL	2 % CHI solution, 1.6 mL	25 % GA solution, 9 mL
7		7.4%	E-OSA5-10%, 30 mL	2 % CHI solution, 1.6 mL	25 % GA solution, 9 mL
8	NC-OSA-GEL-CARR	3% (#)	E-OSA5-5%, 30 mL	10 % GEL solution, 5 mL	1.35 % CARR solution, 15 mL
9	NC-OSA-GEL-GA	1.43% (#)	E-OSA5-5%, 20 mL	10 % GEL solution, 4 mL	5 % GA solution, 45 mL
10		3% (#)	E-OSA5-5%, 30 mL	10 % GEL solution, 6 mL	25 % GA solution, 13.5 mL
11		5.625% (#)	E-OSA11.25-15%, 15 mL	5 % GEL solution, 13.5mL	25 % GA solution, 11.5 mL
12	NC-OSA-GEL-SBP	2.68% (#)	E-OSA5-5%, 30 mL	10 % GEL solution, 6 mL	2 % SBP solution, 20 mL
13		3.26% (#)	E-OSA5-5%, 30 mL	10 % GEL solution, 6 mL	4 % SBP solution, 10 mL
14		5.55% (#)	E-OSA5-10%, 30 mL	5 % GEL solution, 13 mL	4 % SBP solution, 11 mL
15	NC-SBP-CHI-CARR	2.5%	E-SBP2.5-5%, 20 mL	0.2 % CHI solution, 10mL	0.45 % CARR solution, 10 mL
16	NC-GA-CHI-CARR	3.79%	E-GA7-5%, 25 mL	0.6 % CHI solution, 5 mL	1.35 % CARR solution, 3 mL
17	NC-GA-GEL-SBP	1.85% (#)	E-GA7-5%, 20 mL	10 % GEL solution, 24 mL	2 % SBP solution, 10 mL
18	NC-GA-GEL-GA	2.5% (#)	E-GA7-5%, 20 mL	10 % GEL solution, 14 mL	25 % GA solution, 5.6 mL

4.1.4 Preparation of PEG-PLA-10% nanocapsules

The PEG-PLA-10% nanocapsules served as comparison material of the polyelectrolyte nanocapsules during AFM experiments. PEG-PLA-10% nanocapsules were prepared by the method described by Fessi et al. [46]. It is based on interfacial deposition of preformed polymer following solvent displacement. In this process, the polymer (PEG-PLA-10%, poly(lactic) acid with 10 % w/w polyethylene glycol) and the oil (MCT) were dissolved in 10 mL of a semi-polar water-miscible solvent (acetone; HPLC grade, Roth, Karlsruhe, Germany) which was injected into 20 mL of an aqueous solution of Poloxamer 188 under moderate agitation. Nanocapsules were formed instantaneously by rapid diffusion of the solvent into the water phase. Subsequently, the solvents were evaporated to 10 mL under reduced pressure at ambient temperature. The final concentrations were 0.6 % polymer, 2.5 % oil, 0.3 % hydro-philic stabiliser (each w/w) which had successfully led to stable nanocapsules before [14].

4.2 Characterisation methods

4.2.1 Critical micelle formation concentration

The critical micelle formation concentration (CMC) of the surfactant OSA starch was determined using a DCAT 11 device (Dynamic Contact Angle Instruments and Tensiometers, DataPhysics Instruments GmbH, Raiffeisenstraße 34, D-70794 Filderstadt, Germany). It is based on the measurement of the static, time- and temperature-dependent surface, and interfacial tensions of liquids according to the Wilhelmy plate method. A molecular weight of $4 \cdot 10^5$ Da was assumed. Increasing volumes of a $5 \cdot 10^{-4}$ M aqueous solution of OSA starch (20 %) were added to 40 mL of double-distilled water. In each step, a volume of 50 to 500 µL was added automatically, and the mixture was stirred for 30 seconds before the surface tension was defined at 25 °C by a platinum plate moving upwards. 50 data points were acquired by this procedure. The starting point was the surface tension of pure water (approx. 72 mN/m). For each step, the decrease of the surface tension was plotted versus the resulting OSA starch concentration by means of the software SCAT 12. The CMC was obtained graphically as the intersection of two straight lines being tangent to the curve.

4.2.2 Photon correlation spectroscopy (dynamic light scattering)

By means of PCS, particle sizes were determined at 25 °C, using the non-invasive back scattering (NIBS) technology with a laser scattering angle of 173° (High Performance Particle Sizer, Malvern Instruments Ltd., UK). All samples were measured tenfold (each 10 s) immediately after preparation (maximum 1 day later). The samples had to be diluted until transparency in order to ensure free Brownian motion of the particles. Ideal dilution degree was determined to be 1:100 as higher dilution showed constant sizes (Figure 16). Owing to the different oil content, samples were diluted to an equal oil amount of 0.025 % (v/v) (e. g. nanoemulsions with 5 % oil: 1:200; nanocapsules with 2.5 % oil: 1:100). Data treatment was performed by means of the Dispersion Technology Software DTS 4.20 (Malvern Instruments Ltd., UK). A refractive index (RI) of 1.45 and optical absorption of 0.001 for MCT were assumed. The viscosity of the samples was each determined and accounted for individually.
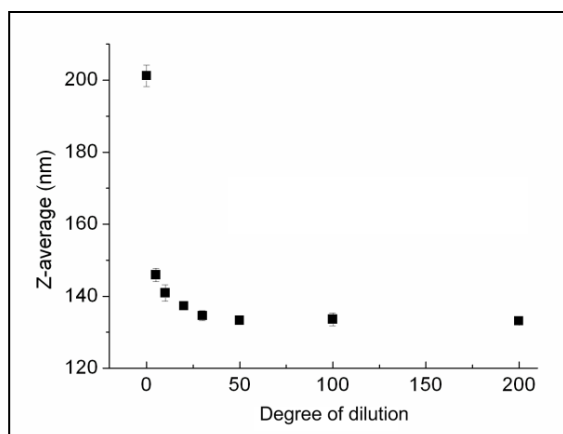
Figure 16 Influence of the degree of dilution on the particle size determined by PCS (E-OSA5-5%, diluted with double-distilled water)

4.2.3 Laser diffraction (static light scattering)

For static light scattering measurements, a Mastersizer 2000 (Malvern Instruments Ltd., UK) was used. All samples were measured five times immediately after preparation (maximum 1 day later). Undiluted samples were injected into the instrument until an optical obscuration of 2 to 5 % was reached. In control experiments even large deviations in the obscuration (up to 10 %, more sample added) had no significant influence on the size result in case of monomodal size distributions. Data treatment was performed by means of Mastersizer Software version 5.22 (Malvern Instruments Ltd., UK) following the Mie theory. Particle size distribution curves of prepared emulsions and nanocapsules are already available [222,223].

4.2.4 ζ-potential

The surface charge after each shell layer was determined by measuring the ζ-potential with the Zetasizer, Malvern Instruments Ltd., UK. All samples were measured in triplicate immediately after preparation (maximum 1 day later). The ideal dilution degree was defined in dilution series (cf. Figure 17). An oil content of 0.025 %, obtained by 1 by 200 dilution of an emulsion containing 5 % (v/v) MCT, was found to be ideal.
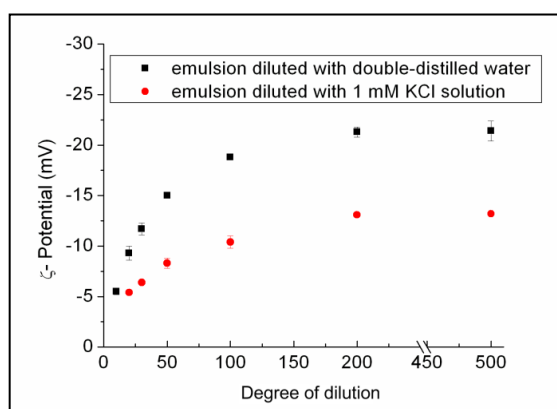
Figure 17 Influence of the degree of dilution on the ζ-potential of E-OSA5-5%

Thus, dilution of the primary nanoemulsion and the nanocapsules was conducted analogue to PCS measurements. The chitosan- or gelatin-covered interstage nanodispersions (second or fourth layer) were diluted down to the same oil content. Dilutions were carried out with double-distilled water. Control measurements with a background of 1 mM potassium chloride resulted in a ζ-potential that was consistently

lower than that from the aqueous dilution due to a compression of the electric double layer by the higher ionic strength [224]. Due to this influence of the ionic strength on the ζ-potential, constant salt concentration or electric conductivity is crucial during the measurement. After each formulation step an inversion of the surface charge was expected since oppositely charged polyelectrolytes followed each other.

4.2.5   Transmission electron microscopy

For electron microscopy, nanocapsules were cryofixed using a propane jet-freeze device JFD 030 (BAL-TEC, Balzers, Liechtenstein). Subsequently, the samples were freeze-fractured at -150 °C without etching with a freeze-fracture/-etching system BAF 060 (BAL-TEC). The surfaces were shadowed with platinum to achieve a good topographic contrast (2 nm layer, shadowing angle 45°) and subsequently with carbon to stabilise the ultra-thin metal film (20 nm layer, shadowing angle 90°). The replica were floated into a sodium hypochlorite solution (4 % available chlorine; Roth, Karlsruhe, Germany) for 30 minutes, rinsed in distilled water (10 minutes), washed in 30 % acetone (Roth, Karlsruhe, Germany) for 30 minutes and rinsed again in distilled water (10 minutes). Afterwards, the replica were mounted on copper grids, coated with a formvar film and observed with a transmission electron microscope (EM 900, Carl Zeiss SMT, Oberkochen, Germany) operating at 80 kV. Pictures were taken with a Variospeed SSCCD SM-1k-120 camera (TRS, Moorenweis, Germany).

4.2.6   High-resolution light microscopy

The samples were investigated by means of the CytoViva® high-resolution optical light microscope system (CytoViva Inc., Auburn, AL, USA), consisting of an Exfo X-cite 120 light source and an Olympus BX-41 microscope combined with a dark field illumination system. It routinely enables to image features in the 150-nm range as well as live cell imaging in real time with high-contrast and high resolution properties. The new technology was developed by Dr. Vitaly Vodyanoy of Auburn University (Auburn, AL, USA). The sample was imaged with 100x magnification after drying on the slide in order to reduce the Brownian motion. The image was generated using a high-resolution dark field condenser.

4.2.7   Theoretical incorporation capacity for lipophilic model drugs

The maximum drug load capacity of the successfully developed nanocapsule formulations was determined for resveratrol (RSV), salicylic acid (SAL), pTHPP, and diazepam (DZP). Their solubility in MCT was identified by dissolving the substances under stirring, heating, ultrasonicating and re-cooling. The maximum amount that was soluble after final cooling to ambient temperature (if no re-crystallisation occurred) or even to +2 °C to +8 °C (refrigerator) was declared to be the solubility in MCT. Using the MCT content of each nanocapsule dispersion, the theoretical solubility in the final samples was calculated.

4.2.8   Asymmetrical flow field-flow fractionation

For AF4 separation, the Eclipse FFF system (Wyatt Technology Europe, Dernbach, Germany) coupled to an isocratic pump and a micro vacuum degasser (Agilent 1100 series, Agilent Technologies, Böblingen, Germany) was used. It was connected to an 18 angle MALS detector (DAWN EOS MALS, Wyatt, scattering angles ranging from 14° to 163°) having a 690 nm GaAs laser, and an RI detector (RID) Shodex 101 (Shoko America, Colorado,

USA). Successfully developed nanocapsule samples were injected into a channel equipped with a trapezoidal-shaped spacer (height 350 μm), and a 5,000 g/mol (MWCO 5 kDa) regenerated cellulose ultrafiltration membrane (Nadir C010F, Microdyn-Nadir GmbH, Wiesbaden, Germany) as accumulation wall. Jumpers were used to attenuate signals with intensity higher than the axis intercept by the factor 100. The cross flow conditions were controlled by the Eclipse software v.2.3.8. (Wyatt). Data was evaluated using ASTRA software v.4.90.08 (Wyatt). Size calculations were done using the particle mode of the software and assuming compact spheres. The root mean square (RMS) radius of the particles at each elution time (measurement interval: 1 s) was calculated applying the Rayleigh-Gans-Debye (RGD) approximation [225] if not stated otherwise.

4.2.8.1 Determination of the molecular weight of OSA starch by AF4-MALS

The moisture content is an important parameter of a substance for the investigation of the molar mass. Thus, initially the moisture content of OSA starch was studied by thermogravimetry (TG) using a thermal gravimetric analysis instrument TG 209 (Netzsch GmbH, Selb, Germany) with a heating rate controller (Netzsch GmbH, Selb, Germany) and an external gas cell for achieving constant conditions (nitrogen atmosphere). Approximately 22 mg of the substance were weighed into an aluminium oxide sample holder. The sample was heated from 20 °C up to 150 °C with a heating rate of 10 K/min, and afterwards kept isothermal at 150 °C for 10 minutes. The thermo balance detected the loss of mass which arose from the evaporation of adhesive water and possibly other volatile compounds. The sample measurement was corrected by a control measurement of the pure sample holder.

The refractive index (RI) increment dn/dc was determined at 30 °C by measuring the RI detector signal (without previous separation in the channel) of five differently concentrated OSA starch solutions preserved with 0.02 % (w/v) sodium azide (NaN$_3$, Fluka/Sigma, Schnelldorf, Germany), each in triplicate. The concentrations of OSA starch given in Table 5, corrected by the determined moisture content, were injected (each 200 μL). The obtained RI signal intensity was plotted versus the corresponding OSA starch concentration. The slope of the linear fitted graph was declared as the dn/dc value.

Table 5 Concentrations of the OSA starch solutions used for dn/dc determination using RID

Level	Prepared concentration (mg/mL)	Concentration corrected by moisture content (mg/mL)
1	0.05	0.047445
2	0.075	0.0711675
3	0.1	0.09489
4	0.125	0.11861
5	1	0.9489

The dn/dc value determined as described above was needed for subsequent calculation of the molecular weight of OSA starch after separation and detection by AF4-MALS. For the experiment, OSA starch solutions with a concentration of 1 mg/mL were prepared in a 50 mM NaCl (Fluka, Schnelldorf, Germany) solution of

double-distilled water, filtered through 0.1 µm hydrophilic PVDF (Durapore membrane filter 47 mm diameter, Millipore, Schwalbach, Germany) and preserved with 0.02 % (w/v) NaN_3. A channel flow of 2 mL/min was maintained using the same NaCl solution, and a linearly decreasing cross flow from 2 mL/min to 0 mL/min over 30 min was used for separation (see Table 6, step 5). The MALS detector signals were captured over a total run time of 60 min. A detector flow of 1.0 mL/min and an inject flow of 0.2 mL/min were applied. Analysis was performed by the Astra 4.9 software version with a baseline correction.

Table 6 Programme for OSA starch separation using A4F-MALS

No.	Step	Duration (min)	Cross flow (mL/min) Start	End	Focus flow (mL/min)
1	Elution	2	2	2	-
2	Focus	1	-	-	2
3	Focus+inj	2	-	-	2
4	Focus	1	-	-	2
5	Elution	30	2	0	-
6	Elution	10	0	0	-
7	Elution+inj	10	0	0	-

4.2.8.2 Size determination of emulsions and nanocapsules by AF4-MALS

The samples were preserved with 0.02 % w/v NaN_3 and adjusted to an equal oil concentration of 0.02 % by addition of a 0.2 % solution of the tenside FL-70 which presented the mobile phase. Each 200 µL of a sample were injected at ambient temperature. A channel flow of 2 mL/min was maintained using a 0.2 % solution of the tenside FL-70. Further method parameters for separation are given in Table 7. The MALS detector signals were captured over a total run time of 60 min.

Table 7 Programme for sample separation using A4F-MALS

No.	Step	Duration (min)	Cross flow (mL/min) Start	End	Focus flow (mL/min)
1	Elution	1	2	2	-
2	Focus	1	-	-	2
3	Focus+inj	2	-	-	2
4	Focus	1	-	-	2
5	Elution	5	2	0.5	-
6	Elution	30	0.5	0	-
7	Elution+inj	10	0	0	-

4.3 Study of the stability of the nanocapsules

4.3.1 Freeze-drying

Among steric and electrostatic stabilisation of dispersions, an extended shelf life of drug formulations can be achieved by drying the dispersion, storing the obtained powder and redispersing it in water if required. Evaporation of the aqueous phase under reduced pressure and application of heat was not appropriate since it destabilised the particles. Thus, sample dispersions were lyophilised using a freeze-drying instrument Alpha 2-4 combined with LDC-1M controller (Christ Gefriertrocknungsanlagen GmbH, Osterode, Germany). Each 4 mL of the samples were deep-frozen at -80 °C and immediately transferred into the vacuum of the instrument for lyophilisation. The pressure was 0.37 mbar and the set point for temperature was -30 °C during the main drying phase. In one case trehalose (D(+)–α,α-Trehalose dehydrate, alpha-D-gluco-pyranoside, M_r 378.33 g/mol, Sigma-Aldrich Chemie GmbH, Steinheim, Germany) was added as cryoprotecting additive during lyophilisation. After lyophilisation the obtained dried substances were redispersed in double-distilled water. The size of the dispersed particles after freeze-drying was determined by LD/PCS and compared to the size values of the originate samples. Finally, conclusions were drawn whether lyophilisation is appropriate to extend the storage stability of the nanocapsules.

4.3.2 Autoclavation

For possibly intravenously administered dosage forms such as the prepared formulations the reduction of germs is not sufficient but sterility is of fundamental importance in order to avoid serious infections. Since the dispersions are aqueous, autoclavation with saturated steam is the ideal sterilisation process. In order to investigate the stability of nanocapsule dispersions over autoclaving, the samples were standardised to 0.5 % (v/v) MCT by dilution with pure double-distilled water. The autoclaving was performed with a bench-top autoclave instrument Systec 5075 EL (Systec GmbH, Wettenberg, Germany) in glass vials for 15 minutes at 121 °C and 2 bar each in triplicate. The evaluation of the formulation stability was performed by a comparison of d(0.9) values obtained from LD before and after treatment.

4.3.3 Isostatic high pressure

The samples were treated with a hydrostatic high-pressure food processor (Foodlab S-FL-085-9-W, Stansted Fluid Power Ltd., Stansted, United Kingdom) which allows a maximal isostatic pressure of 9000 bar (900 MPa). About 2 mL of each sample were filled into polypropylene plastic reaction tubes with polyethylene plastic lids (Brand, Wertheim, Germany) which are stable bewteen -90 °C and +100 °C. They were placed into the pressurising liquid (mixture of 20 % ethanol and 80 % castor oil, both (v/v), Roth, Karlsruhe, Germany) at ambient temperature and treated with pressures between 200 and 800 MPa over periods of 10 minutes, 30 minutes or 6x5 minutes. The temperature control was adjusted to maximum and minimum values of +50 °C and +5 °C which might have occurred during compression or decompression. The z-average size and PDI (PCS) of the samples before and after treatment was compared. From these values statements about the stability over high pressure treatment were concluded.

4.3.4 Temperature stability investigated by ultrasonic resonator technology

This method is also mentioned under section 4.5.3 (p. 47). The measurements were performed with a ResoScan[TM] System by TF Instruments Inc., Monmouth Junction, NJ, USA, using Ultrasonic Resonator Technology. It contains two closed resonator cavities in which samples are prevented from evaporation by gas-tight lids. Since the ultrasound propagation is very sensitive to temperature [115], the measurements were done at constant 25 °C with a thermostat accuracy of ±0.01 K. The frequency of the ultrasonic waves used for the measurements was about 10 MHz. The resolution of the measured ultrasonic velocity was 0.001 m/s.

The samples were adjusted to equal sodium acetate salt and equal oil content to allow for comparison. Two temperature modes were studied. First, the stability of the formulations at physiological temperature was investigated by an isothermal scan of the ultrasound velocity at 37 °C. Therefore, the samples were heated up to 37 °C and the velocity was monitored for 12 hours. The ultrasound velocity was corrected by the acetate buffer velocity (dispersing phase). Secondly, storage of the samples at tropical temperatures was emulated. The ultrasound velocity of the samples (corrected by acetate buffer velocity) was measured in the range between 25 °C and 85 °C to evaluate the stability over increased temperatures. The results were plotted in graphs as difference of velocity (ΔU) versus time or versus temperature.

4.4 Investigation of the light protection capability of the capsule wall

4.4.1.1 Fluorescence spectroscopy

The focus of this study was to find out whether the external fluorescence intensity of incorporated dyes decreased with increasing number of polyelectrolyte layers surrounding the MCT core. Reduction of the intensity would mean a better light protection for incorporated molecules which is essential for light sensitive drugs. Therefore, samples were investigated that were prepared in a sequence: (i) pure MCT, (ii) a primary nanoemulsion, (iii) three- and (iv) five-layered nanocapsules, resulted from capsule shell optimisation. The emulsion and the nanocapsules were adapted to an equal oil content of 1.11 %. Prior to the experiment, the dye DiI was transferred into the samples by means of an ethanolic dye solution. The ethanol was evaporated afterwards. A concentration series of DiI in the range between 0.125 and 4 µg/g was prepared for the four samples. The fluorescence intensity of DiI from the samples was determined using an excitation wavelength of 540 nm, emission at 580 nm and a coarse adjustment of 3 (MPF-44 fluorescence spectrometer, Perkin Elmer Instruments, Überlingen, Germany). The intensities were plotted versus the concentration and compared.

4.4.1.2 Fluorescence imaging

The four samples mentioned under 4.4.1.1 were labelled with DiI as follows: Each 100 µL of each sample and concentration were filled into a 96-well plate. Due to the strong intensity of DiI dissolved in MCT, this concentration series was measured separately. Otherwise the MCT samples would have irradiated fluorescence light over a wide distance and influenced the other samples. The used instrument was a Maestro[TM] *In vivo* Fluorescence Imaging System (Cambridge Research & Instrumentation (CRI) Inc., Woburn, MA, USA), operated with the Maestro software version 2.4.3. During a measurement, the green pass filter set was used for excitation (503 nm to 555 nm) and emission light (580 nm longpass). The tunable emission filter was

automatically stepped in 2 nm increments within the acquisition range of 550 nm to 800 nm while the imaging system captured images at each wavelength interval with constant exposure time (10 ms). The fluorescence intensity (emission at 600 nm) was plotted versus the concentration and compared.

4.5 Methods for the investigation of mechanical properties

4.5.1 ^{1}H nuclear magnetic resonance spectroscopy

The NMR spectra were acquired from a 400 MHz ^{1}H NMR spectrometer (Varian Gemini 2000, Varian Inc., Palo Alto, California). The reference substances (pure polyelectrolytes) were dissolved in deuterium oxide D_2O (Roth, Karlsruhe, Germany). An MCT spectrum was obtained after dissolving it in deuterated chloroform ($CDCl_3$) (Roth, Karlsruhe, Germany). The NMR spectra for the consecutively prepared samples (primary nanoemulsion as well as three-layered nanocapsules) were obtained by measuring the sample dispersion including 30 % (v/v) D_2O (mixing seven parts of sample with three parts of D_2O). An aliquot of each aqueous sample was filled in an NMR tube of borosilicate glass. D_2O (for aqueous samples) or $CDCl_3$ (for measurement of MCT) were added for field login; tetramethylsilane (TMS) was added as chemical shift reference (δ = 0 ppm). The line width at half the signal height was determined by OriginPro 7.5 Software (Origin Lab Corp., Northampton, Maryland).

4.5.2 Atomic force microscopy

Since stiffness analysis on NDDS is still a new field, it was aimed to discover the mechanical properties of three consecutive samples, (i) the nanoemulsion, (ii) nanocapsules with a shell of three (NC3) or (iii) five layers (NC5), by at least two further independent techniques, namely AFM and URT. AFM was employed to confirm the size measurement results of the nanocapsules, to compare the mechanical properties of the three consecutive samples, and to determine the shape and surface morphology of these and further successful formulations.

AFM was performed with a Multi-Mode Microscope instrument combined with a Nanoscope III control system (Veeco Metrology, Santa Barbara, CA 93117, USA) using the software version Nanoscope 5.12r5 (Veeco Metrology, Santa Barbara, CA 93117, USA) for data acquisition. The samples were mounted on negatively charged ultraclean mica sheets (Plano GmbH, Wetzlar, Germany) and scanned in (a) the tapping mode for topographic images, as well as in (b) the contact mode for force-volume analysis in order to derive the development of the mechanical properties of the capsule shell by increasing the wall thickness. Cantilevers with corresponding properties were used in each mode.

4.5.2.1 Topographic analysis

Tapping mode was the mode of operation. The following parameters were used: the image size was 512 samples per line (512×512), the scan rate was <2 Hz, the integral gain was 0.33 and the proportional gain 0.6. The applied rectangular, phosphorus-doped Silicon cantilever MPP-11100-Tap 300 (Veeco Metrology, Santa Barbara, CA 93117, USA, thickness 4 μm, length 125 μm and width 35 μm) presented a relatively hard material due to a spring constant of 40 N/m and a resonance frequency of 300 kHz. The anisotropic tip fixed on the cantilever had a radius of <10 nm, a front angle of 15° and a side angle of 17.5°. Freshly cleaved mica was mounted on a sample holder by means of double-sided adhesive tape. The sample dispersion was diluted 1 by

100, and 10 µL were deposited onto the mica and allowed to dry for about 30 minutes since the instrument controller cannot generate images from the sample in a liquid medium using the tapping mode. Image and data evaluation (height profiles) were conducted with the software WSxM 4.0 Develop 11.1 software [226]. The diameters were measured at half height of the capsules.

4.5.2.2 Force-curve analysis

The three relevant consecutive samples as well as PEG-PLA-10% nanocapsules (prepared according to section 4.1.4), and a parenteral fat emulsion (parentFE, Lipovenös®, see materials section) were investigated as follows. The mode of operation was contact mode. Force volume images were obtained in the relative trigger mode, with the deflection trigger channel. The parameters for data acquisition were 64 numbers of samples, 64 forces per line, 64 samples per line, scan rate 27.9 Hz and a typical force volume scan rate of 0.215 Hz. A general purpose Silicon Nitride triangular cantilever (length 192 µm, width 23 µm) with a conical tip NP-S D (Veeco Metrology, Santa Barbara, CA 93117, USA) was used. The estimated tip radius was 10 nm, the tip height 3 µm and the side angle 35°. The cantilever deflection sensitivity was determined as 0.015 V/nm by scanning pure mica. The spring constant of the relatively soft cantilever was 0.06 N/m (producer information), the resonance frequency was determined with 24 kHz. Freshly cleaved mica was mounted on a sample holder by means of double-sided adhesive tape. The sample dispersion was mounted onto the mica and incubated for 30 minutes. Afterwards unfastened capsules were rinsed off with double-distilled water such that only adhering capsules were scanned. 100 µL of water were added, so the sample maintained in constant humidity during the measurement. This was reached by immediately placing the loaded mica into a liquid cell sample holder (Veeco Metrology, Santa Barbara, CA 93117, USA) which is equipped with an o-ring seal that prevents liquid from evaporating from the sample. The measurements in saturated atmospheric humidity (>70 %) ensured that the sample was permanently kept in moist environment and could not exsiccate. Instead of measuring in dry atmosphere, quantitative force measurements in a liquid medium like water are advantageously due to absence of disturbing capillary forces leading to hysteresis in the force–distance curve [227]. Since the contact mode runs the risk of damaging the sample, an improved adsorption of the negatively charged nanocapsules was aimed by means of incubation of the negatively charged mica surface with a 0.01 % (w/w) Poly-L/D-Lysine solution (positively charged). This is a method widely used for the adsorption of cells, proteins and vesicles [228,229]. However, the attempt was ineffective as the capsules did not show a stronger adhesion compared to the use of pure mica. This was probably due to the fact that the contact area for a spherical particle is very small. Thus, pure mica was used. Force curve analysis was performed by means of an evaluation license of SPIP v.4.6.4 (Image Metrology, Hørsholm, Denmark). The cantilever deflection sensitivity (given by the piezoelectric material) and the slope in the linear part of the approach curves were determined using this software. The obtained y-axis raw data (cantilever deflection piezo voltage) was converted (calculated) into the desired force F by subsequent application of the cantilever deflection sensitivity and the spring constant of the cantilever.

4.5.3 Ultrasonic resonator technology

4.5.3.1 Temperature stability scan

This investigation has been used to study the temperature stability of consecutively prepared nanocapsules in dependence on the shell composition. The procedure has been described under section 4.3.4 (p. 44).

4.5.3.2 Investigation of mechanical properties by ultrasound absorption and velocity

The instrument parameters have been described in section (p. 44). Ultrasound velocity measurements were performed with the aim to investigate the physical phenomenon of ultrasound absorption by polyelectrolyte nanocapsule dispersions featuring different capsule wall compositions. In order to detect small differences between the quite similar investigated, consecutive samples, all influencing factors except the capsule wall composition have to be equal. Particle size [230], dissolved molecules of salt and polyelectrolyte, as well as oil content [231] are known to have a great impact on the velocity. For example, free molecules of salt or other dissolved substances (residual polyelectrolyte molecules) typically increase the ultrasound velocity, while the velocity correlates negatively with increasing oil amount (or other hydrophobic components) due to strong absorption of sound waves. For this reason, the samples were diluted to an equal oil content of 0.5 % (v/v) and adapted to an equal acetate buffer concentration of 15 mM before all measurements. The density of these diluted samples was measured using a DSA 5000 instrument, Anton-Paar, Austria. Furthermore, a similar particle size of the samples ($\approx$150 nm) as well as applying constant temperatures was of crucial importance. Dilution series were prepared and measured for the three samples, the acetate buffer and pure polyelectrolyte solutions. A volume of 180 µL was filled each in the sample and reference cavity. Either double distilled water or acetate buffer, concentrated corresponding to the sample, served as reference medium to compare the measurements. After reaching equilibrium of temperature and initialisation of the measurement, the absolute ultrasonic velocity U and absorption A were continuously measured for at least 2 min with the ResoScan™ instrument and averaged afterwards. For data evaluation, the absolute ultrasound velocity of the samples was reduced by the value of the reference solution (double-distilled water or acetate buffer in the corresponding concentration). In this manner, relative velocities (delta U) were obtained by correcting the absolute ultrasound propagation by the influence of the buffer molecules.

4.6 Methods for the investigation of release behaviour

4.6.1 Dialysis bag experiments

The dialysis bag test (see Figure 18) was conducted for the extremely lipophilic dialkylindo-carbocyanine DiI and the moderately lipophilic dye NR. Nanocapsules labelled with 70 µg NR or DiI/g were diluted 1:15 with 1/15 M phosphate buffer pH 6.8. After certain periods of time the migration of the dye out of the capsule core, through the capsule shell, water phase and dialysis membrane into the MCT phase (10 mL) was detected. Then, the MCT filled dialysis bag was taken out of the water phase, dried and its fluorescence intensity was captured. Spectral fluorescence images *in vitro* were obtained using the Maestro™ *In vivo* Imaging System (CRi Inc., Woburn, MA, USA). A green pass filter was used for emission and excitation of NR and DiI. The tunable filter was stepped in 2 nm increments from 550 to 800 nm while the Cri Maestro™ Multispectral Imaging System

captured images at each wavelength interval with constant exposure time (3 ms). Quantification during the experiment was not possible since the oil could not be measured purely (intensity shielded by the cellulose acetate membrane). Thus only the final concentration of each dye in MCT was accessible after opening the bag. The fluorescence emission of the dialysis bag at 600 nm (both dyes) was plotted versus time.
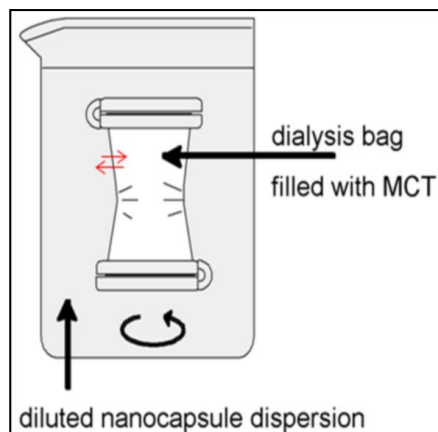

Figure 18 Assembly of the dialysis bag experiment (dispersion heated up to 37 °C)

4.6.2 Modified *in vitro* release simulation into lipophilic medium

This *in vitro* experiment was conducted in order to simulate the *in vivo* release behaviour of the incorporated fluorescence dyes nile red, pTHPP and DiR from the nanocapsules and to investigate their rate of accumulation in MCT which served as a fat-tissue analogue medium. It was performed (i) by covering the sample dispersion with the MCT phase and stirring the dispersion on a heated stirring plate, and (ii) by covering the sample dispersion with the MCT phase and permanent mixing of the phases by means of a rotating temperature-controlled end-over-end apparatus. The procedures are schematically shown in Figure 19.
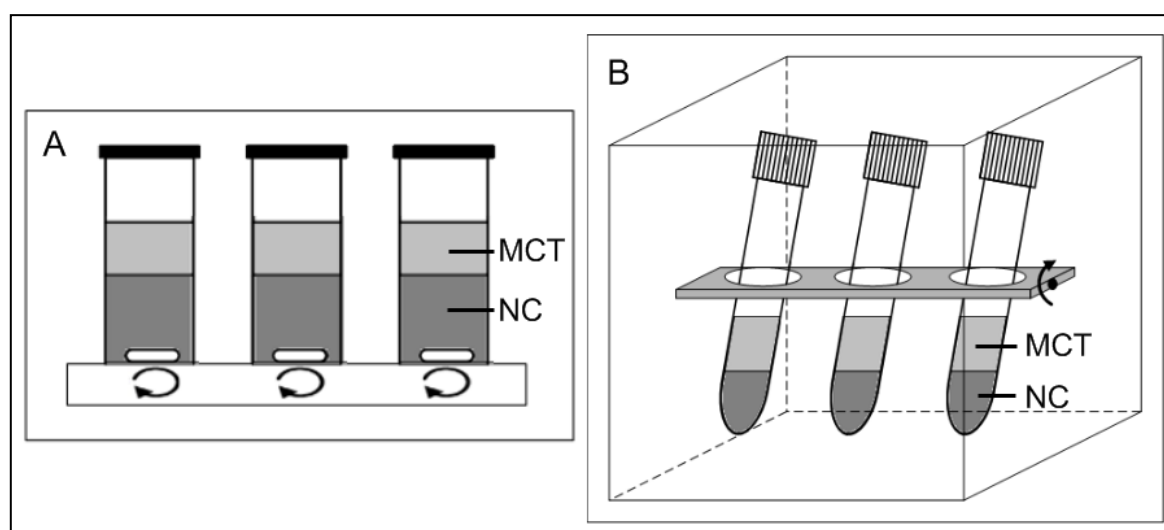

Figure 19 Determination of *in vitro* release behaviour <u>A:</u> on a heated stirring plate, <u>B:</u> in a rotation apparatus (MCT: medium chain triglycerides, NC: diluted nanocapsule dispersion or nanoemulsion)

4.6.2.1 In vitro release on a heated stirring plate

During experiments the release vessels were protected from light and kept at 37 °C. For a 1 by 10 dilution of the sample dispersion, 18 mL of a 0.0333 M acetate buffer pH 4.5 and 10 mL MCT were filled into 40 mL glass

vessels and heated up to 37 °C. Into that two-phase mixture 2 mL of sample were added, each containing 10 µg NR or pTHPP per gram sample. The dispersion in the vessels was mixed with a magnetic stirrer with a speed of about 200 rpm for 24 hours (NR) or 7 weeks (pTHPP). After certain time intervals, 600 µL of the upper MCT phase were withdrawn for quantification of NR and pTHPP and replaced by fresh MCT. For the 1 by 100 dilution, 19.8 mL of the acetate buffer, 5 mL MCT and 200 µL of sample were filled into the glass vessels. 1200 µL MCT were withdrawn from the upper phase and replaced by fresh MCT.

4.6.2.2 In vitro release in a rotation apparatus

During experiments the interior of the rotation apparatus was protected from light and kept at 37 °C. 15 mL of a 0.0333 M acetate buffer pH 4.5 and 10 mL MCT were filled into 30 mL glass vessels and heated up to 37 °C. Into that dispersion, 200 µL of sample were added, each containing 70 µg NR or DiR per gram. This displays a dilution factor of 1:76. The dispersion in the vessels was stirred at a speed of 30 rpm. After certain time intervals, the rotation was stopped, 200 µL of the upper MCT phase were withdrawn and replaced by fresh MCT.

The MCT release medium into which NR, DiR or pTHPP possibly had migrated and was thus removed from the vessels, were diluted down to the calibration range and their fluorescence intensity was measured on a Perkin Elmer MPF-44 fluorescence spectrometer (Perkin Elmer Instruments, Überlingen, Germany) (NR: excitation 535 nm, emission 585 nm; DiR: excitation 690 nm, emission 770 nm; pTHPP: excitation 428 nm, emission 660 nm). For each sample, the release test was performed in triplicate. The concentration was calculated by external calibration. The released portion of model drug was plotted versus time.

4.6.3 Electron paramagnetic resonance spectroscopy

4.6.3.1 Instrumental setup

An EPR spectrometer with a microwave frequency of about 9.5 GHz (X-Band, Miniscope MS 200; Magnetech, Berlin, Germany) was used with the following parameters: modulation frequency 100 kHz, microwave power 10-25 mW, B_0-field 336 mT, scan range 1 mT (acquisition of the 3rd peak only) or 5 mT (acquisition of all 3 peaks of the TB signal), scan time 10 s (3rd peak only) or 30 s (all 3 peaks), modulation amplitude 0.05 mT. Short scan times were necessary for detecting fast releasing behaviour. The superimposed 3rd spectral line was fitted by means of a homemade function for the 1st derivative of a Lorentzian line, implemented into Origin Pro 7.5 software (Origin Lab Corp., Northhampton, Maryland, USA) and plotted with this software. This allowed calculating the fractions of TB each located in the oily and aqueous phase and estimating the release velocity.

TB was incorporated in the oily nanocapsule core by dissolving it in the oil in a concentration of 20 mM before the preparation of the nanoemulsion template. In order to allow a comparison of the samples (nanoemulsion, multi-layered nanocapsules) regarding their release behaviour, they were adapted to an approximately constant content of MCT (1.11 % v/v) by initial dilution, and thereby to a uniform content of TB of 0.222 mM.

4.6.3.2 Dilution assay

In this experiment the aim was to measure the release kinetics of incorporated TB from the nanocapsule core induced by dilution of the three standardized samples with double-distilled water in the dilution factors 1:1 (200 µL + 200 µL water), 1:2 (200 µL + 400 µL water), 1:3 (200 µL + 600 µL water), 1:4 (200 µL + 800 µL water) and 1:9 (200 µL + 1800 µL water). Immediately after mixing, the EPR spectra were recorded over a period of 5 minutes.

4.6.3.3 Reduction assay

In the ascorbic acid reduction assay, the ability of the capsule shell to protect the encapsulated TB from ascorbic acid located in the aqueous environment was investigated. It is based on the reduction of the TB radical to the EPR silent TB hydroxylamine. Rapid loss of the EPR signal intensity indicates a fast reduction and a fast release of TB through the polymer shell into the aqueous environment since it is accessible for the ascorbic acid only in the aqueous phase [182]. The samples were diluted 1:1 (v/v) with 1.6 mmol aqueous ascorbic acid salt solution. Immediately after mixing, the EPR spectra were recorded over a period of 10 minutes.

4.6.4 Ultrafiltration at low pressure

The release of salicylic acid from the nanoemulsion as well as differently layered nanocapsules was investigated by ultrafiltration (UF) at low pressure and subsequent fluorescence spectroscopy. Salicylic acid was used as a model drug because previously studied lipophilic and fluorescent substances (pTHPP, NR, hydroxyethyl and methyl salicalyte) showed strong adsorption onto the studied membranes (polyether sulphone (PES), regenerated cellulose, PVDF). Due to poor permeation through the membrane, these substances could not be separated from the drug carrier dispersion after the release. Thus, in order to facilitate fluorescence analysis after UF anyway, salicylic acid was chosen as release drug as it could permeate through the membrane and could be converted into the fluorescent anion by addition of NaOH after UF. UF was operated in a heatable, home-made stirred cell (Figure 20) equipped with an UF membrane UP 150 made of PES (diameter 47 mm, MWCO 150.000 Dalton, Microdyn-Nadir, Wiesbaden, Germany).

The samples were prepared with a salicylic acid content of 55.9 µg/mL, an oil content of each 1.11 % MCT and a constant acetate buffer concentration of 0.0333 M. Prior to the experiment, 5 mL of the release medium (0.0333 M acetate buffer pH 4.5, or 1/15 M phosphate buffer pH 6.8) were pressed through the membrane using low pressure (< 1 bar) in order to soak it with aqueous liquid and enhance the following fluid flux during release experiments. For each release test a new membrane was used. Afterwards, 32 mL of the release medium (buffer solution) were filled into the stirred cell and heated up to 37 °C. Under stirring, 8 mL of the preheated sample were added (1:5 dilution). During release time the dispersion was stirred at 100 rpm.

After definite points of time, low pressure of < 1 bar was applied on the cell and 300 µL of the release medium (including the portion of model drug released) were filtered through the membrane and collected (the first five droplets were discarded).
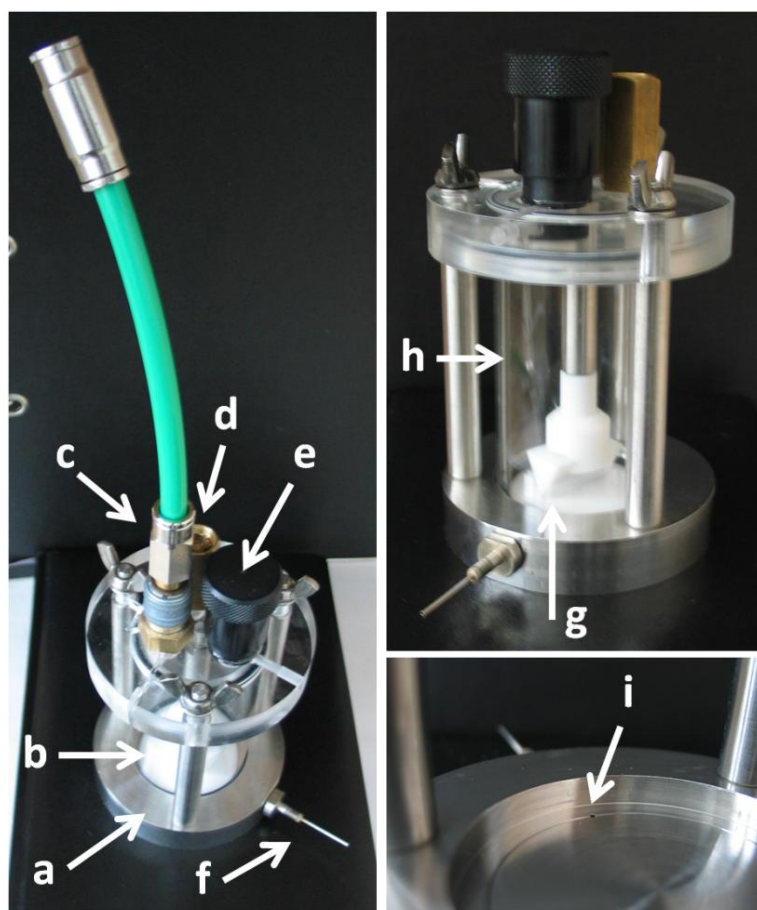
Figure 20 Stirred cell composed of: a: heat-transferring steel plate; **b:** UF membrane; **c:** pressure inlet; **d:** pressure control valve; **e:** sample inlet; **f:** filtration outlet; **g:** magnetic stirrer; **h:** insulating plastic cylinder and release vessel; **i:** filtration orifice below the membrane zone

For fluorescence quantification, the collected filtrate (300 µL) was mixed with 300 µL of the release medium and 600 µL 0.1 M sodium hydroxide solution in order to convert the analyte into the fluorescent salicylate anion. The salicylic acid concentration in the filtrate was determined by external calibration at a MPF-44 fluorescence spectrometer (Perkin Elmer Instruments, Überlingen, Germany) using the wavelengths 321 nm (excitation) and 400 nm (emission). The amounts of salicylic acid released were corrected by the adsorption rate of the drug onto the membrane which was determined by ultrafiltration of a pure drug solution (concentration 4 µg/mL) before.

4.7 Animal study on polyelectrolyte nanocapsules

4.7.1 Investigated samples

The labelling dye NR was firstly dissolved in MCT (1000 µg dye/g MCT). The investigated samples (based on an emulsion with 10 % (v/v) MCT) were prepared as described under section 4.1.2 and 4.1.3.2. High MCT content was necessary to ensure sufficient fluorescence intensity through the animal tissue. Afterwards the samples were transferred into an isotonic state (osmolarity of 286 mosm/kg) by addition of 2.9 % (v/v) glycerol (85 % glycerol *Ph. Eur.*, Bombastus Werke Freital, Germany) to the dispersion. Finally, all samples were adjusted to an equal MCT content of 7 % (v/v), and a dye (NR, DiR) content of 70 µg/g sample by dilution with double-distilled water. In case of DiR, samples were labelled by external addition of ethanolic solution of DiR (645 µg/100 mg) to the adjusted samples containing 7 % MCT. Additionally, samples of both emulsions and both nanocapsule dispersions were mixed for the animal study.

As control sample, a solution of 7 % poloxamer 124 (Synperonic® PE/L 44) with equal dye content (70 µg DiR/g sample) was prepared: A dispersion with a concentration of 1000 µg DiR/g Poloxamer was initially prepared by treatment of the two components with ultrasound. Afterwards double-distilled water was added and the mixture was vortex-mixed. Size was measured by PCS (z-average: 351 nm, PDI 0.177). The dispersion was homogenous and nano-sized. The polarity is similar to those of oil. It is known to spontaneously form systems comparable to self-emulsifying nanoemulsions when mixed with water [232]. It served as control sample because of the similar size compared to the samples of interest. Due to very good water solubility it displays a substitute for the oily phase. Advantageously, poloxamers are not digestible or biodegradable in contrast to the emulsion consisting of oil and modified starch. An overview of the prepared isotonic samples is given in Table 8 and Figure 21.

Table 8 Samples prepared for *in vivo* fluorescence imaging studies (glycerol added for isotonisation) by dilution and dye labelling of the samples E-OSA5-10% and NC-OSA-CHI-CARR-8.6%

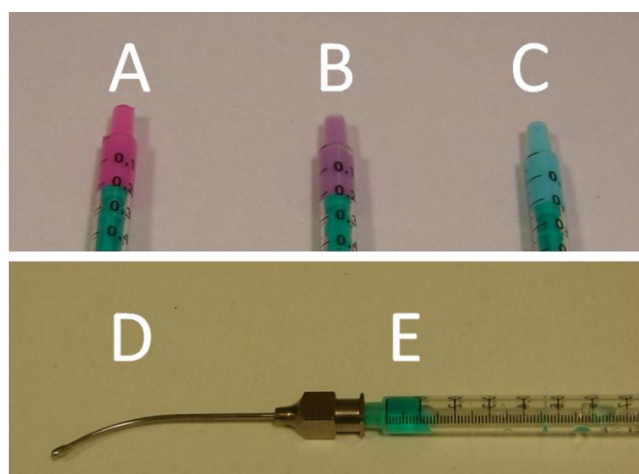| No.	sample	composition
1	E-OSA5-7%-70µgNR/g	OSA emulsion, 7 % MCT, 70µgNR/g
2	NC-OSA-CHI-CARR-7%-70µgNR/g	NC, 7 % MCT, 70µgNR/g
3	E-OSA5-7%-70µgDiR/g	OSA emulsion, 7 % MCT, 70µgDiR/g
4	NC-OSA-CHI-CARR-7%-70µgDiR/g	NC, 7 % MCT, 70µgDiR/g
5	Polox-7%-70µgDiR/g	solution of 7 % poloxamer, 70µgDiR/g
6	Mix-E-NR+DiR-each-35µg/g	1:1 mix of sample 1 and 3
7	Mix-NC-NR+DiR-each-35µg/g	1:1 mix of sample 2 and 4

Figure 21 Samples used for *in vivo* experiments (A, B, C: each 200 µL in a syringe):

A: NR labelled emulsion or nanocapsules;

B: mix of sample A and C;

C: DiR labelled emulsion or nanocapsules;

D: gavage probe used for peroral administration;

E: 100 µL of control sample (Polox-7%-70µgDiR/g)

The isotonisation was conducted due to a potential intravenous administration of the nanocapsules. Intravenous injection of liquids into the blood, as well as local administration of aqueous eye drops, requires isotonic (isosmotic) composition thereof. An aqueous solution or dispersion is isotonic with the blood when its NaCl concentration is 0.9 %, its freeze point temperature reduction is $\Delta t = -0.56$ K, or its osmolarity is 286 mosm/kg. Glycerol is an adequate substance for isotonisation of liquids. Glycerol 85 % was added to the

samples, mixed and the freeze temperature reduction compared to water (0 mosm/kg) was measured with a semi-micro osmometer (Knauer, Asche AG, Berlin, Germany). The determination of the required glycerol volume was performed in triplicate.

4.7.2   *In vivo* fluorescence imaging for studying the *in vivo* fate

The measurements were carried out using the *in vivo* fluorescence imaging system (Maestro, CRI, Woburn, MA, USA) described in section 4.4.1.2, p. 44. The distribution and accumulation of the NR- and DiR-labelled emulsion and nanocapsule samples were studied by measuring the fluorescence intensities of the whole body, covering especially the abdominal region, at predetermined time intervals. For analysis of NR samples, a green excitation filter (503–555 nm) and a 580 nm long-pass emission filter were used. DiR samples were analysed with a deep-red excitation filter (671–705 nm) and a 750 nm long-pass emission filter. Multispectral imaging cube sets were acquired in 2 nm steps (spectral range between 500 and 800 nm) with an exposure time of 100 ms. A solution of NR or respectively DiR in MCT (0.05 µg/g) was used to generate the reference fluorescence spectra for further analyses (for control measurements the control sample Polox-7%-70µgDiR/g was diluted 1:100 for the reference spectrum, 0.7 µg/g). By unmixing and further segmentation it was possible to separate the NR and DiR signals from auto-fluorescence signals of the mice as well as to distinguish between NR and DiR signal in mixed samples. Corresponding images were saved into a series of monochrome images. All procedures of the *in vivo* experiments complied with the standards for use of animal subjects as stated in the guideline from the animal care and use committee of the Martin-Luther-University Halle/Wittenberg.

The *in vivo* studies were performed in nude, male mice (SKH1-Hr) from Charles River Lab. They were withdrawn from feed 6 to 8 hours and from water 15 min before gavage. The weight was balanced initially. Then the fluorescent sample was each slowly administered perorally (200 µL) directly into the stomach by means of a gavage probe (see Figure 21D). For the measurements of the mice, an inhalation anesthesia system was used with a mixture of isofluorane/oxygen and an initial flow of 4 % (v/v) isofluorane (4.0 L/min oxygen) and a steady state flow of 1.5 % (v/v) isofluorane (1.8 L/min oxygen). To protect the mice against cooling, they were placed on temperature controlled plates which were kept at 35 °C.

4.7.3   *Ex vivo* fluorescence imaging for quantification

The aim of this study was the quantification of DiR released from the nanocapsule core after peroral administration of sample NC-OSA-CHI-CARR-7%-70µgDiR/g, and the investigation of the DiR absorption, distribution and accumulation in special organs. Male, nude SKH1-Hr mice were withdrawn from feed 12 hours before the application of 200 µL of the sample. 1 hour (M I), 6 hours (M II), or 12 hours (M III) after application of the sample, the mice were sacrificed in order to quantify the amount of DiR in the spleen, lungs, stomach, liver, large and small intestine. DiR was extracted from the organs (each divided in 3 parts, except of spleen and lungs) using each 2 mL pure ethanol (Roth, Karlsruhe, Germany) and ultrasound for 30 minutes. After centrifugation at 4,000 rpm over a period of 15 minutes, the supernatant was gathered and used for quantification analysis by means of fluorescence spectroscopy (MPF-44 fluorescence spectrometer, Perkin Elmer Instruments, Überlingen, Germany). The parameters used for the measurement were wavelengths of 690 nm (excitation, slit 8 nm) and 770 nm (emission, slit 8 nm), coarse = 1. The amount of DiR extracted from

each a third of the organ and quantified by fluorescence spectroscopy (external calibration) was finally summed up. The recovery rate was calculated by the ratio of extracted to administered DiR amount.

4.7.4 *Ex vivo* confocal laser-scanning microscopy

A lateral cut of a murine small intestine region was prepared and deposited on an object holder, covered by a small cover slip. For orientation reasons, the upper part of the cover slip not directed to the sample was marked with a permanent, waterproof pen. Then the cover slip was fixed with transparent adhesive tape because of use of immersion oil. The sample was examined inversely (e. g. cover slip was at the bottom) with a confocal fluorescence LSM 710 (Laser Scanning Microscope) (Carl Zeiss MicroImaging GmbH, Jena, Germany) using the ZEN (Zeiss efficient navigation) 2008 software. For visualisation of DiR, a helium-neon-laser with a maximum laser power of 5 mW and a wavelength of 633 nm was used for excitation. Immersion oil (Immersol^{TM} 518 F, Oberkochen, Germany) with the same refractive index (n=1.518 at 23 °C) as the object holder and cover slip was deposited between the object holder and the objective lens to improve the image quality by prevention of phase differences. The distance between two optical flats being focussed was 1 µm. Each flat was scanned fourfold and averaged to improve the signal-to-noise ratio. The conditions applied for each image such as scanned layer thickness (100 to 800 µm) and resulting scanning time (8 to 12 minutes), choice of object lens, gain, and laser power were modified individually.

5   Results & discussion

5.1   Preparation and characterisation of nanoemulsion templates

5.1.1   Critical micelle formation concentration of OSA starch

In most polymers, the CMC is not a precise point but located in a certain concentration range. Likewise, OSA starch showed a curved surface tension decay as apparent from Figure 22.
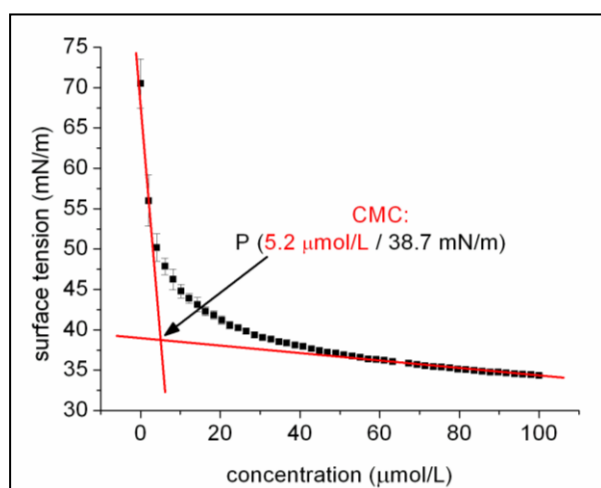

Figure 22 Determination of the CMC of OSA starch at 25 °C

The CMC of OSA starch can be estimated from Figure 22 to be 5.2 µmol/L (intersection point P). In fact, the formation of micelles by OSA starch did not start at a certain point but rather covered a concentration range between 3 and 20 µmol/L. The production of emulsions started on a 5 % (w/w) OSA starch concentration ($1.25 \cdot 10^{-4}$ M) which yielded stable submicron emulsions with oil contents between 5 and 12.5 % (v/v). This concentration is about 20-fold higher than the CMC. Thus, the formation of a stable emulsion in the nanoscale was enhanced because especially small droplets require large amounts of surfactant molecules due to the large surface area. This requirement was fulfilled by working with emulsifier concentrations far above the CMC. The concentration ranges of the remaining emulsifiers (gum arabic, sugar beet pectin) for the preparation of emulsions were decided based on producer information.

5.1.2   Characterisation of the prepared emulsions by size and surface charge

Nanoemulsion templates for the purpose of nanocapsule development were prepared with the emulsifiers OSA starch, sugar beet pectin (SBP), mixtures thereof, or gum arabic (GA). Varying concentrations of the stabiliser and of the oil component (MCT) were investigated with respect to the emulsifying capacity, droplet size and surface charge. The results are presented in Table 9.

Table 9 Results of the prepared emulsions with different stabilisers (OSA: octenyl succinic anhydride-modified starch; GA: gum arabic; SBP: sugar beet pectin) and oil content (MCT: medium chain triglycerides); [*] bimodal size distribution (by volume), # oil droplets rising to the top of emulsion, + high viscous

No.	sample	% (v/v) MCT	Optical quality	z-average (nm)	PDI	d(0.5) (nm)	d(0.9) (nm)	ζ-potential (mV)
1	**E-OSA5**	**5 %**	**stable**	**151**	**0.127**	**118**	**214**	**-23.8 ± 0.7**
2		10 %	stable	164	0.151	133	493	-26.4 ± 0.5
3		12.5 %	stable	185	0.192	159	1133	-26.1 ± 0.6
4		15 %	instable #	198	0.300 [*]	147	1359	-26.6 ± 0.3
5	E-OSA7.5	10 %	stable	156	0.137	115	216	-22.2 ± 0.2
6	E-OSA11.25	15 %	stable	167	0.172	121	242	-21.5 ± 0.2
7	E-OSA15	20 %	instable +	162	0.164	121	246	-22.4 ± 0.3
8	E-OSA18.75	25 %	instable +	198	0.190	122	249	-21.3 ± 0.5
9	**E-GA5**	**5 %**	**instable #**	**422**	**0.198**	**297**	**469**	**-40.8 ± 0.3**
10	E-GA7	5 %	stable	373	0.125	220	393	-39.9 ± 0.2
11	E-GA10	5 %	stable	365	0.088	149	273	-39.7 ± 0.2
12	E-SBP1	5 %	instable #	394	0.112	188	398	-41.7 ± 0.5
13	E-SBP2	5 %	stable	399	0.037	132	255	-39.0 ± 0.1
14	E-SBP2.5	5 %	stable	418	0.107	136	277	-36.2 ± 0.4
15	**E-SBP5**	**5 %**	**stable +**	**477**	**0.129**	**133**	**259**	**-34.3 ± 0.9**
16	E-OSA4.5 /SBP0.5	5 %	instable #	322	0.598 [*]	132	390	-23.2 ± 0.4
17		10 %	instable #	3245	0.326 [*]	236	1558	-25.0 ± 0.6

5.1.2.1 Use of OSA starch as emulsifier

All emulsions with constant OSA starch concentration of 5 % (E-OSA5) showed a similar ζ-potential value (Table 9, entry 1-4). Increasing the oil content from 5 up to 15 % MCT led to an instable emulsion at 15 % MCT content probably due to a lack of OSA starch molecules. A strong hint for that assumption had already been observed during preparation: the foam development (induced by OSA starch) during high sheer mixing decreased with higher oil fraction. This observation can be explained by a decreasing amount of free emulsifier molecules. The OSA starch deficiency with raising MCT content also reflected in the size and homogeneity of the emulsions: the z-average, d(0.5) value and PDI tended to increase.

Increasing both the MCT and the OSA content in the emulsions resulted in emulsion droplets with comparable size if one compares the z-average and the d(0.5) values (Table 9, entry 5-8). However, a slow rise of the particle size and inhomogeneity with higher MCT portion can be assumed (with deviations). The ζ-potential did not show significant differences. Interestingly, the emulsions E-OSA15-20% and E-OSA18.75-25% (entry 7 and 8) showed a very high viscosity after few hours at rest, also possessing thixotropic properties. Very large oil content of 20 % and 25 % was thereby declared as non-suitable for the preparation of nanocapsules thereof.

5.1.2.2 Use of sugar beet pectin as emulsifier

All emulsions containing 5 % MCT and varying amounts of sugar beet pectin from 1 % to 5 % (Table 9, entry 12-15) showed strongly higher ζ-potential values than observed for OSA starch emulsions. However, it decreased with higher pectin contents, which was unexpected. It might be explained by a decrease of the electric double layer or by decreased mobility. With respect to the stability of emulsions, concentrations of at least 2 % pectin should be used since emulsions with only 1 % SBP (entry 12) or less were completely instable (coalescence). The droplet size (PCS) was larger than obtained in OSA starch emulsions. PCS (z-average) and LD (d(0.5) value) showed large size differences. The explanation can be found in the varying principles of both measuring techniques. Z-average and d(0.5) are not well comparable. Other reasons might be hindered droplet diffusion (PCS) because of decreased mobility of the particles due to potential cross-linkages of pectin chains and polymer interaction. This would result in a larger hydrodynamic diameter as measured in PCS. The higher stability of emulsions E-SBP2-5%, E-SBP2.5-5% (entry 13-14) was also reflected in the decrease of PDI and d(0.5) value (homogeneous distribution). Finding the optimal pectin concentration must hence be a compromise between high stability (entry 13-14) and high viscosity (esp. entry 15). In this work, 2.5 % pectin solutions (entry 13) were used for further experiments.

5.1.2.3 Use of OSA starch / sugar beet pectin mixtures as emulsifier

The mixture of 0.5 % SBP and 4.5% OSA (Table 9, entry 16-17) did not yield positive results in terms of stable emulsions with monomodal distribution of the droplet size. After one day the emulsions E-OSA4.5/SBP0.5-5% and -10% had changed; droplets tended to flocculation (aggregation). Size measurements showed already large bimodal particles. Obviously, both emulsifiers do not affect themselves synergistically but disturb each other in the interface between oil and water phase. This might be due to the missing fatty acid chain of pectin. The emulsions were not applicable for nanocapsule preparation.

5.1.2.4 Use of gum arabic as emulsifier

Table 9 (entry 9-11) also presents the properties of the obtained emulsions which contained a varying content of gum arabic (E-GA5-5%, E-GA7-5%, E-GA10-5%) but a constant oil fraction of 5 % MCT. Concentrations smaller than 5 % gum arabic were too low in order to yield a stable emulsion. As the product information recommended, 7 % of gum arabic was needed to obtain a homogeneous emulsion (PDI 0.125) with droplet sizes in the lower nano-range (d (0.5): 220 nm). The ζ-potential did not show significant differences between entry 9 and 11. Emulsion E-GA7-5% (entry 10) was used for later nanocapsule preparation.

5.1.2.5 Comparison of OSA starch, pectin and gum arabic emulsions

In order to compare the three substances concerning their emulsifying potential, results of comparable emulsions containing 5 % MCT and being stabilised by emulsifier solutions in the concentration of 5 % (OSA, SBP or GA) are highlighted in Table 9 (entry 1, 9, 15; words in bold font). The differences in stability attract attention. Gum arabic was not capable of forming stable emulsions in this concentration (5 %) and thereby presented the substance with the lowest emulsifying efficiency. Sugar beet pectin was most effective in stabilizing the emulsions electrostatically since the smallest amount (2.5 %) was required to cover the oil surface while a high ζ-potential (-36.2 mV) was obtained. Long-term studies, however, showed a change in the diameter upon storage, indicating that steric factors have a larger impact on the emulsion stability [233]. However, the gum arabic emulsion yielded the highest ζ-potential (-40.8 mV) which is a strong hint for a higher charge density than of OSA starch and pectin. This is in agreement with the degree of esterification of OSA starch (0.2 %) and the degree of esterification of pectin´s main component galacturonic acid (50 %). Unfortunately, the charge density of gum arabic was not given by the producer. However, both pectin (-34.3 mV) and gum arabic (-40.8 mV) provide higher ζ-potentials than OSA starch emulsions (-23.8 mV) in concentrations of 5 %. With regard to the size of the emulsion droplets, OSA starch yielded the smallest z-average in any investigated concentration both of oil and emulsifier (e. g. E-OSA5-5%: 151 nm). For pectin the larger size (E-SBP5-5%: z-average 477 nm) can be explained by the fact that it adsorbs onto the oil droplets in the manner of multilayers with a plateau thickness of 140 nm (corresponds to the hydrodynamic diameter of the pectin molecules of ≈130 nm) [210]. They consist of protein moieties and galacturonic acid residues which show strong electrostatic interactions. Hence, it is evident that these moieties contribute to the size, and a significant proportion of the polymer segments protrude out into solution. By subtraction of the pectin multilayers from the z-average (477 nm – 2·140 nm = 197nm) the resulting size of the pure SBP stabilised oil droplets ranges in the same order of magnitude like in OSA starch emulsions. Moreover, PCS artefacts cannot be excluded completely. The homogeneity (PDI) of the three types of emulsions, however, is comparable and excellent, especially if one considers the PDI of E-OSA5-5% (0.127), E-SBP5-5% (0.129), and E-GA7-5% (0.125).

In conclusion, it is not possible to call any of the emulsifiers the 'best' one since it depends on the purpose of the emulsion. For toxicity minimisation one would prefer to take pectin since only 2 % are required to form stable emulsions as it was also observed by Funami et. al [212]. Regarding the stability, of course a high ζ-potential is desirable which would give a preference to gum arabic. For oral application all three emulsifiers are suitable. However, for i. v. administration small and homogenous particle size is very important (E-OSA5-5%: PDI 0.127, z-average 151 nm). In order to convert the ζ-potential of the emulsion into the opposite charge for

two times during polyelectrolyte nanocapsule preparation, it might be advantageous to have a rather low ζ-potential (E-OSA5-5%: -23.8 mV). Due to a low charge density of the used emulsifiers, a relatively low ζ-potential reflects the chemical character of polyelectrolytes. Nevertheless, satisfactory stability of emulsion templates could be reached. Since the last aspects mentioned agree with the aims of this work, OSA starch might be the optimal emulsifier for the nanocapsule development.

5.2 Development and characterisation of polyelectrolyte nanocapsules

5.2.1 Screening of polyelectrolytes regarding their complex formation properties

Figure 23 shows the precipitation results obtained from oppositely charged polyelectrolytes in different concentrations and combinations.
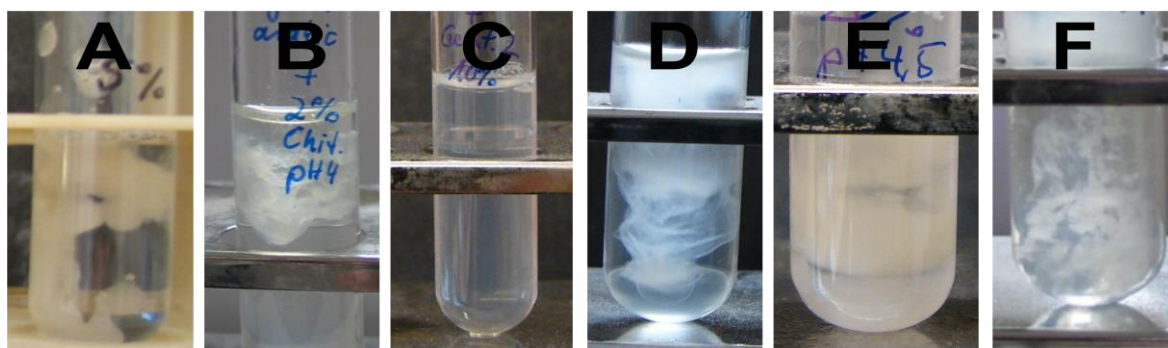
Figure 23 Complex coacervation results between solutions of: <u>A:</u> 0.2 % CHI and 5 % SBP, <u>B:</u> 2 % CHI and 4 % GA, <u>C:</u> 10 % GEL and 5 % OSA, <u>D:</u> 5 % GEL and 1.35 % CARR, <u>E:</u> 20 % GEL and 2 % SBP, <u>F:</u> 5 % GEL and 4 % GA

As apparent, except of OSA starch/gelatin (Figure 23C) all substances were feasible to form visible polyelectrolyte complexes by means of precipitation to a more or less intense extent. Against the expectations, OSA starch and different gelatin type A batches showed no recognizable complex formation although they are oppositely charged and should attract each other. If there was any polyelectrolyte complex reaction it appeared very weak. Eventually, polyelectrolyte complexes were too small to be visible for the human eye.

5.2.2 Development of different nanocapsule formulations

The results of the prepared nanocapsules formulations obtained by PCS, LD and ζ-potential are presented in Table 10 and have been published and discussed in detail in 2009 [223]. Apart from sample NC-OSA-CHI-CARR-CHI-CARR (NC5), all other systems are composed of a three-layered capsule shell. Most of them contain OSA starch as the first layer; i.e. OSA starch had been used most frequently as emulsifier for the preparation of the emulsion template which the nanocapsules are based on. Only three nanocapsule formulations could be developed on the basis of gum arabic emulsions; one successful nanocapsule system derived from a SBP emulsion template.

Three of the polyelectrolyte systems as listed below (based on an emulsion containing 5 % MCT) failed during nanocapsule preparation and thus will not be further mentioned.

NC-SBP-GEL-CARR

In this formulation, even after adding 1 mL of 5 % gelatin solution to 5 mL of the 2 % pectin emulsion E-SBP2-5%, the mixture showed very strong complex formation represented as flocculation and destabilisation by precipitation. Repetition of the experiment with different gelatin concentrations and batches led to the same result. The gelatine-covered interstage, which should have been positively charged, had a ζ-potential of -24.5 mV. Further addition of gelatin was not possible due to flocculation. Apparantly, the polyelectrolyte complexation between these two substances is very strong. Deposition of carrageenan (or other polyelectrolytes) was not investigated since the formulation appeared as not successful.

NC-OSA/SBP-CHI-CARR

Even though for the emulsion gained from OSA starch and SBP (ratio 9:1) coalescence instability was observed after emulsion preparation (see section 5.1.2.3), it did not occur immediately. Thus, the emulsion E-OSA4.5/SBP0.5-5% was used for nanocapsule development. 20 mL of the emulsion were mixed with 6 mL of 0.6 % chitosan solution and 6 mL of carrageenan 1.35 % (cf. system NC-SBP-CHI-CARR). After the preparation, the mixture had tended to form visible aggregates on the Ultra Turrax mixer. The dispersion showed few precipitates after centrifugation. Further investigation of this system was not done since the results showed a bimodal non-homogeneous size distribution (PDI: 0.546). Due to emulsion coalescense and bimodal size distribution, this system was not successful.

NC-GA-GEL-CARR

The emulsion E-GA7-5% was used as template. The conversion of the strongly negative ζ-potential of 10 mL of the emulsion was performed by injecting huge volumes of a 10 % gelatin solution (50 °C) into the emulsion under stirring. However, the ζ-potential could not be turned into positive values. Since higher concentrations of gelatin (gelation in the syringe) and too high volumes of the second and third layer being injected (leading to decrease of the oil content) were not adequate, nanocapsules with a non-positively charged second layer were prepared. They were composed of 20 mL emulsion, 10 mL of gelatin 5 % and 5 mL of carrageenan 1.35 % solutions. The whole mixture began to flocculate after addition of carrageenan, with the tendency to flotate. High-pressure homogenisation was neither possible nor reasonable. System NC-GA-GEL-CARR had to be considered unsuccessful as the used pair gelatin and λ-carrageenan obviously is non-appropriate for the production of nanocapsules. This becomes especially clear by comparing the results with the systems NC-OSA-GEL-CARR (microparticles) and NC-SBP-GEL-CARR (flocculation). Instabilities occurred by addition of carrageenan in all cases.

Table 10 Results of the nanocapsule formulations obtained by PCS (z-av.= z-average), LD (d(0.5) and d(0.9)), and ζ-potential; * samples showed gelation

No.	sample	% (v/v) MCT	z-av. (nm)	PDI	d(0.5) (nm)	d(0.9) (nm)	ζ-potential layer 1	ζ-potential layer 2	ζ-potential layer 3	remarks
1	NC-OSA-CHI-CARR (NC3)	2.5%	134	0.230	123	295	-21.1 mV	8.1 mV	-25.7 mV	successful
2		4.35%	179	0.343	135	959	-23.1 mV	2.1 mV	-37.9 mV	successful
3		8.6%	161	0.233	160	2824	-23.4 mV	6.2 mV	-25.4 mV	successful
4	NC-OSA-CHI-CARR-CHI-CARR (NC5)	1.11%	145	0.310	131	288	layer 1-3: as NC3-2.5%	5.0 mV (layer 4)	-28.1 mV (layer 5)	five-layered nanocapsules successful
5	NC-OSA-CHI-GA	2%	n. d.	n. d.	119	187	-18.9 mV	9.9 mV	-17.5 mV	successf., low ζ-potential
6		3.7%	185	0.188	122	196	-20.9 mV	4.6 mV	-29.5 mV	successful
7		7.4%	317	0.247	136	420	-23.4 mV	10.5 mV	-35.4 mV	successful
8	NC-OSA-GEL-CARR	3%	n. d.	n. d.	136	7055	-22.0 mV	4.7 mV	-38.9 mV	rev. micropart. formation
9	NC-OSA-GEL-GA	1.43%	366	0.369	120	235	-21.3 mV	4.4 mV	-35.9 mV	successful
10	*	3%	229	0.273	123	231	-21.3 mV	2.2 mV	-29.2 mV	successful
11	*	5.625%	233	0.276	122	215	-20.3 mV	3.7 mV	-32.4 mV	successful
12	NC-OSA-GEL-SBP	2.68%	342	0.461	480	898	-23.9 mV	3.1 mV	-23.6 mV	successf., inhomogeneous
13		3.26%	418	0.488	485	1155	-23.9 mV	2.6 mV	-22.2 mV	successf., inhomogeneous
14		5.55%	358	0.200	242	493	-23.4 mV	1.9 mV	-26.2 mV	successful
15	NC-SBP-CHI-CARR	2.5%	353	0.080	132	256	-36.2 mV	-33.1 mV	-37.7 mV	2nd layer: negative ζ-pot.
16	NC-GA-CHI-CARR	3.79%	394	0.077	233	402	-42.6 mV	-29.9 mV	-32.4 mV	2nd layer: negative ζ-pot.
17	NC-GA-GEL-SBP *	1.85%	632	0.333	150	339	-43.7 mV	-11.5 mV	-17.4 mV	low final ζ-potential
18	NC-GA-GEL-GA *	2.5%	n. d.	n. d.	134	241	-43.7 mV	-26.4 mV	-31 mV	2nd layer: negative ζ-pot.

5.2.2.1 Nanocapsules of 5 % MCT emulsions and low concentrated polyelectrolyte solutions

5.2.2.1.1   NC-OSA-CHI-CARR-2.5% and NC-OSA-CHI-CARR-CHI-CARR-1.11%

The suitability of the combination of these polyelectrolytes OSA-CHI-CARR for the preparation of nanocapsules had been investigated before (under use of olive oil) [234]. Solutions of chitosan and carrageenan were injected into the OSA starch emulsion at 50 °C. It was aimed to increase the final ζ-potential of the nanocapsules by increasing the carrageenan amount. This has been reached by using a carrageenan concentration of 0.45 % (-25.7 mV) instead of 0.4 % (-23.5 mV) [223]. Hence it displayed an improvement regarding stability. By further increase of the carrageenan concentration up to 0.5 % a tremendous amount of polymer precipitates emerged during centrifugation. Hence, using a 0.5 % carrageenan solution instead of 0.45 % overloaded the system with the third polyelectrolyte. Due to dilution of 20 mL of the emulsion (5 % MCT) up to 40 mL (cf. Table 4, entry 1, p. 37), the nanocapsule dispersion contained 2.5 % oil. Results for sample NC-OSA-CHI-CARR-2.5% are given in Table 10 (entry 1; PDI: 0.230; d(0.5): 123 nm). The ζ-potential changed from layer 1 to 3 from negative (-21.2 mV) over positive (8.1 mV) again into negative (-25.7 mV). This was the proof for a three-layered shell. The sample was declared as very successful.

For this reason, this nanocapsule system was studied in terms of the question whether a thicker shell layer could be developed (five-layered nanocapsules) with modified mechanical and release properties. By extensive experiments, an advancement of sample NC-OSA-CHI-CARR-2.5% was achieved with the sample NC-OSA-CHI-CARR-CHI-CARR-1.11% (cf. Table 4, entry 4, p. 37). In the preparation process the samples E-OSA5-5%, NC-OSA-CHI-CARR-2.5% (´NC3´) and NC-OSA-CHI-CARR-CHI-CARR-1.11% (´NC5´) were subsequently prepared. Some sections of this work will exclusively deal with these 'consecutively prepared samples' (e. g. 5.5, 0, 5.7.3) in order to investigate the changes of the capsule shell. The sample NC5 (Table 10, entry 4, p. 61) differed from the corresponding three-layered nanocapsules (NC3) by a slight increase of the size (d(0.5): 131 nm) and PDI (0.310), but also possessed a higher ζ-potential (-28.1 mV).

5.2.2.1.2   NC-OSA-CHI-GA-2%

Even though gum arabic emulsions were not useful as a template for nanocapsule preparation due to high ζ-potential (similar to pectin) it was further investigated regarding applicability as the third shell layer. Based on system NC-OSA-CHI-CARR, gum arabic was replacing carrageenan. In a small scale, 10 mL of 5 % OSA starch emulsion were mixed with 5 mL of chitosan 0.2 % and an increasing volume of gum arabic 5 %. As presented in Figure 24A, the nanocapsules reached a maximum surface charge of -21 mV. Higher gum arabic amounts did not increase the ζ-potential. The surface was saturated. Transferred to a large scale as needed for HPH (duplication of the volume), nanocapsules were prepared with the composition as given in Table 4 (entry 5). Due to stronger dilution of the emulsion by injection of the further polyelectrolytes compared to NC-OSA-CHI-CARR-2.5% the oil content was reduced to 2 %.

The characterisation of size and ζ-potential yielded the results presented in Figure 24B and Table 10, entry 5 (p. 61). LD measurements showed a homogeneous and small particle size (d(0.5): 119 nm). System NC-OSA-CHI-GA displayed another successful combination of polyelectrolyte layers even though the ζ-potential was quite low (-17.5 mV).
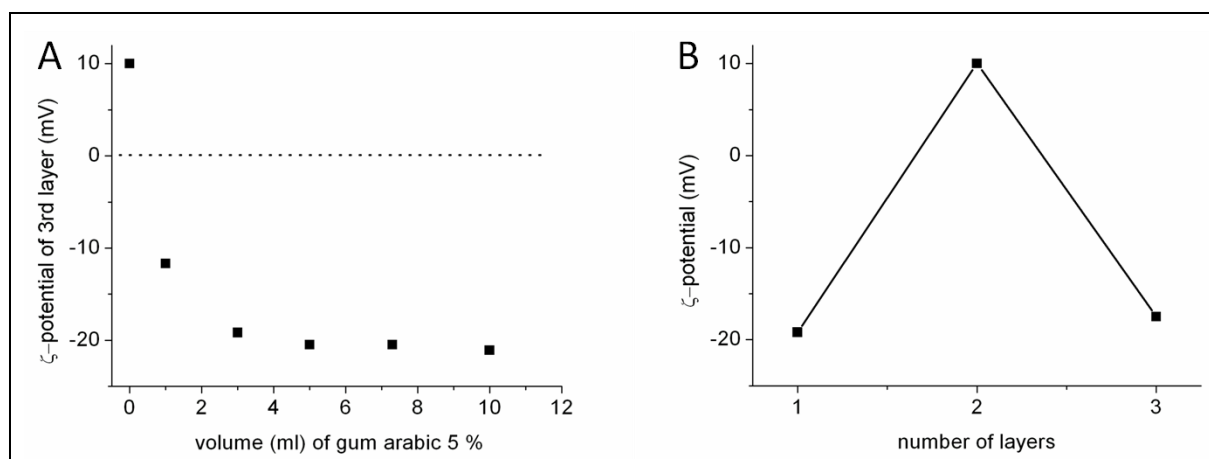
Figure 24 ζ-potential of NC-OSA-CHI-GA-2%, A: with increasing gum arabic, B: inversion in the layers

5.2.2.1.3   NC-OSA-GEL-CARR-3%

In this system chitosan was replaced by gelatin A as second layer of the capsule wall. The development also started with a 5 % MCT emulsion stabilised with OSA starch. The first step was the determination of the necessary gelatin amount for converting the ζ-potential of the emulsion into a positive value. Therefore, different volumes of 5 and 10 % gelatin solutions (50 °C) were added to 5 mL of the emulsion under high sheer mixing. After each step the ζ-potential was determined as illustrated in Figure 25.
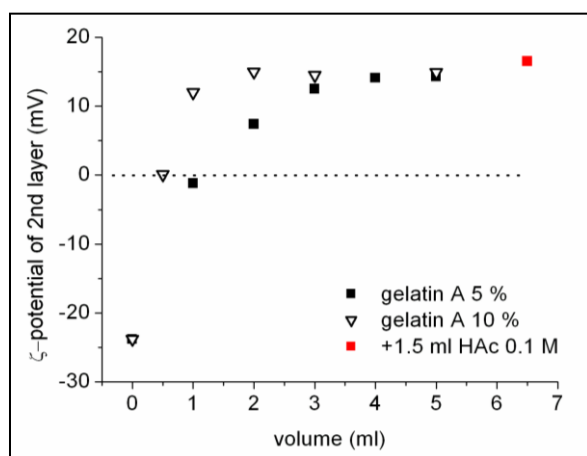
Figure 25 Inversion of the negative ζ-potential of 5 mL of E-OSA5-5% to positive charge by addition of different volumes of 5 % and 10 % gelatin A solution; 🟥 ζ-potential by finally adding 1.5 mL HAc 0.1 M

1 mL of 10 % gelatin (12 mV) and 2 mL of 5 % gelatin solution (7.4 mV) respectively, resulted in a positive ζ-potential of the gelatin covered interstage. More protein yielded a ζ-potential plateau at 15 mV. By addition of acetic acid (HAc) 0.1 M to the mixture of 5 mL emulsion and 5 mL gelatin 5 %, the ζ-potential increased even more (16.5 mV). This is due to stronger protonation of gelatin´s free amino groups in acidic milieu. The ratio of emulsion to gelatin solution (5 mL : 2 mL (5 %), and 5 mL : 1 mL (10 %), respectively) was then upscaled to a volume needed for HPH. Varying concentrations and amounts of carrageenan solution (also 50 °C) were injected after gelatin to obtain the nanocapsule dispersion. Only one of the prepared formulations (NC-OSA-GEL-CARR-3%, preparation cf. Table 4, entry 8, p. 37) remained a homogeneous suspension after centrifugation (with around 4 mm high sedimentations in the 15 mL test tube). The other formulations showed sedimentation or flotation. Further modification of the composition could not reduce the sedimentation amount. The characterisation of NC-OSA-GEL-CARR-3%, measured at 35 °C immediately after preparation without

centrifugation, yielded the results shown in Table 10 (entry 8; d(0.5): 136 nm). The size of the capsules was as large as of the emulsion template. The combination OSA–GEL–CARR was basically capable of covering the oily core of the nanocapsules with three oppositely charged polyelectrolytes following each other since the ζ-potential reversed after each layer. However, regarding the size of the nanocapsules, an interesting phenomenon was observed. After cooling down to ambient temperature and centrifugation, it seemed that particles aggregated to microparticles (d(0.5): 15.75 µm) despite a ζ-potential of -38.9 mV. The size distribution curve showed very homogenous microparticles which gives hint to a controlled aggregation. The aggregation was reversible, since the cool dispersion re-heated to 50 °C had the identical size distribution as immediately after preparation. Due to these thermal effects on the size, PCS could not be measured because cooling and microparticle formation could not be prevented during sample dilution for PCS. Even though aggregation was reversible, system NC-OSA-GEL-CARR-3% is considered unsuccessful in terms of particle size since aim of this work was to prepare nanocapsules, not microcapsules. Besides, after several weeks particles were precipitating at the bottom of the test tube. However, microparticles are of interest for oral administration and would justify further investigation.

5.2.2.1.4   NC-OSA-GEL-SBP-2.68%

As a variation of the previous system, which was not successful due to aggregation of carrageenan-covered nanocapsules into microparticles, the carrageenan was replaced by sugar beet pectin in the third layer. Composition of layer 1 and 2 was transferred from system NC-OSA-GEL-CARR. Hence, only the amount of pectin had to be determined in order to obtain a ζ-potential as negative as possible. Therefore, 30 mL of the E-OSA5-5% template was high sheer mixed with 5 mL of 10 % gelatin (50 °C) and with an increasing volume of 2 % pectin solution. In this preliminary test, the ζ-potential of the gelatin covered interstage was still slightly negatively charged. Hence 20 % more gelatin was taken for further preparation (cf. Table 4, entry 12). The effect of the addition of a 2 % pectin solution on the ζ-potential of the third layer is apparent from Figure 26A.
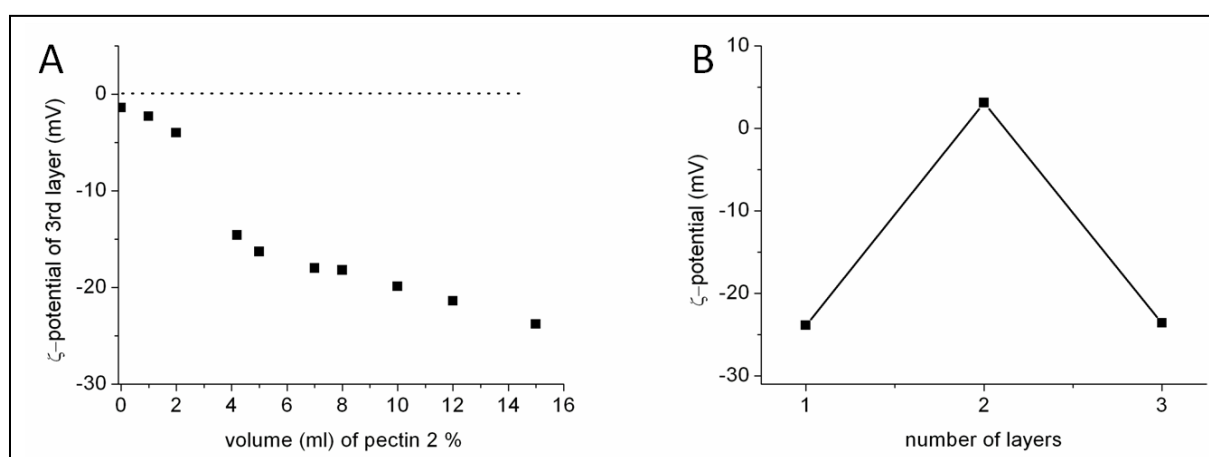

Figure 26 Development of the ζ-potential for NC-OSA-GEL-SBP-2.68%, A: Increase of the negative ζ-potential (layer 3) by addition of pectin, B: Final inversion of the ζ-potential in the three layers

The results of the final composition NC-OSA-GEL-SBP-2.68% with improved ζ-potential values in the 2nd (+3.1 mV) and 3rd layer (-23.6 mV) are given in Table 10, entry 12 (p. 61) and Figure 26B. Despite a high PDI of

0.461 (wide size distribution), system NC-OSA-GEL-SBP was successful since the LD size curve (d(0.5): 480 nm) showed monomodal distribution.

5.2.2.1.5   NC-OSA-GEL-GA-1.43%

In analogy to the previous system NC-OSA-GEL-SBP, nanocapsules with gum arabic instead of pectin were prepared. The volumes of E-OSA5-5% and the gelatin solution needed could be transferred. Finding the optimal volume of gum arabic was achieved by mixing 20 mL of the emulsion with 4 mL of 10 % gelatin and adding an increasing volume of gum arabic 5 % (cf. Figure 27A). The final composition is given in Table 4 (entry 9, p. 37). A high final ζ-potential of -35 mV could be reached. Therefore, a quite large volume (45 mL) of the 5 % gum arabic solution was needed. Hence, the initial oil content of the emulsion (5 %) was decreased down to 1.43 % by dilution. Nevertheless, system NC-OSA-GEL-GA presented a further successful complex coacervation based nanocapsule formulation. The size and ζ-potential results are shown in Figure 27B and Table 10 (entry 9, p. 61). The size determined by LD was 120 nm (d(0.5)).
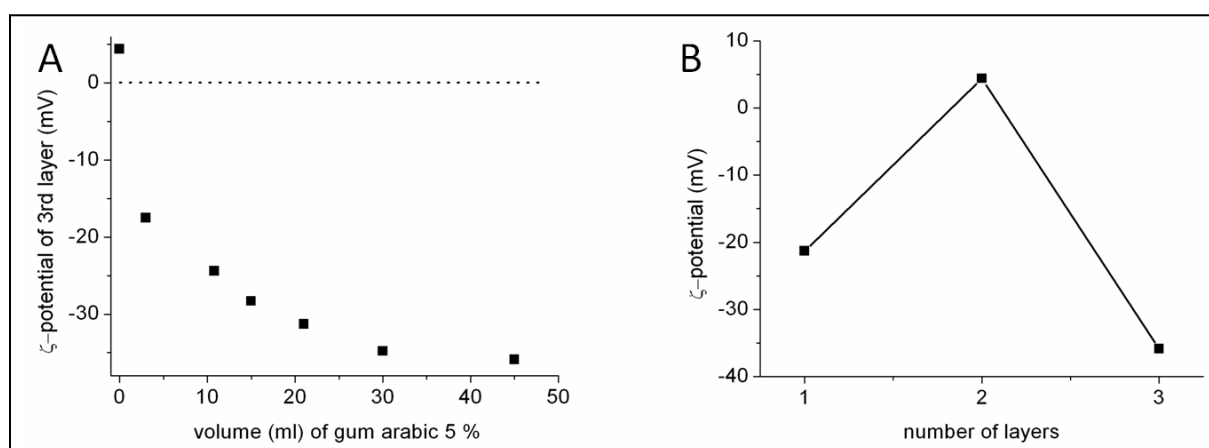
Figure 27 ζ-potential results for system NC-OSA-GEL-GA-1.43%, <u>A:</u> Influence of the gum arabic volume on the ζ-potential, <u>B:</u> Inversion of surface charge during preparation

5.2.2.1.6   NC-SBP-CHI-CARR-2.5%

As mentioned in chapter 5.1.2.2, 2.5 % pectin solutions were chosen for the emulsion preparation which the following nanocapsules are based on. First step in the development was the determination of the necessary chitosan amounts to convert the ζ-potential of the emulsion E-SBP2.5-5% into a positive value. A positive ζ-potential would prove that the second layer of chitosan had completely covered the oily core. The experiments started on a small scale: 4 mL E-SBP2.5-5% were mixed with 2 mL of different concentrations of chitosan (under high sheer mixing). By addition of 0.2 % chitosan solution to the emulsion, the ζ-potential was still negative; however, adding 2 mL of 1 % chitosan solution already led to flocculation of the mixture. An interpolation between these concentrations was carried out. The optimal chitosan amount was found to be 2 mL of 0.6 % (no flocculation). Results are given in Figure 28A. The highest possible concentration with a stable dispersion was 0.6 % chitosan. Adding 2 mL of 0.7 % chitosan to 4 mL of emulsion E-SBP2.5-5% resulted in flocculation of the mixture due to too strong interaction forces. Possibly, chitosan displaced the pectin from the emulsion interface and interacted with the oil (acetic groups) and water phase (protonated amino groups). Thereby a complex shell structure with diffuse layers would have been formed.
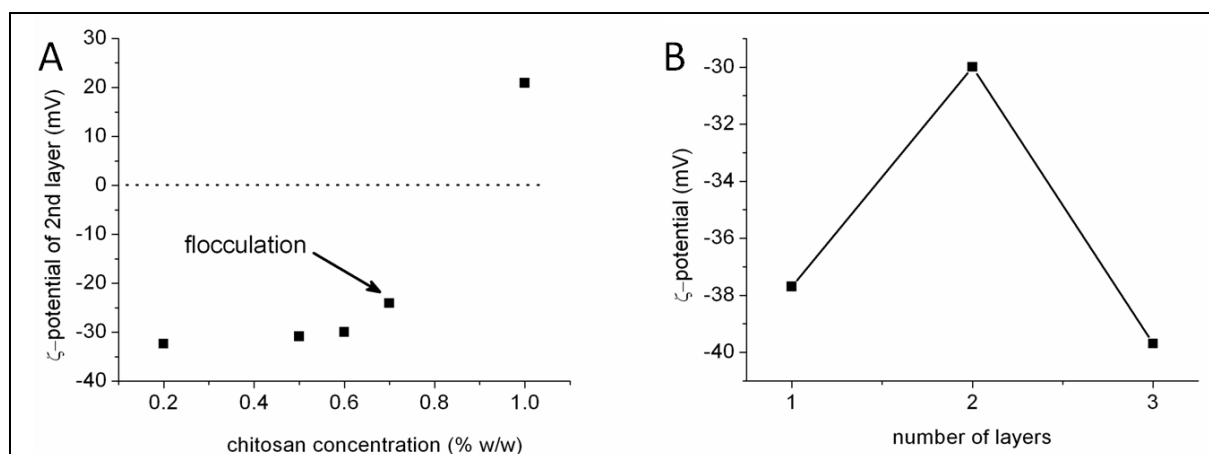
Figure 28 ζ-potential results for NC-SBP-CHI-CARR-2.5%, <u>A:</u> ζ-potential of the chitosan-covered interstage by 2 mL of different concentrations, <u>B:</u> ζ-potential change during preparation

Pectin and chitosan might have formed precipitates. In this mixture the the ζ-potential of the second layer could not be inverted from negative into positive. However, attempts have been made to prepare nanocapsules from this system. In analogy to system NC-OSA-CHI-CARR, in which the ratio of chitosan to carrageenan was 0.2 : 0.45 (each 10 mL), a concentration of carrageenan of 1.35 % (10 mL) was concluded (for composition cf. Table 4, entry 15, p. 37), if following after 20 mL E-SBP2.5-5% and 10 mL of 0.6 % chitosan. The result of NC-SBP-CHI-CARR-2.5% (optimal formulation due to smallest PDI of 0.080) is shown in Table 10 (entry 15), p. 61. Yet, after each of the three layers, the ζ-potential was negative although it was aimed to yield a positive second layer (cf. Figure 28B). Obviously, chitosan is not charged enough to neutralize the negative charges of pectin. Hence, the second layer of the capsule shell was not completely covered by chitosan. In conclusion, nanocapsules were obtained which possessed a small particle size (d(0.5): 132 nm; z-average: 353 nm; LD and PCS yielded again varying results), good homogeneity (PDI 0.08), and a comparably high ζ-potential (-37.7 mV). Apart from the incomplete charge reversion in the second layer, the properties of NC-SBP-CHI-CARR-2.5% were considered as promising even though not ideal. The still negatively charged chitosan-covered interstage may be explained by unexpected behaviour of the polyelectrolytes in the capsule shell such as the formation of interferences (no discrete layers), or migration of the polyelectrolytes within the shell driven by charge equalisation.

5.2.2.1.7   NC-GA-CHI-CARR-3.79%

Finally, gum arabic emulsions were introduced as a template for the development of nanocapsules. Chitosan was firstly investigated regarding its capability to convert the strongly negative ζ-potential of -42.6 mV (Table 10, entry 16, p. 61) of the gum arabic emulsion E-GA7-5%. The volume of a 0.6 % chitosan solution (dissolved in acetate buffer pH 4) was transferred from system NC-SBP-CHI-CARR since both pectin and gum arabic had resulted in emulsions with high ζ-potential. 4 mL of E-GA7-5% were mixed with an increasing volume of 0.6 % chitosan solution. The ζ-potential increase is shown in Figure 29A. The same flocculation phenomenon as in system NC-SBP-CHI-CARR was observed at >3 mL chitosan, however the surface charge was still highly negative. In conclusion, chitosan was also not able to invert the negative charge of gum arabic emulsions. Nanocapsules could only be prepared with an incomplete reversion of the charge in the second step.
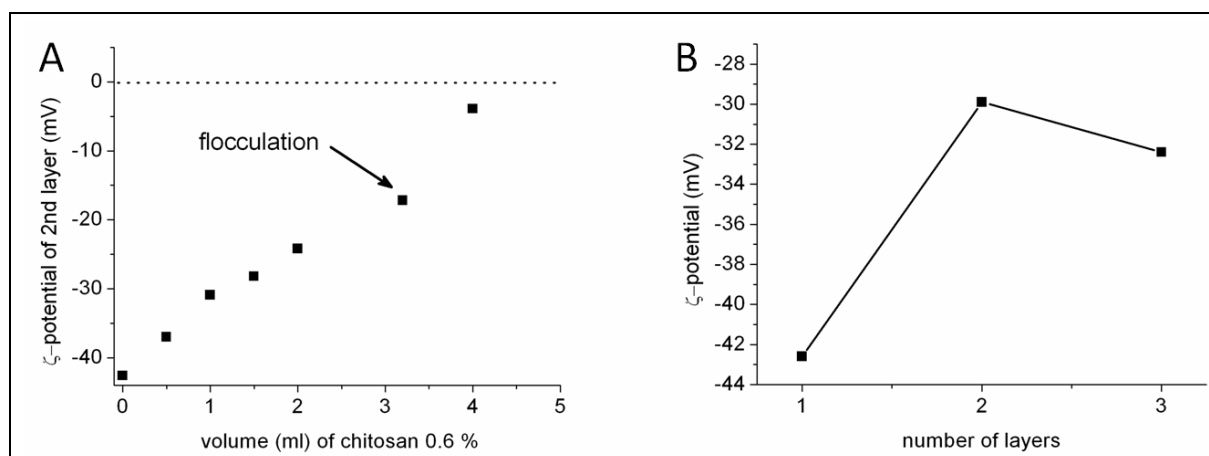
Figure 29 ζ-potential results of system NC-GA-CHI-CARR-3.79%, <u>A:</u> Determination of the chitosan amount for ζ-potential inversion, <u>B:</u> Change in the ζ-potential

Under these conditions, the optimized formulation NC-GA-CHI-CARR-3.79% was prepared as given in Table 4 (p. 37, entry 16). The ζ-potential of all layers was strongly negative as illustrated in Figure 29B. The results of PCS and LD reflect that the nanocapsules (d(0.5): 233 nm) and the emulsion template (d(0.5): 220 nm) have a similar size (see Table 10, entry 16, p. 61). The capsules are very homogeneous (PDI: 0.077) due to an addition of only few amounts of the polyelectrolytes in layer 2 and 3. In conclusion, the systems NC-SBP-CHI-CARR-2.5% and NC-GA-CHI-CARR-3.79% were comparable (Table 10, entry 15 and 16, p. 61). In both cases the chitosan-covered interstage (2nd layer) was still negatively charged. This incomplete charge reversion of the emulsion can be explained by the very high emulsion template ζ-potential (-36.2 mV and -42.6 mV) as well as the possible formation of mixed layers driven by electrostatic attraction of the oppositely charged polyelectrolytes. The samples were not considered as ideal, but they fulfilled the remaining requirements for nanocapsules, especially in terms of the homogeneity (PDI 0.080 and 0.077) and the small size (d(0.5) 132 nm and 233 nm).

5.2.2.1.8   NC-GA-GEL-SBP-1.85%

The final two systems are variations of system NC-GA-CHI-CARR where chitosan was replaced by gelatin in the second layer and the third layer contained either pectin or gum arabic. As observed from the unsuccessful system NC-GA-GEL-CARR, which was quite similar to the present system, it was tolerated to inject 12 mL of a 10 % gelatin solution into 10 mL of a 7 % gum arabic emulsion. Hence, this part started with a similar experiment, but with less gelatin, since for complex coacervation a mass ratio of gum arabic to gelatin = 1:1 was recommended by Parmentier GmbH [235]. 20 mL of E-GA7-5% were mixed with 14 mL of a 10 % gelatin solution. Moreover, the pH value of the environment was slowly decreased below pH 5 as it is commonly done during complex coacervation between the classical polyelectrolyte pair gum arabic and gelatin type A for microencapsulation [192]. Thus 0.5 mL of 0.1 M HCl was slowly injected under mixing. The pH value decreased down to 4.5. Unfortunately, the coacervation was very strong, effecting a destabilisation of the emulsion and sedimentation of the solid coacervate components. The ζ-potential was measured before and after addition of HCl in order to determine the effect of acidification on the surface charge of the gelatin covered interstage. Even by pH reduction (which theoretically should have increased the number of protonated amine groups of gelatin) the surface could not achieve a positive charge (ζ-potential decreased from -26 mV to -18.7 mV).

For the nanocapsule development it was concluded, that the addition of acid was not transferrable from microencapsulation (where precipitated capsules are finally dried and stored) to the preparation of liquid nanocapsule dispersion (where dispersed nanocapsules have to be stabilised in a 2-phase system against sedimentation, aggregation, or flotation). The conclusion was supported by the fact that the addition of HCl had no considerable effect on the ζ-potential of the second layer. Finally, for the remaining two systems it was still the task to prepare nanocapsules after discovering the amount of gelatin being necessary to obtain a second layer with a positive charge. 15 mL of a 10 % gelatin solution, added to 10 mL of the emulsion, yielded a gel-like non-fluid mass with the maximum ζ-potential value of -3 mV. Finally, the aim to get a positively charged second shell layer was abandoned. The best but still suboptimal composition for system NC-GA-GEL-SBP was found to be formulation NC-GA-GEL-SBP-1.85% as given in Table 4 (entry 17), p. 37. No flocculation was observed during injection of pectin. Sample NC-GA-GEL-SBP-1.85% with the results given in Table 10 (entry 17, p. 61) can be classified together with those of system NC-GA-CHI-CARR (entry 16) and NC-SBP-CHI-CARR (entry 15) due to no positively charged second shell layer. Moreover, owing to a large (z-average: 632 nm; d(0.5): 150 nm) and inhomogeneous size (PDI: 0.333), a low final ζ-potential (-17.4 mV), and gelation that occurred after cooling of the dispersion to ambient temperature, system NC-GA-GEL-SBP is considered as not successful.

5.2.2.1.9   NC-GA-GEL-GA-2.5%

For the sake of completeness, the polyelectrolyte combination NC-GA-GEL-GA was realised for preparation of nanocapsules although results of systems NC-GA-GEL-CARR and NC-GA-GEL-SBP demonstrated that no improvement was to expect. The disadvantages of system NC-GA-GEL-SBP (which were a negatively charged second layer, the need of huge amounts of gelatin, and as a consequence a gelling dispersion) would be equal. In order not to repeat the formulation just by replacing pectin by gum arabic in the third layer, less gelatin was used (Table 4, entry 18, p. 37). The results are given in Table 10 (entry 18: ζ-potential -26.4 mV; d(0.5): 134 nm). The sample also showed gelation. The system is declared as not optimal due to reasons mentioned above, comparable to sample NC-SBP-CHI-CARR-2.5%.

5.2.2.2   *Increasing the oil content of the successful nanocapsule systems*

The original idea of increasing the final oil content of the nanocapsule dispersions (in order to optimise the incorporation capacity for lipophilic model drugs) by evaporation of the aqueous dispersant under reduced pressure was not pursued further after the test on the system NC-OSA-CHI-CARR did not yield any promising results. After evaporation at 30 °C and 50 °C, large particles of up to 40 μm emerged and the particle size distribution became strongly bimodal. The nanosized drug carrier was destroyed. Size distribution curves after evaporation at ambient temperature (20 °C) did not differ considerably from untreated samples. Still, evaporation of water without heating required very low pressure (30 mbar or less) and was very time consuming (hours). To increase the oil content of the dispersions, solvent evaporation thereby did not prove to be applicable on large scale. The remaining successful nanocapsule systems (Table 10, entry 1, 5, 9, 12, p. 61) were not treated with evaporation under reduced pressure.

In contrast, the oil content was supposed to be increased by:

(i)   use of higher concentrated polyelectrolyte solutions injected into the emulsion

(ii)   starting on emulsions with higher oil content (instead of 5 % MCT).

So far the preparation of nanocapsule dispersions by injecting low concentrated polyelectrolyte solutions of layer 2 and 3 into the primary emulsion was described. For nanocapsules the oil content of the emulsion is the more diluted the lower the concentration is. Thus, higher concentrated solutions were used in order to reach an oil amount for the capsule dispersion being similar to that of the emulsion (close to 5 %). In some cases the absolute amount of the substances in layer 2 and 3 had to be increased using higher concentrations. This is due to the fact, that following Ostwald´s dilution law the dissociation of electrolytes reaches a maximum only in extremely diluted solutions [236]. In higher concentrated systems the degree of dissociation and thereby the number of charges decreases. Increasing concentration was limited by solubility (chitosan), occurrence of gelation (gelatin) and high viscosity (carrageenan, pectin, gum arabic). In general, an increase of viscosity of the dispersions was observed, which decreased by high-pressure homogenisation. System NC-OSA-GEL-GA showed gelation due to increased gelatin content. Nanocapsule compositions with higher polyelectrolyte concentrations were each already presented in the second row of the corresponding sample system in Table 4 (entry 2, 6, 10, 13), p. 37. The characterisation results are given in Table 10 (entry 2, 6, 10, 13), p. 61.

Compared to the results of the original samples (refer to Table 10, entry 1, 5, 9, 12), the use of high polyelectrolyte concentrations yielded similar formulations with increased PDI except of system NC-OSA-GEL-GA (Table 10, entry 9-10). Strong interaction forces possibly induced a complex capsule shell structure with diffuse layers or cross-linking. System NC-OSA-CHI-CARR (entry 1-2) is preferable regarding ζ-potential, followed by system NC-OSA-CHI-GA (entry 5-6) and NC-OSA-GEL-GA (entry 9-10). System NC-OSA-GEL-SBP (entry 12-13) exhibits a low ζ-potential and a high PDI combined with a large size. These attributes are rather disadvantageous. System NC-OSA-CHI-GA (entry 6) displayed a homogeneous size ditribution (lowest PDI of 0.188) and a small particle size (100-200 nm). It was considered as the best of the investigated formulations obtained by higher polyelectrolyte concentrations.

Finally, the oil content of the nanocapsules was enhanced by preparation based on emulsions with increased oil content (10 or 15 % MCT), stabilised with 5 or 11.25 % OSA starch (for composition cf. Table 4, entry 3, 7, 11, 14). The best results combining these oil-loaded emulsions with high polyelectrolyte concentration were obtained for the formulations given in Table 10 (entry 3, 7, 11, 14). The maximum oil content of 8.6 % could be reached for NC-OSA-CHI-CARR (Table 10, entry 3), followed by 7.4 % for NC-OSA-CHI-GA (entry 7). The highest ζ-potential was observed for NC-OSA-CHI-GA-7.4% (-35.4 mV). Sample NC-OSA-CHI-CARR-8.6% showed the smallest and most homogenous capsule size (z-av. 161 nm, d(0.5) 160 nm, PDI 0.233). In system NC-OSA-GEL-GA (Table 10, entry 10-11) gelation occured.

To prevent system NC-OSA-GEL-SBP and NC-OSA-GEL-GA from gelation, the gelatin solution concentration was reduced to 5 % again (Table 4, entry 11 and 14, p. 37). However, NC-OSA-GEL-GA still showed gelation. Further minimizing of gelatin concentration would have decreased the oil content which was not desired. Due to high

viscosity of injected carrageenan solution and gel formation of gelatin, respectively, all systems except of NC-OSA-CHI-GA (produced at ambient temperature) required heating of all solutions to 50 °C during preparation.

5.2.3 Transmission electron microscopy images

TEM photomicrographs of a single freeze-fractured emulsion droplet and of single capsules of the interesting consecutively prepared samples (emulsion template E-OSA5-5%, NC-OSA-CHI-CARR-2.5% (NC3), and NC-OSA-CHI-CARR-CHI-CARR-1.11% (NC5)), respectively, are shown in Figure 30. Overview images (not shown) confirmed the results of preliminary methods: the particle size was not absolutely homogeneous, but ranging from 50 nm up to 500 nm with highest frequency around 100 nm. As apparent from Figure 30, the structures are strongly spherical. Both the core as main part and the thin shell can be distinguished. A shell of the nanoemulsion (Figure 30A), consisting of the non-oilsoluble surfactant only, is hardly visible. The capsules (Figure 30B and C) show a discrete shell whose thickness can be estimated to be between 3 nm and 8 nm.
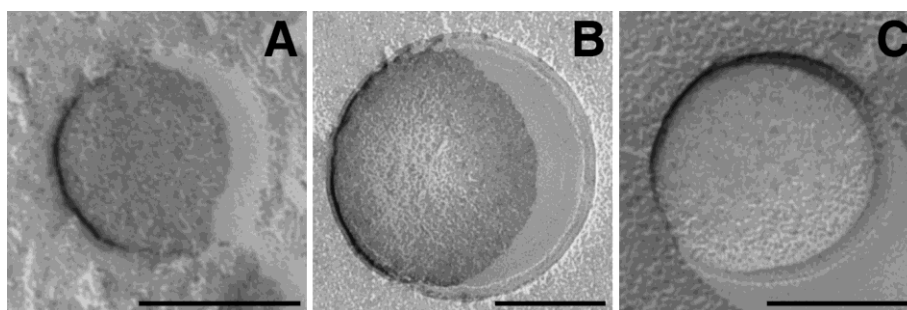
Figure 30 TEM images of <u>A:</u> nanoemulsion E-OSA5-5%, <u>B:</u> NC-OSA-CHI-CARR-2.5% (NC3), and <u>C:</u> NC-OSA-CHI-CARR-CHI-CARR-1.11% (NC5) (bars represent 100 nm)

The emulsion droplet, cf. Figure 30A, does not exhibit a clear contour between core and shell, a sharp transition is not visible. That is why the thickness can only be roughly estimated. The emulsifier OSA starch does not form a distinct shell as it is located interfacially in the shell (polar fraction) as well as in the core periphery (unpolar fraction). Figure 30B and C are identical in terms of core-shell structure. Especially Figure 30B shows the layered constitution of the shell which gives hint on several shell components. The estimated wall thickness value of 10 nm in maximum confirms the results of earlier publications reporting on nanocapsule shell thicknesses of 5 nm [237], 10 nm [14], or 20 nm [238,239]. However, it is important to note that the membrane thickness determination using TEM of freeze-fractured samples remains very difficult and often subjective [240]. Only a small portion of nanocapsules were correctly broken and readily observable. The studied pictures have to be representative of the whole sample [35,159,240]. In the present study, electron microscopy pictures have been selected with the priority to display the core–shell structure of the nanocapsules. Even though this aim was achieved, one has to keep in mind that those pictures only represent an insight into a small fraction of the sample. In addition, the membrane thickness varies depending on the freeze-fracture plane, particle damaging during sample preparation and because poor quality images were discarded. To improve the reliability of shell thickness calculation even further, small angle neutron scattering could be used. However, this method is only appropriate for defined particles and rather difficult to apply for polydisperse samples [35,159,240]. Thus, is does not yet represent a standard method. Figure 31 shows a representative selection of TEM images of the four successful nanocapsule systems each with highest possible

oil content. The overall size of each sample was between 100 nm and 200 nm with a spherical shape, sample NC-OSA-GEL-SBP-5.55% contained few fractured capsules of approx. 800 nm in diameter (not shown).
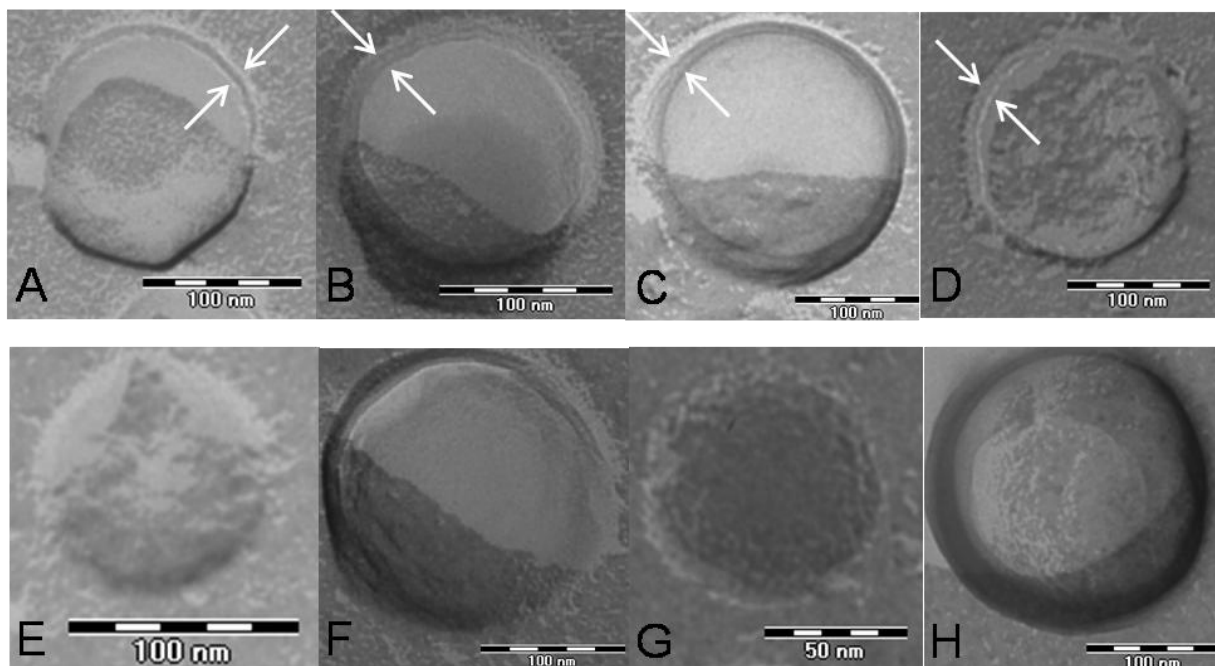

Figure 31 TEM images of broken nanocapsules, top row: arrows mark layered shell structure, bottom row: (partly) unbroken capsules with rough surface; A+E: NC-OSA-CHI-CARR-8.6%, B+F: NC-OSA-GEL-SBP-5.55%, C+G: NC-OSA-CHI-GA-7.4%, and D+H: NC-OSA-GEL-GA-5.625%

Due to a PDI of around 0.2, which indicates a certain width of particle size distribution, it would not be reasonable to give an average size for each nanocapsule system but to categorize them by a size range. Generally, the TEM micrographs confirmed the results of the particle size determination techniques PCS and LD. The top row of Figure 31 (A-D) represents one capsule of each of the four nanocapsule systems which was freeze-fractured during preparation procedure. Thereby, a spherical oily core surrounded by a thin polymer shell of approximately 10 nm to 20 nm is illustrated. The shell clearly demonstrates a composition of several layers, confirming the deposition of oppositely charged polyelectrolytes onto the MCT core. In comparison to the fractured nanocapsules (A-D) with a smooth shell edge, the (partly) unbroken capsules (pictures E-H) exhibit a rough surface which can be attributed to the presence of polysaccharide chains protruding from the capsule shell.

5.2.4 High-resolution light microscopy images

The nanocapsules NC-OSA-CHI-CARR-2.5% were studied exemplarily. When drying on the slide, the reduction in Brownian motion of the nanocapsules allowed for better images. Figure 32 suggests that there possibly appeared to be two different types of materials in the samples: few large 'doughnut' shaped particles and a main fraction of very small particles. In conclusion, most of the particles appeared smaller than 1 µm. By focusing effects in the different layers some nanocapsules might have appeared larger than they really were.
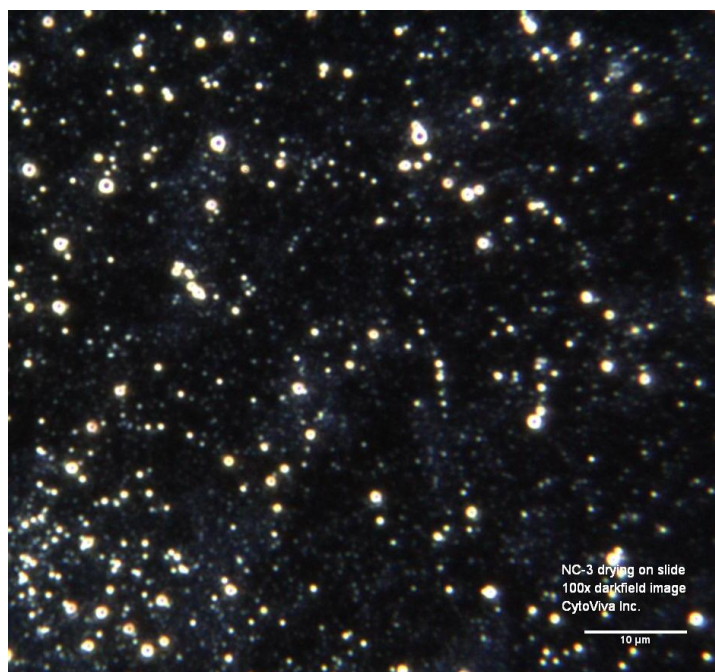
Figure 32 CytoViva image of NC-OSA-CHI-CARR-2.5%

5.2.5 Theoretical incorporation capacity for lipophilic model drugs

The solubility of different model drugs in MCT at 5 °C was determined as presented in Table 11. Although they have partly similar log$P$ values, water and MCT solubilities vary strongly. Only the porphine molecule pTHPP is extremely lipophilic compared to the other drugs.

Table 11 Drug load capacity (mg/g) in water, in MCT, in the nanocapsules (1) NC-OSA-CHI-CARR-8.6%, (2) NC-OSA-GEL-SBP-5.55%, (3) NC-OSA-CHI-GA-7.4%, (4) NC-OSA-GEL-GA-5.625%, and the emulsion template (E)

drug	log$P$[6]	in water[7]	in MCT	in (1)[8]	in (2)[8]	in (3)[8]	in (4)[8]	in E-OSA5-10% template[8]
RSV	3.08	0.030	0.0605	0.0052	0.003	0.0045	0.0034	0.006
DZP	2.9	practically insoluble	21 ± 1.3	1.80	1.16	1.55	1.18	2.1
SAL	2.26	2	34.4 ± 0.7	2.96	1.91	2.55	1.93	3.44
pTHPP	7.6	practically insoluble	> 30	> 2.6	> 1.66	> 2.22	> 1.69	> 3

For the four nanocapsule samples (1), (2), (3), and (4) the theoretical drug solubility was calculated based on their maximum achievable oil content, as given in the sample name, and on the determined MCT solubility. For sample (1) = NC-OSA-CHI-CARR-8.6%, nanocapsules were exemplarily prepared with the drug containing MCT.

The size, integrity and surface charge was not influenced by encapsulated molecules since the characteristics were comparable with unloaded nanocapsule dispersions. Resveratrol (RSV) showed a very low solubility in

---

[6] from Public Chemical Database (2009): http://www.ncbi.nlm.nih.gov/sites/entrez?db=pccompound [257]
[7] from The Merck Index 14th ed.
[8] calculated by means of the oil content

MCT, followed by diazepam (DZP), pTHPP, and salicylic acid (SAL). Solubility of pTHPP in MCT was very high and thus not determined exactly for cost reasons. Compared to other oils, MCT displays a moderate solubiliser for resveratrol with a solubility of 60.5 µg/g (cf. coconut oil 179.75±8.28 µg/g, corn oil 85.72±6.77 µg/g, olive oil 47.93±7.27 µg/g [241]). In spite of structural similarity with coconut oil (saturated medium-chain triglycerides), MCT showed only a third of its solubility. Due to poor oil solubility and low MCT content in the nanocapsules, RSV solubility in aqueous solutions is even tenfold better compared to nanocapsule dispersions. However, the oral bioavailability from the nanocapsules might be increased since a better uptake can be expected. Nevertheless, the polyelectrolyte nanocapsules do not display an optimal drug delivery system for RSV. Recently, liposomes proved to be capable of incorporating the tenfold RSV amount compared to coconut oil (1.8 mg/g [242]) which is evidently preferable. A much better solubility improvement over aqueous media could be achieved for drugs that show better oil solubility, such as DZP and pTHPP. They are practically water-insoluble, but very well soluble in MCT. The best dissolution rate in MCT was observed for salicylic acid. Thus, the four successful nanocapsule formulations given in Table 11 might be excellent drug carriers for these model substances since a high drug load can be achieved. Due to moderately higher oil content, the drug incorporation capacity of the emulsion template E-OSA5-10% was slightly higher than of the nanocapsules.

5.2.6 Summary and discussion

The varying combination of the six available polyelectrolytes led to 12 systems being investigated. In this section, the development of these 12 differently composed polyelectrolyte nanocapsule systems is summarised regarding suitability as potential drug delivery systems. The results of 9 of the 12 systems (some with several possibilities of the oil content) were given in Table 10 (p. 61). The three remaining combinations of the available polyelectrolytes in the nanocapsule shell were excluded earlier due to different reasons of instability.

Initially, a fundamental result shall be discussed, which is that the simple theoretical aspects of complex coacervation were not always in agreement with practical observations. A typical example successfully applied in the pharmaceutical technology is the microencapsulation of drugs or DNA by coacervation between solutions of gelatin and gum arabic (not yet commercial due to steric problems of interactions). However, in this case their charges are neutralized and a non-charged coacervate is formed. Moreover the coacervate particles are isolated and dried as a powder which means they do not require dispersion stabilisation. Hence, microencapsulation is different from the presented preparation process of nanocapsules. This might be a reason why the phase separation technique used in this work was successful in only four of the systems. These were (cf. Table 10, p. 61): NC-OSA-CHI-CARR (entry 1-4), NC-OSA-CHI-GA (entry 5-7), NC-OSA-GEL-GA (entry 9-11), and NC-OSA-GEL-SBP (entry 12-14). Under consideration of two further promising systems NC-SBP-CHI-CARR (entry 15) and NC-GA-CHI-CARR (entry 16), which could not be developed with a positively charged second layer, six polyelectrolyte combinations were successful.

Besides, in contrast to anionic substances, there is still a lack of cationic polyelectrolytes based on polysaccharide structure (one example is chitosan). For this reason, proteins had to be used in order to enable certain variability. However, the coacervation between proteins and polysaccharides is not fully understood so far due to only few research results published. Frequently, they rather result in precipitation than in the

formation of liquid dispersed coacervate phases, especially for strong acids. An inhomogeneous or even unknown charge distribution exhibits another difficulty because the charge density of the poly-ions is mainly determining the stoichiometric composition of polyelectrolyte complexes. Steric hindrance can complicate the complexation since polymers can form different structures (helices, coils). Most formed systems (in case of liquid coacervates) have a high dynamic structure, are deformable and are subject to external influences like temperature and salt ions [243]. Facing these problems, it is maybe no more surprising that only 4 of the 12 investigated systems were successful in developing nanocapsules meeting the required demands.

Secondly, a fact that attracts attention is that all 4 positively developed systems contain the same emulsifier, which is the OSA starch. This may be a consequence of obtaining stable emulsions by relatively low OSA concentrations, but rather can be explained with its low charge density. This results in a relatively low (negative) ζ-potential of the emulsion which is advantageous since a smaller amount of the second layer polyelectrolyte is required for converting the surface charge into positive. A low positive charge of the second shell layer was sufficient because this already indicated the complete covering of the core with the second polyelectrolyte.

In the second layer, gelatin and chitosan were suitable with the same preference. The termination of the nanocapsule shell was successful with carrageenan, but also pectin and gum arabic. System OSA-CHI-GA was the only one which did not require heating during production process. System OSA-CHI-CARR yielded nanocapsules with the highest oil content (8.6 %), followed by system OSA-CHI-GA (7.4 %), and thereby exhibited the highest loading capacity. Particles larger than 1 µm were rarely observed. System OSA-GEL-SBP was not adequate because the nanocapsules tended to show particle growth (mechanism not known; possibly coalescence, aggregation or Ostwald ripening or a mix thereof) after storage at 2-8 °C over 4 weeks. In terms of ζ-potential, it mostly featured the lowest values (independent of the oil content) compared to the other three systems. This might be the reason for poor stability. Moreover, as mentioned earlier, the formulations were stored unpreserved to minimise a potential impact of the preservative on the emulsion and nanocapsule stability. Microbial contamination of the polyelectrolyte solutions could effectively be reduced by use of low concentrations (max. 2.5 % for emulsification) and only short storage intervals at 2-8 °C. In the prepared nanocapsule samples no germ growth was observed, which may be explained by reduction of the pectin content (down to max. 1.25 % in sample NC-SBP-CHI-CARR) in the dispersion compared to pure solutions. Hence, the dispersions did not represent a good nutrient medium for germs, anymore. However, it should be considered whether there might be an influence of the potential presence of microorganisms on the particle size, growth, and charge.

System OSA-CHI-GA showed a desirable particle size distribution at low oil contents, which broadened with increasing MCT content. System OSA-GEL-GA rarely showed particles larger than 300 nm. This may be explained by gelation of this sample (for the formulation with highest oil content of 5.625 %) as a consequence of the contained gelatin and gum arabic amounts. The nanocapsules were stabilised in the gel framework and did not require high ζ-potential for electrostatic charge stabilisation. However, the applicability of gelling

nanocapsule dispersions is questionable. But potentially, system OSA-GEL-GA can be utilised after lyophilisation and further processing in solid dosage forms.

In conclusion, system OSA-CHI-CARR and OSA-CHI-GA are considered to be optimal. Possible reasons for obtaining 8 non-successful combinations of polyelectrolytes have been addressed above. In most cases, only a partial charge neutralisation of the emulsifier and the second layer (chitosan or gelatin) was reached, but a complete charge inversion was not possible (flocculation). In few cases, even the addition of marginal volumes of the next polyelectrolyte layer led to flocculation of the complexes. Hence, flocculation was the most frequently observed phenomenon, disabling the formation of a liquid coacervate. Gelatin combined with carrageenan categorically displayed an unsuitable polyelectrolyte pair. Occurrence of flocculation between gelatin and different hydrocolloids (e. g. carrageenan, low methoxylated pectin, gum arabic) had been mentioned by Schrieber, already [192]. They could be confirmed in this work, but further analysis of their steric structure should be done to find reason for the problems (eventually steric hindering of the charges). Emulsions of pectin or gum arabic were theoretically very good templates for nanocapsules (system SBP-CHI-CARR and GA-CHI-CARR), but due to their high initial ζ-potential (high degree of esterification of pectin and fraction of glucuronic acid in gum arabic) neither gelatin nor chitosan were capable of yielding a positive charge of the second capsule wall layer. These formulations are promising but were discarded since they did not exhibit three complete polymer layers in the nanocapsule wall. Regarding the mechanical rigidity and stability as compared to the emulsion template, adverse properties have to be expected in contrast to the 4 successful systems OSA-CHI-CARR, OSA-GEL-SBP, OSA-CHI-GA, and OSA-GEL-GA. However, further investigation on system NC-SBP-CHI-CARR (PDI: 0.080) and NC-GA-CHI-CARR (PDI: 0.077) would be justified by the promising particle size distribution and ζ-potential results (especially system NC-SBP-CHI-CARR: -37.7 mV).

5.3 Further investigation of the nanocapsule size

5.3.1 Asymmetrical flow field-flow fractionation

5.3.1.1 Determination of the molecular weight of OSA starch by AF4-MALS

The thermogravimetry (TG) experiment yielded a thermal mass loss of OSA starch of 5.11 %, 5.11 %, and 5.12 % during the heating period from 20 °C to 150 °C. The evaporated molecules can be referred to adhering water. Thus the OSA starch moisture content can be assumed to be approximately 5.11 %. This value was used for the determination of the refractive index increment dn/dc and thereby contributed to the determination of the molar mass of OSA starch by AF4-MALS.

Figure 33 describes the dependence of the RI signal on the OSA starch concentration. The dn/dc value which is reflected by the slope of linearly fitted graph was determined to be equal to 0.1759 cm^3/g (correction of the moisture content included). The dn/dc increment served for the determination of the molar mass of OSA starch in the following section.
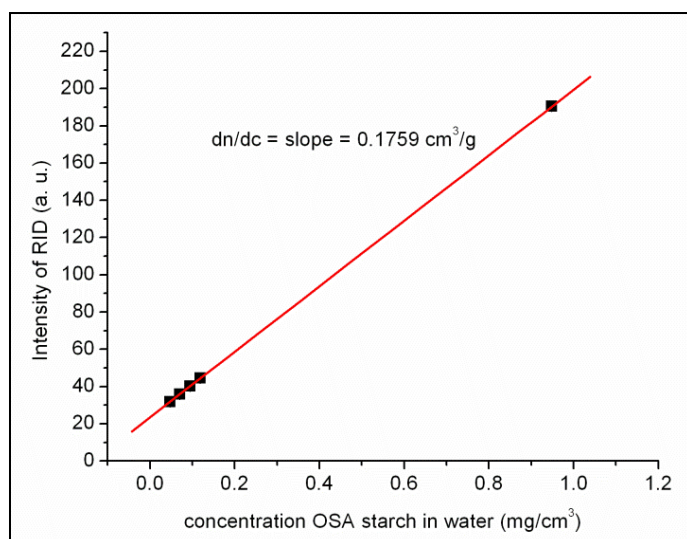
Figure 33 Plot of RID signal intensity versus OSA starch concentration for the determination of the refractive index increment dn/dc

The AF4 elugrams for OSA starch are shown in Figure 34, where the obtained light scattering and differential RI signals as well as the molar mass are plotted as a function of elution time. Both the MALS as well as the RI detector signals indicate that the molar mass of OSA starch covers a wide size range. Determination of the weight average molar mass (M_w) was performed for the elution time range from 9.5 to 35.5 minutes because after that the RI signal decayed to zero. For each point of elution time a Zimm plot was generated in order to calculate the molecular weight.
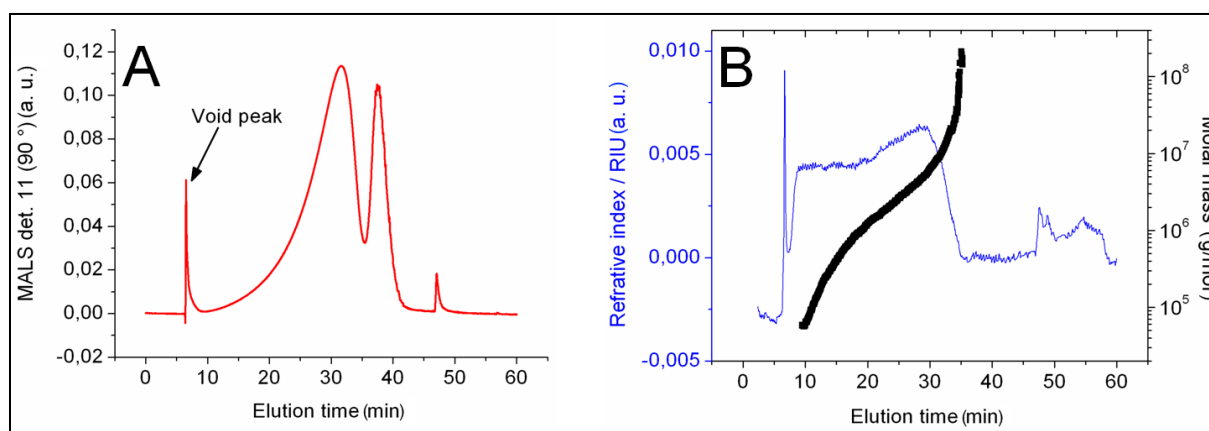
Figure 34 Elugrams of an OSA starch solution showing the A: MALSD signal, and B: RI signal and molar mass

By means of Equation (13) and each individual Zimm plot, which is exemplarily given in Figure 35A for the mass fraction eluting in the MALSD peak at 31.5 minutes, the weight average molar mass (M_w) of OSA starch could be obtained since it is equal to the reciprocal of $K*c/R(\theta)$ value when $sin^2(\theta/2) = 0$. OSA starch eluting at 31.5 minutes had a molar mass of 9.6×10^6 g/mol. Figure 35B shows the differential molar mass distribution of the OSA starch sample in a logarithmic plot detected during the mentioned elution time. The sample´s molar mass ranged from 5×10^4 to 3×10^7 g/mol, the main fraction being sized from 10^6 to 10^7 g/mol. The modal score (most frequently occurred molecular weight in the data set) obtained from the frequency distribution curve in Figure 35B amounts to 2.26×10^6 Da and can be referred to as the best description of an average molar mass determined for OSA starch.
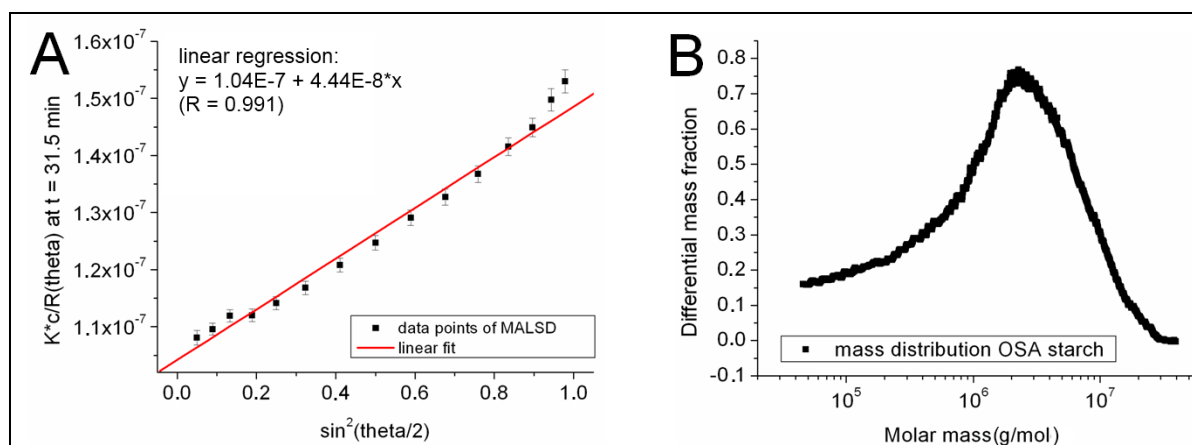
Figure 35 <u>A:</u> Zimm plot at time t=31.5 min (example). For each elution time, M_w is calculated by $Kc/R_\theta = 1/M_w$ at $\sin^2(\theta/2) = 0$. For t=31.5 min, M_w (OSA starch) = 9.6×10^6 Da. <u>B:</u> Resulting differential mass distribution with an approximate average molar mass (OSA starch) of $M_{modal} = 2,26 \times 10^6$ Da (modal score).

This result did not consider particles being responsible for the signals after the main MALSD peak, i.e. from 35.5 to 41 minutes because they cannot reliably be identified as OSA starch molecules due to the missing RID signal at that time range. Generating a Zimm plot over the whole range (9.5 to 41 min) was not possible due to poor data fit quality. That is why the value of the modal score can only be given approximately (2.26×10^6 Da).

Figure 36 demonstrates the size development of the dissolved OSA starch molecules with increasing molar mass. Those with a molar mass of less than 10^6 g/mol do not appear is this graph because their RMS radius is far smaller than 1 nm. It is shown that the fraction with a molar mass of less than approximately 2×10^6 g/mol is smaller than 15 nm and shows a strong increase in size with increasing molar mass, whereas larger particles do not show such a strong dependence of the size on the molar mass. The RMS radius is maximum 53 nm large.
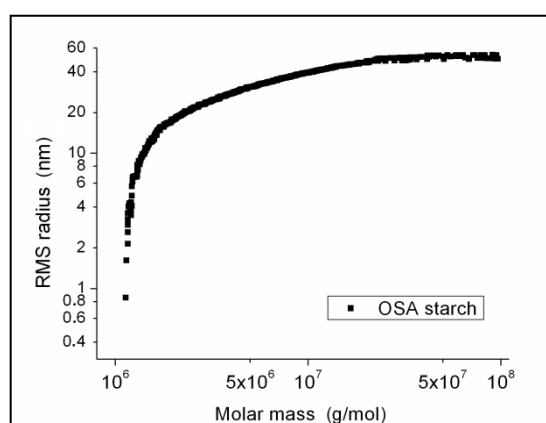
Figure 36 RMS radius versus molar mass of OSA starch

5.3.1.2 Size determination of emulsions and nanocapsules by AF4-MALS

AF4 coupled to MALSD was used to study the size of the samples which are listed below:

(i) E-OSA5-5%

(ii) NC-OSA-CHI-CARR-2.5% (NC3)

(iii) NC-OSA-CHI-CARR-CHI-CARR-1.11% (NC5)

(iv) NC-OSA-CHI-CARR-8.6%

(v) NC-OSA-GEL-SBP-5.55%

(vi) NC-OSA-GEL-GA-5.625%

(vii) NC-OSA-CHI-GA-3.7%

They present the selection of the successfully developed nanocapsule samples from Table 4 (p. 37) as well as their nanoemulsion template. The elugram for the sample E-OSA5-5% is shown in Figure 37.
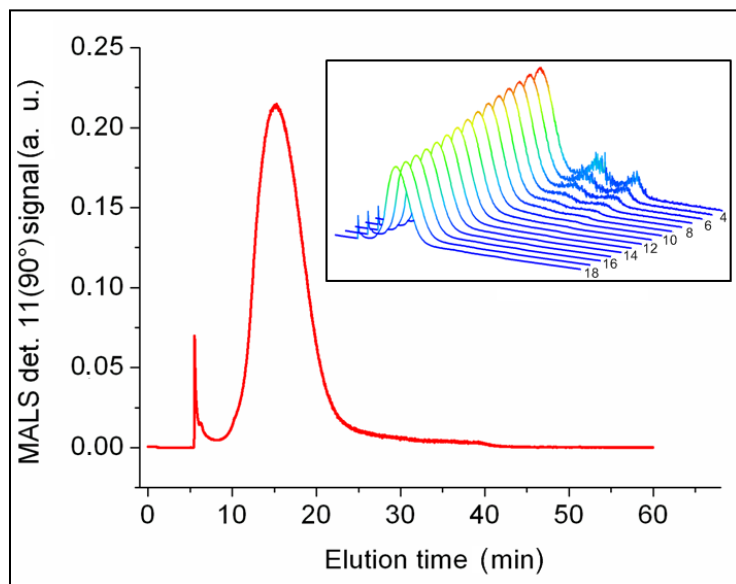
Figure 37 AF4-MALSD elugram of E-OSA5-5% (det. 11, 90° angle) and 3D overview (detectors 4 to 18)

Best representation of the particle size is usually reflected by the given 90° angle view (detector 11). For comparison, the 3D image shows how the MALSD signal varied from detector 4 (26°) to detector 18 (163°) for the emulsion. The main peak at 16 min was detected at each scattering angle. However, at small light scattering angles such as detector 4 (26°) the signal showed further peaks at approx. 30 min and 40 min elution time which are hardly visible at 90°. They were induced by very few particles eluting later and being slightly larger than the main fraction which can be concluded later from the geometric radius distribution of Figure 38A (left). The particle size obtained for the emulsions and nanocapsules was each related to the elution time as given by Equation (8). The weight average geometric radius (R_w) was calculated from RMS radius by Equation (15) (assumption of spherical shape). This calculation showed an excellent data fit for the emulsion over the whole scattering angle width. However, for polyelectrolyte NCs poor data fit quality was observed in the Zimm plot for very small and very large scattering angles (detectors 4, 5, 6, 18). Possibly the spherical shape of the capsules has been influenced by polymer chains directing out of the particle. Another reason for poor fit data at the mentioned detectors could be interaction of the particles with the membrane. Hence, the curve fit was optimised by neglecting the mentioned scattering angles. Scattering angles No. 7 (52°) to 17 (153°) were applied for particle size determination of all samples. A summary of the size results is given in Table 12.

The AF4-MALS results of all investigated samples are given in the following figures. Figure 38 shows the elugrams of the consecutively prepared samples (OSA emulsion template, three- and five-layered NCs consisting of OSA, chitosan and carrageenan). The elugram peak maximum was reached at approx. 16 min for each of the three samples of Figure 38. In general, the elugrams look very similar. The geometric radius was calculated in the elution time range from 9 to 43 min. It mainly increased with increasing elution time in the range from 10 min to 30 min which indicates that the particles mostly eluted normally but not sterically. The region after the main peak (from 30 to 43 min) shows some variations of the size. However, these signals derived from only very few particles.

Table 12 Size results (in nm) obtained by AF4; $^{\#}$calculated from RMS radius of scattering detectors 7-17

sample name	average geometric radius$^{\#}$ (R_w)	average geometric diameter	d (0.1) from cumulative mass fraction	d (0.9) from cumulative mass fraction
E-OSA5-5%	120.8	241.6	45.07 · 2	78.57 · 2
NC-OSA-CHI-CARR-2.5%	143.8	287.6	53.76 · 2	91.97 · 2
NC-OSA-CHI-CARR-CHI-CARR-1.11%	125.9	251.8	59.45 · 2	91.76 · 2
NC-OSA-CHI-CARR-8.6%	146.2	292.4	67.65 · 2	166.0 · 2
NC-OSA-GEL-SBP-5.55%	91.3	182.6	86.31 · 2	94.4 · 2
NC-OSA-CHI-GA-3.7%	121.4	242.8	48.6 · 2	106.8 · 2
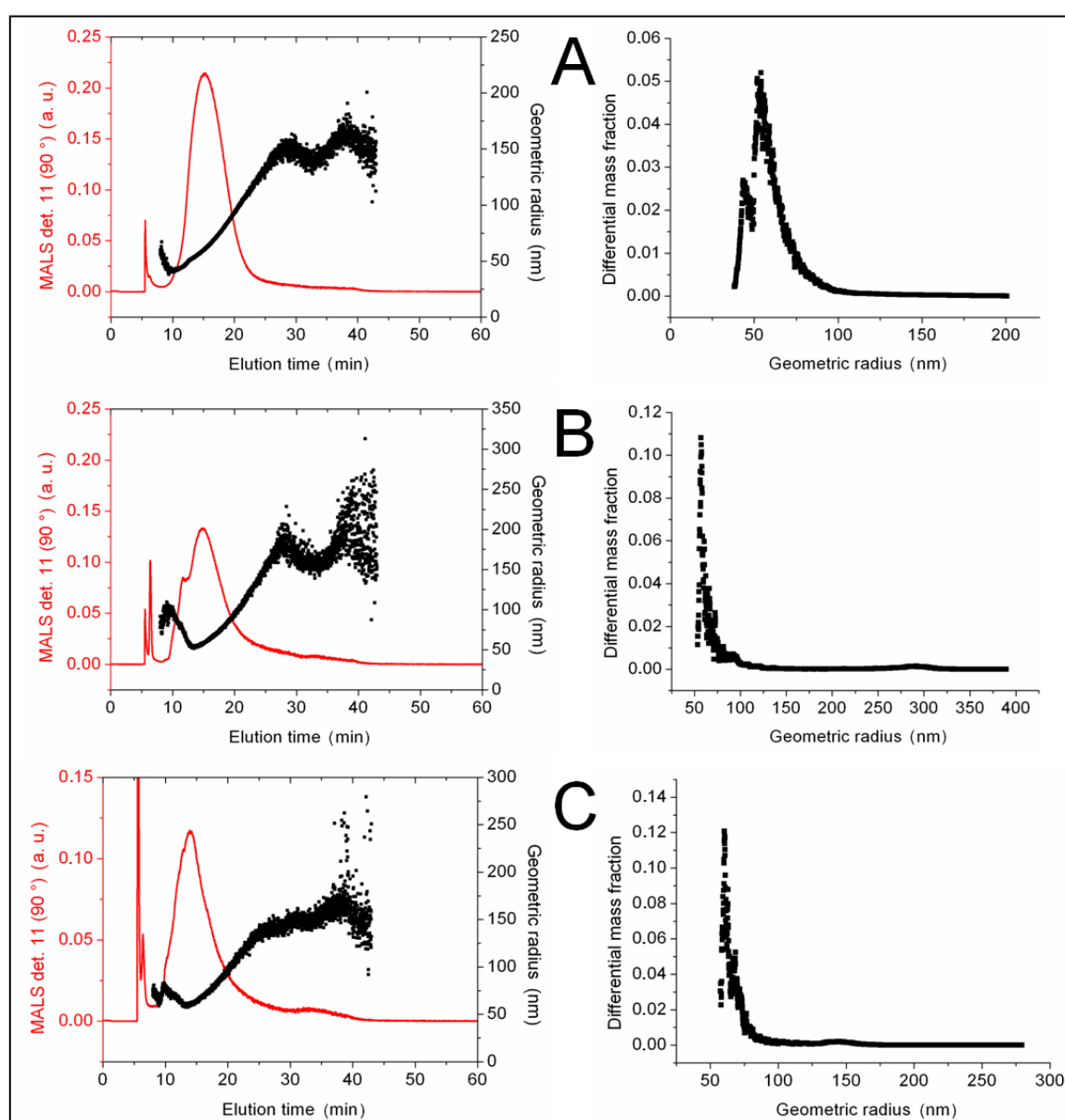
Figure 38 Elugrams from AF4-MALSD (90°), geometric radius of the particles (both left column) and the differential mass distribution (right column) of samples A: E-OSA5-5%, B: NC-OSA-CHI-CARR-2.5% (NC3), C: NC-OSA-CHI-CARR-CHI-CARR-1.11% (NC5).

Moreover, their statistical relevance is not proven because for all three samples the calculated size between 30 and 43 min elution time rises and decreases again. A superimposition of normal and steric elution in this region cannot be excluded definitely. As obtained from the cumulative mass fraction (see Table 12, p. 79), the particle radius (r(0.9) = ½ · d(0.9)) is smaller than 100 nm for 90 % of the particles in the 3 samples. A narrow size distribution of the radius between 40 and 100 nm is shown in the graphs of Figure 38 (right column). In conclusion, emulsion droplets of 240 nm and NCs of 250 to 290 nm (average geometric diameter, Table 12) were detected by AF4-MALS. The emulsion droplets (Figure 38A) were slightly smaller than the subsequently prepared NCs (Figure 38B, C). This result is appropriate to confirm the fact that emulsion, three- and five-layered NCs were prepared after each other. Figure 39 shows the AF4 results of the further NC formulations with highest possible oil content (NC-OSA-CHI-CARR-8.6%; NC-OSA-GEL-SBP-5.55%; NC-OSA-CHI-GA-3.7%).
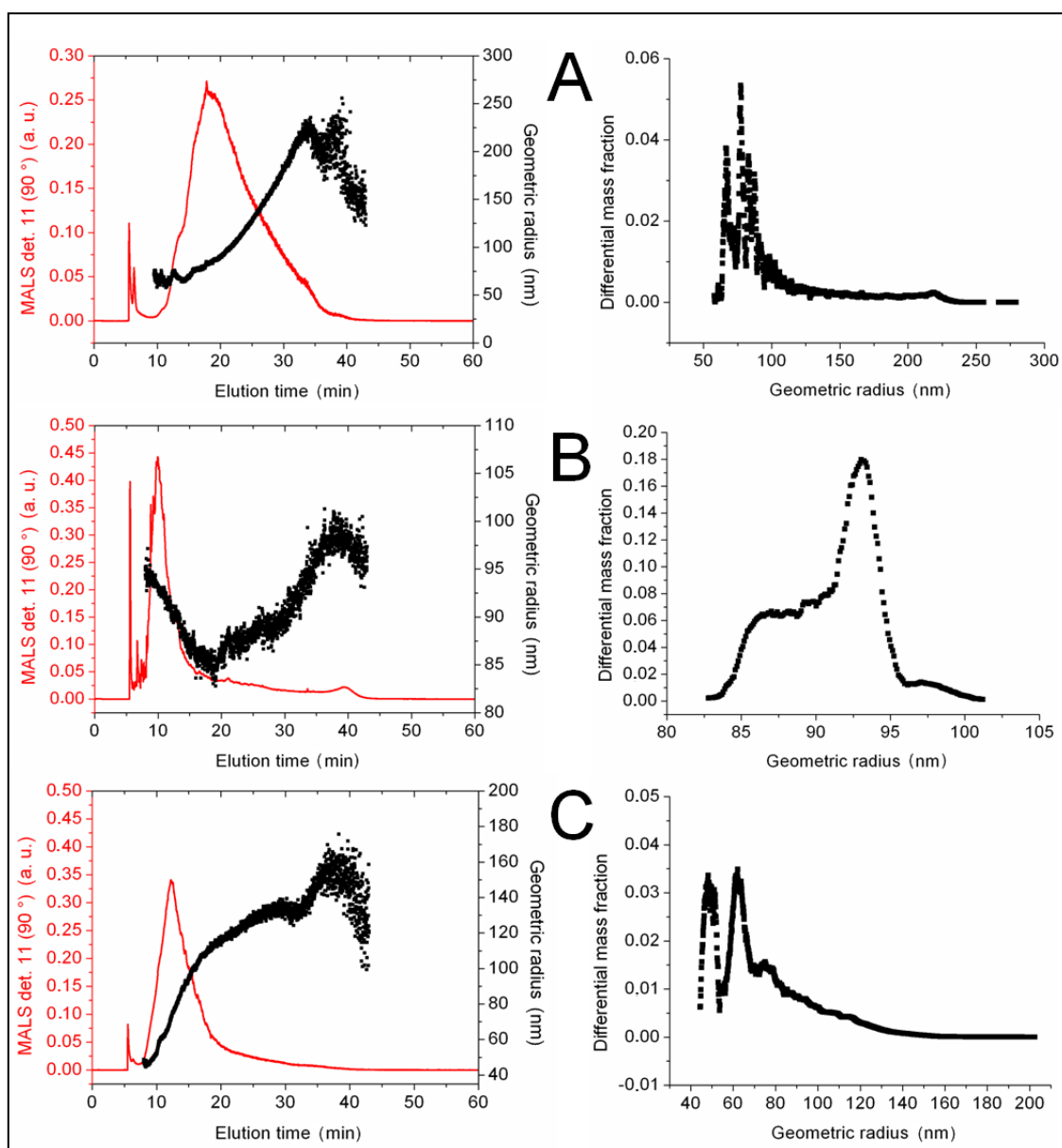
Figure 39 Elugrams from AF4-MALSD (90°), geometric radius of the particles (both left column) and the differential mass distribution (right column) of samples A: NC-OSA-CHI-CARR-8.6%, B: NC-OSA-GEL-SBP-5.55%, C: NC-OSA-CHI-GA-3.7%.

In contrast to the three samples of Figure 38, the elugrams of Figure 39 (left column) apparently differ from each other. While particles of sample A (NC-OSA-CHI-CARR-8.6%, composed similarly to the NCs in Figure 38B and C) eluted during the whole AF4 elution step (10 to 40 min, cf. Table 7, p. 42), the main fraction of samples B (NC-OSA-GEL-SBP-5.55%) and C (NC-OSA-CHI-GA-3.7%) eluted already between 10 and 20 min.

Since the cross flow decreased from minute 10 to 40 of the separation program, larger particles should elute later than smaller ones in case of normal elution behaviour. So if eluted normal, it can be concluded that particles of sample A might be larger in average than those of sample B and C. The geometric radius (calculated from the elution range of 9 to 43 min) mainly increased during the elution of the main fraction of sample A and C (range of 9 min to 35 min) which again indicates predominant normal (but not sterical) elution behaviour. However, sample B showed steric elution (<u>de</u>creasing geometric radius) in the range of its main fraction (9 to 20 min). Only the particles eluting between 20 and 40 min showed normal elution behaviour (<u>in</u>creasing geometric radius). Hence, the elution behaviour of the particles of sample B is hard to describe because a superimposition of normal and steric elution in the whole elution step (10 to 40 min) has to be considered. As the size distribution of these particles was determined as to be very narrow, an interaction of the separation membrane with the external polyelectrolyte (sugar beet pectin, SBP) is assumed to be the reason for the steric elution behaviour of sample B. As obtained from the cumulative mass fraction (not shown, see Table 12), the radius of 90 % of the particles (r(0.9) = ½ · d(0.9)) is smaller than 166 nm in sample A, but even smaller than 95 nm and 107 nm in sample B and C. This result confirms the conclusion drawn from the elugrams, that particles of sample A would be larger than of sample B and C. A narrow size distribution of the radius of sample B between 80 and 100 nm is shown in the differential mass fraction graph of Figure 39 (right column). The particle size of sample A, however, is widely distributed between 50 and 250 nm, the radius of sample C ranges from 40 to 150 nm. In conclusion, smallest (R_w 92 nm) and most homogeneous particles eluting partly sterically were detected by in sample B (NC-OSA-GEL-SBP-5.55%). Particles of sample C (NC-OSA-CHI-GA-3.7%; R_w 121 nm) and A (NC-OSA-CHI-CARR-8.6%; R_w 146 nm) were larger and less homogenous (R_w: from Table 12, p. 79).

The elugram of sample NC-OSA-GEL-GA-5.625% is not given because it could not reliably be evaluated due to a very poor data fit. This could be a result of the superimposition of both normal and steric elution. Another reason could be a wide size distribution. Additionally, the presence of gelatin should be considered as a possible influencing factor, especially because sample NC-OSA-GEL-SBP-5.55% (Figure 39B) also showed both steric and normal elution behaviour. Gelatin chains potentially interacted with or adhered to the membrane.

5.3.2 Atomic force microscopy: topographic analysis and height profile

5.3.2.1 Consecutively prepared samples

Topographic analysis was applied for the investigation of the size and surface morphology of the emulsion template as well as of the three- and five-layered nanocapsules given below (consecutive sample preparation):

(i) E-OSA5-5% (A) (iii) NC-OSA-CHI-CARR-CHI-CARR-1.11% (NC5) (C)

(ii) NC-OSA-CHI-CARR-2.5% (NC3) (B)

In order to confirm the PCS, LD, TEM, and AF4 results, AFM served as an additional method to demonstrate whether the prepared samples could be classified as DDS in the nanoscale. Besides, this technique allowed the determination of their vertical height profile and their shape, giving information whether the emulsion droplets and nanocapsules were spherical. Although AFM was introduced for high-resolution surface profilometry, the height image records the surface topography and particle size exactly only when no deformation occurs on the surface. *A priori*, it is difficult to say whether the tip-to-sample force is large enough to induce surface deformation [82]. Thus, deformation influencing the height profile was possible. The results are shown in Figure 40.
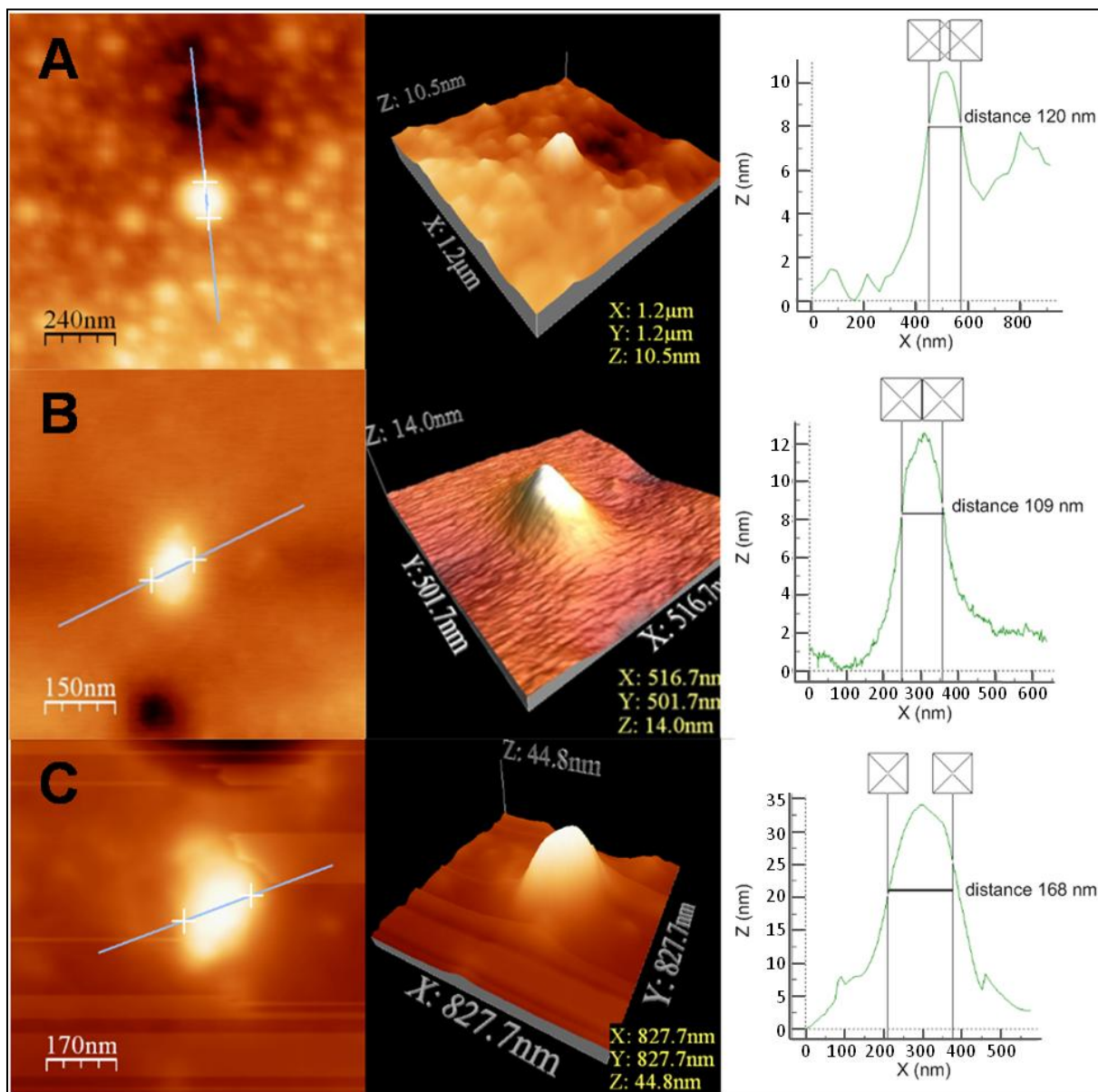
Figure 40 Topographic AFM images generated in tapping mode, <u>left column:</u> 2D-images (with height profile lines), <u>centre column:</u> 3D-images, <u>right column:</u> height profiles; <u>row A:</u> nanoemulsion E-OSA5-5%, <u>row B:</u> NC-OSA-CHI-CARR-2.5% (NC3), <u>row C:</u> NC-OSA-CHI-CARR-CHI-CARR-1.11% (NC5).

As expected from the dynamic and static light scattering measurements, the average size of the three samples did not show considerable differences. Overview images (not shown) presented emulsion droplets and

capsules, respectively, ranging from 50 nm up to 500 nm. Emulsion droplets were mainly approximately 80 nm in diameter, only few showed a size of more than 130 nm. Sizes between 100 nm and 250 nm showed the highest frequency in the nanocapsules samples (NC3 and NC5). In general, the samples were definitely nanosized. The results of the particle size determination obtained by PCS, LD, A4F, and TEM approximately are in accordance with those of the AFM images. Furthermore, the size distribution was not very narrow as it is common for emulsions. This was already observed in the PCS measurements (PDI ≈0.1). All capsules were spherically shaped which is in agreement with the TEM pictures. The surface structure featured no significant phenomena, thus a smooth surface can be assumed. The height profiles, giving information about vertical dimension of the particle, are displayed in the right column of Figure 40.

However, the vertical and horizontal diameters of the emulsion droplets as well as of the capsules are not identical. There are two possible reasons for this phenomenon. Firstly, it can be assumed that the height information of one single capsule got partly lost by embedding in the sample dispersion due to drying of the sample on mica. As lately observed for hollow particles by Kepczynski et al. [244], another reason for the flattening of soft particles can be seen in the pressure applied by the tip during scanning. Interestingly, in both the cited literature (4 nm height/40 nm diameter) and the present investigations (10 nm height/100 nm diameter in case of the nanoemulsion and three-layered nanocapsules NC3-OSA-CHI-CARR-2.5%) the average height amounted to around 10 % of the lateral size. The five-layered nanocapsules NC5-OSA-CHI-CARR-CHI-CARR-1.11% presented an exception concerning the ratio of vertical/horizontal dimension (35 nm/170 nm). Its height is even about 20 % of the lateral diameter. The assumption that the tip pressure induced flattening of the particles would allow to state that the five-layered nanocapsules possess a harder wall than the emulsion and the three-layered nanocapsules. A harder wall might be the reason why the five-layered nanocapsules were less deformable than the emulsion and the three-layered nanocapsules by an equal tip pressure, leading to a weaker indentation and a larger vertical particle dimension.

5.3.2.2 Further polyelectrolyte nanocapsules developed during screening

Further samples were topographically analysed by AFM regarding their shape, size, and height profile:

(i)	NC-OSA-CHI-CARR-8.6% (A)	(iii)	NC-OSA-CHI-GA-3.7% (C)
(ii)	NC-OSA-GEL-SBP-5.55% (B)	(iv)	NC-OSA-GEL-GA-5.625% (D)

The 2D-images of the left column of Figure 41 show representative capsules of each sample (A-D). The sample shown in row A (NC-OSA-CHI-CARR-8.6%) is almost identically composed like sample B of the consecutively prepared nanocapsules of Figure 40 (NC3-OSA-CHI-CARR-2.5%). They only differ in oil content. The shape and height profile are comparable. The size rose from 109 nm to 163 nm which, however, cannot be statistically proven. Higher viscosity of the sample with 8.6 % MCT is probably responsible for the larger size. Increasing the oil content from 2.5 % up to 8.6 % did not have a considerable impact on the nanocapsule topography.
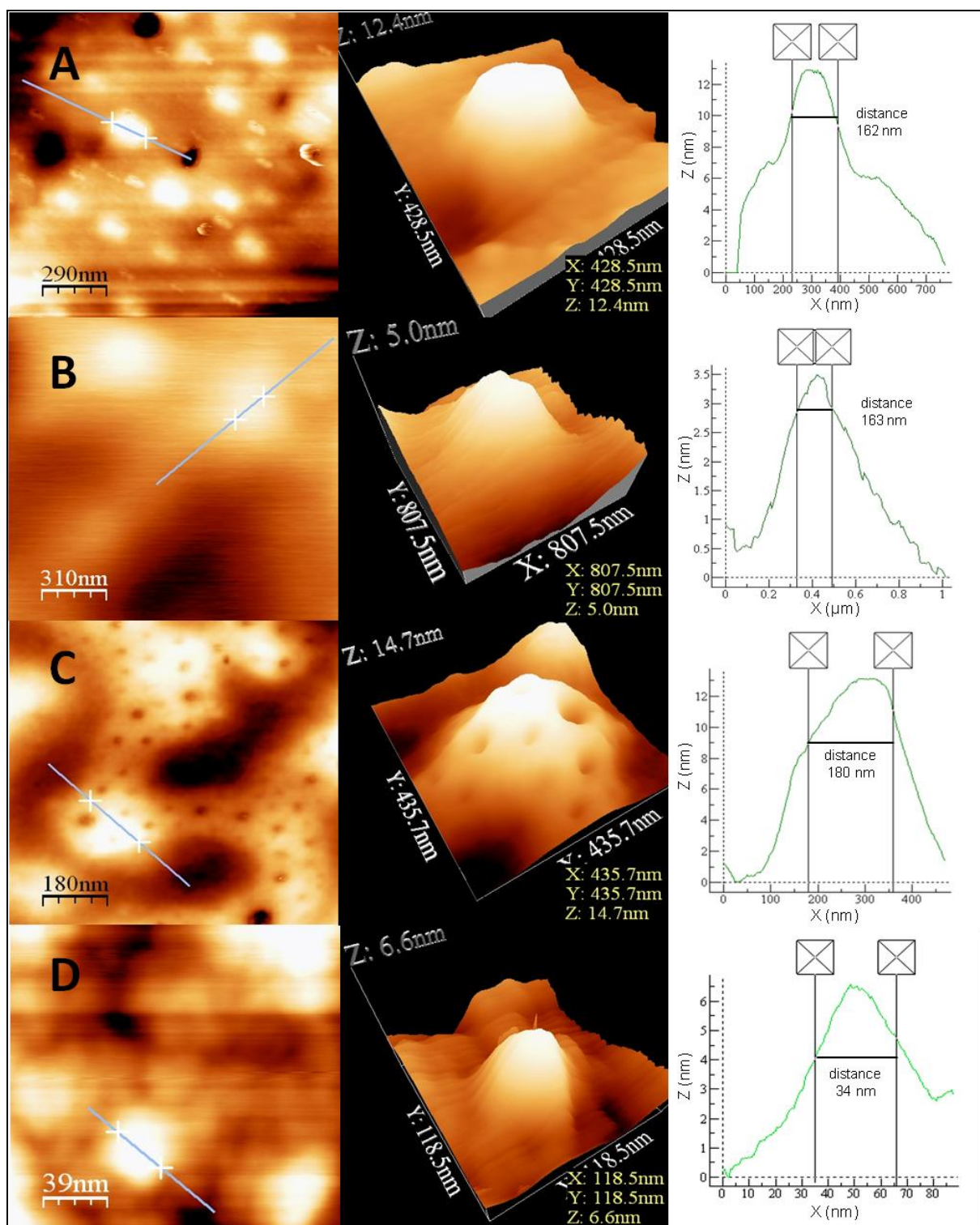
Figure 41 Topographic AFM images of further samples, <u>left column:</u> 2D-images (with height profile lines), <u>centre column:</u> 3D-images, <u>right column:</u> height profiles; <u>row A:</u> NC-OSA-CHI-CARR-8.6%, <u>row B:</u> NC-OSA-GEL-SBP-5.55%, <u>row C:</u> NC-OSA-CHI-GA-3.7%, and <u>row D:</u> NC-OSA-GEL-GA-5.625%

The sample shown in row B (NC-OSA-GEL-SBP-5.55%) contains gelatin as second shell layer. The moderate image quality is possibly due to a loss of most of the height information by the tip scanning. This might be an indication for a very flexible shell which could have developed because of presence of gelatin leading to a gel-like state in the shell. The shell seems to be softer than in non-gelatin-containing nanocapsules. Regarding the

size, the capsules appeared as large as sample A. A spherical shape can be assumed from the AFM pictures. Sample C (NC-OSA-CHI-GA-3.7%) is composed quite similar to sample A. Only in the external layer of the shell, carrageenan was replaced by gum arabic. The slight increase of the capsule size from 162 nm to 180 nm originates from the estimated selection of a capsule representing the average size, and is thus not of statistical significance. The height profiles of sample A and C behave quite identical, too. Hence concerning size, shape and shell rigidity the substitution of carrageenan by gum arabic did not have a huge impact. However, as the 2D and 3D images of sample C reflect, the capsule shell of NC-OSA-CHI-GA-3.7% features small pores.

They have not yet been observed in any other sample and cannot be explained only by the presence of gum arabic since sample D (NC-OSA-GEL-GA-5.625%) is covered by a gum arabic layer, too, but does not feature holes like pores on the surface. If gum arabic is responsible for these pore structures, then only in combination with chitosan. Likely chitosan and gum arabic formed a polyelectrolyte complex of strong electrostatic affinity to each other resulting in pore-like structures. Sample D whose shell contains gelatin, too, rather resembles sample B in terms of height profile. Thus both of the gelatin-containing samples seem to have a softer shell than those samples containing chitosan instead (height profile). The size shown for sample D (34 nm) is not representative for the whole sample as larger capsules with a size of about 1 micrometer were observed, too.

5.3.3 Summary and discussion

To summarize the results of size determination of the successfully prepared nanocapsule formulations, the obtained particle sizes of the corresponding methods used are collected in Table 13.

Table 13 Summary of size determination results by different methods (size in nm); TEM (cf. [222,223]) and AFM data (size range) estimated from images; n. d.: not determined; d. e. n. r.: data evaluation not reliable

sample name	z-av. (PCS)	d (0.5) (LD)	d (0.9) (LD)	main size (TEM)	average geom. diameter (AF4)	main size (AFM)
E-OSA5-5%	151	118	214	≈100 (60-135)	241.6	≈80 (50-180)
NC-OSA-CHI-CARR-2.5%	134	123	295	≈90 (70- 240)	287.6	≈110 (70-550)
NC-OSA-CHI-CARR-CHI-CARR-1.11%	145	131	288	≈80 (60-180)	251.8	≈120 (80-200)
NC-OSA-CHI-CARR-8.6%	161	160	2824	≈130 (90- 150)	292.4	≈120 (90-280)
NC-OSA-GEL-SBP-5.55%	358	242	493	≈140 (120 -280)	182.6	≈250 (170-390)
NC-OSA-CHI-GA-3.7%	185	122	196	≈90 (80-150)	242.8	≈145 (90-205)
NC-OSA-CHI-GA-7.4%	317	136	420	≈200 (100-200)	n. d.	n. d.
NC-OSA-GEL-GA-5.625%	233	122	215	≈200 (160-220)	d. e. n. r.	≈180 (34-1700)

It is worth mentioning that the use of the term 'nano'-capsules is justified since most particle size determination methods yielded an overall size (diameter) of far smaller than one micrometer for the majority of the developed samples. Especially the size of the emulsion template, which was used for the subsequent preparation of all of the nanocapsule samples, can reliably be described to be smaller than 250 nm since all applied size determination techniques gave size results between 80 nm (AFM) and 240 nm (AF4). In the majority of cases, imaging methods such as TEM and AFM produced smaller size results than the optical methods PCS, LD and AF4. This might be based on the procedure of these techniques. During sample preparation for TEM and AFM analysis larger droplets were possibly removed by washing and rinsing steps. However, the optical methods LD and AF4-MALS that detected emulsion droplet sizes of larger than 200 nm, usually yield larger size results which is based on the volume weighted data acquisition of the particle size. Since the light scattering of larger particles is much stronger than of smaller particles, volume-weighted methods such as LD automatically put the focus on larger particles because the signal intensity of very small particles will partly be neglected. Unlike LD and (AF4-)MALS, PCS is a method whose measuring principle is based on particle diffusion. As very small particles diffuse much faster than larger ones, this method can ideally detect the smallest particles. On the other hand, PCS detects not only the particle size but also its hydrate shell (hydrodynamic diameter). Hence, for a sample consisting of differently sized particles (wide distribution), every measuring principle preferably records a certain kind of species, leading to different size calculations.

It has to be concluded that based on the nature and the measuring principle of all mentioned particle size determination techniques it is hardly possible to obtain identical size results unless the investigated sample features a totally homogeneous and narrow size distribution. This was obviously not the case in most of the nanocapsule samples. Additionally, the size parameters given in Table 13 such as the d(0.9) value, the z-average, and the diameters observed in TEM, AFM or AF4 are just one aspect of the size. These values can only be identical for strongly spherical particles because a sphere is the only geometric shape that can be described just by one value, the diameter. The presence of some cylindrical or oval or other irregular shaped particles would not fit into the calculation models and would thereby lead to deviations. Besides the size parameters cannot easily be compared to each other as they do not always describe the same fraction of the size distribution curve and thus cannot yield equal overall sizes. The d(0.9) includes 90 % of the particles which are smaller than this value, while only ≈50 % of the corresponding particles are described by the d(0.5) value (LD) and the average diameters obtained from PCS, TEM, AF4 and AFM. Thus, the d(0.9) value has to be the largest characteristic size number, which was observed in most of the samples. Hence, the d(0.9) value represents supplemental information to describe the entirety of a sample. In conclusion, the different results of size determination should not be seen competitively but additionally in order to obtain a comprehensive idea of the prepared samples.

5.4 Stability of selected nanocapsules

5.4.1 Freeze-drying

The method had been applied exemplarily to the following samples:

(i)   NC-OSA-CHI-CARR-2.5% (NC3)   (ii)   NC-OSA-GEL-GA-5.625%

(containing 15 % (w/w) trehalose)   (without trehalose)

One gelatin containing sample was chosen because it showed gelation after preparation and cooling down. Thus, a comparison between a gelling and a non-gelling sample might be possible. The PCS size results of the samples before and after lyophilisation are shown in Table 14 and Figure 42. As a comparison to the lyophilisation effect, the samples were stored over 4 months at 2-8 °C and the size was monitored without lyophilisation, too. Immediately after preparation, sample NC3-OSA-CHI-CARR-2.5% showed smaller (z-average 168 nm) particles sizes than sample NC-OSA-GEL-GA-5.625% (z-average 286 nm). Both samples modified during the storage period of 4 months. Sample NC3-OSA-CHI-CARR-2.5% underwent a size increase (z-average 256 nm) and finally possessed a bimodal particle size distribution being described by two peaks of which one presented that around 50 % of the particles had grown to sizes larger than 1000 nm (Figure 42 top, green line). During storage of sample NC-OSA-GEL-GA-5.625% the particle size kept stable (Figure 42, bottom, z-average of 286 nm and 264 nm). A slight bimodality was observed, but all particles were nanoscaled. The good stability against cool storage can be explained by the state of the sample. While sample NC3-OSA-CHI-CARR-2.5% was liquid, sample NC-OSA-GEL-GA-5.625% had formed a gel due to the content of gelatin in the second layer of the capsule shell. Particles were immobilised by the gel lattice which reduced all possibilities of destabilisation such as aggregation, sedimentation or Ostwald ripening.

Table 14 Influence of lyophilisation on the particle size (PCS) of the investigated samples

sample name	z-average	PDI	diameter (nm) peak 1	% peak 1 (volume-weighted)	diameter (nm) peak 2	% peak 2 (volume-weighted)
NC3-OSA-CHI-CARR-2.5%-after-preparat.	168 nm	0.295	173 nm	100 %	-	-
NC3-OSA-CHI-CARR-2.5%-after-4-months	256 nm	0.410	254 nm	34 %	1830	65 %
NC3-OSA-CHI-CARR-2.5%-lyophilised	384 nm	0.636	680 nm	100 %	-	-
NC-OSA-GEL-GA-5.625%-after-preparat.	286 nm	0.256	54.4 nm	3 %	494 nm	96 %
NC-OSA-GEL-GA-5.625%-after-4-months	264 nm	0.249	64 nm	11 %	446 nm	88 %
NC-OSA-GEL-GA-5.625%-lyophilised	353 nm	0.343	532 nm	100 %	-	-
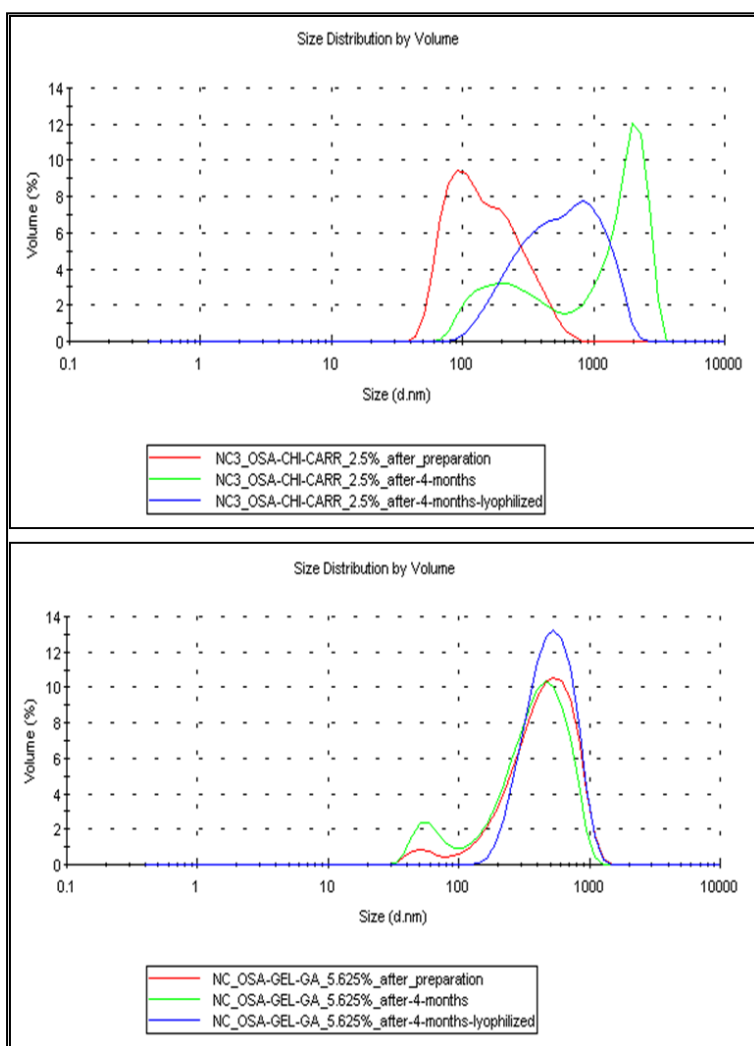
Figure 42 Size distribution by PCS. **Top:** **NC-OSA-CHI-CARR-2.5%;** **bottom:** **NC-OSA-GEL-GA-5.625%**

After 4 months of storage, the nanocapsules were freeze-dried. This treatment did not have a negative effect of the particle size and homogeneity of both samples. The bimodal size of sample NC3-OSA-CHI-CARR-2.5% (containing trehalose as cryoprotecting agent) converted into a more homogeneous but wide distribution (monomodal, z-average 384 nm) which indicates that the capsules possibly had aggregated before lyophilisation, and disaggregated during re-dissolution after lyophilisation. Sample NC-OSA-GEL-GA-5.625% (without trehalose) can be described by only one main peak before and after lyophilisation. The size distribution of this sample remained quite constant. The majority was smaller than 1 μm.

To summarise, the lyophilisation success strongly depends on the sample quality before treatment. The gelling sample behaved advantageously in comparison to the liquid sample. To prevent particle growth during storage, lyophilisation should be performed as early as possible after sample preparation. An influence of trehalose cannot be claimed.

5.4.2 Stability over autoclavation

Autoclavation was studied with the following promising samples:

(i)   NC-OSA-CHI-CARR-2.5% (= NC3)   (iii)   NC-OSA-CHI-GA-2%

(ii)   NC-OSA-GEL-SBP-2.68%   (iv)   NC-OSA-GEL-GA-3%

After autoclaving, the size of the samples was measured with LD and the d(0.9) values before and after treatment were compared. The results are illustrated in Figure 43. For all investigated systems, the d(0.9) value was smaller than 0.6 µm before treatment. The autoclaved samples (3) NC-OSA-CHI-GA-2% and (4) NC-OSA-GEL-GA-3% showed no change in particle size, whereas capsules prepared of (1) NC-OSA-CHI-CARR-2.5% and (2) NC-OSA-GEL-SBP-2.68% showed a moderate (1) to extreme (2) increase in particle size. In conclusion, autoclaving was an adequate germ reduction method for all nanocapsule systems except of (2) NC-OSA-GEL-SBP-2.68% which was not physically robust over autoclaving. This may be explained by increased electrostatic interaction between the protein structure of gelatin and the pectin induced by the high temperature and pressure. However, investigation of the chemical stability of the samples was not covered by this experiment. Due to the protein structure of gelatin, a thermal degradation of this shell component of NC-OSA-GEL-SBP-2.68% has to be considered which might have led to the destruction of the capsules.
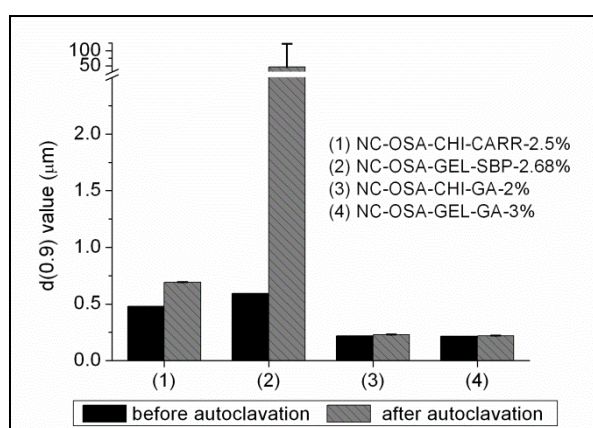
Figure 43 Nanocapsule size (d(0.9) value obtained from LD) before and after autoclavation of selected nanocapsules

5.4.3 Isostatic high pressure

The sample NC-OSA-CHI-CARR-2.5% was treated with isostatic high pressure. The effect of different pressure treatments on the nanocapsule is given in Figure 44. The initial size (nm) and PDI (before high pressure treatment) was set to 100 %. Figure 44A illustrates that low pressures between 200 and 400 MPa did not influence the particle size widely. The size ranged between 98 % and 104 % compared to the initial z-average. The pressurising time (10 min, 30 min or 6x5 min) had no impact on the size result.
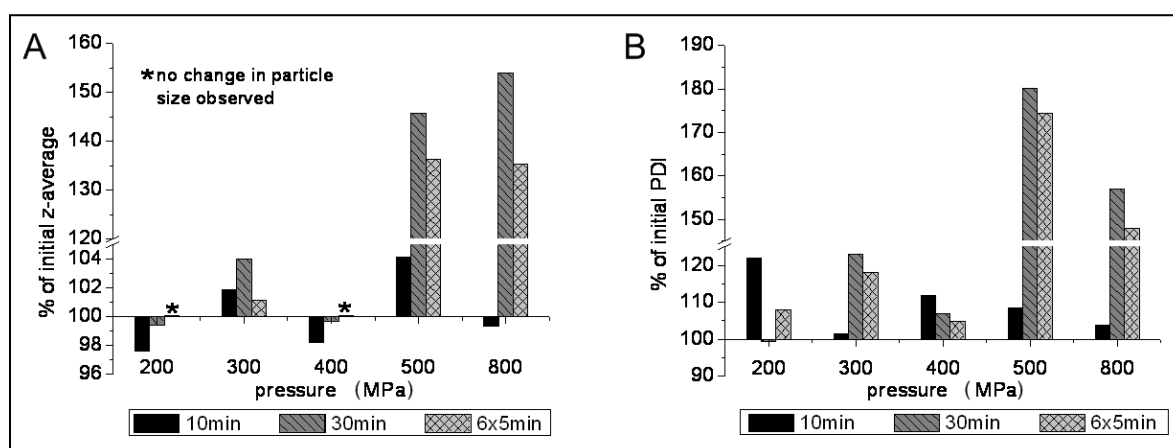
Figure 44 Effect of isostatic high pressure on A: the size, and B: the PDI of the sample NC-OSA-CHI-CARR-2.5%

However, larger pressures of 500 or 800 MPa induced a sudden rise of the particle size of up to 50 % in case of 30 min and 6x5 min pressurising. Large pressure was tolerated by the sample only for a period of 10 min or less. Regarding the homogeneity (expressed by the PDI in Figure 44B), the PDI correlated with the described particle growth. Large pressure (>500 MPa) for 30 min or 6x5 min led to a considerable increase of the PDI. In contrast, the PDI increase compared to the initial value was not larger than 22 % in case of low pressure values from 200 to 400 MPa independent of the time, and in case of high pressure combined with short pressurising time of 10 min, respectively. In conclusion, a pressure of 500 MPa or higher led to larger and less homogeneous particles in the formulation. Possibly the compression of the sample by large pressure made the particles tending to aggregation, which counteracts the electrostatic repulsion of equal surface charges. Potentially the Lennard-Jones-potential reached a minimum distance value between neighboured particles leading to irreversible attraction thereof. The combination of high pressure and longer pressurising time might had prolonged the period in which temperatures around 50 °C (maximum tolerated temperature) had occured and thereby destabilised the sample because the electrostaticcally stabilised capsule shell assembly was disturbed. However, integrity of the nanocapsule shell and stable particles sizes were observed applying low pressures from 200 to 400 MPa over a period of up to 30 minutes. The results allow the statement that the investigated nanocapsules might effectively be treated with isostatic high pressure for germ reduction purposes.

5.4.4 Temperature stability

The influence of an isothermal temperature scan at 37 °C on the ultrasound velocity U, reflecting the stability at physiological temperature (Figure 45A), was studied on the following consecutive samples:

(i)   E-OSA5-5% (PE)   (iii)   NC-OSA-CHI-CARR-CHI-CARR-1.11% (NC5)

(ii)   NC-OSA-CHI-CARR-2.5% (NC3)
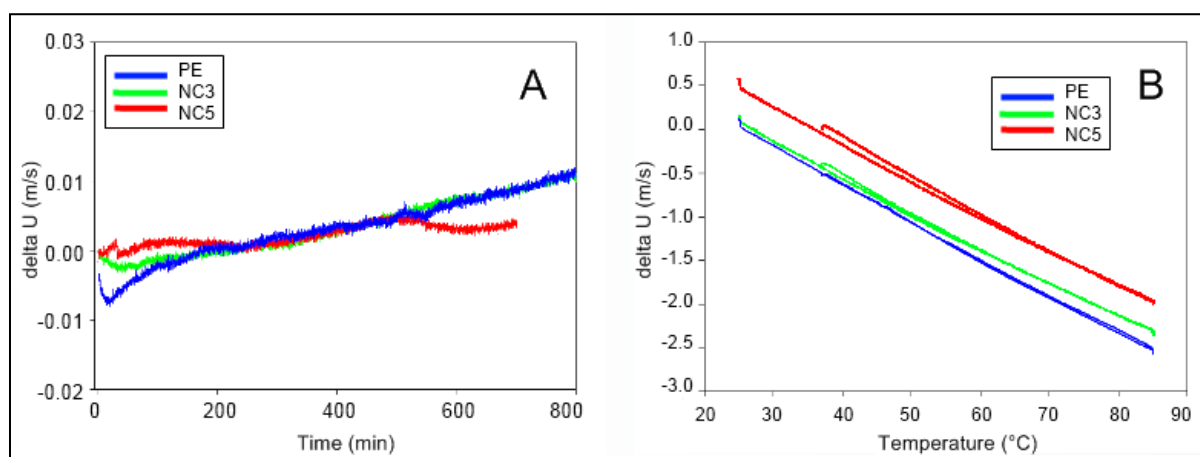
Figure 45 Changes in the ultrasound velocity U during URT. A: isothermal scan at 37 °C over 12 hours, B: temperature scan from 25 °C to 85 °C and vice versa (PE = E-OSA5-5%; NC3 = NC-OSA-CHI-CARR-2.5%; NC5 = NC-OSA-CHI-CARR- CHI-CARR-1.11%)

No significant changes of the signal over 12 hours were observed for the three consecutively prepared and investigated samples. Instrument instability is probably responsible for the slight drift over time. The relatively constant ultrasound velocity at 37 °C reflects that the samples are probably stable under physiological

conditions for at least 12 hours after application. As apparent from Figure 45B, small changes in ultrasound velocity were detectable over the applied temperature range. The two curves of heating (from 25 °C to 85 °C) and cooling (from 85 °C to 40 °C) of each sample showed only a small hysteresis area which indicates that probably no changes in the emulsion and nanocapsule assembly had occurred. In conclusion, the samples are obviously resistant over a large scale of temperature for several hours.

5.4.5 Summary and discussion

The aim of the past section was to investigate the stability of selected nanocapsule samples by different methods. Lyophilisation appeared to have no negative impact on the homogeneity (kept constant or improved) of the nanocapsule samples investigated. Moreover, the lyophilisation success depended on the original sample quality. The gelling sample was better capable of stabilising its size over a period of 4 months than the liquid sample. This phenomenon can be explained by immobilised particles in the gel lattice and thus reduction of aggregation, sedimentation or Ostwald ripening. The presented liquid nanocapsule dispersion NC-OSA-CHI-CARR-2.5% did not show good long-term stability concerning particle size. The electrostatic repulsive forces achieved by the ζ-potential of approximately -30 mV were apparently not sufficient to stabilise polyelectrolyte nanocapsule dispersions over a long period of time. In consequence, storage-induced particle growth in liquid samples can potentially be prevented by early lyophilisation after sample preparation in future.

Autoclaving was an adequate germ reduction method for all investigated nanocapsule systems except of NC-OSA-GEL-SBP-2.68% which was not robust over autoclaving. This may be explained by increased electrostatic interaction between the protein structure of gelatin and the pectin induced by the high temperature and pressure. However, most of the samples showed a stable particle size in spite of the drastic treatment. Autoclavation is hence a method that should be considered as an alternative to chemical preservation.

Additionally isostatic high pressure was examined in terms of qualification for germ reduction for sample NC-OSA-CHI-CARR-2.5%. A pressure of 500 MPa or higher led to larger and less homogeneous particles in the formulation. Especially the combination of high pressure (> 500 MPa) with long pressurising time (30 min) and temperatures around 50 °C (maximum tolerated temperature) destabilised the samples because the electrostatic interactions were disturbed. However, integrity of the nanocapsule shell and stable particles sizes were observed applying lower pressures from 200 to 400 MPa over a period of up to 30 minutes while the PDI showed only moderate increase. Hence, the electrostaticcally stabilised capsule shell was mainly robust over these mild pressurising conditions.

The stable ultrasound velocity at 37 °C observed by isothermal URT reflected a good stability of the three consecutively prepared samples under physiological conditions for at least 12 hours after potential application. During the phases of heating and cooling between ambient temperature and 85 °C, the samples showed only a small hysteresis area which indicates that probably no changes in the emulsion and nanocapsule assembly had occurred. In conclusion, the samples are obviously resistant over a wide scale of temperature for several hours.

5.5 Light protection capability of the capsule wall

5.5.1 Fluorescence spectroscopy and fluorescence imaging

The following consecutively prepared samples were investigated:

(i)   pure MCT   (iii)   NC-OSA-CHI-CARR-2.5% (= NC3)

(ii)   E-OSA5-5% (PE)   (iv)   NC-OSA-CHI-CARR-CHI-CARR-1.11% (NC5)

As apparent from Figure 46 and Figure 47, pure MCT showed the highest light intensity both in fluorescence spectroscopy and fluorescence imaging. Emulsifying the oil (primary emulsion template, PE) led to strongly reduced fluorescence intensity. This can be explained by dispersion of the oil in water forming nanometre scaled droplets in an opaque emulsion which is not as transparent for visible light as clear oil due to refraction of light at the droplet surface. The nanocapsules emitted even less fluorescence light than the emulsion which is highlighted by the magnification in Figure 46 (right). Besides, the nanocapsule samples NC3 and NC5 differ in their intensity, as well. By increasing the number of shell layers around the MCT core from one layer (PE) to three (NC3) and five layers (NC5), the fluorescence intensity could be reduced further. That means the thicker the capsule shell was the less excitation and emission light could pass through it.
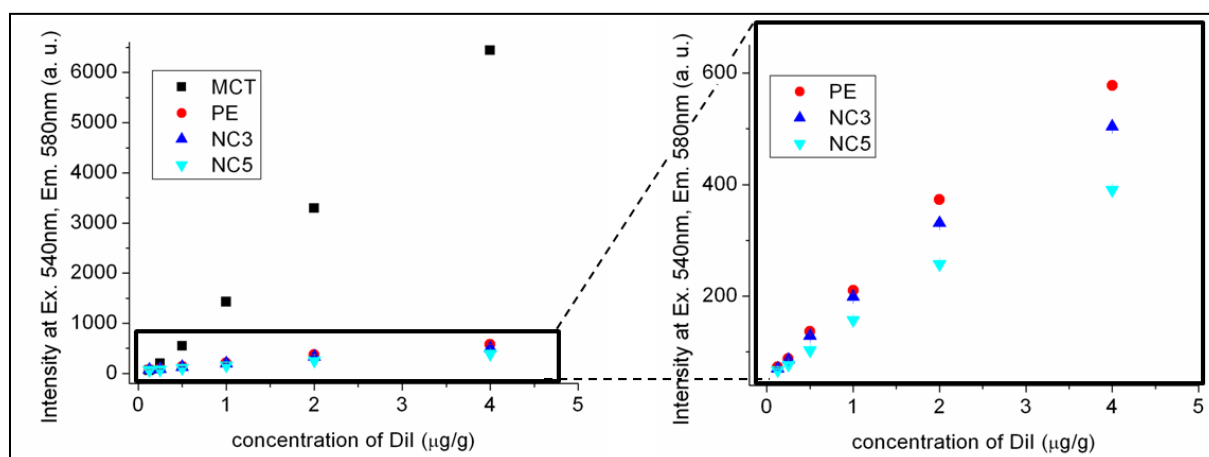
Figure 46 Fluorescence spectroscopy intensity of DiI-labelled samples with concentrations of 0.125 to 4 µg/g; PE: E-OSA5-5%, NC3: NC-OSA-CHI-CARR-2.5%, NC5: NC-OSA-CHI-CARR-CHI-CARR-1.11%

The same result was obtained applying fluorescence imaging (Figure 47). However, this technique was not ideal for fine quantification issues since neighboured samples in the well plate might have influenced each other in light intensity, and equal illumination of each well could not be ensured. Thus, NC3 and NC5 could hardly be distinguished by their intensity. Nevertheless, both nanocpasule samples showed less fluorescence emission compared to the emulsion template.

In conclusion, both experiments showed that the capsules are better capable of protecting the incorporated dye DiI from light excitation than the emulsion, which is a potent hint for the thicker capsule wall to be responsible for that. Thus, for photosensitive drugs nanocapsules present a more protective and hence preferable dosage form than emulsions do.
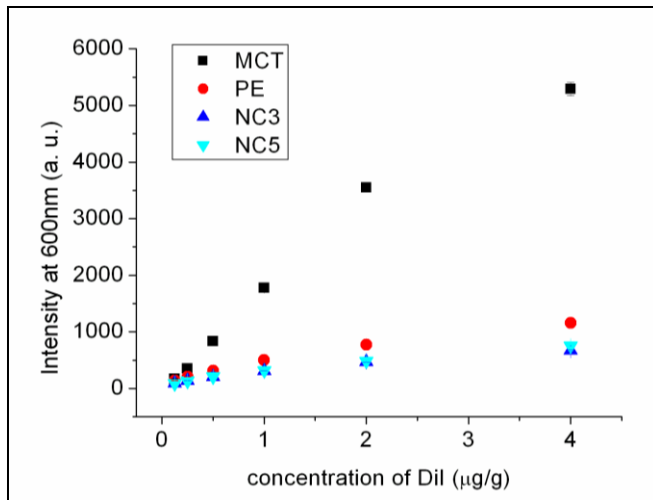
Figure 47 Fluorescence imaging intensity of DiI-labelled samples (concentration series from 0.125 to 4 µg/g)

5.6   Mechanical properties of the nanocapsules

5.6.1   [1]H nuclear magnetic resonance spectroscopy

The proton NMR spectra of the primary nanoemulsion E-OSA5-5% and the nanocapsules NC-OSA-CHI-CARR-2.5% (NC3) (Figure 48A) show typical peaks of the solvent (*, water H_2O-d_1) at 4.6 ppm, of MCT (peaks a–f) [24] as well as of acetate (α).
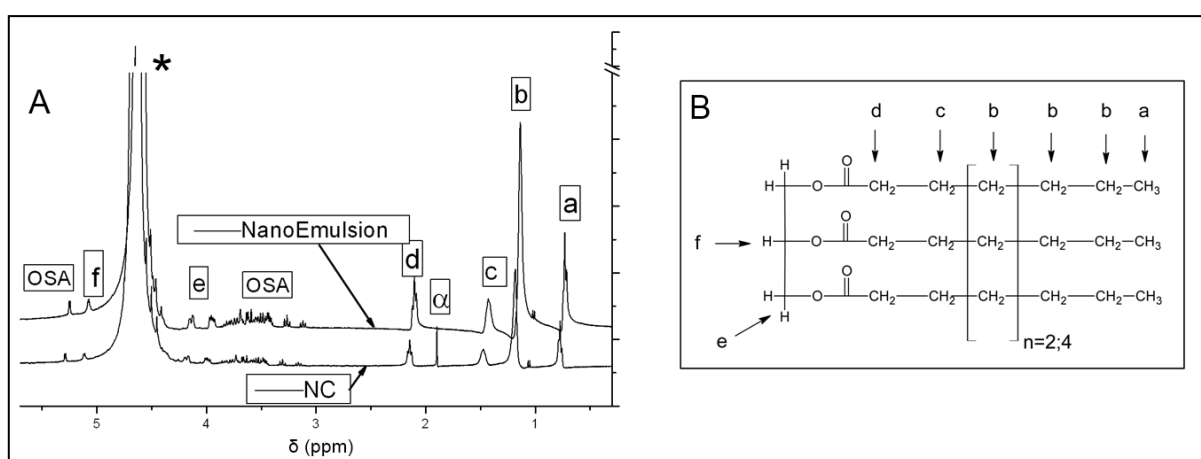

Figure 48 <u>A:</u> **NMR spectra of the emulsion E-OSA5-5% and nanocapsules NC3-OSA-CHI-CARR-2.5% (NC) dissolved in H_2O-d_1 (*), <u>B:</u> Structure of MCT with corresponding assignment of the ^{1}H NMR signals**

The sharp signals a, b, c, d, as well as peaks e and f occur from different protons of MCT (cf. Figure 48B). The chemical shift δ of the MCT methyl and methylene protons (a = -CH_3: 0.7 ppm, and b = -CH_2-: 1.2 ppm) are typical for alkyl chains of triglycerides. Protons located near or at the glycerol part of the lipid (signals c and d) have higher ppm values (1.4 and 2.2). MCT can be specified as bulk oil in the capsules with the same properties as emulsified oil because the line widths at half the signal height (nanocapsules: 0.036 ppm, nanoemulsion: 0.034 ppm, for MCT signal b) and the relation of the single peak integrals are almost identical. As expected, the nanoemulsion shows narrow signals in the aliphatic region, a result that is consistent with the liquid state of its oily core. Aliphatic groups with highly mobile chains in the liquid state (narrow signals) are also observed in the nanocapsules spectrum, which indicates that the capsules indeed feature a liquid core [245].

The alkyl chains of OSA starch might overlap with a, b, c, and d of MCT. However, only the areas between 3.0 and 3.8 ppm and the peak at 5.3 ppm are exclusively induced by the glucose protons of OSA. Signal α (1.9 ppm) can be assigned to acetate, which was the counterion to chitosan in the stock solution. If one compares the NMR signals from the nanoemulsion and the nanocapsules, differences are hardly visible. Signal α is the only characteristic that allows a differentiation. Its presence in the nanocapsule spectrum is an indication that chitosan (dissolved in acetate buffer) was added to the nanoemulsion, but it is not an evidence for complexation and immobilisation (solidification) of the polyelectrolyte by integration into the capsule wall. However, the assembly of chitosan in the capsule shell can be concluded from the zeta potential which changed into a positive charge after adding chitosan. Besides, no precipitating aggregates occurred during centrifugation. The absence of further signals of chitosan and carrageenan could have several reasons. One

aspect is their low concentration. Moreover, it might be interpreted as a solid state of chitosan and carrageenan in the shell since only mobile ingredients are detected under the experimental conditions [24]. In this case, missing lines can be explained by the fact that NMR spectra of associated macromolecular aggregates exhibit broad unresolved lines [108,246]. This is due to the inherent anisotropy of nuclear interactions, which are dependent on the orientation and conformation of the molecule with respect to the magnetic field direction. Whereas in solution fast molecular tumbling ensures isotropic averaging of the nuclear interactions, the relaxation times of molecules associated in complexes are slow. As a consequence, the anisotropic properties of these interactions are reflected in the broad NMR line shapes of immobilised molecules. In such spectra the signals that arise from different sites tend to overlap and remain largely unresolved [246]. However, even the ^{1}H NMR spectra of the pure polymer solutions were very difficult to detect under the experimental conditions because of the large ^{1}H NMR line widths deriving from their restricted mobility (induced by high viscosity or gelation). Thus, the immobilisation of chitosan and carrageenan and solidification by complex coacervation could not be proven unequivocally by missing NMR signals. It can only be assumed that signals were missing (i) in pure polyelectrolyte solutions due to immobilisation because of high viscosity, and (ii) in the nanocapsule dispersion due to immobilisation caused by complex coacervation. For further information about the nanocapsule shell rigidity, AFM and URT studies were carried out.

5.6.2 Atomic force microscopy: force-curve analysis

Unfortunately, NMR was not feasible to demonstrate whether complex coacervation of the polyelectrolytes forming the nanocapsule shell led to a solid state of the capsule wall. The absence of NMR signals could not reliably be interpreted as solid state of the hydrocolloids because other reasons mentioned above might be responsible for missing signals. Therefore atomic force microscopy (AFM) was utilised as a futher technique for the investigation of mechanical properties of the nanocapsule wall. Information on the mechanical properties of natural and artificial, flat or otherwise shaped samples can be delivered by AFM in the force-volume mode [228]. The force-volume images of the three consecutively prepared samples (abbreviations PE, NC3, NC5 used)

(i)   E-OSA5-5% (PE)   (iii)   NC-OSA-CHI-CARR-CHI-CARR-1.11% (NC5)

(ii) NC-OSA-CHI-CARR-2.5% (NC3)

obtained in humid environment were gathered and are shown in Figure 49 (left column). The bright areas represent hills generated by the existence of droplets or capsules. The resolution and image quality is poor due to the scanning conditions in contact mode. That is why they were not useful for topographic images but for force-curve analysis. There are only few capsules visible because they are spherical and therefore had only small contact area and weak adhesion forces to the mica surface. Twelve positions of droplets or capsules in the force-volume images were chosen and their approaching force-curves were gathered, averaged and plotted in force-distance graphs (see Figure 49, right column). The more the tip approached the sample surface (z-position decreases moving from right to left), the stronger the interaction forces got, and tip and sample got into contact. In the sloped left part of the graphs the tip touched the sample and the cantilever deflection was proportional to the loading force and the sample height [247]. The slope of the force-distance curve in the contact region is a measure of the stiffness of the sample [82,228,248,249].
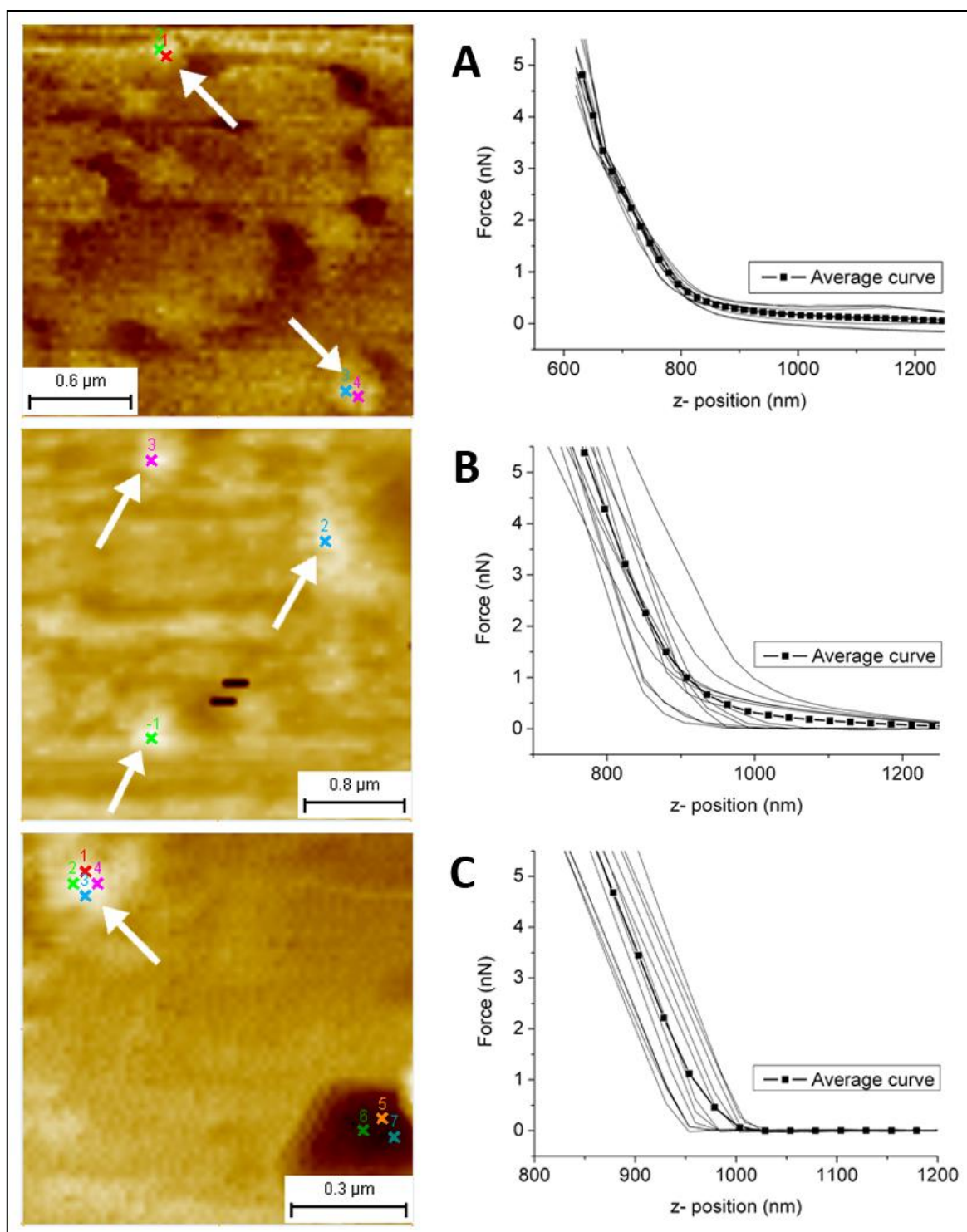
Figure 49 <u>Left column:</u> **AFM force-volume images generated in contact mode, arrows show particles used for force curve analysis;** <u>Right column:</u> **12 force-distance curves (approaching part) and average curve;** <u>A:</u> **PE (E-OSA5-5%);** <u>B:</u> **NC3 (NC-OSA-CHI-CARR-2.5%);** <u>C:</u> **NC5 (NC-OSA-CHI-CARR-CHI-CARR-1.11%).**

In order to compare the hardness of the three samples by the slope, the averaged force-distance curves including the curve for pure mica were plotted in one diagram (Figure 50A). Emulsion and both nanocapsule samples showed a milder slope than pure mica which indicates the three samples to be softer. Furthermore, the graph shows a steeper slope for those samples with an increased number of layers (PE < NC3 < NC5) surrounding the oily core. This allows for the conclusion that the polyelectrolyte nanocapsules based on a

nanoemulsion feature a stiffer and thus mechanically more resistant shell, the more layers the shell is composed of. Absolute values for the slope of the samples are given in Figure 52A.
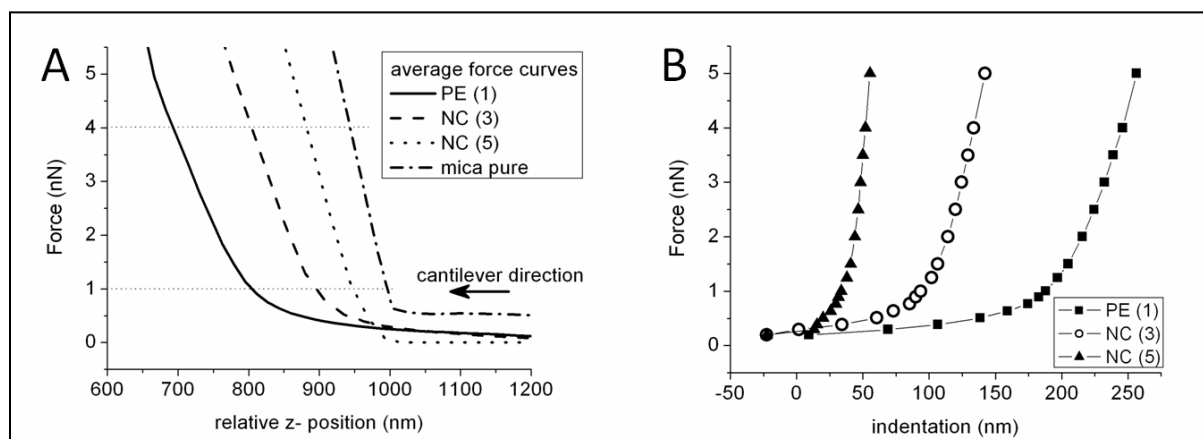
Figure 50 Comparison of <u>A:</u> force-distance curves, and <u>B:</u> force-indentation curves of: PE(1) = E-OSA5-5%, NC(3): NC3-OSA-CHI-CARR-2.5%, and NC(5): NC5-OSA-CHI-CARR-CHI-CARR-1.11%.

Furthermore, the results become clear by plotting them in a force-indentation graph (Figure 50B). It was obtained by recording the applied load on the tip, which is used as an indenter, with the corresponding penetration depth of the tip. Nanoindentation by AFM is done by moving the sample towards the cantilever tip with a constant velocity. Upon contact, indentation starts and the cantilever bends while applying a load. Due to this mechanism, the indentation is neither load controlled nor piezo-displacement controlled. Although penetration depth can be obtained as mentioned above, the rate at which this happens cannot be influenced but simply depends on the material [250]. The contact point of tip and sample, which is the estimated point of transition from horizontal into sloped region [247,248], was each adapted to the same z-position of ≈1000 nm for determination of the indentation (see Figure 50A). Identification of the exact point of contact between the AFM tip and the sample is a large source of error in estimating mechanical properties from indentation tests. On stiff samples, the contact point is detected readily as a discontinuity in the slope (cf. mica). However, this often is ineffective when applied to indentations on soft samples because the transition from pre-contact to post-contact is smooth and amounts a quite wide range instead of a distinctive point [248]. For this reason, the indentation depth can only be estimated and shall serve for relative comparison but not as absolute values.

The difference between the deflection of the cantilever detected on the hard and soft material (marked with arrows in Figure 50A) describes the deformation of the soft sample under the tip load, i.e. how much the tip indents the sample [251,252]. Plotting the applied force against the obtained indentation gives force-versus-indentation curves. For calculating the indentation it is important to use the approaching part of the force curve since the use of the retracting part might lead to wrong results due to adhesive and capillary forces [252]. The load on the tip was applied through a bending cantilever, which is usually not stiff enough to indent metals or ceramic materials or mica. For this reason, AFM nanoindentation is mainly useful to measure mechanical properties of soft matter, especially biological materials and polymers [250], which can be deformed more easily than hard surfaces.

In Figure 50B the confident contact point is situated in the beginning of the steep rise of force near 1 nN. Consequentially, the indentations for the five- and three-layered nanocapsules as well as the nanoemulsion can be estimated to be 20 nm, 40 nm, and 60 nm for the identical loading force range between 1 nN and 4 nN (cf. Figure 51). For soft particles sized from 100 nm and 300 nm, and consisting of an oily core that makes up the majority of the whole particle, an indentation of 20 nm to 60 nm seems to be a reasonable distance. A significant capsule size dependence of the indentation could not be observed. Burnham and Colton investigated elastomers and graphite and found penetration depths of 450 nm and 85 nm [251], respectively, displaying indentations in the same order of magnitude. The presented indentation experiment confirms the statement made from the differences in the force–distance curve slope, namely that the capsules with a multilayered shell behaved more robust against mechanical exposure than the nanoemulsion droplets did due to smaller indentation depth.
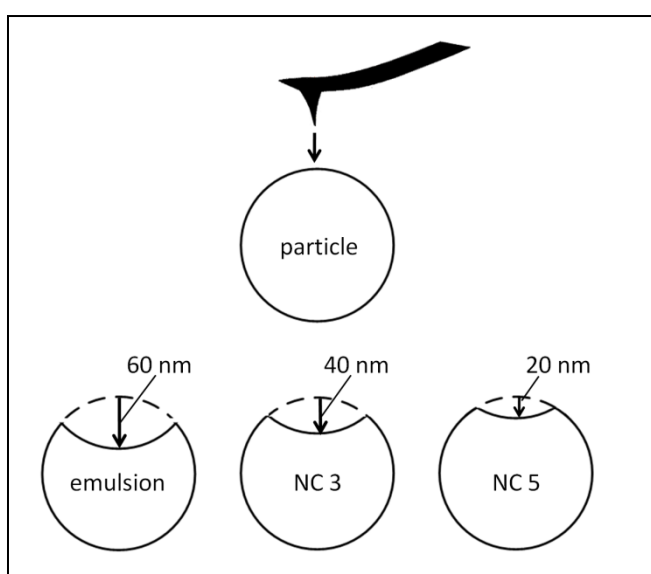
Figure 51 Resulting indentation depth of the AFM tip into consecutively prepared samples with different shell composition. Emulsion = PE (1): E-OSA5-5%, NC3: NC-OSA-CHI-CARR-2.5%, NC5: NC5-OSA-CHI-CARR-CHI-CARR-1.11%.

In order to support this result, similar sized nanoscaled systems were investigated concerning the stiffness by means of AFM force-curve analysis. Therefore, PEG-PLA-10% nanocapsules were prepared as described by Rübe [14]. PEG-PLA-10% nanocapsules and a commercially available phospholipid-stabilised parenteral fat emulsion (parentFE) served as comparison examples for the polyelectrolyte nanocapsules and the prepared primary nanoemulsion. The slope of their force-distance curves is given in the bar plots in Figure 52B and C.
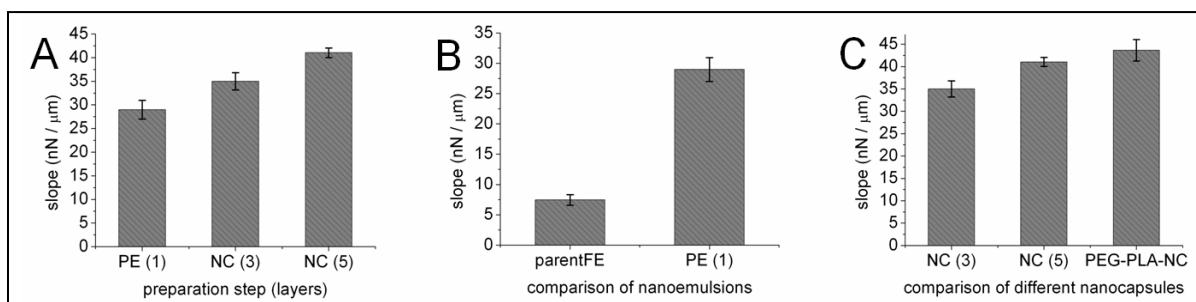
Figure 52 Comparison of absolute slope ± s.d. of AFM approach force-distance curves of different samples

Figure 52A shows the raising slope and shell stiffness with increasing number of polyelectrolyte layers surrounding the oily capsule core. Investigation of a further emulsion (parentFE) results in a much lower slope and stiffness than found for the template E-OSA5-5% (PE) of the polyelectrolyte NCs (Figure 52B). Figure 52C illustrates the varying stiffness (slope) of NCs prepared by different methods. The polyelectrolyte NCs (NC3, NC5) showed a softer shell than the PEG-PLA-10% NCs although they consisted of more layers around the core. Obviously, the interfacial polymer deposition after solvent displacement method by Fessi et al. [46] yields a more rigid shell than the injection and coacervation of oppositely charged polyelectrolytes. Despite, the three capsule formulations did not show large differences in their mechanical properties. It could rather be shown that differences in the hardness between nanoemulsions (slope < 30 nN/μm) and nanocapsules (35 nN/μm < slope < 45 nN/μm) are easily and reliably detectable. In summary, AFM force curve analysis demonstrated a suitable technique to distinguish nanocapsules from nanoemulsions by mechanical properties, an outcome that was still outstanding until now. Besides, the increasing solidity of the polyelectrolyte NCs shell detected by AFM proved the assembly of a solid shell by complex coacervation between OSA, CHI, and CARR.

5.6.3 Ultrasonic resonator technology

The ultrasound velocity of the aqueous liquid samples amounted around 1500 m/s as expected (see section 4.5.3.2, p. 47). Comparison of absolute velocities showed that ultrasound propagation increased with increasing number of shell layers (Figure 53A) for all dilution degrees.
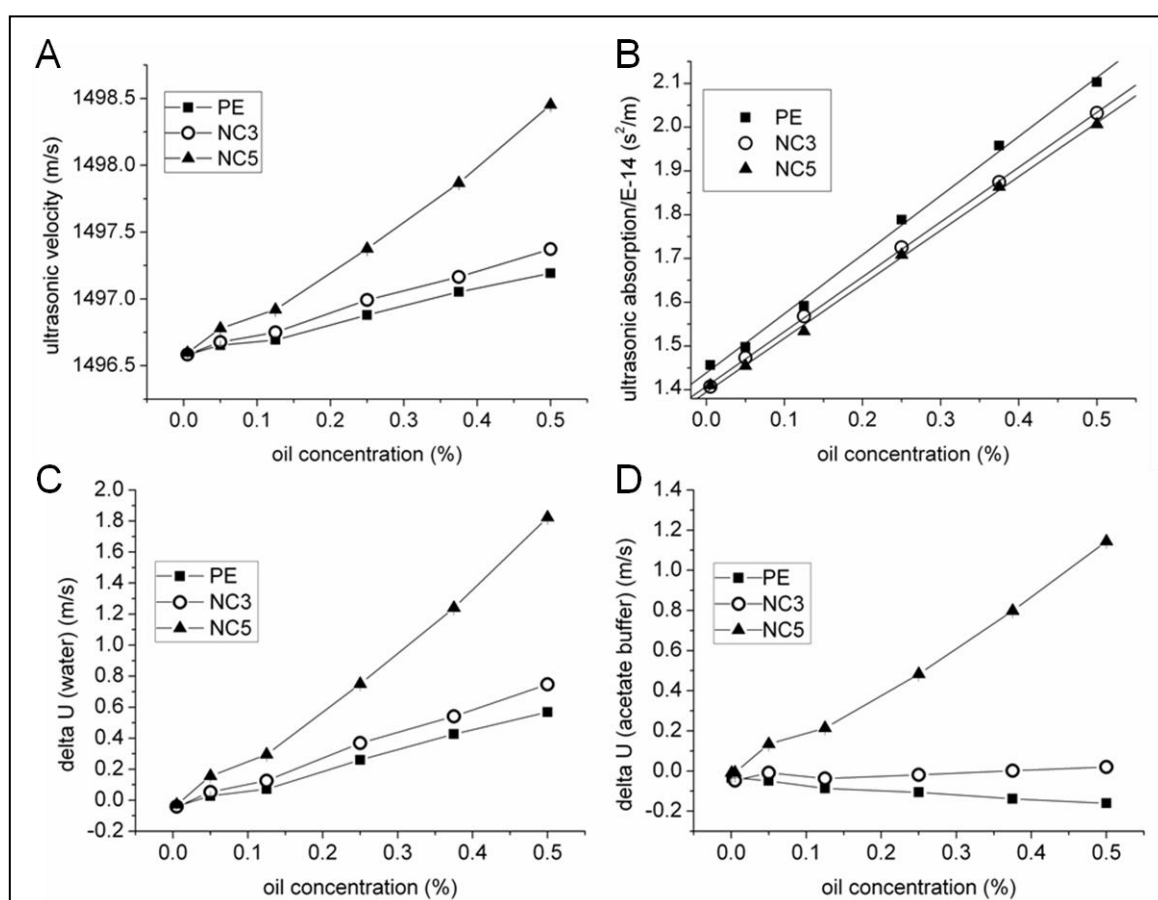
Figure 53 <u>A:</u> Absolute ultrasonic velocity and <u>B:</u> absorption of the three samples; <u>C:</u> relative ultrasonic velocity referring to water, and <u>D:</u> referring to acetate buffer (in corresponding concentration)

The difference between three and five polyelectrolyte layers was much larger than between three and one layer. Since the samples were each adapted to equal oil and buffer concentration, it is thus proposed that the mechanical properties of the shell have a great impact on the sound propagation differences. The relative velocity delta U (water) (obtained by subtracting the propagation velocity in double-distilled water from that in the samples, Figure 53C) showed no significant changes compared with the graphs of the absolute velocity U of the samples (Figure 53A) except on the y-axis. This is because water showed a slower velocity than all of the three samples. The reasonable conclusion is that the influence of the solvent water on the result is neglectible. Larger distinctions were drawn by plotting the relative velocity delta U (acetate buffer) (Figure 53D), obtained by subtracting the propagation velocity of acetate buffer from that of the samples. Again, the samples showed large deviations in the ultrasound velocity. But only the primary nanoemulsion showed a slower velocity than the corresponding acetate buffer concentration, visible due to the decay of the emulsion curve into negative delta U values with increasing oil content, in contrast to both nanocapsule formulations. In case of the emulsion, the ultrasound velocity, reduced by the acetate buffer effect, even decreased with rising oil content. This is not surprising since it reflects typical behaviour of emulsions [231] due to a high ultrasonic absorption rate for lipophilic substances (Figure 53B). All the more the question comes up, why the nanocapsules did not show this typical behaviour although they featured the same oil concentration like the emulsion. It can be explained by the only distinction between capsules and an emulsion droplet: they possess a solid shell instead of an emulsion interface. In suspensions, this property yields a higher stiffness and thereby increases the sound velocity in case of equal mean density [117]. For the density of the three samples (determined at an oil content of 0.5 % (v/v)), no significant differences were detected (0.9987 to 0.9990 g/cm^3). As seen for both nanocapsule formulations, the influence of the stiffness (increasing the velocity) did not only superimpose the absorbing effect of higher oil content (decreasing the velocity), it even outweighed it. This effect of reduced ultrasonic absorption compared to the emulsion was again stronger visible for the five-layered nanocapsules than for the three-layered nanocapsules (Figure 53D), supporting the theory of a benefit in stiffness with increasing layers. As illustrated in Figure 54, free polyelectrolyte (A) or acetate (B) molecules increased the ultrasound velocity.
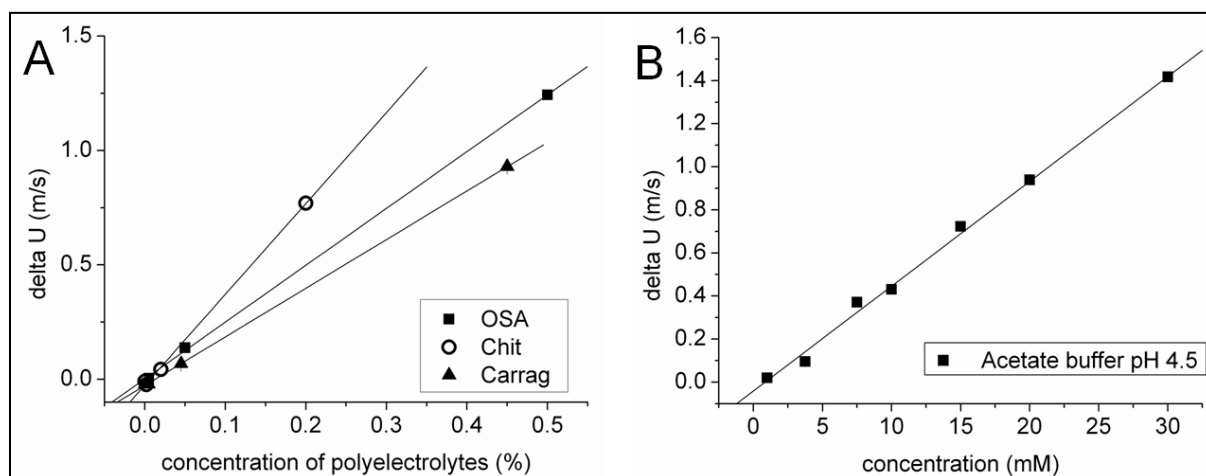

Figure 54 Impact of A: solute polyelectrolytes, and B: acetate buffer molecules on the sound velocity

For this reason, it had been important to adapt the samples on equal acetate concentration very precisely since a deviation of ±1 mM would make it hard to pinpoint ultrasound differences between the primary nanoemulsion and the three-layered nanocapsules. An effect of dissolved polyelectrolyte molecules can be excluded since free molecules would have formed aggregates showing sedimentation during centrifugation.

5.6.4 Summary and discussion

The investigation of the mechanical properties of the nanocapsules and of their emulsion template, respectively, yielded that the composition of the shell surrounding the MCT core evidently influenced the particle rigidity. By means of NMR spectra it could be concluded that the oily core phase (MCT) possessed identical properties to bulk oil. The core of the investigated emulsion and the nanocapsules featured liquid properties in spite of the submicron particle size. However, from NMR spectra no confident conclusions about the state of the polyelectrolyte shell formed by complex coacervation could be stated.

Despite, AFM force-curve analysis could be successfully applied to nanocapsules by stiffness investigation. The AFM results were supported by URT measurements. Both methods were first-time applied on nanocapsules and proved the transformation of an emulsion into a solid capsule wall with an increasing number of layers which contributes to the understanding of the presented preparation process. Moreover, AFM could be utilised to distinguish between nanoemulsions and nanocapsules by mechanical properties. This method can be operated independently of parameters such as oil or salt concentration whereas URT is very sensitive to salt molecules. However, as all influencing parameters had been eliminated before URT measurements, the different propagation velocities of ultrasound of the investigated samples can only be explained by the different shell composition. Besides, URT enabled a very fast data acquisition compared to AFM. By transformation of emulsion droplets into polyelectrolyte nanocapsules with a shell composed of three or five layers, a higher stiffness of the wall with increasing number of shell layers could be observed using AFM and URT. Both techniques yielded concurrent results and might be feasible for a stiffness correlation plot (slope of approaching force-distance curve of AFM versus the relative ultrasonic velocity corrected by acetate buffer velocity obtained from URT). The increase in stiffness of the wall is furthermore an evidence for the solidifying of the deposited oppositely charged polyelectrolytes by complex coacervation. Thus, the ζ-potential inversion after each layer is a strong hint for the assembly of the corresponding polyelectrolyte into the capsule shell. TEM allowed calculating the shell thickness to be approximately 3-10 nm. Thus, one can conclude that nanocapsules possess a higher rigidity and thereby higher stability referring to coalescence and improved capability of prolonging drug release compared to emulsions. The stiffer capsule wall compared to emulsion droplets might be advantageous during storage and intravenous application due to better mechanical resistance.

5.7 Release behaviour of the nanocapsules

5.7.1 Dialysis bag experiments

This experiment was conducted exemplarily for sample NC-OSA-CHI-CARR-2.5%. Figure 55 displays the fluorescence intensity of the MCT filled dialysis bag by time. The increase of intensity reflects a migration of the model drugs nile red and DiI from the three-layered nanocapsule core into the dialysis bag. However, nile red appeared much faster in the MCT filled dialysis bag than DiI did. While DiI could not pass through the large hydrophilic water phase barrier into the MCT inside the bag, nile red showed a good transfer through the capsule shell, the aqueous dispersion, and the dialysis tube over 7 weeks, and accumulated in the MCT. This cannot be explained by the similar partition coefficient log$P$ (nile red: 3.8 [253]; DiI: 3.76 [254], determined between PCL-b-PEO and water) but rather by the relatively good water solubility of nile red (low) in contrast to DiR (extremely poor). Hence, the aqueous release medium displayed a strong migration barrier for DiI, but not for nile red. For nile red the profile can be interpreted as a sustained release following a first order kinetic during six weeks.
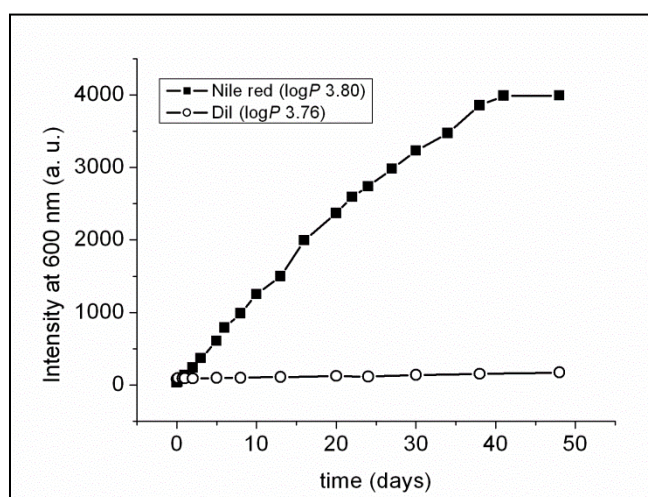
Figure 55 Increase of fluorescence intensity of the dialysis bag by time during 7 weeks (release from NC-OSA-CHI-CARR-2.5% = NC3)

However, the profile is a combination of three kinetics: (i) diffusion through the capsule wall, (ii) partition and transfer through the water phase (release medium), and (iii) permeation through the dialysis membrane. Probably the sustaining release effect derived from the aqueous medium which displays the largest barrier for lipophilic substances. This is evident from the extremely slow migration of the poorly water soluble DiI compared to nile red. The dialysis bag experiment is obviously not suitable to distinguish bewteen the release behaviour from the nanocapsules and the influences of an aqueous barrier and adialysis membrane. The pure diffusion kinetic from NDDS cannot be determined with the dialysis bag technique, as was pointed out before [156,158,255]. Diffusion through the capsule wall into the release medium likely was artificially prolonged.

5.7.2 Modified *in vitro* release simulation into lipophilic medium

5.7.2.1 In vitro release on a heated stirring plate

Figure 56 illustrates the release rate of (A) nile red and (B) pTHPP determined on a stirred plate, each after 1 by 100 and 1 by 10 dilution of sample NC-OSA-CHI-CARR-2.5% (NC3). Both the release from the capsule core and

the migration into the upper MCT phase influenced the final release profile. For both dyes, the 1:100 dilution of the dispersion induced a faster release and migration than the 1:10 dilution. This can be explained by almost perfect sink conditions in case of the higher dilution degree. For nile red, the maximum amount was released after 6 to 24 hours, in contrast the release plateau of pTHPP was reached only after 3 to 7 weeks.
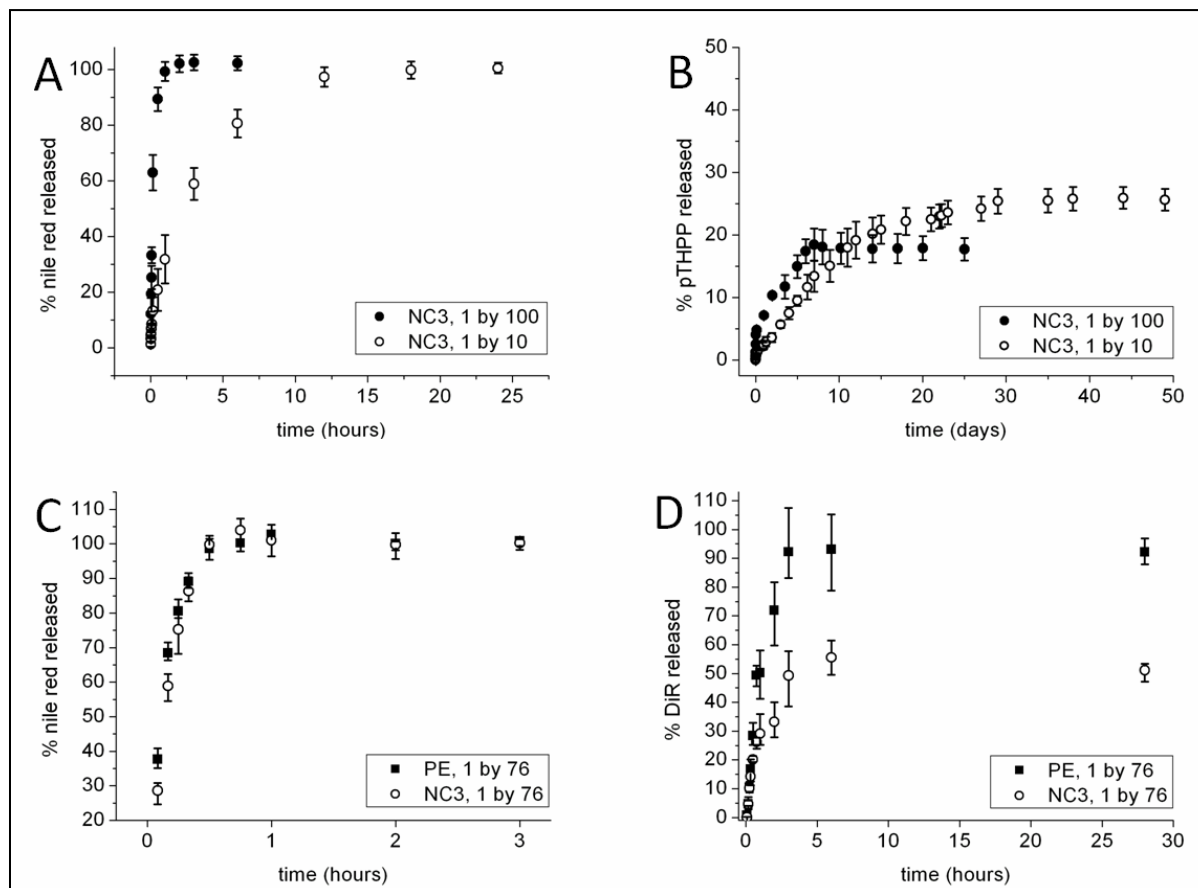

Figure 56 *In vitro* **release profiles of <u>A:</u> nile red, <u>B:</u> pTHPP each on a heated stirring plate obtained from NC-OSA-CHI-CARR-2.5% (NC3) after 1 by 10 and 1 by 100 dilution; <u>C:</u> nile red, <u>D:</u> DiR each in a rotation apparatus obtained from E-OSA5-5% (PE) and the three-layered nanocapsules (NC3) after 1 by 76 dilution**

The faster liberation of nile red compared to pTHPP is due to its much better water solubility. It has a higher affinity to the water phase than pTHPP which results in a faster achievement of the partition equilibrium between the capsule core (MCT) and water, and the water phase and the covering MCT phase, respectively. Finally, differences in the maximum release portion were observed. While the incorporated amount of nile red had migrated into MCT completely in both dilution degrees, only 18 % to 26 % of the pTHPP encapsulated were finally found in the upper MCT layer. The incomplete liberation of pTHPP is probably related to its lipophilicity. Water displayed an extreme diffusion barrier for pTHPP, leading to hindered distribution in the aqueous phase. Besides, despite the light protection, it is possible that the fluorescence activity of pTHPP decreased over the long experiment time in terms of photo bleaching effect since complete darkness could not be assured, e. g. during sampling.

5.7.2.2 In vitro release in a rotation apparatus

As shown in Figure 56C and D, the release profile of both model drugs nile red and DiR differed between emulsion and nanocapsules. Nile red (Figure 56C) was completely released from both NDDS after one hour which is indicated by a plateau value. Initially, the emulsion liberated higher amounts of nile red into the MCT phase than the capsules did. After 30 minutes, the emulsion and the nanocapsules showed a similar profile. The initial higher liberation velocity of nile red from the emulsion might be explained by the dispersion of the release medium MCT in the aqueous sample, facilitated by the emulsifier OSA starch, as observed during rotation. This resulted in a higher exchange surface and thereby a faster release. In case of DiR (Figure 56D) the emulsion liberated approximately 95 % of the model drug while the nanocapsules released only around 55 %. The incomplete liberation of DiR from nanocapsules might arise due to the suppositions mentioned above for pTHPP, or an accumulation of DiR molecules in the capsule wall. Compared to nile red, the maximum release point was reached only after six hours. Again, the release speed from the emulsion was faster than from the nanocapsule. This result derived from the mentioned dispersion of MCT in the nanoemulsion. Hence a possible release-sustaining effect of the nanocapsule wall compared to the emulsion cannot be claimed in general. However, for very lipophilic substances such as DiR the release profile from nanocapsules differed enormously from that of the nanoemulsion. The slower and incomplete liberation of DiR from the capsule core into the release medium can only be explained by the presence of a solid wall around the oily core since this is the only difference from the emulsion. Possibly the assembly of DiR into the wall material is the reason for this liberation behaviour. This would signify that for very lipophilic substances the charged capsule wall indeed displays a diffusion barrier that might be capable of sustaining their release to a certain extent.

5.7.2.3 Comparison of stirring plate and rotation apparatus

The data obtained from the stirring plate experiments show that the dilution factor of 100 is preferred over the factor 10. Due to a faster release profile the 1 by 100 dilution displayed almost perfect sink conditions. Hence these results are more realistic than those obtained from 1 by 10 dilution. Comparing the two model drugs concerning their lipophilicity, water solubility and release rate from the nanocapsules one can conclude that highly lipophilic and poorly water soluble molecules (pTHPP) are released slower than moderately lipophilic and good water soluble molecules (nile red). This is confirmed by the rotation apparatus results if one compares nile red and DiR. For both of these two model drugs the emulsion showed faster release than the nanocapsules. Possible causes for this observation might be the dispersed (drop-shaped) state both of the release medium MCT and the aqueous sample in each other in case of the emulsion (formation of an O/W/O double-emulsion facilitated by OSA starch), and the polar polyelectrolyte capsule wall displaying a diffusion barrier for lipophilic substances in case of the nanocapsules.

Finally, strongly lipophilic model drugs (pTHPP, DiR) were not released completely from the capsule core. Reasons could be the poor water solubility arising from the very high partition coefficient, reduced fluorescence activity due to photo bleaching or assembly into the capsule wall. The latter two aspects are not very likely since the release proceeded under light protection and the capsule wall is very polar in contrast to pTHPP and DiR. The data of nile red from the three-layered nanocapsules (Figure 56A and C) reflect that the rotation apparatus yields faster and more truthful release profiles than the stirred plate.

5.7.3 Electron paramagnetic resonance

Since nanocapsules undergo dilution both during experimental work and *in vivo* application, this dynamical process was studied to monitor the distribution kinetics of the spin probe TB between the capsule core and the water phase. The dispersion allowed for a fast distribution of TB between the drug carrier and its environment.

5.7.3.1 Dilution assay

The complete EPR spectra of the three-layered nanocapsules (NC3) are given exemplarily in Figure 57. The nanoemulsion template (E-OSA5-5%) and the five-layered nanocapsules (NC5) behaved similarly.
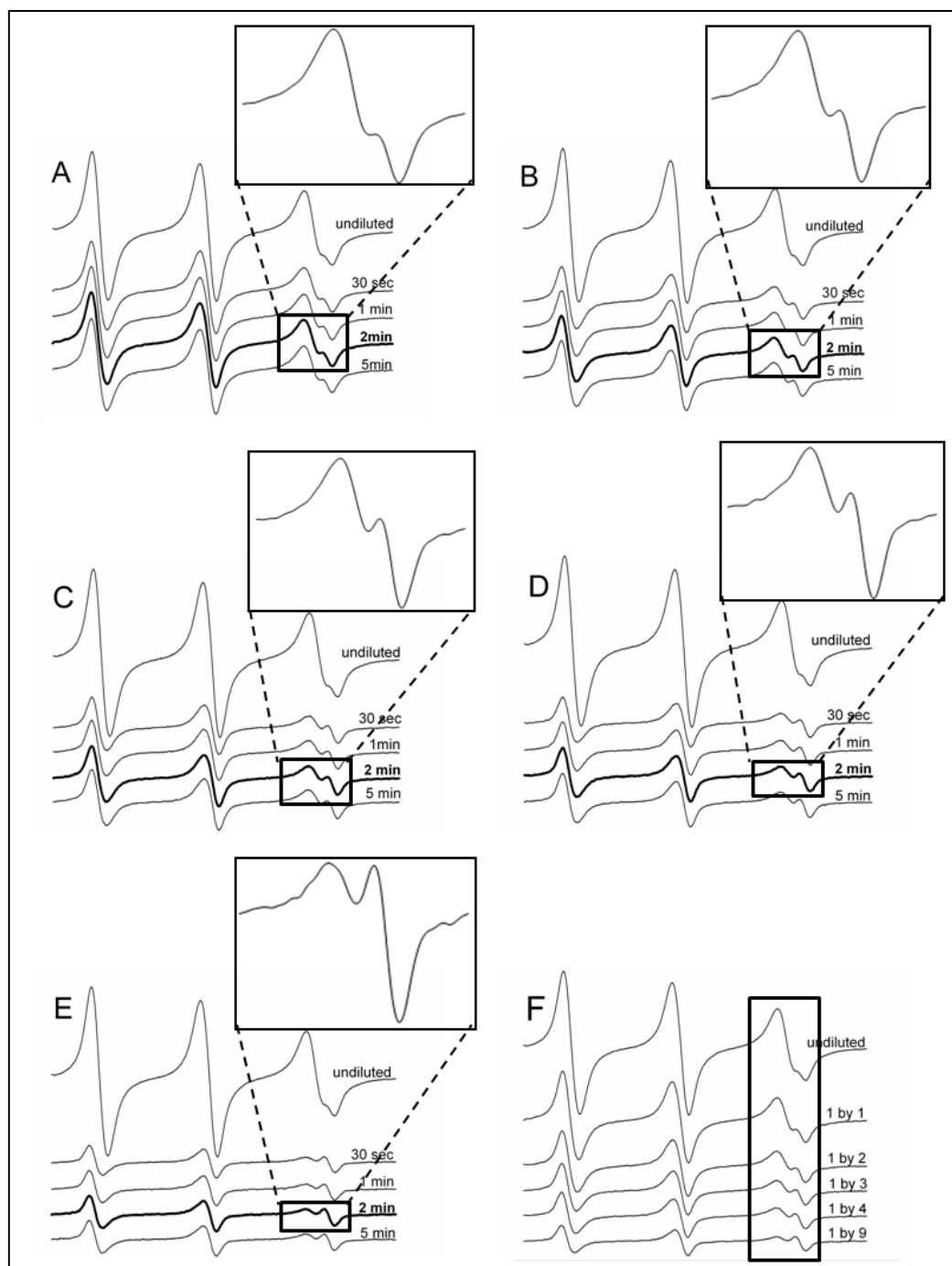
Figure 57 Time-dependent dilution assay TB-EPR spectra (A: 1 by 1 diluted, B: 1 by 2, C: 1 by 3, D: 1 by 4, E: 1 by 9) of NC-OSA-CHI-CARR-2.5% (NC3). F: highlighted 3rd peaks of A-E after equilibration time (2 min).

Contemplating the time-dependent development of the spectra after dilution, it can be stated that the distribution equilibrium was reached after a time span of less than five minutes. This was observed for each of the three stable samples and can be estimated from Figure 57A-E. The fractions of TB in water and oil become clear especially in the third peak of the signals (water and oil signal of TB are strongly superimposed) which is for this reason highlighted in Figure 57F (two-minute signals of NC3). As viewed in absolute terms, the shape and amplitude of the TB signal in water (larger a_N) stayed more or less constant. In contrast, and in relation to the oil signal (smaller a_N), both signals calculated as proportions, the TB content in water increased by time (and by higher dilution degree). This can be interpreted as a model drug release which was equilibrated in few minutes. With increasing dilution degree of the samples, the amplitude of the signals decreased approximately by the factor of dilution. However, the distribution of TB between the oil and water phase was shifting more and more in favour of water. This is in agreement with the distribution behaviour of a lipophilic molecule like TB, whose log$P$ has been calculated to be 2.46 [14].

In Figure 58A the decay of the area of the TB signal (3rd peak) in the oil and water phase during dilution is presented quantitatively for the three-layered nanocapsules after equilibration time. Due to dilution, the absolute TB content in the nanocapsule dispersion was reduced by the factor of dilution. For this reason both areas decreased (from right to left on the x-coordinate). The decay of the amount of TB in the oily core reduced approximately 4 times stronger than the amount of TB in the aqueous phase. This is already an evidence for the release of TB out of the capsule core.
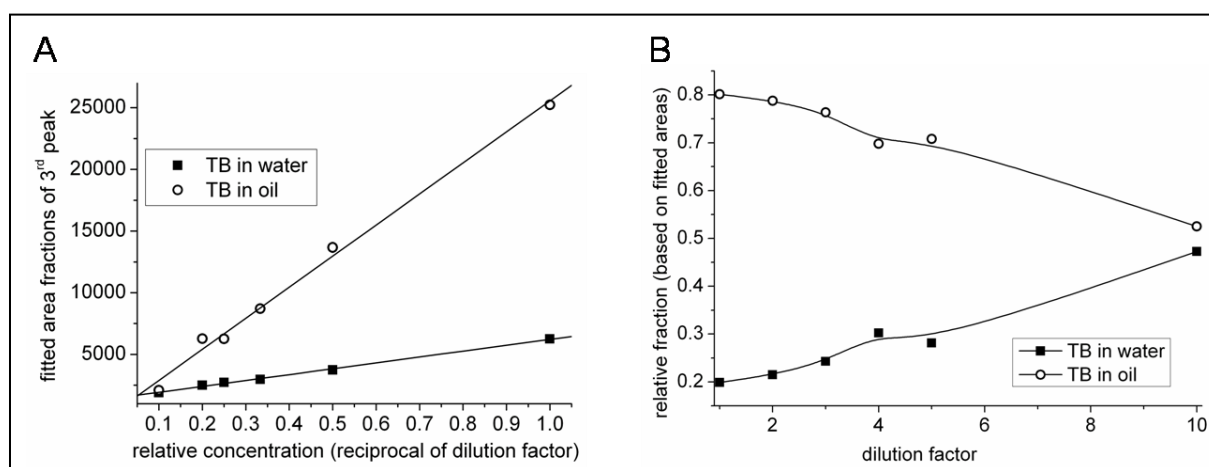
Figure 58 <u>A:</u> **Area decay of TB signals (3rd peak) in water and MCT during dilution of NC-OSA-CHI-CARR-2.5%, <u>B:</u> Distribution of TB in water and MCT phase at different degrees of dilution (2min values)**

After fitting the areas of the two TB species, the relative fractions of TB in both environments (MCT and water) could be calculated. The result is illustrated in Figure 58B. In the beginning (undiluted), 80 % of TB were located in the oily capsule core (MCT phase) of the three-layered nanocapsules. Since this dispersion contains only 2.5 % oil, already 20 % of TB were situated in the aqueous environment. For the lowest dilution factor 2 (1 by 1), 21 % of TB were released, and 47 % were released for the highest dilution factor 10 (1 by 9) each within the equilibration time of 2 minutes.

An increasing number of shell layers in the nanocapsule dispersion didn't show a significant prolongation of release for TB. Moreover, there was only a very small difference between the release profiles of the primary nanoemulsion and the two nanocapsule systems. In all cases, a large fraction of TB was still left in the oily nanocapsule core due to the hydrophobicity and partition coefficient of the model drug. For extremely lipophilic model molecules a much lower release rate has to be expected (e. g. as observed for HD-PMI I, $\log P > 6$, [14]). In conclusion, the release of model drugs was found to be strongly influenced by their partition coefficients and water solubility. Besides, the dilution factor has a main impact on the signal amplitudes. For all dilution degrees the distribution equilibrium was reached after few minutes. A sustained release rate can probably only be achieved for highly hydrophobic molecules which show only small affinity to the aqueous release medium. A significant impact of the nanocapsule´s wall composition on the release kinetics of TB could not be observed with the dilution experiment. Both colloidal drug carriers, the submicron emulsion and the nanocapsule dispersions, behaved quite similar with respect to fast drug release. This is not surprising, considering the short diffusion pathway and analogue results observed by Magalhaes et al. in 1995 [255].

5.7.3.2 Reduction assay

The protection capability of the capsule shell for incorporated TB was investigated by exposure of the nanocapsule formulation with ascorbic acid. Due to the 1 by 1 (v/v) dilution of the sample with the ascorbic acid salt solution, this procedure represents a combination of dilution and reduction kinetics. Only the portion of TB that was released into the aqueous phase was accessible to reduction by ascorbic acid because ascorbic acid is too hydrophilic to diffuse into the core. The results are given in Figure 59.

The EPR signal loss of TB was reached after 10 minutes (Figure 59A, B, C) for the three-layered nanocapsules. Again, the distribution of TB between oil and water phase can be determined from the 3rd peak of the signals by area fitting. The amplitudes of each phase and the change in the superimposed 3rd peak are given in Figure 59C. The half-logarithmic plot of amplitudes versus time leads to an almost linear decay of both amplitudes during the first five minutes. Thereafter the amplitudes decrease very slowly. Thus, the majority of the TB molecules are reduced in few minutes, induced by dilution of the nanocapsule dispersion. After the partition equilibrium of TB is reached, further reduction can be prevented over several minutes. One can conclude that the graph in Figure 59C arised from overlapping of two kinetics: during the first five minutes a fast release of TB, followed by a fast reduction of TB by ascorbic acid in the aqueous phase, which is the rate-determining step of this part, takes place. Afterwards, the reduction gets slower because the distribution equilibrium of TB is permanently but slowly changing due to the effect of ascorbic acid. The reduction of the TB portion located in the oil proceeds slower than in water since the spin probe has to diffuse out of the core before.

In conclusion, the protection capability of the nanocapsule shell against environmental effects could be proven since the TB molecules in the capsule core were not affected by ascorbic acid. Rather the early release of TB is the reason for the fast reduction. Thus, slow release and thereby good protection could be achieved by a low dilution degree or the encapsulation of very lipophilic substances.
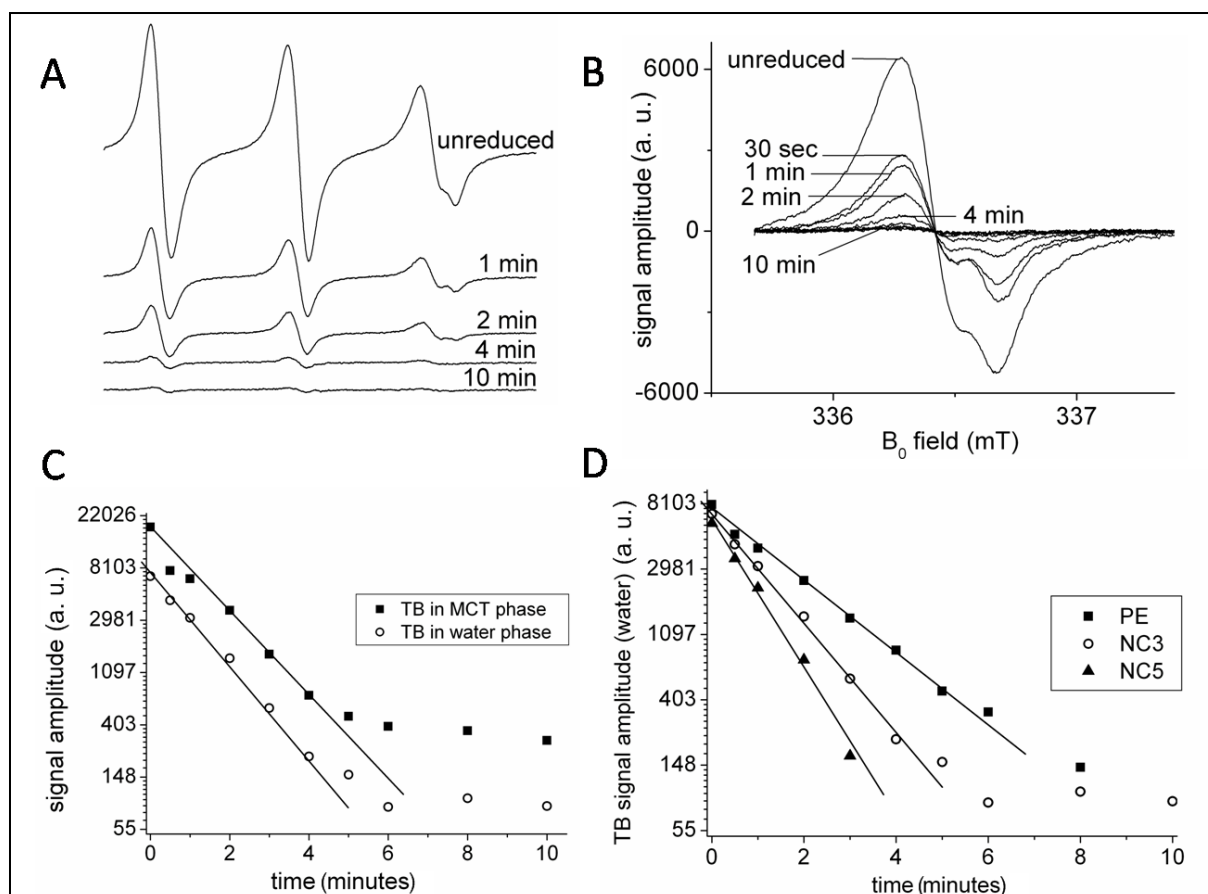
Figure 59 Reduction assay results A: Time dependent EPR spectra of TB incorporated in NC3; B: Change of the 3rd signal peak by time for NC3, C: Fitted amplitude decay of 3rd peak of TB signals in MCT and water phase of the NC3, D: Fitted amplitude decay of TB signal in water phase for the three samples

Interestingly, raising the number of polyelectrolyte shell layers around the oily core from one to five did not fulfil the expectations of an increased protection capability for incorporated molecules. As illustrated in Figure 59D, even inverse kinetic effects were observed. The reduction of TB by ascorbic acid (signal loss down to amplitudes near 148 a. u.) took around 8 minutes in the nanoemulsion, but only 5 minutes and 3 minutes for the three- and five-layered nanocapsules in spite of a harder capsule wall. This might be explained by a diffusion of ascorbic acid into the hydrophilic wall components of the capsules that would improve the contact between TB and the reducing agent. Although a significant difference in the samples was noticed by EPR, in each case the reduction was finished after 10 minutes.

5.7.4 Ultrafiltration at low pressure

The three consecutively prepared drug delivery systems E-OSA5-5%, NC3-OSA-CHI-CARR-2.5%, and NC5-OSA-CHI-CARR-CHI-CARR-1.11% showed a quite fast liberation of the incorporated drug during ultrafiltration tests. As apparent from Figure 60, the release of salicylic acid from the nanoemulsion (PE) and the nanocapsules (NC3 and NC5) was completed after 5 minutes for both pH values used. At pH 4.5 the maximum release rate was 98.4 %, at pH 6.8 it was 96.2 %. Although the three release curves run very similar at both pH values (Figure 60A and B), release from the primary emulsion was each the slowest. The release profiles of the three- and five-layered nanocapsules superimposed themselves at both pH values. They showed almost equal release

behaviour. In the neutral pH milieu (pH 6.8) the curve progression of the three dosage forms can be described as almost congruent.
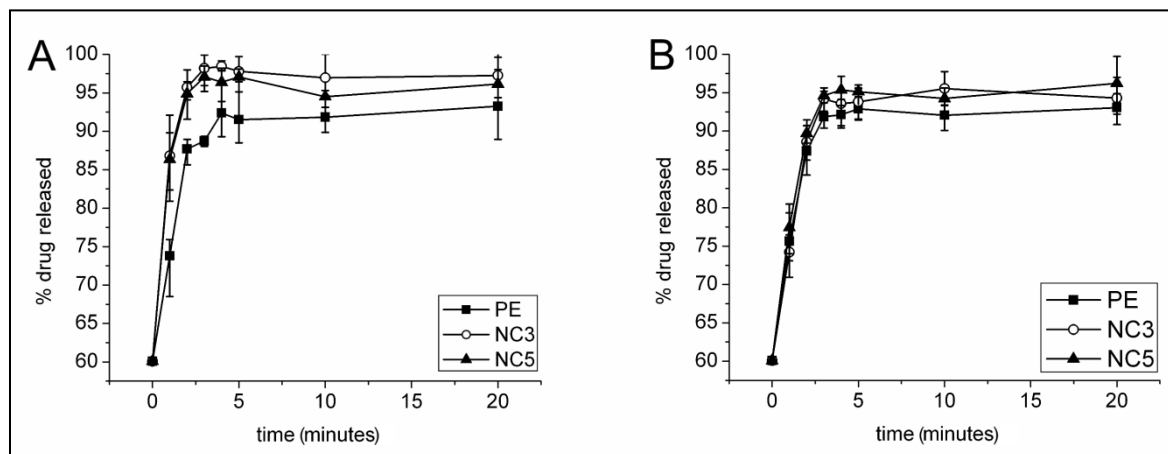
Figure 60 Release profile of salicylic acid after ultrafiltration at low pressure at <u>A:</u> pH 4.5; <u>B:</u> pH 6.8

Finally, at both pH values the curves resemble each other quite strongly. Considering the measuring uncertainty (superimposing error bars) it appears unreasonable to state a distinction between the samples regarding the salicylic acid liberation. From these results, it cannot be claimed that the release of salicylic acid is sustained with increasing polyelectrolyte layers around the oily core. Moreover, the ultrafiltration-at-low-pressure method does not seem to be suitable for the detection of very fine differences between the presented nanocapsules and nanoemulsion in the release rate of the model drug used within five minutes.

5.7.5 Summary and discussion

The results of this study show that the use of the terms 'controlled' or 'sustained' release should be considered very critically and only in strong linkage with the technique which served for data acquisition and drawn conclusions based thereon. In case of the presented nanoemulsion and polyelectrolyte nanocapsules, the four methods applied on the investigation of their release profile yielded completely different results. Believing the rotation apparatus and dialysis bag results, the liberation could be described as sustained over one day until even seven weeks. However, it was not controlled by the NDDS but by other diffusion barriers such as the dialysis membrane or aqueous medium.

The other two methods, ultrafiltration as well as EPR, may have benefits over dialysis methods for measurement of drug release from colloidal drug delivery systems. Both methods allow the colloidal dispersion to be diluted directly in the release medium, and also provide a 'snapshot' of drug distribution between the colloidal particles and free solution at the time of filtration (ultrafiltration) and signal acquisition (EPR), respectively. In contrast to the dialysis method, these experiments proved that both the emulsion and the nanocapsule systems present fast releasing dosage forms (within minutes). This statement is at least applicable for drugs with moderate lipophilicity with log$P$ values of around 3 or lower, and certain water solubility. The release of extremely lipophilic, not water soluble molecules proceeded much slower as observed in the stirring plate and rotation apparatus tests. However, this is not the effort of the delivery system but of the chemical properties. Very lipophilic substances cannot completely migrate through the polar capsule wall. Hence the

release profile is strongly depending on the water solubility and MCT-water partition coefficient of the incorporated drug molecule. Thus, the nanocapsules cannot ensure a sustained release of incorporated drugs in general since it follows diffusion controlled mechanisms.

Moreover, the three investigated systems did not show considerable differences in their release rate of medium lipophilic drugs such as nile red, salicylic acid and TB. An increasing number of polyelectrolyte layers surrounding the MCT core could not prolong the liberation of those substances. Rather, EPR spectra gave hint to contrary behaviour: the reduction of encapsulated TB was even faster in the nanocapsule dispersion than in the emulsion. However, for NDDS with liberation times of only few minutes it is questionable if there is any therapeutic relevance for the question whether they release the model drug during two, three or four minutes.

The presented capsule walls of three and five polyelectrolyte layers do not present a strong diffusion barrier for moderate lipophilic molecules as they were released in few minutes. The reason probably has to be seen in the thin shell representing a diffusion path of only a few nanometres. Although different nanocapsules with prolonged release behaviour were presented by other scientists, the EPR and ultrafiltration results cannot confirm nanocapsules to be an appropriate controlled release dosage form in general. However, among intravenous application of the nanosized drug carrier and transport of lipophilic active ingredients through biological barriers, fast release characteristics could serve for the local administration of active ingredients directly into the site of action, and for fast effecting pharmaceuticals like antidotes. Furthermore, parenteral nutrition is a potential application field for the nanocapsules. The protection capability of the capsule shell for incorporated drugs was proven by the EPR reduction assay. Furthermore, encapsulation of extremely lipophilic drugs such as pTHPP or Temoporfin should be considered as well since sustained release was achieved due to poor water solubility.

5.8 Animal study on polyelectrolyte nanocapsules

5.8.1 *In vivo* fluorescence imaging

It has been shown that *in vivo* fluorescence imaging is a powerful tool for studying the fate of biomedical materials and anatomical changes in the body of animals [256-259]. The aim of the experiments was to follow the fate of the labelled nanocapsules, emulsion, and poloxamer solution after peroral gavage in mice. The images obtained for the NR- or DiR-labelled E-OSA5-7% and NC-OSA-CHI-CARR-7%, each either from the green filter set (which detects NR) or the deep-red filter set (to detect DiR), are given in Figure 61A-D.
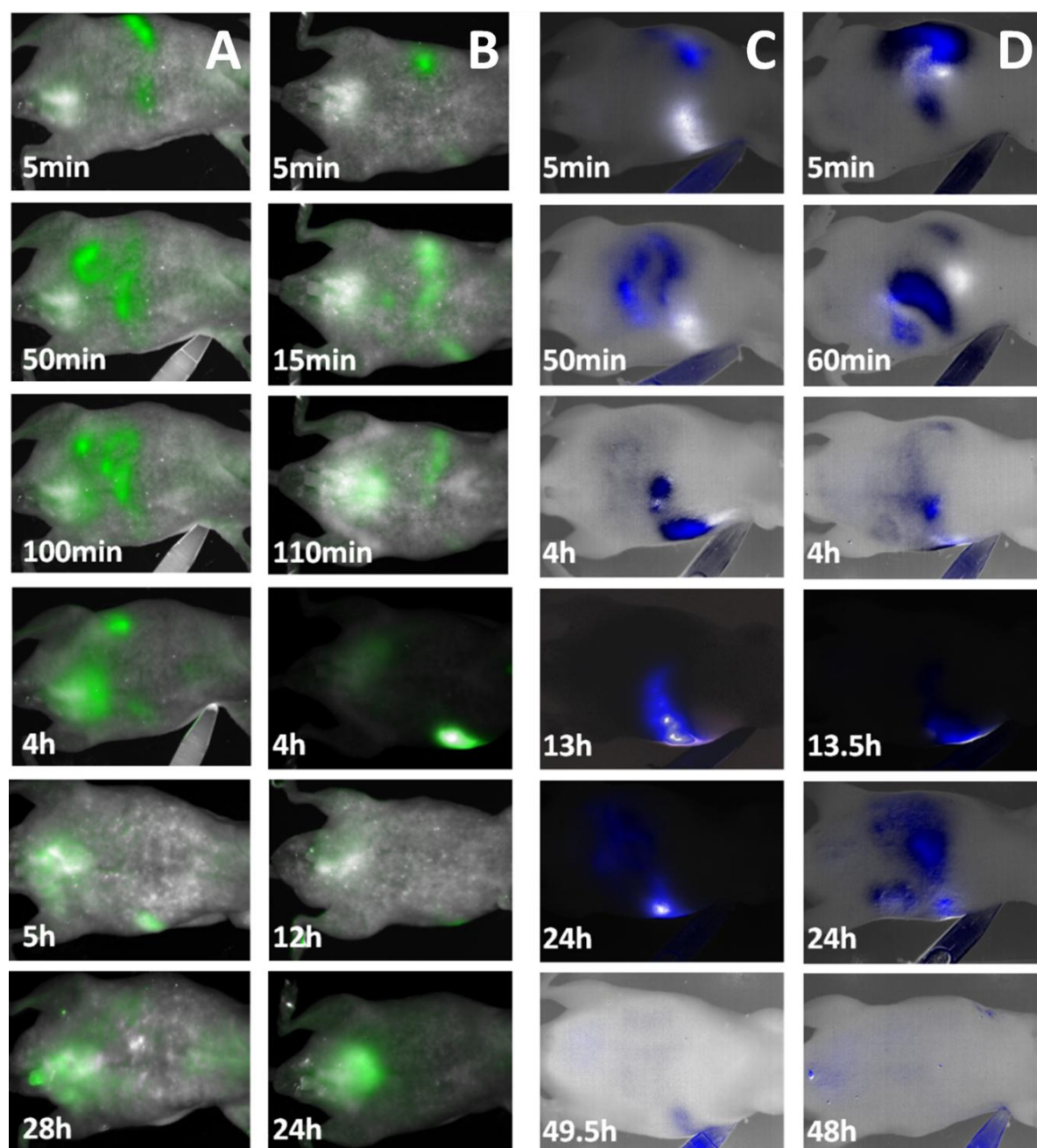
Figure 61 *In vivo* **fluorescence imaging results after administration of <u>A:</u> E-OSA5-7%-70µgNR/g; <u>B:</u> NC-OSA-CHI-CARR-7%-70µgNR/g; <u>C:</u> E-OSA5-7%-70µgDiR/g; <u>D:</u> NC-OSA-CHI-CARR-7%-70µgDiR/g**

NR samples were investigated over 24 hours (Figure 61A and B); DiR samples showed signals until 2 days after peroral administration (Figure 61C and D). As shown in Figure 61A and B (NR), immediately after administration and inhalation anesthesia, fluorescence emerged from the upper intestine parts for both of the samples which indicates that they had already partly left the stomach. Emptying of the samples from the stomach seemed to be finished after 10 minutes to 2 hours after administration. However, the stomach might be anatomically hidden below the liver. Especially the emulsion had already reached the lower intestine after 5 minutes where a rapid distribution could be followed. Signals of the NR-labelled naocapsule sample were less intensive which sometimes made it difficult to identify its position. The transport of the nanocapsules seemed to occur slower compared to the emulsion. However this might be due to inter-individual deviations. At 2 hours the bladder began to fluoresce which is a strong hint for systemic absorption of NR or the oil from the samples. In addition, renal elimination of the dye NR seems reasonable due to a molecular weight of M_r 318.37 g/mol which is quite close to the human renal size border of < 300 Dalton. After 3 hours to 5 hours, in case of the nanocapsules (4 hours) a very intensive signal emerged from the stomach region. But in mice the spleen is quite close to the stomach; moreover it cannot be safely excluded that no further intestine segment is located there. Even the posture of the animal has a large impact on which organs are visible, especially considering the shielding effect of the liver. Thus, the source of the sudden and strong fluorescence emission after 4 hours could not be identified. Between 12 and 24 hours all NR signals decreased except of the bladder, explainable by dilution of the sample with body fluids, or slow diffusion of NR out of the core. Obviously, elimination of NR took place and was almost finished after one day after administration.

The results of the administration of DiR labelled samples (emulsion and nanocapsules) are presented in Figure 61C and D. During the first 4 hours, the samples behaved similar to the NR labelled samples. However, the sudden occurrence of fluorescence intensity near the stomach or spleen region after 4 hours disappeared much later that observed with NR. After 12 to 24 hours the fluorescence was still quite intense. After 24 hours even parts of the intestine still showed high intensity. After 2 days the signals from the stomach region had weakened strongly. In contrast to NR, the bladder did not emit any DiR signals. This might be due to the larger size of M_r 1013.41 g/mol. After three days, no DiR fluorescence could be detected anymore.

In general, the *in vivo* experiments showed that the labelled emulsions mostly emitted fluorescence light of stronger intensity than the labelled nanocapsules did. This attenuation can probably be explained by the capsule shell possessing a certain light protection capability as described in section 5.5.1, p. 92. Moreover, nile red signals were detectable only for a period of maximum 12 hours whereas DiR labelled samples showed much stronger and longer-lasting fluorescence. DiR with its longer excitation and emission wavelengths featured less superimposition with murine tissue auto-fluorescence, and thereby yielded signals with a lower limit of detection and higher signal-to-noise ratio. Thus, even smaller DiR concentrations after dilution of the sample in the animal body were detectable. This offered the possibility of long-term investigations.

Figure 62 presents the images obtained by mixed samples containing both NR and DiR (emulsion: left column, nanocapsules: centre column) as well as by the DiR containing poloxamer control sample (right column).
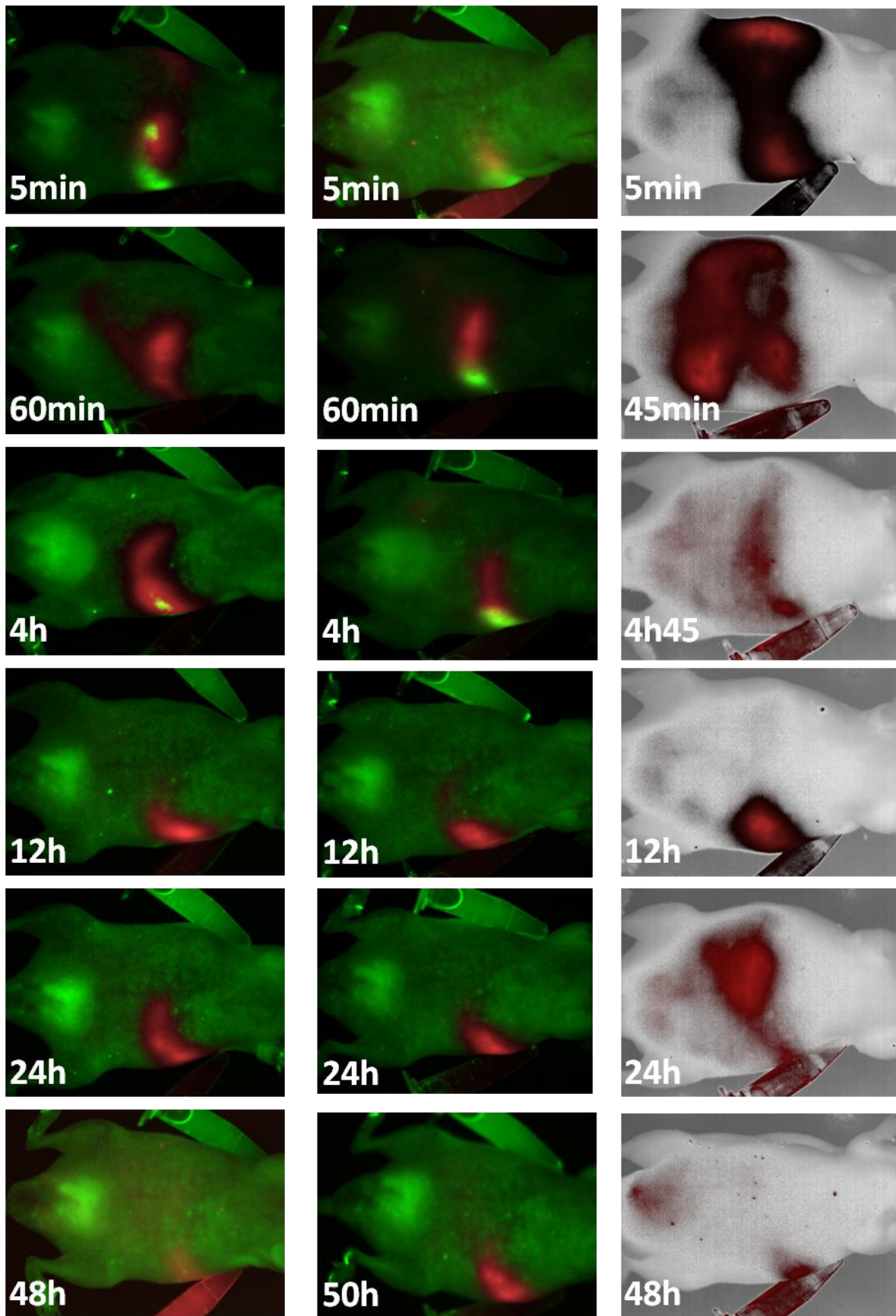
Figure 62 Unmixed images obtained by *in vivo* **fluorescence imaging during 2 days.** <u>Left column:</u> **Mix-E-NR+DiR-each-35µg/g;** <u>centre:</u> **Mix-NC-NR+DiR-each-35µg/g;** <u>right column:</u> **Polox-7%-70µgDiR/g (control). Green coloured fluorescence induced by nile red (NR), red fluorescence induced by DiR.**

By mixing of the differently labelled samples it was possible to directly compare the behaviour of the two dyes since they were applied under equal conditions and in the same individual. After application of the mixed samples containing both NR and DiR, the corresponding fluorescence signals could be identified by unmixing the emission spectra of the two filter sets by means of the Maestro 2.4.3 software. As control served the poloxamer solution containing 70 µg/g DiR. In the mixed samples (mix-E-NR+DiR-each-35µg/g and mix-NC-NR+DiR-each-35µg/g), the two differently labelled nanocapsule species moved simultaneously through the digestion system during the first four hours after administration. It only seemed like DiR labelled samples moved faster because the NR filter set was measured first; one minute later the DiR fluorescence filters followed. The emulsion signals (Figure 62, left) were still more intensive than those emitted from the nanocapsules during the first 4 hours. Large portions of the sample remained in the stomach until that point of time. Distribution of both samples into the intestine was visible. After 12 hours, the NR labelled samples were again not further detectable due to low intensity and possible interference with murine tissue or DiR signals. However, the DiR labelled samples from then on gave hint that both the emulsion and the nanocapsules were still mainly located in the stomach region (i.e. in the stomach itself, in the spleen, or in intestine sections nearby). Nevertheless, for the identification of the precise sample position, *in vivo* experiments were not sufficient. After 3 days, no further DiR signals were observed anymore due to elimination. DiR could not be detected in the bladder at all during the three days of investigation.

The images of the control sample in Figure 62 (right column) support the theory that the sample had left the stomach during the first 4 to 5 hours after administration. During that time the whole abdomen of the mouse (stomach and intestine in that order) was fluorescing. After 5 hours only residual fluorescence was observed in these organs. However after 12 hours a rapid increase of long-wave fluorescence occurred in the region where the stomach and the spleen are located. This was followed by a phase in which the intestine also emitted DiR signals again (at 24 hours). After 2 days DiR could be weakly identified in the bladder as well as in the stomach region. This might indicate that systemic absorption of the dye had taken place, and that an accumulation of the dye in the stomach (or spleen or unknown intestine regions) over 48 hours had occured. After 3 days there were no signals observed anymore. In conclusion, the control sample (Figure 62, right) behaved similar to the DiR labelled emulsion (Figure 61C) and nanocapsules (Figure 61D), but effected stronger DiR spreading.

A quantification of the dye release from the nanocapsules by *in vivo* fluorescence imaging, as originally desired, was finally hardly possible to be implemented due to numerous influencing factors. The signal intensity was not only reduced by drug release but also influenced by the position of the fluorescing organs (distance from the body surface), the time elapsed after administration, the resulting concentration of the dye as a consequence of distribution and dilution in the body, and possible quenching effects at very high concentrations or large fluorescing areas. Moreover, potential spectral shapes of the dye dissolved either in MCT, in any aqueous body liquids (after release from the oily core), or integrated into cellular membranes might have overlapped with each other and thereby distorted the actual fluorescence spectrum. Furthermore, the Maestro® software exhibited an upper limit of detection of 4000 a. u. If fluorescence signals were more intensive, the exceeding fluorescence was cut off so that information got partly lost. However, in general a reduction of the fluorescence was observed by time. But due to the possible influencing aspects it cannot undoubtfully be

assigned to release of the dye from the capsule core, in particular not proportionally. Nevertheless, the DiR fluorescence spectrum did not change during 2 days. This indicates that the dye was still dissolved in MCT; hence a very slow release can be assumed (much slower than *in vitro* studies showed). Much more extensive animal studies would be necessary to investigate the *in vivo* release behaviour quantitatively. To study of the actual origin of the signals from the stomach region, subsequently *ex vivo* experiments were essential.

5.8.2 *Ex vivo* – quantification of DiR accumulation in certain organs

Diffuse emission of fluorescence has been observed at *in vivo* images. Thus, it was not always possible to assign the location of the signal source to certain murine organs. After sacrificing three mice (skin-covered abdomen: Figure 63a and b), the same phenomenon was observed. Only by removing the skin from the abdomen (Figure 63c), the fluorescence origins were identifiable more distinct. The images after autopsy gave more information about the distribution of DiR in the body at different points of time after gavage of NC-OSA-CHI-CARR-7%-70µgDiR/g than the *in vivo* images. 1 hour after gavage (Figure 63c, M I), the stomach was fluorescing quite strong. Large parts of the intestine were well filled with DiR containing sample. After 6 hours (Figure 63c, M II), the intestinal intensity had decreased enormously, which was not supposed from Figure 63a, M II. The stomach still showed intense fluorescence. After 12 hours (Figure 63c, M III), only residual signals were emitted from the intestine. The intensity of the stomach region was still high, but the signal shape had differed, arguing against the stomach as the origin. These results show that the sample had arrived in the intestine during the first hour after gavage, but also that the dye was retained in the stomach region or the gastric wall for several hours.
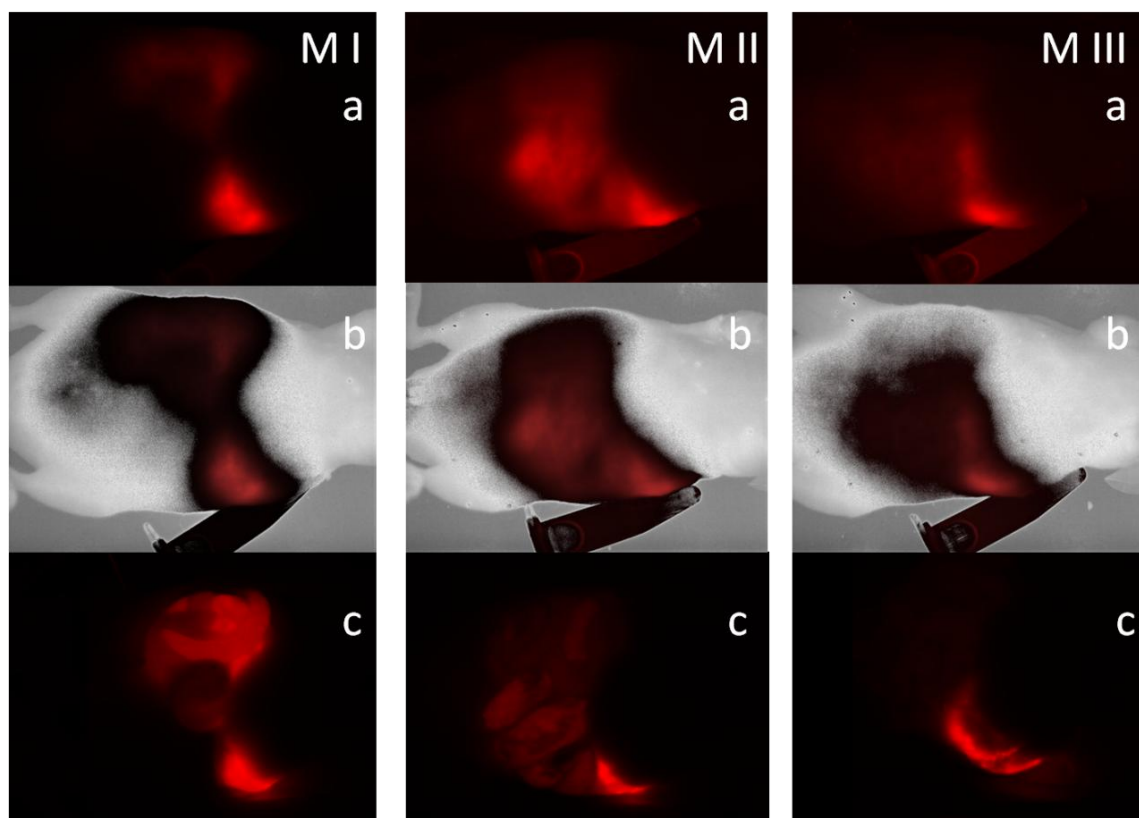
Figure 63 Fluorescence imaging 1 hour (mouse M I), 6 hours (M II), and 12 hours (M III) after peroral gavage of NC-OSA-CHI-CARR-7%-70µgDiR/g. <u>a:</u> fluorescence with abdominal skin (as during *in vivo* investigations); <u>b:</u> unmixed images corresponding to a; <u>c:</u> signals after skin removal during preparation for *ex vivo* studies.

Further investigation of the accumulation of DiR in certain organs was performed by *ex vivo* ethanolic extraction of DiR from the organs and quantification via fluorescence spectroscopy by external calibration. The calibration curve for DiR in ethanol is shown in Figure 64. Concentrations higher than 2 µg/g were out of the linear range due to fluorescence quenching effects.
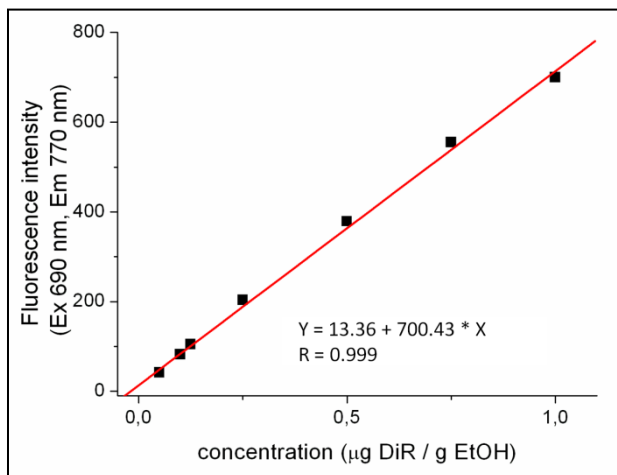

Figure 64 Calibration curve of DiR in ethanol for fluorescence spectroscopy (slit: 8 nm, coarse: 1)

The fluorescence spectroscopy after *ex vivo* investigation of the mice yielded the results shown in Figure 65. One hour after administration of the DiR labelled nanocapsules, the main fraction (84 %) of the dye was still retained in the stomach. The residual 16 % had been transported into the small intestine. After 6 hours, a large portion (39 %) had already reached the large intestine. However, 59 % of DiR were still located in the stomach. Almost no dye molecules (2 %) could be extracted from the small intestine. 12 hours after gavage of the sample, there was no DiR at all in the small intestine. Only a small fraction (17 %) of DiR was found in the large intestine. As already seen in Figure 63c (M III), high fluorescence intensity was still emitted from the stomach region after 12 hours. *Ex vivo* extraction could now show that even after such a long period of time still 83 % of DiR had been accumulated in the stomach. During the 12 hours of investigation, the dye could be extracted neither from the liver nor from the spleen or the lungs at any point of time. This knowledge could not be gained from *in vivo* studies.
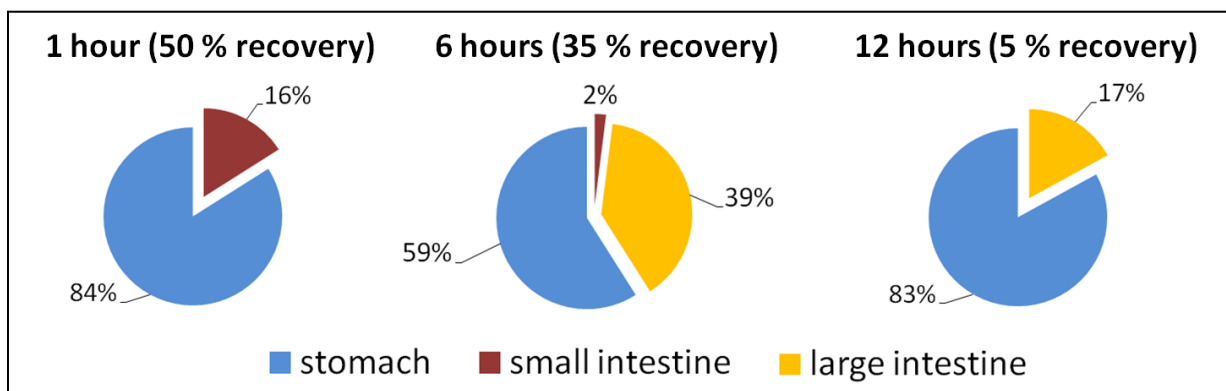
Figure 65 Accumulation of DiR after 1 hour, 6 hours, and 12 hours in male, nude mice of stock SKH1-Hr after peroral gavage of NC-OSA-CHI-CARR-7%-70µgDiR/g and *ex vivo* extraction with ethanol

However, in all cases a quantitative extraction of the dye could not be achieved. This is reflected by the recovery rate which rapidly decreased with increasing time between administration and sacrificing of the animals from 50 % (1 hour) over 35 % (6 hours) to only 5 % (12 hours). At low recovery rates as obtained especially for the 12 hour value, the confidence of the results loses in reliability. However, these quantitative accumulation data for DiR is consistent with the fluorescence imaging data. Yet reasons for low recovery at all shall be discussed in this place. Firstly, elimination from the body has to be considered. Since 38.8 % of the dye was already found in the large intestine after 6 hours, elimination via the faeces is quite likely, especially due to the molecular weight of DiR (M_r 1013.41 g/mol) which is considerably larger than the human biliary size border of > 500 Dalton. Besides, systemic absorption from the small intestine might have occurred. This would explain why during all the time only small amounts were extracted from this organ. Systemic absorption would be followed by distribution of the dye in other compartments as well as in the blood circulation. The fraction of DiR in the blood or other body fluids or organs than those mentioned in Figure 65 has not been investigated. Elimination of DiR by the bladder is rather unlikely (M_r 1013.41 g/mol) since the molecule might be too large for the renal route (in humans preferred when M_r < 300 Dalton). Finally the possible incidence of measuring artefacts should be mentioned. This could be developed due to physiological tissue components which might have been extracted by ethanol, too, and could have influenced the excitation or emission fluorescence spectrum or intensity. In conclusion, the low recovery does not necessarily mean a loss of analytes but rather indicates systemic absorption of DiR in the small intestine.

5.8.3 *Ex vivo* confocal laser-scanning microscopy

Firstly, a photobleaching sensitivity of DiR could be excluded by exciting a certain section of the small intestine for more than 8 minutes with the 633 nm laser light. The intensity kept constant, thus the photo-stability of DiR as reported by the producer (in membranes) was confirmed [191]. Investigation of the lateral cuts each 1 hour (M I), 6 hours (M II), and 12 hours (M III) after the gavage of the DiR labelled nanocapsules NC-OSA-CHI-CARR-7%-70µgDiR/g by CLSM showed considerable fluorescence at all times. The small intestine after 12 hours was chosen for interpretation because in that sample no DiR could be extracted during *ex vivo* study. A photograph of the intestine preparation of M III (after 12 hours) was taken under a light microscope (Figure 66), and shows the region that was used for CLSM. Blue coloured areas indicate that the tissue contains DiR.
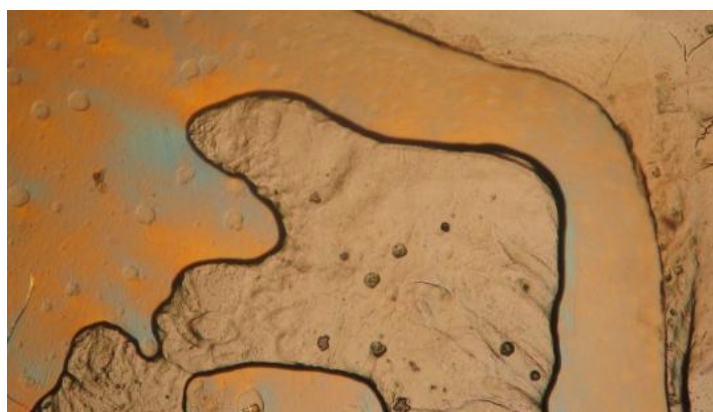

Figure 66 Biological preparation of the small intestine of M III, 12 hours after peroral gavage of NC-OSA-CHI-CARR-7%-70µgDiR/g, under light microscope. DiR in high concentration appears in blue.

In Figure 67 CLSM images in different magnifications recorded after 12 hours are presented. The fluorescence signals were coloured red in accordance with the long-wave excitation maximum of DiR. Figure 67A shows an overall fluorescence emission in the whole small intestine section investigated (10x magnification). Thus, it can be excluded that DiR had entirely been resorbed systemically within 12 hours after peroral administration. Although during *ex vivo* tissue extraction of the dye with ethanol no fluorescence could be detected by fluorescence spectroscopy, the CLSM instrument proved an accumulation in the small intestine wall. This result is in agreement with the property of DiR described by the producer to be highly fluorescent when incorporated into membranes, and can be explained by a lower limit of detection of the CLSM compared to fluorescence spectroscopy due to targeted excitation and emission, better photon efficiency, and better resolution.
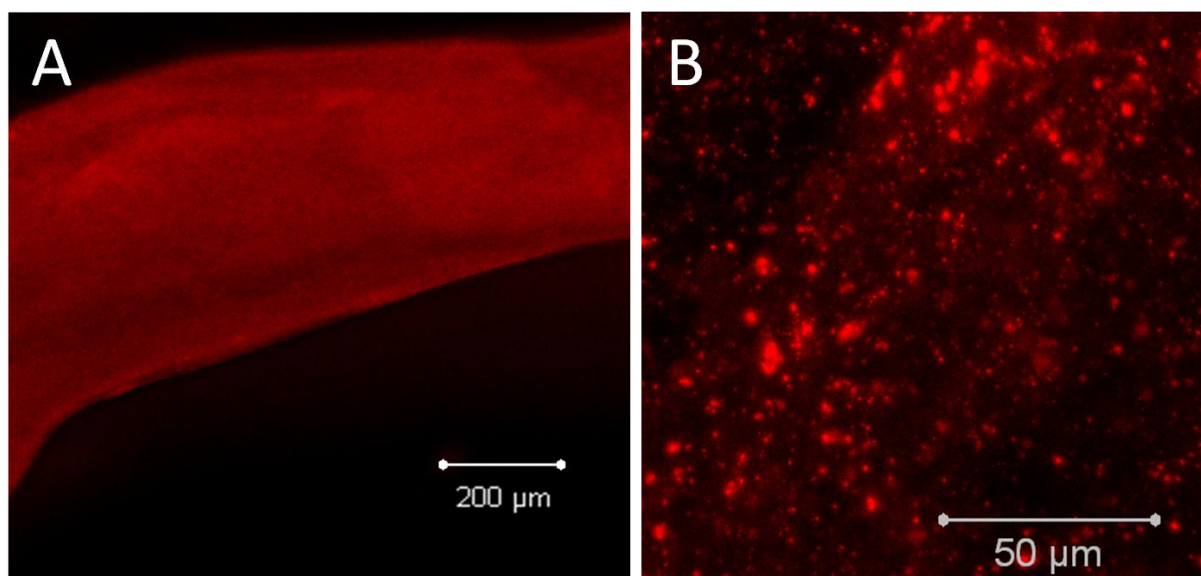
Figure 67 CLSM images of the small intestine 12 hours after peroral gavage of sample NC-OSA-CHI-CARR-7%-70µgDiR/g into a male SKH1-Hr mouse. Parameters A and B: excitation laser 633 nm (50.0 % power), pinhole: 600 µm, filter: 672–758 nm, digital gain: 0.30; A: image size 848 x 848 µm, height (z) 282 µm (plane), objective: EC Plan-Neofluar 10x/0.30 M27, average line 2; B: maximum intensity projection, image size 135 x 135 µm, objective: Plan-Apochromat 63x/1.40 Oil DIC M27, average line 4.

Figure 67B was obtained by zooming into the image A with higher magnification (63x objective). This maximum intensity projection image was obtained by reconstruction of the highest fluorescence intensities of all scanned layers (z-planes) into one two-dimensional image. One can see that the fluorescence was always emitted punctiformly, the dye is distributed inhomogeneously. This result argues against diffusion-induced absorption of the dye (after release from the nanocapsules) since in this case a homogeneous staining would have been expected. It rather supports the theory that entire nanocapsules had been absorbed by the intestine wall, especially under consideration of the fluorescence dot size (mainly < 1 µm) which is consistent with the results of particle size determination. The transit of NDDS through mucosa, membranes and other biological barriers is feasible and has been reported about earlier [8,260-265]. However, this assumption cannot be proven since the fluorescence emission spectrum was not available by hindsight. In case of a spectral shift of the emission curve of DiR compared to the solvent MCT one could have concluded that the environment of DiR had changed. This would prove that DiR had been released from the oily core nanocapsules, absorbed and diffused into lipid components of the small intestine cell membranes via aqueous body fluids.

5.8.4 Summary and discussion

The *in vivo* fluorescence imaging study of NR and/or DiR labelled emulsion and nanocapsules, perorally administered to nude mice, showed that large portions of the samples remained in the stomach until 4 hours after gavage. Afterwards, distribution of emulsion and nanocapsules into the intestine was visible. After 12 hours, the NR labelled samples were not further detectable except of in the bladder, indicating systemic absorption of NR or the NR-containing MCT in mice and renal elimination of the dye. The DiR labelled samples from then on reflected that both the emulsion and the nanocapsules were still considerably located in the stomach region after 12 hours. Between day one and two this fluorescence strongly decreased. After three days the DiR signals finally disappeared, too. In contrast to NR, the bladder did not emit any DiR signals, which argues for biliary elimination, especially considering its molecular weigt of >500 Dalton. The *in vivo* experiments furthermore showed that the dye labelled emulsions emitted more intense fluorescence light than the dye-labelled nanocapsules did. This was explained by the light protection capability of the capsule shell. Unfortunately, *in vivo* fluorescence imaging alone was not capable of identifying the concrete origin (distinct organs) of fluorescence and thus the *in vivo* murine fate of the samples. Especially the signals from the stomach region even after two days could not definitely be assigned to the actual organ (stomach, spleen, or intestine sections). The development of the fluorescence intensity and spectral shape argues for a long residence time especially of DiR in the stomach. However, already within the first hour signals were detected from the intestine. Hence, discharge of the sample from the stomach had occurred at least partly, unless even completely. Moreover, a residence time in the stomach of 48 hours is unlikely. Thus, one possibility for the signal source is a staining of gastric membranes by DiR. But this is relatively unlikely since extremely low water solubility and slow diffusion of DiR out of the capsule core are known or had been observed *in vitro*. Thus, a loop of the intestine being located near by the stomach and very close under the animal skin would rather be imaginable for emitting strong signals. Additionally, fluorescence originating from the spleen (which is located near the stomach) is possible since negatively charged particles preferably accumulate in that organ (apart from the liver and lungs). This organ as light source might be explained by systemic absorption of DiR (in the gut) followed by enrichment in the spleen via blood circulation. Nevertheless, anatomically the spleen is frequently covered by the liver which is not permeable for fluorescence due to a relatively high content of physiological iron compounds. Hence, a fluorescence emission of the spleen would probably not be visible in this case.

In conclusion, the sudden increase of fluorescence intensity which appeared from the stomach region between 4 and 48 hours could not be explained from the *in vivo* data. One can only assume that the drug carrier had already left the stomach while DiR might have accumulated in the gastric wall (membrane staining). In addition, it could not be determined from the *in vivo* data whether the fluorescence originated from the intact sample (nanocapsule), degraded sample (possible enzymatic degradation of the polyelectrolytes while DiR remained dissolved in the MCT), or from cell membranes where the dye might have diffused and being assembled into. Corresponding to the emission spectrum, however, DiR had obviously been kept dissolved in an MCT environment in all experiments. Anyway, *ex vivo* had been necessary to study the fate of the nanocapsules.

During *ex vivo* studies, localisation of DiR and quantification of its distribution in gastrointestinal organs 1 hour, 6 hours, and 12 hours after gavage could be determined. At each point of time most of the administered DiR amount (59 to 84 %) was located in the stomach. Hence, the stomach could be identified as the questionable location of DiR at 12 hours after gavage. However, information about the environment of DiR (MCT or gastric membranes) of DiR could not be gathered. Only small fractions were extracted from the large intestine (0, 17 or 39 %). Apart from 16 % of DiR being found after 1 hour, the dye was not observed in the small intestine after 6 and 12 hours (despite presence in the large intestine). As this is the main position where absorption into the blood circulation takes place, systemic uptake can be assumed. The thesis of systemic intestinal DiR absorption was supported by low recoverie rates, decreasing by time from 50 % (1 h) over 35 % (6 h) to 5 % (12 h). During the 12 hours of investigation, the dye could be extracted neither from the liver nor from the spleen or the lungs. This knowledge could not be gained from *in vivo* studies.

CLSM investigation of the lateral cuts of the small intestine after 1, 6, and 12 hours confirmed that the tissue contained DiR, even despite non-detectability by *ex vivo* ethanolic extraction and subsequent fluorescence spectroscopy after 12 hours. The overall fluorescence emission in the entire intestinal section (12 hours after gavage) observed during CLSM was explained by the lower limit of detection of the CLSM compared to fluorescence spectroscopy due to confocal assembly, resulting in targeted excitation and emission, better photon efficiency and resolution. The dye was distributed very inhomogeneously (punctiformly). This result indicated that entire nanocapsules had been absorbed by the intestine wall, especially under consideration of the fluorescence dot size being in accordance with the results of particle size determination methods.

6   SUMMARY AND CONCLUSION OF THE THESIS

In this thesis, the development and preparation of polyelectrolyte nanocapsules by application of high-pressure homogenisation and complex coacervation is presented. The procedure started with the production of a nanoemulsion which could subsequently be converted into core-shell structured nanocapsules with a solid wall of polyelectrolytes (cf. Figure 14 and Figure 15, p. 35). The shell assembly proceeded with the sequential deposition of three or five oppositely charged polyelectrolytes on a charged emulsion surface. During this process, a solid coacervate phase representing the polymeric capsule shell was formed while the core still consisted of liquid oil (medium-chain triglycerides, MCT) as it was in the emulsion template. A great advantage of this emulsion-based preparation method is that, in contrast to most published nanocapsule preparation procedures such as the layer-by-layer technique, no tedious separation steps are required. It is furthermore minimum time-consuming since high-pressure homogenisation can be applied continuously once the ratio of the components has been developed. As the use of organic solvents is completely avoided, and non-toxic, biocompatible raw materials are employed, the presented procedure succeeded in the treatment of physiologically tolerable ingredients only.

Via screening of the different polyelectrolytes octenyl succinic anhydride-modified (OSA) starch, sugar beet pectin (SBP), gum arabic (GA), λ-carrageenan (CARR), gelatin (GEL) type A, and chitosan (CHI), nanocapsules with various shell compositions were developed (cf. Table 4, p. 37). Thanks to the capsule core containing MCT, a diversity of lipophilic model drugs with log$P$ values ranging from 2.3 (salicylic acid) to 7.6 (pTHPP) could be encapsulated (cf. Table 11, p. 72). The oil content of the successful nanocapsule dispersions could be enhanced compared to the original MCT content. In dependence on the initial oil content of the emulsion template and the specific composition of each successful formulation, dispersions with 5.55 % to 8.6 % MCT (cf. Table 10, p. 61) were obtained, allowing for an improved drug incorporation rate. In few cases, enlargement of the particle size, increased viscosity, or loss in stability (e. g. aggregation) was observed simultaneously.

After the development, the nanocapsules were well characterised physico-chemically and *in vitro* in order to identify whether the required properties could be achieved. One main focus was the determination of the particle size which was desired to be in the submicron range to justify the term 'nano'-capsules and to allow for intravenous injection of the capsule dispersion. By application of several independent techniques such as PCS, LD, TEM, AFM, and FFF, based on different measuring principles, a comprehensive knowledge of the true capsule size was obtained for each formulation. Since slight differences in their results were reasonable and could be attributed to their varying operation principles, the generation of measurement artefacts could be excluded. The successful nanocapsules as produced by the described procedure featured sizes between 118 nm and 493 nm (cf. Table 13, p. 85). The final ζ-potential of the developed samples served for the estimation of the long-term dispersion stability. Values of up to -37.9 mV were obtained and gave hint to sufficient electrostatic repulsion of the electric charges for the prevention of particle aggregation during storage. Selected nanocapsules showed that freeze-drying as a beneficial stabilisation method for dispersions with low ζ-

potential could keep the size distribution constant. However, the lyophilisation success strongly depended on the initial sample quality. Thus, negative storage impacts can be prevented by lyophilisation early after sample preparation. Physical stability of the investigated liquid nanocapsule dispersions over germ reduction methods such as autoclavation (121 °C, 15 min, 2 bar) and isostatic high pressure could be proven by treatment of the samples with conventional conditions. Only one of the investigated samples showed a strong increase in the capsule size during autoclavation which was explained by the potential degradation of gelatin under the conditions of humid heat (Figure 43, p. 89). The sample investigated by isostatic high pressure was robust over up to 400 MPa for a period of 30 minutes (Figure 44, p. 89). In conclusion, an overall storage stability could be achieved by a ζ-potential of the capsule dispersion of > |±30| mV, or by lyophilisation. Investigation of selected samples reflected their physical stability against at least one of the germ reduction methods (autoclavation or isostatic high pressure) in most cases.

For one of the nanocapsule formulations the shell composition could be improved in terms of the number of layers. The sample whose three-layered shell was originally composed of OSA starch, CHI and CARR (NC3-OSA-CHI-CARR-2.5%), was also developed with a five-layered capsule shell (NC5-OSA-CHI-CARR-CHI-CARR-1.11%; cf. Table 4, entry 2 and 3, p. 37, and section 5.2.2.1.1, p. 62). The characterisation of the emulsion template E-OSA5-5% and the three- and five-layered nanocapsules (consecutively prepared samples) was performed with the aim to discover a possible impact of the shell enlargement on the mechanical, release, temperature stability, and light protection properties of the nanocapsules. Briefly, with increasing number of shell layers around the oily core, a higher thickness, stiffness, rigidity, and light attenuation, as well as a slower drug release was theoretically expected. Moreover, the stiffer capsule wall compared to emulsion droplets might be advantageous during storage and intravenous application due to better mechanical resistance.

The shell thickness of the three consecutive samples was accessible by TEM. Studying freeze-fractured samples using TEM was accompanied by difficulties such as only a small portion of capsules being correctly broken, particle damaging during sample preparation, and the shell thickness being dependent on the fracture plane. However, the capsule shell thickness of the three samples could be estimated to be between 3 and 8 nm (Figure 30, p. 70). The mechanical properties, represented by the mobility of the shell components, as well as the stiffness, solidity, and indentation resistance of the shell, could be investigated by ^{1}H NMR, AFM force-curve analysis, and URT. While NMR could deliver information about the liquid state of the oily capsule core (bulk oil properties of MCT), this technique also reflected that NMR was not capable of proving a complex coacervation by immobilisation of the polyelectrolytes in the capsule shell. For further information on the mechanical state of the capsule shell in dependence on the shell composition, AFM force-curve analysis and URT measurements were carried out. These studies showed that the composition of the shell surrounding the MCT core evidently influenced the particle rigidity. Both AFM and URT were first-time applied on nanocapsules. The methods could demonstrate that increasing the number of polyelectrolyte layers yielded thicker and mechanically more resistant nanocapsule shells which might be capable of prolonging the release of incorporated drug molecules. Both parameters representing a measure of the capsule shell stiffness, firstly the slope of the approaching force-distance curve (AFM result), and secondly the relative ultrasonic velocity corrected by acetate buffer velocity (obtained from URT), increased with the number of polyelectrolyte shell

layers (cf. Figure 52 A, p. 98; and Figure 53 D, p. 99). Besides, the indentation depth of the tip into the particles at identical cantilever loading force decreased with increasing number of shell layers (cf. Figure 51, p. 98) and supported the idea of enhanced rigidity by polyelectrolyte complexation. Thus, by transformation of the emulsion droplets into polyelectrolyte nanocapsules with a shell composed of three or five layers, a higher stiffness of the wall could be observed using AFM and URT. These concurrent results of independent techniques are an evidence for the solidifying of the oppositely charged polyelectrolytes deposited on the oily core by complex coacervation. This idea contributes to the understanding of the nanocapsule preparation process presented in this work. Furthermore, AFM force-curve analysis indicated that the emulsion E-OSA5-5% featured a softer 'shell' than the multilayered nanocapsules did due to a less steep slope. Investigation of further emulsions and nanocapsules showed that AFM is feasible of distinguishing differently composed nanoemulsions and nanocapsules from each other by their force-curve slopes (Figure 52 B and C, p. 98).

URT also delivered information about the temperature stability of the consecutive nanocapsule samples which is important during storage or after administration. Thereby, their stability at physiological conditions over 12 h could be proven during isothermal treatment at 37 °C (Figure 45 A, p. 90). Ultrasound velocity also kept quite constant in the temperature range between 25 °C and 85 °C (Figure 45 B, p. 90), indicating resistance over considerable temperature fluctuations and thus stability against increasing storage temperatures.

Another aspect of the study was the light protection capability of the nanocapsule shell for encapsulated drugs in dependence on the shell composition. In agreement with the mechanical properties observed for the three consecutive samples, which is a thicker and more resistant and rigid shell with increasing polyelectrolyte layers, during fluorescence spectroscopy and imaging the five-layered capsule shell showed higher light attenuation compared to the three-layered capsules and the emulsion template (Figure 46, p. 92, and Figure 47, p. 93). Thus, photo-sensitive incorporated drugs could be better protected from light the more polyelectrolyte layers were surrounding the oily core. In this regard, polyelectrolyte nanocapsules were unequivocally preferable over the emulsion.

Finally, four different methods were applied to study a potential impact of a thicker and stiffer shell of the consecutive nanocapsules on the release of model drugs, and whether sustained release could be achieved by this modified capsule shell. While experiments with the diffusion limited techniques (i) dialysis bag and (ii) rotation apparatus pretended sustained liberation from the polyelectrolyte nanocapsules over days until weeks (Figure 55, p. 102, and Figure 56, p. 103), (iii) ultrafiltration (Figure 60, p. 109) and (iv) EPR studies (Figure 57, p. 105, and Figure 59, p. 108) demonstrated that the investigated nanoscaled drug delivery systems rather present fast releasing dosage forms (within minutes) for moderately lipophilic drugs ($\log P \leq 3$; TB and SAL). This discrepancy reflects that using the terms 'controlled' or 'sustained' release is meaningful only when mentioned in strong linkage to the analysis method which the data are based on. In case of polyelectrolyte nanocapsules, the first two methods mentioned did not present the true release properties of the NDDS, but the migration through the dialysis membrane, and the aqueous medium, respectively. However, ultrafiltration and EPR yielded much more reasonable and reliable results, since the colloidal dispersion could each be directly diluted with the release medium. Slow release could be observed during release tests only for extremely lipophilic

drugs such as DiI, DiR, and pTHPP ($3.7 < \log P \leq 7.6$; cf. Figure 55, p. 102, and Figure 56, p. 103). However, this is not the effort of the delivery system but of the drug´s chemical properties ($\log P$, water solubility). Between the three consecutive samples, no considerable differences in their release rate could be detected during EPR and ultrafiltration. In summary, increasing the number of shell layers of the polyelectrolyte nanocapsules improved their mechanical properties, but had no therapeutically relevant impact on the release profile of encapsulated drugs. The fast release of drugs can be explained by the very short diffusion pathways of 3-8 nm (shell thickness), representing only a weak diffusion barrier. On the basis of the EPR and ultrafiltration results, the polyelectrolyte nanocapsules cannot be claimed to be a controlled release dosage form. However, their fast release characteristics could serve for intravenous or local administration of fast effecting pharmaceuticals such as antidotes or analgetics, or parenteral nutrition.

The last focus of the thesis was to characterise selected nanocapsules concerning their *in vivo* release behaviour and physiological fate by fluorescence-labelling. *In vivo* fluorescence imaging could provide information about the *in vivo* distribution of the encapsulated model drugs nile red (NR) and DiR in the murine body without the need for sacrificing the animals. The pathway from the stomach through the intestine until the elimination via the bladder, indicating systemic absorption of NR, was well pursuable in the narcotised animal due to the fluorescence properties of the dyes (especially of DiR) and the advantage of nude mice being devoid of a disturbing coat. However, the *in vivo* release rate was not accessible because the *in vivo* fluorescence signal intensity strongly depended on many variable quantities such as the dye concentration, the area of interest, the position of the dye beneath the murine skin, the solvent environment, as well as possible quenching effects and the unidentified individual anatomy of the viscera. Thus, from fluorescence imaging a quantitative correlation between *in vitro* and *in vivo* release kinetics could not be established. Moreover, the time span consumed by peroral gavage, inhalation anaesthesia, and following multispectral imaging was multiplicative higher than the *in vitro* release rate of the nanocapsules determined by EPR and ultrafiltraion. A qualitative evaluation of the obtained *in vivo* images, however, showed that the main fraction of both dyes was eliminated renally (NR) or biliary (DiR) within 48 hours after gavage. As the visceral position of the dye or the samples, respectively, could not always be defined precisely, *ex vivo* extraction and quantification of DiR via fluorescence spectroscopy was necessary. Each after 1, 6, and 12 hours, the majority of DiR (59 to 84 %) was found in the stomach. Only small fractions of DiR were extracted from the large intestine (0, 16, and 38 %) and the small intestine (16, 0, and 0 %). From absence of the dye in the small intestine despite presence in the large intestine, systemic uptake of DiR from the colloidal drug carrier can be assumed. The thesis of systemic intestinal DiR absorption was supported by low recovery rates between 50 % (1 h) and 5 % (12 h). At all points of time investigated, the dye could not be extracted from the liver, the spleen, or the lungs (cf. Figure 65, p. 116). This information was not accessible from *in vivo* studies. Despite non-detectability of DiR by fluorescence spectroscopy, an overall fluorescence emission of the small intestinal section investigated by CLSM was observed, which is based on a lower limit of detection of CLSM. The dye was distributed punctiformly, with a dot size being in accordance with the nanocapsule size, indicating the absorption of entire nanocapsules by the intestine wall. Thus, CLSM could demonstrate the functionality of polyelectrolyte nanocapsules as drug delivery system suitable for transport through biological barriers.

LITERATURE REFERENCES

[1] S. Lenhert, A brief history of nanotechnology, http://www.nanoword.net/pages/history.htm (2009).

[2] N. Taniguchi, On the basic concept of nano-technology: Part II, Conference Proceeding, Proceedings: International Conference of Product Engineering (ICPE), Tokyo, Japan, 1974.

[3] A.S. Ziegler, Nanopartikel - pharmazeutische "Zwerge" mit Know-how, Medizinische Monatsschrift für Pharmazeuten 12 (31) (2008) 455-466.

[4] R.A. Freitas Jr., Nanomedicine, Volume I: Basic Capabilities, Landes Bioscience, Georgetown, TX, 1999.

[5] G.L. Amidon, H. Lennernas, V.P. Shah, J.R. Crison, A theoretical basis for a biopharmaceutic drug classification: the correlation of in vitro drug protect dissolution and in vivo bioavailability, Pharm. Res. 12 (1995) 413-420.

[6] J.B. Dressmann, C. Reppas, In vitro-in vivo correlations for lipophilic, poorly water-soluble drugs, Eur. J. Pharm. Sci. 11 (2000) 73-80.

[7] R. Löbenberg, G.L. Amidon, Modern bioavailability, bioequivalence and biopharmaceutical classification system. New scientific approaches to international regulatory standards, Eur. J. Biopharm. 50 (2000) 3-12.

[8] R. Gref, P. Couvreur, Nanocapsules: Preparation, Characterization and Therapeutic Applications. In: Nanoparticulates as Drug Carriers (12), (2006) 255-276.

[9] B.M. Discher, Y.-Y. Won, D.S. Ege, J.C.-M. Lee, F.S. Bates, D.E. Discher, D.A. Hammer, Polymersomes: Tough Vesicles Made from Diblock Copolymers, Science 284 (1999) 1143-1146.

[10] S. Karger, Zielgerichtete Therapie mit liposomalen Arzneimitteln, Onkologie (Beilage) 24 (1) (2001)

[11] N. Anton, J.P. Benoit, P. Saulnier, Design and production of nanoparticles formulated from nanoemulsion templates - A review, J. Control. Rel. 128 (3) (2008) 185-199.

[12] K.H. Bauer, K.-H. Frömming, C. Führer, Lehrbuch der Pharmazeutischen Technologie, 7th ed., Wissenschaftliche Verlagsgesellschaft, Stuttgart, 2002, p. 361-365.

[13] R. Voigt, Pharmazeutische Technologie, 10th ed., Deutscher Apotheker Verlag, Stuttgart, 2006, p. 553-557.

[14] A. Rübe, Development and physico-chemical characterization of nanocapsules, Thesis/Dissertation. Martin-Luther-University Halle/Wittenberg, Germany (2007).

[15] P. Couvreur, G. Couarraze, J. Devissaguet, F. Puisieux, Microencapsulation: Methods and Industrial Applications, Marcel Dekker, New York, 1996, p. 183.

[16] A. Dingler, Feste Lipid-Nanopartikel als kolloidale Wirkstoffträgersysteme zur dermalen Applikation, Thesis/Dissertation. Freie Universität Berlin, Germany (1998).

[17] W. Mehnert, A. zur Mühlen, A. Dingler, H. Weyhers, R.H. Müller, Solid lipid nanoparticles - ein neuartiger Wirkstoff-Carrier für Kosmetika und Pharmazeutika, 2. Mitteilung: Wirkstoff-Inkorporation, Freisetzung und Sterilisierbarkeit, Pharmazeutische Industrie 59 (1997) 511-514.

[18] R.H. Müller, W. Mehnert, J.-S. Lucks, A. zur Mühlen, H. Weyhers, C. Freitas, D. Rühl, Solid lipid nanoparticles (SLN) - an alternative colloidal carrier system for controlled drug delivery, Eur. J. Biopharm. 41 (1995) 62-69.

[19] R.H. Müller, K. Mäder, S. Gohla, Solid lipid nanoparticles (SLN) for controlled drug delivery - a review of the state of the art, Eur. J. Biopharm. 50 (2000) 161-177.

[20] E. Ugazio, R. Cavalli, M.R. Gasco, Incorporation of cyclosporine A in solid lipid nanoparticles (SLN), Int. J. Pharm. 241 (2002) 341-344.

[21] W. Mehnert, K. Mäder, Solid lipid nanoparticles: production, characterization and applications, Adv. Drug Deliv. Rev. 47 (2001) 165-196.

[22] K. Westesen, H. Bunjes, M.H.J. Koch, Physicochemical characterization of lipid nanoparticles and evaluation of their drug load capacitiy and sustained release potential, J. Control. Rel. 48 (1997) 223-236.

[23] K. Westesen, B. Siekmann, Investigation of the gel formation of phospholipids-stabilized solid lipid nanoparticles, Int. J. Pharm. 151 (1997) 35-45.

[24] K. Jores, Lipid nanodispersions as drug carrier systems - a physicochemical characterization, Thesis/Dissertation. Martin-Luther-University Halle/Wittenberg, Germany (2004).

[25] G. Birrenbach, Über Mizellpolymerisate, mögliche Einschlussverbindungen (Nanokapseln) und deren Eignung als Adjuvantien, Thesis/Dissertation. ETH Zürich, Switzerland (1973).

[26] G.B. Sukhorukov, E. Donath, S. Davis, H. Lichtenfeld, F. Caruso, V.I. Popov, H. Möhwald, Stepwise polyelectrolyte assembly on particle surfaces: a novel approach to colloid design, Polym. Adv. Technol. 9 (1998) 759-767.

[27] G.B. Sukhorukov, E. Donath, A.A. Antipov, pH-Controlled Macromolecule Encapsulation in and Release from Polyelectrolyte Multilayer Nanocapsules, Macromol. Rapid Commun. 22 (2001) 44-46.

[28] F. Cannone, R. Milani, G. Chirico, A. Diaspro, S. Krol, B. Campanini, Voltage regulation of single green fluorescent protein mutants, Biophys. Chem. 125 (2007) 368-374.

[29] M. Saphiannikova, I. Radtchenko, G.B. Sukhorukov, Molecular-dynamics simulations and x-ray analysis of dye precipitates in the polyelectrolyte microcapsules, J. Chem. Phys. 118 (19) (2003) 9007-9014.

[30] D. Crespy, K. Landfester, Preparation of Nylon 6 Nanoparticles and Nanocapsules by Two Novel Miniemulsion/Solvent Displacement Hybrid Techniques, Macromol. Chem. Phys. 208 (2007) 457-466.

[31] H. Hillaireau, T. Le Doan, H. Chacun, J. Janin, P. Couvreur, Encapsulation of mono- and oligo-nucleotides into aqueous-core nanocapsules in presence of various water-soluble polymers, Int. J. Pharm. 331 (2007) 148-152.

[32] Wu, Wang, Huang, Sheu, Lo, Tsai, Shieh, Yeh, Porous Iron Oxide Based Nanorods Developed as Delivery Nanocapsules, Chem. Eur. J. 13 (2007) 3878-3885.

[33] G. Berth, A. Voigt, H. Dautzenberg, E. Donath, H. Möhwald, Polyelectrolyte Complexes and Layer-by-Layer Capsules from Chitosan/Chitosan Sulfate, Biomacromolecules 3 (2002) 579-590.

[34] S. Ogawa, E. Decker, D. McClements, Production and Characterization of O/W Emulsions Containing Droplets Stabilized by Lecithin-Chitosan-Pectin Mutilayered Membranes, J. Agric. Food Chem. 52 (3) (2004) 595-600.

[35] A. Rübe, G. Hause, K. Mäder, J. Kohlbrecher, Core-shell structure of Miglyol/poly(D,L-lactide)/Poloxamer nanocapsules studied by small-angle neutron scattering, J. Control. Rel. 107 (2) (2005) 244-252.

[36] H.P. Fiedler, Lexikon der Hilfsstoffe für Pharmazie, Kosmetik und angrenzende Gebiete, Editio Cantor Verlag, Aulendorf, Germany, 1996.

[37] H.G. Bungenberg de Jong, Colloid Science II, 2nd ed., Elsevier Publishing Company, New York, 1949, p. 232-480.

[38] Y.O. Popov, J. Lee, G.H. Fredrickson, Field-Theoretic Simulations of Polyelectrolyte Complexation, Journal of Polymer Science: Part B: Polymer Physics 45 (2007) 3223-3230.

[39] F.W. Tiebackx, Gleichzeitige Ausflockung zweier Kolloide, Z. Chem. Ind. Kolloide 8 (1911) 198.

[40] H.G. Bungenberg de Jong, H.R. Kruyt, Coacervation (Partial miscibility in colloid systems), Conference Proceeding, Proc. Konikl. Ned. Akad. Wetershap 32, 1929, p. 849-856.

[41] A. Lamprecht, N. Ubrich, P. Maincent, Oral low molecular weight heparin delivery by microparticles from complex coacervation, Eur. J. Pharm. Biopharm. 67 (2007) 632-638.

[42] F. Weinbreck, R. de Vries, P. Schrooyen, C.G. de Kruif, Complex Coacervation of Whey Proteins and Gum Arabic, Biomacromolecules 4 (2003) 293-303.

[43] M.G. Sankalia, R.C. Mashru, J.M. Sankalia, V.B. Sutariya, Reversed chitosan-alginate polyelectrolyte complex for stability improvement of alpha-amylase: Optimization and physicochemical characterization, Eur. J. Pharm. Biopharm. 65 (2007) 215-232.

[44] J.T.G. Overbeek, M.J. Voorn, Phase separation in polyelectrolyte solutions. The Theory of complex coacervation, J. Cell. Comp. Physiol. 49 (S1) (1965) 7-26.

[45] S. Mao, U. Bakowsky, A. Jintapattanakit, T. Kissel, Self-Assembled Polyelectrolyte Nanocomplexes between Chitosan Derivatives and Insulin, J. Pharm. Sci. 95 (5) (2006) 1035-1048.

[46] H. Fessi, F. Puisieux, J.P. Devissaguet, N. Ammoury, S. Benita, Nanocapsule formation by interfacial polymer deposition following solvent displacement, Int. J. Pharm. 55 (1) (1989) R1-R4.

[47] K. Fujimoto, T. Toyoda, Y. Fukui, Preparation of Bionanocapsules by the Layer-by-Layer Deposition of Polypeptides onto a Liposome, Macromolecules 2007 (2007).

[48] X. Qiu, E. Donath, H. Möhwald, Permeability of Ibuprofen in various polyelectrolyte multilayers, Macromol. Mater. Eng. 286 (91) (2001) 597.

[49] S. Ye, C. Wang, X. Liu, Z. Tong, Multilayer nanocapsules of polysaccharide chitosan and alginate through layer-by-layer assembly directly on PS nanoparticles for release, J. Biomat. Sci. Polymer Edn. 16 (2005) 909-923.

[50] S. Schultz, G. Wagner, J. Ulrich, Hochdruckhomogenisation als ein Verfahren zur Emulsionsherstellung, Chemie Ingenieur Technik 74 (7) (2002) 901-909.

[51] T. Tadros, P. Izquierdo, J. Esquena, C. Solans, Formation and stability of nano-emulsions, Adv. Colloid Interface Sci. 108-109 (2004) 303-318.

[52] I. Reiche, Herstellung und Charakterisierung von polymerstabilisierten Nanokapseln (Diploma), Thesis/Dissertation. Martin-Luther-University Halle/Wittenberg, Germany (2006).

[53] L. Jia, Nanoparticle Formulation Increases Oral Bioavailability of Poorly Soluble Drugs: Approaches, Experimental Evidences and Theory, Current Nanoscience 1 (2005) 237-243.

[54] B.A. Bergenstahl, P.M. Claesson, Surface forces in emulsions. In: Food Science and Technology 2nd ed. (81), (1990) 41-55.

[55] H. Mirhosseini, C.P. Tan, N.S.A. Hamid, S. Yusof, Optimization of the contents of Arabic gum, xanthan gum and orange oil affecting turbidity, average particle size, polydispersity index and density in orange beverage emulsion, Food Hydrocolloids 22 (7) (2008) 1212-1223.

[56] M. Jumaa, P. Kleinebudde, B.W. Müller, Mixture experiments with the oil phase of parenteral emulsions, Eur. J. Pharm. Biopharm. 46 (1998) 161-167.

[57] K. Urban, Zum Emulgieren mit Dispergierscheiben, Rotor-Stator- und Hochdruck-Systemen, Thesis/Dissertation. Martin-Luther-University Halle/Wittenberg, Germany (2006).

[58] H. Wennerstroem, Thermodynamic theory of surfactant phases, Curr. Opin. Colloid Interface Sci. 1 (3) (1996) 370-375.

[59] A. Ben-Shaul, W.M. Gelbart, Statistical thermodynamics of amphiphile self-assembly: Structure and phase transitions in micellar solutions, Micelles, Membr., Microemulsions, Monolayers (1994) 1-104.

[60] H. Schott, Existence of spherical micelles. Comments, J. Pharm. Sci. 62 (1) (1973) 162-166.

[61] A.K. Rakshit, Micelles: A short review, J. Indian Chem. Soc. 85 (12) (2008) 1289-1300.

[62] M. Gradzielski, Self-assembling amphiphilic systems, Schr. Forschungszent. Juelich, Mater. 10 (Soft Matter: Complex Materials on Mesoscopic Scale) (2002) B8-1-B8/24.

[63] K.A. Yoon, D.J. Burgess, Effect of nonionic surfactant on transport of model drugs in emulsions, Pharm. Res. 13 (3) (1996) 433-439.

[64] J.-F. Gohy, Block Copolymer Micelles. In: Adv. Polym. Sci. 190 (2005) 65-136.

[65] N. Anton, P. Gayet, J.P. Benoit, P. Saulnier, Nano-emulsions and nanocapsules by the PIT method: An investigation on the role of the temperature cycling on the emulsion phase inversion, Int. J. Pharm. 344 (1-2) (2007) 44-52.

[66] A. Calvör, Herstellung bioabbaubarer Mikropartikel mittels Hochdruckhomogenisation, Thesis/Dissertation. Christian-Albrechts-University Kiel, Germany (1997).

[67] G. Binnig, H. Rohrer, Ch. Gerber, Surface studies by scanning tunnelling microscopy, Phys. Rev. Lett. 49 (1982) 57-61.

[68] G. Binnig, C.F. Quate, Ch. Gerber, Atomic force microscope, Phys. Rev. Lett. 56 (1986) 930-933.

[69] H.J. Butt, B. Cappella, M. Kappl, Force measurements with the atomic force microscope: Technique, interpretation and applications, Surface Science Reports 59 (1-6) (2005) 1-152.

[70] L. Matyus, A. Jenei, S. Damjanovich, Atomic force microscopy in cell biology, Fluoresc. Microsc. Fluoresc. Probes, 2nd ed. (1998) 41-46.

[71] S.A.C. Gould, J.B. Shulman, D.A. Schiraldi, M.L. Occelli, Atomic force microscopy (AFM) studies of liquid crystalline polymer (LCP) surfaces, J. Appl. Polym. Sci. 74 (9) (1999) 2243-2254.

[72] H.P. Lang, M. Hegner, E. Meyer, C. Gerber, Nanomechanics from atomic resolution to molecular recognition based on atomic force microscopy technology, Nanotechnology 13 (5) (2002) R29-R36.

[73] A.J. Malkin, M. Plomp, A. McPherson, Unraveling the architecture of viruses by high-resolution atomic force microscopy, Methods Mol.Biol. 292, Totowa, NJ, USA, (2005) 85-108.

[74] C. Gorzelanny, T. Goerge, E. Schnaeker, K. Thomas, T.A. Luger, S.W. Schneider, Atomic force microscopy as an innovative tool for nanoanalysis of native stratum corneum, Exp. Dermatol. 15 (5) (2006) 387-391.

[75] Y.L. Lyubchenko, L.S. Shlyakhtenko, A.A. Gall, Atomic force microscopy imaging and probing of DNA, proteins, and protein DNA complexes: silatrane surface chemistry, Methods Mol. Biol. 543 (2009) 337-351.

[76] R. Kostic, M. Miric, T. Radic, M. Radovic, R. Gajic, Z.V. Popovic, Optical characterization of graphene and highly oriented pyrolytic graphite, Acta Phys. Pol., A 116 (4) (2009) 718-721.

[77] J.L. Hutter, J. Bechhoefer, Calibration of atomic-force microscope tips, Rev. Sci. Instrum. 64 (7) (1993) 1868-1873.

[78] H. Takano, J.R. Kenseth, S.-S. Wong, J.C. O´Brien, M.D. Porter, Chemical and Biochemical Analysis Using Scanning Force Microscopy, Chem. Rev. 99 (10) (1999) 2845-2890.

[79] E. Balnois, G. Papastravrou, K.J. Wilkinson, Force microscopy and force measurements of environmental colloids. In: Environmental Colloids and Particles: Behaviour, Separation and Characterisation (9), (2007) 405-467.

[80] J. Nalaskowski, A.V. Nguyen, J. Hupka, J.D. Miller, Study of particle-bubble interaction using atomic force mocroscopy - current possibilities and challenges, Physicochemical Problems of Mineral Processing 36 (2002) 253-272.

[81] D. Keller, C. Bustamante, Attaching molecules to surfaces for scanning probe microscopy, Biophys. J. 64 (1993) 896-897.

[82] S.N. Magonov, D.H. Reneker, Characterization of polymer surfaces with atomic force microscopy, Annu. Rev. Mater. Sci. 27 (1997) 175-222.

[83] Q. Zhong, D. Innis, K. Kjoller, V.B. Elings, Fractured polymer/silica fiber surface studied by tapping mode atomic force microscopy, Surf. Sci. Lett. 290 (1993) L688-L692.

[84] M. Fritz, M. Radmacher, J.P. Cleveland, M.W. Allersma, R.J. Stewart, R. Gieselmann, P. Janmey, C.F. Schmidt, P.K. Hansma, Imaging globular and filamentous proteins in physiological buffer solutions with tapping mode atomic force microscopy, Langmuir 11 (1995) 3529-3535.

[85] Y. Martin, C.C. Williams, H.K. Wickramasinghe, Atomic force microscope - force mapping and profiling on a sub 100-Å scale, J. Appl. Phys. 61 (1987) 4723-4729.

[86] F.J. Giessibl, Atomic resolution of the silicon (111)-(7x7) surface by atomic force microscopy, Science 267 (1995) 68-71.

[87] M. Benzanilla, B. Drake, E. Nudler, M. Kashlev, P.K. Hansma, H.G. Hansma, Motion and enzymatic degradation of DNA in the atomic force microscope, Biophys J 67 (1994) 2454-2459.

[88] R.H. Müller, C. Jacobs, O. Kayser, Nanosuspensions as particulate drug formulations in therapy: Rationale for development and what we can expect for the future, Adv. Drug Deliv. Rev. 47 (2001) 3-19.

[89] J.C. Giddings, Nonequilibrium theory of field-flow fractionation, J. Chem. Phys. 49 (1) (1968) 81-86.

[90] Wyatt Technology Corporation, Liposome Characterization by FFF-MALS-QELS (application note), www.wyatt.com/files/literature/Field_Flow_Fractionation-Liposome_Characterization.pdf (2011)

[91] J.C. Giddings, Field-Flow Fractination Handbook, Wiley-Interscience, New York, USA, 2000, p. 3-30.

[92] J.S. Tan, D.E. Butterfield, C.L. Voyckeck, K.D. Caldwell, J.T. Li, Surface modification of nanoparticles by PEO/PPO block copolymers to minimize interactions with blood components and prolong blood circulation in rats, Biomaterials 14 (11) (1993) 823-833.

[93] C. Augsten, Asymmetrische Fluß Feld-Fluß Fraktionierung in Verbindung mit Mehrwinkellichtstreu-detektion - Eine neue bedeutende Methode der Pharmazeutischen Analytik zur Charakterisierung von Makromolekülen und Nanopartikeln, Thesis/Dissertation. Martin-Luther-University Halle/Wittenberg, Germany (2008).

[94] K.D. Caldwell, Field-flow fractionation, Anal. Chem. 60 (17) (1988) 959-971.

[95] C. Augsten, K. Maeder, Asymmetrical Flow Field-Flow Fractionation combined with Multi-Angle Light Scattering - a new method of growing importance in pharmaceutical analytics, Pharm. Ind. 68 (12) (2006) 1412-1419.

[96] J.C. Giddings, Field-flow fractionation of macromolecules, J. Chromatogr. 470 (2) (1989) 327-335.

[97] J.C. Giddings, Field-flow fractionation: analysis of macromolecular, colloidal, and particulate materials, Science 260 (5113) (1993) 1456-1465.

[98] S. Stolnik, B. Daudali, A. Arien, J. Whetstone, C.R. Heald, M.C. Garnett, S.S. Davis, L. Illum, The effect of surface coverage and conformation of poly(ethylene oxide) (PEO) chains of poloxamer 407 on the biological fate of model colloidal drug carriers, Biochim. Biophys. Acta 1514 (2001) 261-279.

[99] B. Roda, A. Zattoni, P. Reschiglian, M.H. Moon, M. Mirasoli, E. Michelini, A. Roda, Field-flow fractionation in bioanalysis: A review of recent trends, Anal. Chim. Acta 635 (2009) 132-143.

[100] L. Illum, I.M. Hunneyball, S.S. Davis, The effect of hydrophilic coatings on the uptake of colloidal particles by the liver and by peritoneal macrophages, Int. J. Pharm. 29 (1986) 53-65.

[101] W. Van de Sande, A. Persoons, The size and shape of macromolecular structures: Determination of the radius, the length and the persistance length of rod-like micelles of dodecyldimethylammonium chloride and bromide, J. Phys. Chem. 89 (1985) 404-406.

[102] C. Passirani, G. Barratt, J.P. Devissaguet, D. Labarre, Long-circulating nanoparticles bearing heparin or dextran covalently bound to poly(methylmethacrylate), Pharm. Res. 15 (1998) 1046-1050.

[103] R. Weissleder, A. Bogdanov, E.A. Neuwelt, M. Papisov, Long circulating iron oxides for MR imaging, Adv. Drug Deliv. Rev. 16 (1995) 321-334.

[104] C. Washington, Particle size analysis in pharmaceutics and other industries - theory and practice, Ellis Horwood Ltd., Chichester, England, 1992, p. 155-163.

[105] M. Hendrickx, L. Ludikhuyze, I. van den Broeck, C. Weemaes, Effects of high pressure on enzymes related to food quality, Trends Food Sci. Technol. 9 (197) (1998) 203.

[106] D. Knorr, Novel approaches in food-processing technology: new technologies for preserving foods and modifying function, Curr. Opin. Biotechnol. 10 (1999) 485-491.

[107] V.V. Lulevich, D. Andrienko, O.I. Vinogradova, Elasticity of polyelectrolyte multilayer microcapsules, J. Chem. Phys. 120 (8) (2004) 3822-3826.

[108] P.M. Macdonald, K.J. Crowell, C.M. Franzin, P. Mitrakos, D. Semchyschyn, ^{2}H NMR and poly-electrolyte-induced domains in lipid bilayers, Solid State Nucl. Magn. Reson. 16 (1-2) (2000) 21-36.

[109] Y.F. Dufrêne, G.U. Lee, Advances in the characterization of supported lipid films with the atomic force microscope, Biochim. Biophys. Acta, Biomembr. 1509 (1-2) (2000) 14-41.

[110] M. Radmacher, Kraftmikroskopie an weichen Proben, Thesis/Dissertation. Technical University Munich, Germany (1993).

[111] S. Roes, Scanning force microscopic investigations of membrane characteristics and membrane protein interaction effects, Thesis/Dissertation. Christian- Albrechts- University Kiel, Germany (2004).

[112] A. Rosa-Zeiser, E. Weilandt, S. Hild, O. Marti, The simultaneous measurement of elastic, electrostatic and adhesive properties by scanning force microscopy: pulsed-force mode operation, Meas. Sci. Technol. 8 (11) (1997) 1333-1338.

[113] J. Schwiertz, W. Meyer-Zaika, L. Ruiz-Gonzalez, J.M. Gonzalez-Calbet, M. Vallet-Regi, M. Epple, Calcium phosphate nanoparticles as templates for nanocapsules prepared by the layer-by-layer technique, J. Mater. Chem. 18 (32) (2008) 3831-3834.

[114] N.A. Burnham, R.J. Colton, Scanning Tunnelling Microscopy and Spectroscopy (1993) p. 191.

[115] M.J.W. Povey, Ultrasonic Techniques for Fluids Characterization, Academic Press, San Diego, CA, USA, 1997.

[116] W. Schaaffs, Landolt-Börnstein: Zahlenwerte und Funktionen aus Naturwissenschaften und Technik. Group II: Atomic and Molecular Physics, Vol. 5: Molecular Acoustics, Springer-Verlag, Berlin, 1967.

[117] A.B. Wood, A Textbook of sound, Bell and Sons, London, UK, 1941, p. 360-361.

[118] D. Moinard-Checot, Y. Chevalier, S. Briancon, H. Fessi, S. Guinebretiere, Nanoparticles for drug delivery: review of the formulation and process difficulties illustrated by the emulsion-diffusion process, J. Nanosci. Nanotechnol. 6 (9/10) (2006) 2664-2681.

[119] C.S. Leopold, Coated dosage forms for colon-specific drug delivery, Pharm. Sci. Technol. Today 2 (5) (1999) 197-204.

[120] P. Menei, C. Montero-Menei, M.C. Venier, J.P. Benoit, Drug delivery into the brain using poly(lactide-co-glycolide) microspheres, Expert Opin. Drug Deliv. 2 (2) (2005) 363-376.

[121] P.I. Hair, M.P. Curran, S.J. Keam, Tramadol extended-release tablets, Drugs 66 (15) (2006) 2017-2027.

[122] A.J. Miller, K.J. Smith, Controlled-release opioids, Pain (2003) 449-473.

[123] K. Rickels, Alprazolam extended-release in panic disorder, Expert Opin. Pharmacother. 5 (7) (2004) 1599-1611.

[124] G.L. Bakris, E.A. Tarka, B. Waterhouse, M.R. Goulding, A. Madan, K.M. Anderson, Cardiovascular risk factors in hypertension: rationale and design of studies to investigate the effects of controlled-release carvedilol on regression of left ventricular hypertrophy and lipid profile, Am. J. Cardiol. 98 (7A) (2006) 46L-52L.

[125] K.P.R. Chowdary, Y.S. Rao, Mucoadhesive microspheres for controlled drug delivery, Biol. Pharm. Bull. 27 (11) (2004) 1717-1724.

[126] S. Freiberg, X.X. Zhu, Polymer microspheres for controlled drug release, Int. J. Pharm. 282 (1-2) (2004) 1-18.

[127] C.R. Chapple, Night time symptom control with omnic (tamsulosin) oral controlled absorption system (OCAS), Eur. Urol., Suppl. 4 (7) (2005) 14-16.

[128] D. Gallardo, B. Skalsky, P. Kleinebudde, Controlled Release Solid Dosage Forms Using Combinations of (meth)acrylate Copolymers, Pharm. Dev. Technol. 13 (5) (2008) 413-423.

[129] D.M. Tenero, L.S. Henderson, C.A. Baidoo, A.H. Harter, A.M. Campanile, T.M. Danoff, D. Boyle, Pharmacokinetic properties of a new controlled-release formulation of carvedilol, Am. J. Cardiol. 98 (7A) (2006) 5L-16L.

[130] K.C. Waterman, A critical review of gastric retentive controlled drug delivery, Pharm. Dev. Technol. 12 (1) (2007) 1-10.

[131] M.A. Weber, D.A. Sica, E.A. Tarka, M. Iyengar, R. Fleck, G.L. Bakris, Controlled-release carvedilol in the treatment of essential hypertension, Am. J. Cardiol. 98 (7A) (2006) 32L-38L.

[132] W.I. Higuchi, N.F.H. Ho, H.P. Merkle, Design of oral drug delivery systems - past, present and future, Drug Dev. Ind. Pharm. 9 (7) (1983) 1227-1239.

[133] P. Singh, V. Sihorkar, V. Mishra, B. Saravanababu, N. Venkatesan, S.P. Vyas, Osmotic pumps. From present view to newer perspectives in pharmaceutical industry, East. Pharm. 42 (503) (1999) 39-46.

[134] F. Theeuwes, Oros osmotic system development, Drug Dev. Ind. Pharm. 9 (7) (1983) 1331-1357.

[135] R. Wakode, R. Bhanushali, A. Bajaj, Development and evaluation of push-pull based osmotic delivery system for pramipexole, PDA J. Pharm. Sci. Technol. 62 (1) (2008) 22-31.

[136] M. Madan, S. Lewis, J.A. Baig, Biodegradable injectable implant systems for sustained delivery using poly (lactide-co-glycolide) copolymers, Int. J. Pharm. Sci. 1 (Suppl. 1) (2009) 103-107.

[137] C. Matschke, U. Isele, P. van Hoogevest, A. Fahr, Sustained-release injectables formed in situ and their potential use for veterinary products, J. Control. Rel. 85 (2002) 1-15.

[138] T.M. Allen, T. Mehra, C. Hansen, Y.C. Chin, Stealth liposomes: an improved sustained release system for 1-beta-D-arabinofuranosylcytosine, Cancer Res. 52 (9) (1992) 2431-2439.

[139] I. Colombo, M. Grassi, R. Lapasin, S. Pricl, Determination of the drug diffusion coefficient in swollen hydrogel polymeric matrixes by means of the inverse sectioning method, J. Control. Rel. 47 (3) (1997) 305-314.

[140] N. Faisant, J. Akiki, F. Siepmann, J.P. Benoit, J. Siepmann, Effects of the type of release medium on drug release from PLGA-based microparticles: Experiment and theory, Int. J. Pharm. 314 (2) (2006) 189-197.

[141] D. Klose, F. Siepmann, K. Elkharraz, J. Siepmann, PLGA-based drug delivery systems: Importance of the type of drug and device geometry, Int. J. Pharm. 354 (1-2) (2008) 95-103.

[142] A.C. Newns, G.S. Park, Diffusion coefficient of benzene in a variety of elastomeric polymers, Journal of Polymer Science, Polymer Symposia 22 (Pt. 2) (1969) 927-937.

[143] M. Paulsson, K. Edsman, Controlled Drug Release from Gels Using Lipophilic Interactions of Charged Substances with Surfactants and Polymers, J. Colloid Interface Sci. 248 (1) (2002) 194-200.

[144] J. Siepmann, N. Faisant, J. Akiki, J. Richard, J.P. Benoit, Effect of the size of biodegradable microparticles on drug release: experiment and theory, J. Control. Rel. 96 (1) (2004) 123-134.

[145] R. Srikar, A.L. Yarin, C.M. Megaridis, A. Bazilevsky, V, E. Kelley, Desorption-limited mechanism of release from polymer nanofibers, Langmuir 24 (3) (2008) 965-974.

[146] X. Zhang, U.P. Wyss, D. Pichora, M.F.A. Goosen, A. Gonzal, C.L. Marte, Controlled release of testosterone and 17b-estradiol from biodegradable cylinders, J. Control. Rel. 29 (1-2) (1994) 157-161.

[147] N. Faisant, J. Akiki, F. Siepmann, J.P. Benoit, J. Siepmann, Effects of the type of release medium on drug release from PLGA-based microparticles: Experiment and theory, Int. J. Pharm. 314 (2) (2006) 189-197.

[148] M. Paulsson, K. Edsman, Controlled Drug Release from Gels Using Lipophilic Interactions of Charged Substances with Surfactants and Polymers, J. Colloid Interface Sci. 248 (1) (2002) 194-200.

[149] J. Siepmann, N. Faisant, J. Akiki, J. Richard, J.P. Benoit, Effect of the size of biodegradable microparticles on drug release: experiment and theory, J. Control. Rel. 96 (1) (2004) 123-134.

[150] R. Srikar, A.L. Yarin, C.M. Megaridis, A. Bazilevsky, V, E. Kelley, Desorption-limited mechanism of release from polymer nanofibers, Langmuir 24 (3) (2008) 965-974.

[151] X. Zhang, U.P. Wyss, D. Pichora, M.F.A. Goosen, A. Gonzal, C.L. Marte, Controlled release of testosterone and 17b-estradiol from biodegradable cylinders, J. Control. Rel. 29 (1-2) (1994) 157-161.

[152] A.R. Allnatt, A.B. Lidiard, Statistical theories of atomic transport in crystalline solids, Rep. Prog. Phys. 50 (4) (1987) 373-472.

[153] M.A. Islam, Einstein-Smoluchowski diffusion equation: A discussion, Physica Scripta 70 (2-3) (2004) 120-125.

[154] E.A. Moelwyn-Hughes, Physical Chemistry. 2nd ed, Pergamon Press, London, 1961, p. 1333.

[155] F. Langenbucher, D. Benz, W. Kuerth, H. Moeller, M. Otz, Standardized flow-cell method as an alternative to existing pharmacopoeial dissolution testing, Pharm. Ind. 51 (11) (1989) 1276-1281.

[156] B.J. Boyd, Characterisation of drug release from cubosomes using the pressure ultrafiltration method, Int. J. Pharm. 260 (2) (2003) 239-247.

[157] B. Magenheim, M.Y. Levy, S. Benita, A new in vitro technique for the evaluation of drug release profile from cooloidal carriers - ultrafiltration technique at low pressure, Int. J. Pharm. 94 (1993) 115-123.

[158] K.M. Rosenblatt, D. Douroumis, H. Bunjes, Drug release from differently structured monoolein/poloxamer nanodispersions studied with differential pulse polarography and ultrafiltration at low pressure, J. Pharm. Sci. 96 (6) (2007) 1564-1575.

[159] A. Rübe, K. Mäder, Electron Spin Resonance Study on the Dynamics of Polymeric Nanocapsules, J. Biomed. Nanotechnol. 1 (2) (2005) 208-213.

[160] G. Jeschke, Electron paramagentic resonance: recent developments and trends., Curr. Opin. Solid State Mater. 7 (2003) 181-188.

[161] I. Katzhendler, K. Mäder, M. Friedman, Structure and hydration properties of hydroxypropylmethyl cellulose matrices containing naproxen and naproxen sodium, Int. J. Pharm. 200 (2000) 161-179.

[162] C. Kroll, W. Herrmann, R. Stosser, H.H. Borchert, K. Mäder, Influence of drug treatment on the microacidity in rat and human skin - an in vitro electron spin resonance imaging study, Pharm. Res. 18 (2001) 525-530.

[163] K.i. Matsumoto, T. Yahiro, K. Yamada, H. Utsumi, In vivo EPR spectroscopic imaging for a liposomal drug delivery system, Magn. Reson. Med. 53 (2005) 1158-1165.

[164] K. Mäder, Pharmaceutical Application of electron spin resonance spectroscopy (ESR), PZ Prisma 5 (1998) 202-212.

[165] A. Rübe, S. Klein, K. Mäder, Monitoring of in vitro fat digestion by Electron Paramagnetic Resonance Spectroscopy, Pharm. Res. 23 (2006) 2024-2029.

[166] T. Yamaguchi, S. Itai, H. Hayashi, S. Soda, A. Hamada, H. Utsumi, In vivo ESR studies on pharmacokinetics and metabolism of parenteral lipid emulsion in living mice, Pharm. Res. 13 (1996) 729-733.

[167] K. Mäder, G. Bacic, A. Domb, H.M. Swartz, Characterization of microstructures in drug delivery systems by EPR spectroscopy, Conference Proceeding, 22nd, 1995, p. 780-781.

[168] K. Mäder, Monitoring drug release and polymer erosion from therapeutically used biodegradable drug carriers by EPR and MRI in vitro and in vivo, Radiol. Oncol. 32 (1) (1998) 89-94.

[169] K. Mäder, B. Bittner, Y. Li, W. Wohlauf, T. Kissel, Monitoring microviscosity and microacidity of the albumin microenvironment inside degrading microparticles from poly(lactide-co-glycolide) (PLG) or ABA-triblock polymers containing hydrophobic poly(lactide-co-glycolide) A blocks and hydrophilic poly(ethylene oxide) B blocks, Pharm. Res. 15 (5) (1998) 787-793.

[170] D.J. Lurie, K. Mäder, Monitoring drug delivery processes by EPR and related techniques-principles and applications, Adv. Drug Deliv. Rev. 57 (8) (2005) 1171-1190.

[171] S. Strübing, H. Metz, K. Mäder, Mechanistic analysis of drug release from tablets with membrane controlled drug delivery, Eur. J. Pharm. Biopharm. 66 (1) (2007) 113-119.

[172] I. Katzhendler, K. Mäder, M. Friedman, Correlation between drug release kinetics from protein matrix and matrix structure: EPR and NMR study, J. Pharm. Sci. 89 (3) (2000) 365-381.

[173] J.E. Wertz, J.R. Bolton, Electron Spin Resonance; Elementary Theory and Practical Applications., McGraw-Hill Inc., McGraw-Hill Series in Advanced Chemistry, New York, 1972, p. 497.

[174] L.J. Berliner, J. Reuben, Editors., Biological Magnetic Resonance, Vol. 8: Spin Labeling: Theory and Applications, Plenum, New York, 1989, p. 650.

[175] L.J. Berliner, Editor., In Vivo EPR (ESR) Theory and Application, Kluwer Academic/Plenum Publishers, New York, 2003, p. 656.

[176] S.S. Eaton, G.R. Eaton, Electron paramagnetic resonance spectroscopy, Charact. Mater. 2 (2003) 792-804.

[177] A. Faucitano, A. Buttafava, L. Montanari, F. Cilurzo, B. Conti, I. Genta, L. Valvo, Radiation-induced free radical reactions in polymer/drug systems for controlled release: an EPR investigation, Radiat. Phys. Chem. 67 (1) (2003) 61-72.

[178] R.L. Magin, P.D. Morse, II, Rapid measurement of drug release from temperature-sensitive liposomes by electron paramagnetic resonance and radioisotope techniques, Biochim. Biophys. Acta, General Subjects 760 (3) (1983) 357-362.

[179] K. Mäder, H.H. Borchert, R. Stoesser, N. Groth, T. Herrling, Model studies of the localization and mobility of drugs within polymer foils by EPR tomography, Pharmazie 46 (6) (1991) 439-442.

[180] K. Mäder, Y. Crémmilleux, A.J. Domb, J.F. Dunn, H.M. Swartz, In vitro/in vivo comparison of drug release and polymer erosion from biodegradable P(FAD-SA) polyanhydrides-a noninvasive approach by the combined use of electron paramagnetic resonance spectroscopy and nuclear magnetic resonance imaging, Pharm. Res. 14 (6) (1997) 820-826.

[181] N. Rapoport, L. Pitina, Intracellular Distribution and Intracellular Dynamics of a Spin-Labeled Analog of Doxorubicin by Fluorescence and EPR Spectroscopy, J. Pharm. Sci. 87 (3) (1998) 321-325.

[182] K. Jores, W. Mehnert, K. Maeder, Physicochemical investigations on solid lipid nanoparticles and on oil-loaded solid lipid nanoparticles: a nuclear magnetic resonance and electron spin resonance study, Pharm. Res. 20 (8) (2003) 1274-1283.

[183] L. Heinrich, A.-M. Freyria, M. Melin, Y. Tourneur, R. Maksoud, J.-C. Bernengo, D.J. Hartmann, Confocal laser scanning microscopy using dialkylcarbocyanine dyes for cell tracing in hard and soft biomaterials, J. Biomed. Mater. Res. B: Appl. Biomater. 81 (2006) 153-161.

[184] F. Lottspeich, J.W. Engels, Bioanalytik; section 8.6 Konfokale Laser-Scanning Mikroskopie, 2nd ed., Spektrum Verlag, Elsevier GmbH, Munich, Germany, 2006, p. 193.

[185] B.V.R. Tata, B. Raj, Confocal laser scanning microscopy: applications in material science and technology, Bull. Mater. Sci. 21 (4) (1998) 263-278.

[186] S.A. Stricker, M. Whitaker, Confocal laser scanning microscopy of calcium dynamics in living cells, Microsc. Res. Tech. 46 (6) (1999) 356-369.

[187] J. Itoh, A. Matsuno, Y. Yamamoto, K. Kawai, A. Serizawa, K. Watanabe, Y. Itoh, R.Y. Osamura, Confocal laser scanning microscopic imaging of subcellular organelles, mRNA, protein products, and the microvessel environment, Acta Histochem. Cytochem. 34 (4) (2001) 285-297.

[188] M. Roderfeld, S. Matern, E. Roeb, Confocal laser scanning microscopy: a deep look into the cell, Dtsch. Med. Wochenschr. 128 (48) (2003) 2539-2542.

[189] N. Loren, M. Langton, A.M. Hermansson, Confocal fluorescence microscopy (CLSM) for food structure characterisation, Understanding Controlling Microstruct. Complex Foods (2007) 232-260.

[190] B.J. Haupt, A.E. Pelling, M.A. Horton, Integrated confocal and scanning probe microscopy for biomedical research, The Scientific World 6 (Dec.) (2006) 1609-1618.

[191] Invitrogen, Product information on DiR (1,1'-dioctadecyl-3,3,3',3'-tetramethylindotricarbocyanine iodide (DiIC$_{18}$(7), catalog number D-12731), http://products.invitrogen.com/ivgn/product/D12731?ICID=search-product (2010)

[192] R. Schrieber, H. Gareis, Gelatine Handbook - Theory and Industrial Practice, WILEY-VCH Verlag, Weinheim, Germany, 2007

[193] R.A.A. Muzzarelli, Handbook of Hydrocolloids, 2nd ed., Woodhead Publishing Limited, Cambridge, England, 2009

[194] J. Kristl, J. Šmid-Korbar, E. Štruc, M. Schara, H. Rupprecht, Hydrocolloids and gels of chitosan as drug carriers, Int. J. Pharm. 99 (1993) 13-19.

[195] T.J. Podlas, P. Ander, Interaction of Sodium and Potassium Ions with kappa- and lambda-Carrageenan in Aqueous Solutions with and without Added Salt, Macromolecules 2 (4) (1969) 432-436.

[196] W. Meier, Polymer nanocapsules, Chem. Soc. Rev. 29 (5) (2000) 295-303.

[197] Ö. Çelik, J. Akbuga, Preparation of superoxide dismutase loaded chitosan microspheres: Characterization and release studies, Eur. J. Pharm. Biopharm. 66 (2007) 42-47.

[198] Z.Z. Denchev, Biodegradation Studies of Biopolymer Blends and Composites. In: in: Handbook of Engineering Biopolymers: Homopolymers, Blends, and Composites (ed. Fakirov, Stoyko and Bhattacharyya, Debes) (27), (2007) 799-841.

[199] A. Viswanathan, Effect of degree of substitution of octenyl succinate starch on enzymic degradation, J. Environ. Polym. Degradation 7 (4) (1999) 185-190.

[200] T. Spychaj, K. Wilpiszewska, S. Spychaj, Starch-Urethane Polymers: Physicochemical Aspects, Properties, Application. In: in: Handbook of Engineering Biopolymers: Homopolymers, Blends, and Composites (ed. Fakirov, Stoyko and Bhattacharyya, Debes) (5), (2007) 155-189.

[201] A. Domb, S. Amselem, J. Shah, M. Maniar, Degradable Polymers for Site-specific Drug Delivery, Polym. Adv. Technol. 3 (1992) 279-292.

[202] S. Fakirov, Gelatin and gelatin-based biodegradable composites: manufacturing, properties and biodegradation behavior. In: in: Handbook of Engineering Biopolymers: Homopolymers, Blends, and Composites (ed. Fakirov, Stoyko and Bhattacharyya, Debes) (14), (2007) 419-466.

[203] CP Kelco, Safety data sheet of GENU pectin type beta, ecological information, 2006.

[204] M. Guibet, S. Colin, T. Barbeyron, S. Genicot, B. Kloareg, G. Michel, W. Helbert, Degradation of l-carrageenan by *Pseudoalteromonas carrageenovora* l-carrageenase: a new family of glycoside hydrolases unrelated to k- and i-carrageenases, Biochem. J. 404 (2007) 105-114.

[205] F. Michel, J.F. Thibault, C. Mercier, F. Heitz, F. Pouleande, Extraction and characterization of pectins from beet pulp, J. Food Sci. 50 (1985) 1499-1500.

[206] R. Chanamai, D.J. McClements, Depletion Flocculation of Beverage Emulsions by Gum Arabic and Modified Starch, J. Food Sci. 66 (3) (2001) 457-463.

[207] M.S. Katsuda, D.J. McClements, L.H.S. Miglioranza, E.A. Decker, Physical and Oxidative Stability of Fish Oil-in-Water Emulsions Stabilized with ß-Lactoglobulin and Pectin, J. Agric. Food Chem. 56 (2008) 5926-5931.

[208] CP Kelco, Product information, gelling mechanism og GENU pectin, www.cpkelco.com (2009)

[209] E.L. Pippen, R.M. McCready, H.S. Owens, Gelation properties of partially acetylated pectins, J. Am. Chem. Soc. 72 (1950) 813.

[210] C.K. Siew, P.A. Williams, S.W. Cui, Q. Wang, Characterization of the Surface-Active Components of Sugar Beet Pectin and the Hydrodynamic Thickness of the Adsorbed Pectin Layer, J. Agric. Food Chem. 56 (2008) 8111-8120.

[211] C.K. Siew, P.A. Williams, Emulsification properties of sugar beet pectin, Conference Proceeding, 235th ACS National Meeting 2008,

[212] T. Funami, M. Nakauma, S. Noda, S. Ishihara, S. Al-Assaf, G.O. Phillips, Enhancement of the performance of sugar beet pectin as an emulsifier, Foods and Food Ingredients Journal of Japan 213 (4) (2008) 347-356.

[213] V.J. Morris, A.P. Gunning, A.R. Kirby, A.J. MacDougall, Pectin-protein complexes - new roles for pectin extracts, Special Publication of the Royal Society of Chemistry - Gums and Stabilizers for the Food Industry 316 (14) (2008) 477-483.

[214] T. Funami, G. Zhang, S. Noda, M. Nakauma, I. Asai, S. Al-Assaf, G.O. Phillips, Does pectin emulsification mechanism operate via an AGP (Arabinogalactan protein) type fraction?, Foods and Food Ingredients Journal of Japan 211 (3) (2006) 255-263.

[215] W. Ternes, A. Täufel, L. Tunger, M. Zabel, Lebensmittellexikon, Behr´s Verlag, Hamburg, 2005, p. 747-748.

[216] F. v.Bruchhausen, M. Albinus, H. Hager, W. Reuss, Hagers Handbuch der pharmazeutischen Praxis, Band 4, Stoffe A-D, Springer Verlag, Berlin, 1993, p. 26-28.

[217] S. Stach, Polysaccharide aus marinen Bakterien und der Mikroalge *Chlorella vulgaris*, Cuvillier Verlag, Göttingen, 2005, p. 196-200.

[218] S.S. Koide, Chitin-chitosan: properties, benefits and risks, Nutr. Res. 18 (1998) 1091-1101.

[219] C. Augsten, K. Mäder, Characterizing molar mass distributions and molecule structures of different chitosans using asymmetrical flow field-flow fractionation combined with multi-angle light scattering, Int. J. Pharm. 351 (2008) 23-30.

[220] H.-D. Belitz, W. Grosch, P. Schieberle, Lehrbuch der Lebensmittelchemie, 5th ed., Springer Verlag, Berlin, 2001, p. 907.

[221] C. Preetz, A. Rübe, I. Reiche, G. Hause, K. Mäder, Preparation and characterization of biocompatible oil-loaded polyelectrolyte nanocapsules, Nanomedicine 4 (2) (2008) 106-114.

[222] C. Preetz, A. Hauser, G. Hause, A. Kramer, K. Mäder, Application of atomic force microscopy and ultrasonic resonator technology on nanoscale: Distinction of nanoemulsions from nanocapsules, Eur. J. Pharm. Sci. 39 (2010) 141-151.

[223] C. Preetz, Development and physicochemical characterization of polyelectrolyte nanocapsules as modern drug delivery system for lipophilic food and drug molecules (Diploma), Thesis/Dissertation. Martin-Luther-University Halle/Wittenberg, Germany (2009).

[224] K. Romøren, S. Pedersen, G. Smistad, Ø. Evensen, B.J. Thu, The influence of formulation variables on in vitro transfection efficiency and physicochemical properties of chitosan-based polyplexes, Int. J. Pharm. 261 (1-2) (2003) 115-127.

[225] M. Andersson, B. Wittgren, K.G. Wahlund, Accuracy in multiangle light scattering measurements for molar mass and radius estimations. Model calculations and experiments, Anal. Chem. 75 (2003) 4279-4291.

[226] I. Horcas, R. Fernandez, J.M. Gomez-Rodriguez, J. Colchero, J. Gomez-Herrero, A.M. Baro, WSXM: a software for scanning probe microscopy and a tool for nanotechnology, Rev. Sci. Instrum. 78 (1) (2007) 013705-1-013705/8.

[227] A. Janshoff, M. Neitzert, Y. Oberdorfer, H. Fuchs, Force spectroscopy of molecular systems - single molecule spectroscopy of polymers and biomolecules, Angew. Chem. Int. Ed. Engl. 39 (18) (2000) 3212-3237.

[228] A.K. Awizio, F. Onofri, F. Benfenati, E. Bonaccurso, Influence of synapsin I on synaptic vesicles: an analysis by force-volume mode of the atomic force microscope and dynamic light scattering, Biophys. J. 93 (3) (2007) 1051-1060.

[229] H. Schillers, T. Danker, H.J. Schnittler, F. Lang, H. Oberleithner, Plasma membrane plasticity of Xenopus laevis oocyte imaged with atomic force microscopy, Cell. Physiol. Biochem. 10 (1-2) (2000) 99-107.

[230] Y. Wang, M.J.W. Povey, A simple and rapid method for the determination of particle size in emulsions from ultrasound data, Colloids Surf. B Biointerfaces 12 (3-6) (1999) 417-427.

[231] R.B. Shah, A.S. Zidan, T. Funck, M.A. Tawakkul, A. Nguyenpho, M.A. Khan, Quality by design: Characterization of self-nano-emulsified drug delivery systems (SNEDDs) using ultrasonic resonator technology, Int. J. Pharm. 341 (1-2) (2007) 189-194.

[232] C. Bruesewitz, A. Schendler, A. Funke, T. Wagner, R. Lipp, Novel poloxamer-based nanoemulsions to enhance the intestinal absorption of active compounds, Int. J. Pharm. 329 (1-2) (2007) 173-181.

[233] M. Nakauma, T. Funami, S. Noda, S. Ishihara, S. Al-Assaf, K. Nishinari, G.O. Phillips, Comparison of sugar beet pectin, soybean soluble polysaccharide, and gum arabic as food emusifiers. 1. Effect of concentration, pH, and salts on the emulsifying properties, Food Hydrocolloids 22 (7) (2008) 1254-1267.

[234] K. Mäder, H.M. Swartz, R. Stoesser, H.H. Borchert, The application of EPR spectroscopy in the field of pharmacy, Pharmazie 49 (2-3) (1994) 97-101.

[235] W. Parmentier, B. Grouber, Mikroverkapselung durch komplexe Koazervation mit Gelatine, http://www.parmentier.de/gelatine/mikrovkps.htm (2008)

[236] G. Jander, E. Blasius, Lehrbuch der analytischen und präparativen anorganischen Chemie, 13th ed., S. Hirzel Verlag, Stuttgart, 1989, p. 51.

[237] J.M. Rollot, P. Couvreur, L. Roblot-Treupel, F. Puisieux, Physicochemical and morphological characterization of polyisobutyl cyanoacrylate nanocapsules, J. Pharm. Sci. 75 (4) (1986) 361-364.

[238] J.P. Wang, X.P. Zhao, D.W. Wang, Preparation of nanocapsules containing the two-phase core materials, J. Microencapsul. 24 (8) (2007) 757-766.

[239] W.s. Wang, J. Zeng, D.l. Ruan, F. Zhong, C.y. Pan, Production of nanocapsules by in-situ polymerization, Gaofenzi Cailiao Kexue Yu Gongcheng 17 (4) (2001) 34-36.

[240] D. Moinard-Checot, Y. Chevalier, S. Briancon, H. Fessi, S. Guinebretiere, Nanoparticles for drug delivery: review of the formulation and process difficulties illustrated by the emulsion-diffusion process, J. Nanosci. Nanotechnol. 6 (9/10) (2006) 2664-2681.

[241] C.-F. Hung, J.-K. Chen, M.-H. Liao, H.-M. Lo, J.-Y. Fang, Development and Evalution of Emulsion-Liposome Blends for Resveratrol Delivery, J. Nanosci. Nanotechnol. 6 (9/10) (2006) 2950-2958.

[242] J.-Y. Fang, C.-F. Hung, M.-H. Liao, C.-C. Chien, A study of the formulation design of acoustically active liposheres as carriers for drug delivery, Eur. J. Pharm. Biopharm. 67 (2007) 67-75.

[243] C.G. de Kruif, F. Weinbreck, R. de Vries, Complex coacervation of proteins and anionic polysaccharides, Curr. Opin. Colloid Interface Sci. 9 (2004) 340-349.

[244] M. Kepczynski, J. Lewandowska, M. Romek, S. Zapotoczny, F. Ganachaud, M. Nowakowska, Silicone Nanocapsules Templated Inside the Membranes of Catanionic Vesicles, Langmuir 23 (13) (2007) 7314-7320.

[245] M. Garcia-Fuentes, M.J. Alonso, D. Torres, Design and characterization of a new drug nanocarrier made from solid–liquid lipid mixtures, J. Colloid Interface Sci. 285 (2005) 590-598.

[246] B. Bechinger, C. Aisenbrey, P. Bertani, The alignment, structure and dynamics of membrane-associated polypeptides by solid-state NMR spectroscopy, Biochim. Biophys. Acta, Biomembr. 1666 (1-2) (2004) 190-204.

[247] M. Radmacher, M. Fritz, C.M. Kacher, J.P. Cleveland, P.K. Hansma, Measuring the viscoelastic properties of human platelets with the atomic force microscope, Biophys. J. 70 (1) (1996) 556-567.

[248] K.D. Costa, Single-cell elastography: probing for disease with the atomic force microscope, Dis. Markers 19 (2-3) (2003) 139-154.

[249] S. Steltenkamp, C. Rommel, J. Wegener, A. Janshoff, Membrane stiffness of animal cells challenged by osmotic stress, Small 2 (8-9) (2006) 1016-1020.

[250]   D. Tranchida, Z. Kiflie, S. Piccarolo, Atomic Force Microscopy Nanoindentations to Reliably Measure the Young´s Modulus of Soft Matter. In: Modern Research and Educational Topics on Microscopy 3 (2007) 737-746.

[251]   N.A. Burnham, R.J. Colton, Measuring the nanomechanical properties and surface forces of materials using an atomic force microscope, Journal of Vacuum Science & Technology, A: Vacuum, Surfaces, and Films 7 (4) (1989) 2906-2913.

[252]   A. Vinckier, G. Semenza, Measuring elasticity of biological materials by atomic force microscopy, FEBS Lett. 430 (1,2) (1998) 12-16.

[253]   Public Chemical Database, Public Chemical Database, http://pubchem.ncbi.nlm.nih.gov/summary/summary.cgi?cid=65182&loc=ec_rcs (2009)

[254]   P.L. Soo, L. Luo, D. Maysinger, A. Eisenberg, Incorporation and Release of Hydrophobic Probes in Biocompatible Polycaprolactone-block-poly(ethylene oxide) Micelles: Implications for Drug Delivery, Langmuir 18 (25) (2002) 9996-10004.

[255]   N.S.S. Magalhaes, H. Fessi, F. Puisieux, S. Benita, M. Seiller, An in vitro release kinetic examination and comparative evaluation between submicron emulsion and polylactic acid nanocapsules of clofibride, J. Microencapsul. 12 (2) (1995) 195-205.

[256]   Y. Jiang, A. Schaedlich, E. Amado, C. Weis, E. Odermatt, K. Maeder, J. Kressler, In-vivo studies on intraperitoneally administrated poly(vinyl alcohol), J. Biomed. Mater. Res. B Appl. Biometar. 93B (1) (2010) 275-284.

[257]   M.L. Levenson, J.R. Mansfield, Multispectral imaging in biology and medicine: Slices of life., Cytometry A 69 (2006) 748-758.

[258]   X. He, H. Nie, K. Wang, W. Tan, X. Wu, P. Zhang, In vivo study of bio-distribution and urinary excretion of surface-modified silica nanoparticles, Anal. Chem. 80 (2008) 9597-9603.

[259]   S.B. Raymond, J. Skoch, I.D. Hills, E.E. Nesterov, T.M. Swager, B.J. Bacskai, Smart optical probes for near-infrared fluorescence imaging of Alzheimer´s disease pathology, Eur. J. Nucl. Med. Mol. Imaging 35 (2008) 93-98.

[260]   Z. Cai, Y. Wang, L.J. Zhu, Z.Q. Liu, Nanocarriers: a general strategy for enhancement of oral bioavailability of poorly absorbed or pre-systemically metabolized drugs, Curr. Drug Metab. 11 (2) (2010) 197-207.

[261]   E.O. Akala, Strategies for transmembrane passage of polymer-based nanostructures, RSC Nanosci. Nanotechnol. 9 (Polymer-Based Nanostructures) (2010) 16-80.

[262]   S.K. Lai, Y.Y. Wang, J. Hanes, Mucus-penetrating nanoparticles for drug and gene delivery to mucosal tissues, Adv. Drug Deliv. Rev. 61 (2) (2009) 158-171.

[263]   K.A. Janes, P. Calvo, M.J. Alonso, Polysaccharide colloidal particles as delivery systems for macromolecules, Adv. Drug Deliv. Rev. 47 (1) (2001) 83-97.

[264]   E. Rytting, M. Bur, R. Cartier, T. Bouyssou, X. Wang, M. Krueger, C.M. Lehr, T. Kissel, In vitro and in vivo performance of biocompatible negatively-charged salbutamol-loaded nanoparticles, J. Control. Rel. 141 (1) (2010) 101-107.

[265]   B. Pitard, M. Bello-Roufai, O. Lambert, P. Richard, L. Desigaux, S. Fernandes, C. Lanctin, H. Pollard, M. Zeghal, P.Y. Rescan, D. Escande, Negatively charged self-assembling DNA/poloxamine nanospheres for in vivo gene transfer, Nucleic Acids Res. 32 (20) (2004) e159-1-e159/8.

CURRICULUM VITAE

Name	Claudia Nyakas (née: Preetz)
Date of Birth	8 January 1982
Place of Birth	Stendal, Germany
Nationality	German
Marital status	married

2. Education

10/2006 to present	Martin-Luther-University Halle-Wittenberg, Institute of Pharmacy, Pharmaceutical Technology, PhD student in Karsten Mäder´s group
06/2009 – 09/2009	Central Institute of the German Armed Forces Medical Service, Munich, practical training for food chemists topic: *Determination of histamine and further biogenic amines in fish by HPLC-FLD*
10/2009 – 05/2010	Bayerisches Landesamt für Gesundheit und Lebensmittelsicherheit Erlangen, course in Food Chemistry (state examination)
10/2006 – 04/2009	Martin-Luther-University Halle-Wittenberg, two-and-a-half-year course in Food Chemistry (diploma) topic: *Development and physicochemical characterization of polyelectrolyte nano-capsules as modern drug delivery system for lipophilic food and drug molecules*
04/2006 – 09/2006	Central Institute of the German Armed Forces Medical Service, Munich, practical training for pharmacists, topic: *Supercritical fluid extraction (SFE) of drugs from dermal pharmaceuticals*
10/2005 – 03/2006	Pharmacy 'Apotheke am Tulpenbrunnen' Halle (Saale), practical training for pharmacists
10/2001 – 09/2005	Martin-Luther-University Halle-Wittenberg, four-year course in Pharmacy (approbation to practice pharmacy in 12/2006, state examination)
01/2001 – 09/2001	Military Service in the German Armed Forces Medical Service
10/2000 – 12/2000	Technical University Braunschweig, 3-month course in Pharmacy
06/2000	A-Levels at the Jan-Amos-Comenius grammar school in Stendal

3. Professional Experience

06/2010 to present	Central Institute of the German Armed Forces Medical Service, Munich, Authorised expert on food chemistry with focus on analysis of genetically modified organisms in food, analysis of potable water, and method development

PUBLICATIONS

Reasearch articles and diploma

[1] C. Preetz, A. Rübe, I. Reiche, G. Hause, K. Mäder, Preparation and characterization of biocompatible oil-loaded polyelectrolyte nanocapsules. Nanomedicine 4 (2) (2008) 106-114.

[2] C. Preetz, Development and physicochemical characterization of polyelectrolyte nanocapsules as modern drug delivery system for lipophilic food and drug molecules (Diploma). Martin-Luther-University Halle/Wittenberg, Germany (2009).

[3] C. Preetz, A. Hauser, G. Hause, A. Kramer, K. Mäder, Application of atomic force microscopy and ultrasonic resonator technology on nanoscale: Distinction of nanoemulsions from nanocapsules. European Journal of Pharmaceutical Sciences 39 (2010) 141-151.

Poster presentations

[1] C. Preetz, A. Rübe, G. Hause, I. Reiche, K. Mäder, Development and characterisation of polymeric nanocapsules as drug delivery systems. 1st European Science Foundation Summer School in Nanomedicine (10th – 15th June 2007), Cardiff, UK.

[2] C. Preetz, K. Mäder, Release behavior of Polyelectrolyte Nanocapsules as Drug Delivery Systems. 7th International Symposium on Polymer Therapeutics 2008: from Laboratory to Clinical Practice (26th – 28th May 2008), Valencia, Spain.

[3] C. Preetz, Development and physicochemical characterization of polyelectrolyte nanocapsules as modern drug delivery system for lipophilic food and drug molecules. Diploma presentation (30th April 2009), Department of Food Chemistry, Martin-Luther-University Halle/Wittenberg, Halle/Saale, Germany.

DECLARATION / SELBSTÄNDIGKEITSERKLÄRUNG

Hiermit erkläre ich gemäß § 5 (2) Buchstabe b der Promotionsordnung der Mathematisch-Naturwissenschaftlich-Technischen Fakultät der Martin-Luther-Universität Halle-Wittenberg, dass ich die Ergebnisse der vorliegenden Dissertationsarbeit

"Polyelectrolyte nanocapsules as modern drug delivery system for lipophilic drug candidates"

am Institut für Pharmazie, Institutsbereich 'Pharmazeutische Technologie und Biopharmazie', der Martin-Luther-Universität Halle-Wittenberg unter Anleitung von Herrn Prof. Dr. Karsten Mäder selbständig erarbeitet und die Dissertationsarbeit ohne fremde Hilfe verfasst habe. Dabei habe ich keine anderen als die von mir angegebenen Quellen und Hilfsmittel benutzt und die den benutzten Werken wörtlich oder inhaltlich entnommenen Stellen als solche kenntlich gemacht.

Weiterhin habe ich diese Arbeit bisher an keiner in- oder ausländischen Fakultät als Dissertationsschrift vorgelegt.

Halle (Saale), 16.07.2012

Claudia Nyakas

ACKNOWLEDGEMENTS / DANKSAGUNG